Theoretical investigations of terahertz generation in laser-induced microplasmas

Illia Thiele

université de BORDEAUX

THÈSE PRÉSENTÉE
POUR OBTENIR LE GRADE DE

DOCTEUR DE

L'UNIVERSITÉ DE BORDEAUX

ÉCOLE DOCTORALE
DES SCIENCES PHYSIQUES ET DE L'INGÉNIEUR
LASERS, MATIÉRE, NANOSCIENCES

Par Illia THIELE

Theoretical investigations of terahertz generation in laser-induced microplasmas

Sous la direction de: Stefan SKUPIN

Soutenue le 19 octobre 2017

Membres du jury :

M. Eric CORMIER	Prof. Dr.	Univ. Bordeaux - CNRS - CEA	Président du jury
M. Stefan SKUPIN	Dr.	Univ. Bordeaux - CNRS - CEA	Directeur de thèse
M^{me} Rachel NUTER	Dr.	Univ. Bordeaux - CNRS - CEA	Co-encadrant
M^{me} Olga KOSAREVA	Prof. Dr.	Lomonosov Moscow State University	Rapporteur
M^{me} Tünde FÜLÖP	Prof. Dr.	Chalmers University	Rapporteur
M. Mark THOMSON	Dr.	Goethe Universität Frankfurt	Examinateur
M. Luc BERGÉ	Dr.	CEA-DIF	Examinateur
M. Patrick MOUNAIX	Dr.	Univ. Bordeaux - CNRS - CEA	Examinateur
M. Evangelos SIMINOS	Dr.	Chalmers University	Invité

Résumé en français

Au cours de cette thèse, nous avons étudié théoriquement la production de rayonnement Tera-Hertz (THz) dans des microplasmas générés par des laser femtosecondes. Cette approche semble prometteuse pour créer de manière efficace des sources THz compactes et à large spectre. Le rayonnement THz intéresse de nombreuses applications comme par exemple, l'identification spectroscopique de substances dangereuses, l'imagerie en médecine ou biologie, la mesure d'épaisseur dans les processus industriels, le contrôle qualité ou encore le contrôle non-destructif de la matière (voir Chap. 1). Ces applications nécessitent la plupart du temps des sources pulsées et compactes couvrant idéalement la totalité du spectre THz allant de 0.3 à 30 THz. Elles requièrent aussi des puissances moyennes de sortie de l'ordre du μW; le contrôle non destructif, par exemple, nécessite des amplitudes THz supérieures à 0.1 MV/cm.

Les sources THz conventionnelles comme les lasers à cascade quantique, les interrupteurs photo-conducteurs et les schémas basés sur des cristaux nonlinéaires répondent aux nombreuses exigences de ces applications THz. Ensemble, elles couvrent la totalité du spectre THz. De plus, elles produisent des puissances moyennes allant jusqu'au mW avec des taux de conversion d'énergie laser supérieure à 10^{-4}, permettant d'atteindre des champs intenses de 1 MV/cm. Cependant, aucune de ces sources ne couvre, seule, le spectre THz tout entier. Mais, surtout, ces techniques sont limitées par la tenue au flux des matériaux.

Quelques unes de ces précédentes limitations peuvent être résolues en produisant un rayonnement THz dans des plasmas générés par des lasers femtosecondes. Les premiers travaux sur le sujet ont montré la production de THz à partir d'un gaz neutre ionisé par un faisceau laser (voir Sec. 1.3.1.1). Considérer un plasma permet, en effet, de s'affranchir de la limite au flux imposée par le seuil d'endommagement du matériau. Cependant, les taux de conversion énergétique atteints dans ces montages expérimentaux n'excèdent pas 10^{-8}, des valeurs bien plus faibles que celles obtenues pour les sources conventionnelles. Deux solutions ont été proposées pour augmenter cette efficacité. Tout d'abord, l'ajout un champ statique externe au faisceau laser (voir Sec. 1.3.2). Puis, une autre solution, couramment utilisée, consiste à choisir un faiceau laser à 2 couleurs. Dans ces deux cas, les taux de conversion énergétique dépassent 10^{-4} (voir Sec. 1.3.3). Ces schémas ont l'avantage certain de produire un rayonnement THz dont le spectre couvre la totalité du spectre THz. Cependant, tout comme les sources conventionnelles, ces approches basées sur l'utilisation de plasma nécessitent des lasers intenses de l'ordre du mJ, ce qui limite la portabilité et miniaturization de ces sources THz.

Afin de miniaturiser les sources THz basées sur les plasmas, Buccheri and Zhang (Sec. 1.3.1.3) ont généré du rayonnement THz en focalisant fortement un faisceau laser peu énergétique, env. 1μJ, dans un gaz. Contrairement aux approches précédentes où les lasers mJ créent des plasmas millimétriques, ce cas permet la formation de microplasma, plasma dont le taille est de quelques micromètres. Cependant, là encore, les taux de conversion énergétiques restent faibles.

Dans le but de réaliser des sources THz efficaces et de faible encombrement, cette thèse s'est focalisée sur l'étude théorique de la génération de rayonnement THz à partir de microplasma généré par des lasers femtosecondes. Pour cela, nous avons tout à la fois modélisé l'émission THz par de larges simulations fortement parallélisés résolvant les équations de Maxwell couplées à celles de la matière, mais aussi par de petits modèles analytiques simplifiés. Ces deux approches complémentaires nous ont permis d'apporter une meilleure description et compréhension des rayonnements THz observés expérimentalement. De plus, nous avons appliqué les techniques d'ajout de champ électrostatique (DC bias) et d'utilisation de laser à deux couleurs, connues pour rendre plus efficace la génération de THz dans les plasma millimétriques, aux microplasmas. Les principales étapes réalisées et résultats obtenus sont présentés ci-dessous.

Nous avons développé un modèle analytique basé sur les équations de Maxwell couplées à l'équation de Vlasov non relativiste pour les électrons, dans lequel les équations de taux d'ionisation multiples et les collisions élastiques electron-ion sont prises en compte (voir Chap. 2). Dans les conditions expérimentales générant des microplasmas, intensité laser supérieure à 10^{14} W/cm^2 et laser fortement focalisé, la réponse des électrons liés aux ions (polarisation linéaire et nonlinéaire) est négligeable devant la réponse des électrons libres. Nous avons développé les trois premiers ordres des équations aux moments de l'équation de Vlasov. Ces trois équations conduisent respectivement aux équations de continuité, d'Euler et de conservation d'énergie. Ces équations couplées aux équations de Maxwell ont été développées au moyen d'une méthode d'analyse multi-échelle. Nous supposons que les quantités microscopiques peuvent être écrites sous forme de séries perturbatives. Cela résulte dans des ensembles d'équations hiérarchisés dont chacun peut être associé à un mécanisme générant le rayonnement THz.

L'ordre le plus bas décrit le mécanisme appelé "courant d'ionization" (IC). Il tient compte des courants macroscopiques et d'ionisation produits par le champs électrique. De plus, l'analyse multi-échelle donne une équation énergétique qui tient compte du chauffage des gaz d'électrons. Cela permet d'inclure une fréquence de collision electron-ion dépendant de l'énergie des electrons. Cet ensemble d'équations modélise en particulier la production de THz dans des microplasmas générés par des lasers à 1 couleur auxquels un champ statique extérieur est appliqué, ou encore par des lasers à deux couleurs. Parfois, l'émission THz par IC peut être décrite par la méthode de propagation d'impulsions unidirectionnelles. Cependant, cette approche n'est pas adaptée à notre cas, à savoir les microplasmas, car elle ne modélise pas l'émission THz pour de grands angles d'ouverture, tout comme elle ne modélise pas les phénomènes de séparation de charge qui nécessitent la résolution des équations de Maxwell. Cela est rendu possible grâce à l'ordre le plus bas de notre modèle analytique.

L'ordre suivant de l'ensemble des équations décrit le mécanisme appelé "Cherenkov-transition" (TC). Il tient compte de l'excitation du plasma par une source pondéromotrice, mais aussi, de termes sources additionnels décrivant l'ionization, les collisions et le chauffage. Tous les termes du second ordre sont exprimés à partir des quantités calculées au premier ordre. Cet ensemble d'équations décrit la génération THz dans des microplasmas générés par des lasers de plusieurs cycles optiques.

Afin de résoudre ces équations, nous avons utilisé et/ou développé différents outils numériques. La résolution de l'équation de Vlasov a été faite avec les codes Particle In Cell (PIC) OCEAN et CALDER. La résolution des équations multi-échelle a été réalisée à l'aide du code fluide ARCTIC, développé à partir de la version "type Yee" du code OCEAN. Le code ARCTIC a été validé en comparant les spectres THz obtenus par des microplasmas générés à partir de faisceaux "2 couleurs" en géométrie 3D à ceux obtenus avec le code PIC OCEAN (voir Chap. 3).

Nous travaillons avec des faisceaux laser fortement focalisés. Il a donc été indispensable de développer, pour les codes PIC et fluide, un algorithme modélisant les faisceaux laser au-delà de l'approximation paraxiale. Cet algorithme a le grand avantage de permettre l'introduction d'impulsions laser possédant tout type de forme spatiale et/ou temporelle dans les codes électromagnétiques, par une simple description de sa forme spatio-temporelle dans un plan (voir Sec. 3.3). Il est à noter que cette approche nouvelle est forte utile pour une large communauté travaillant sur les codes électromagnétiques, en particulier, pour ceux tranvaillant dans le domaine de l'interaction avec de la lumière "structurée" ou avec des faisceaux laser fortement focalisés.

Nous avons considéré l'ensemble de ces outils numériques ainsi que notre modèle multi-échelle pour étudier la génération de THz dans des microplasma produits par des faisceaux laser femtosecondes fortement focalisés (voir Chap. 4). L'analyse des termes source de courant révèlent que le mécanisme IC est négligeable pour des lasers de plusieurs cycles optiques et que le mécan-

isme TC joue le rôle principal. Dans ce cas, les sources pondéromotrices dominent la pression de radiation, la convection ainsi que la diffusion. Dans le cas de faisceaux gaussiens, les courants transverses excités par TC ne génèrent pas de rayonnement THz. Cela provient de leur caractère anti-symétrique par rapport aux coordonnées spatiales transverses qui conduit à des intérférences destructives dans le champ lointain. Cependant, les courants longitudinaux excités par TC sont quant à eux symétriques et conduisent à du rayonnement électromagnétique. La polarization longitudinale des courants rayonnants et la longueur du plasma de l'ordre de 10 microns resultent dans un cone d'émission creux avec large angle d'ouverture (supérieur à 70°). Ces résultats obtenus avec les simulations PIC sont en accord avec les mesures expérimentales récemment publiées (voir Sec. 1.3.1.3).

Dans le cas des faisceaux laser de plusieurs cycles optiques, les simulations PIC ont montré une émission THz allant jusqu'à 20 THz, bien en dessous du pic de la fréquence plasma qui se trouve autour de 50 THz dans nos simulations. Nous observons, malgré tout, une force oscilation du plasma à la fréquence plasma locale. Nous avons présenté une solution analytique montrant que dans un plasma inhomogène, les oscillations à la fréquence plasma peuvent exister sans pour autant rayonner en champ lointain. De tels courants non-rayonnants ont un rotationel nul. De précédents modèles imposaient une structure articfielle au plasma, détruisant par la même, cette propriété du rotationel nul, ce qui introduisait un rayonnement artificiel à la fréquence plasma (voir Sec. 1.3.1). Nos résultats montrent que la réponse plasma et la forme spatiale du plasma doivent être correctement modélisés afin d'éviter un rayonnement artificiel autour de la fréquence plasma. Nous avons aussi développé un modèle simplifié (modèle d'une plaque plasma) qui tient compte de la réponse du plasma en forme de "plaque". La réponse du plasma "plaque" à l'application de la source pondéromotrice longitudinale reproduit très bien les spectres THz obtenus à partir des simulations PIC (voir Sec. 5.4.5). Nous avons aussi obtenu des oscillations non-rayonnantes des champs électriques à la fréquence locale plasma perpendiculaires au gradient de densité électronique, et nous les avons identifiées comme étant des polaritons plasmons de volume.

L'absence d'émission résonnante nous autorise à considérer le modèle du courant local modifié pour prédire des taux de conversion énergétiques laser/THz pour différents paramètres laser. L'efficacité de conversion sature pour des valeurs autour de $10^{-6} - 10^{-7}$ pour de grandes énergies laser dans différentes conditions de focalisation. L'opacité du plasma aux fréquences THz joue un rôle crucial dans le phénomène de saturation. Les résultats sont en bon accord avec les simulations PIC.

De plus, nous avons regardé l'influence de la pression des gaz sur l'efficacité de conversion. En accord avec des mesures expérimentales, nous avons trouvé un comportement quadratique pour les basses pressions. Cela confirme que l'émission THz a lieu dans un régime non-résonant. Pour les grandes pressions, l'efficacité de conversion tend à saturer.

Un comportement similaire est observé pour les microplasmas générés par un faisceau "1 couleur" complété par un champ électro-statique (voir Sec. 4.4). En augmentant la pression du gaz et l'amplitude du champ statique, nous augmentons l'efficacité de conversion de deux ordres de grandeur par rapport à un cas sans champ statique additionnel. Dans ce cas, les courants d'émission THz sont excités par un champs electrostatique externe constant et peuvent être modélisés par le mécanisme IC. Les simulations faites avec ARCTIC ont montré que lorsque le plasma est excité par un champ statique externe longitudinal, le rayonnement THz est émis avec un spectre dont la fréquence maximale est bien plus faible que la fréquence plasma. Et ceci, malgré le fait que le plasma oscille à la fréquence plasma locale. Nous avons montré que la situation change lorsque le champs statique externe est transverse. Par opposition à l'excitation longitudinale, dans ce cas transverse, un rayonnement autour de la fréquence plasma est émis. Cela montre que la forme du plasma est importante pour le spectre d'émission THz.

En plus des faisceaux “1 couleur”, nous nous sommes intéressés à l’émission THz à partir de microplasmas générés par des faisceaux “2 couleurs” (voir Chap. 5). Dans ce cas, l’émission THz est générée par le mécanisme IC que nous modélisons avec le code ARCTIC en géométrie 3D. Dans le cas de très forte focalisation, la plasma émetteur agit comme un source ponctuelle d’émission THz. La polarisation du courant d’émission THz peut être directement déterminée par un profil de rayonnement toroïdal. Cette opportunité apparaît seulement pour les microplasmas les plus petits car pour les grands plasmas émetteurs, le profil de rayonnement dirigé vers l’avant est déterminé par les longueurs et épaisseurs du plasma. Nous avons montré que les plasmas, avec une épaisseur de l’ordre ou plus petite que la plus petite longueur d’onde plasma le long de la direction de polarisation, rayonne en régime résonant. Nous avons trouvé, pour les faisceaux lasers gaussiens polarisés linéairement, un élargissement spectral de l’émission THz jusqu’à la fréquence plasma maximale de 50 THz pour un gaz entierement ionisé à pression ambiante. Pour des faibles pressions de gaz, le plasma rayonne de manière résonante avec un pic plus bas que la fréquence plasma maximale et qui dépend de la pression.

Pour interpréter ces résultats par un modèle simplifié pour de futures potentielles expériences, nous avons proposé d’exploiter des faisceaux laser avec des formes spatiales transverses différentes générant ainsi des plasmas aux profils de densité elliptiques. Les simulations 3D ont montré que le spectre THz obtenu à partir de faisceaux elliptiques sont fortement dépendants de la direction du champs électrique laser. Les champs THz émis peuvent être décrits à partir d’état de polarization superposant deux cas fondamentaux : le cas quasi-électrique transverse (TE) et le cas quasi-magnétique transverse (TM). Pour le cas TM, le champs electrique laser pointe dans la direction où le plasma est fin. Dans ce cas, le spectre d’émission s’étend jusqu’à la fréquence plasma maximale. En revanche, pour le cas TE, le champs electrique laser pointe dans la direction où le plasma est épais. Ce cas ne donne pas de spectre THz large. Ce comportement a pu être expliqué par notre modèle de plasma “plaque” (voir Sec. 5.4.3). Dans le cas TM, les polaritons de surface et de volume sont excités. Cela donne des caractéristiques résonnantes qui dépendent de la pression du gaz et expliquent l’élargissement spectral. Le cas TE ne présente pas de caractéristiques résonantes expliquant l’absence d’élargissement spectral. Ces études s’orientent vers la plasmonique THz dans des plasmas.

De plus, nous avons développé un modèle 3D qui permet de prédire les lois d’échelle pour l’efficacité de conversion laser/THz pour différentes énergies laser et conditions de focalisation d’un faisceau laser gaussien (voir Sec. 5.2). Selon notre modèle, les conditions de focalisation conduisant à la simple ionisation totale au point focal sont optimales aussi longtemps que les effets de propagation nonlinéaires sont faibles. Dans ce cas, l’augmentation de l’énergie laser avec la taille transverse du faisceau tout en maintenant l’intensité laser constante augmente l’efficacité de conversion par le carré de l’énergie laser pour le cas optimal. En considérant ce type de configuration, nous avons montré que l’utilisation des faisceaux micro-joules “2 couleurs” produit des taux de conversion énergétique excédant 10^{-4}. Deux effets jouent en faveur d’une forte émission THz à partir de microplasmas irradiés par des faisceaux “2 couleurs”. Tout d’abord, la nature transverse des courants d’ionisation est avantageuse pour un accroissement du taux de conversion avec la longueur plasma en comparaison avec le mécanisme TC, et l’opacité du plasma aux ondes THz apparaît insignifiante. Ces avantages fondamentaux du mécanisme IC tiennent pour des plasmas grands et petits. Deuxièmement, exclusivement pour les microplasmas, l’émetteur rayonne de manière cohérente du fait des petites tailles transverses de la source.

Au delà des efficacités de conversion intéressantes, les faisceaux “2 couleurs” produisent des amplitudes THz jusqu’à 0.5 MV/cm dans le voisinage du plasma. Cependant, séparer l’impulsion laser de l’impulsion THz près du plasma reste difficile. Nous avons montré que les faisceaux elliptiques fortement focalisés produisent des impulsions THz avec des amplitudes 10 kV/m émises selon la direction de propagation laser (voir Sec. 5.3).

D'autres études sont planifiées pour explorer l'intérêt de la lumière structurée. En considérant notre algorithme permettant d'introduire les faisceaux laser de forme arbitraire développé dans le code ARCTIC (voir Chap. 3), nous pouvons exploiter des faisceaux laser plus exotiques. Par exemple, nous prévoyons d'utiliser des faisceaux dits "caustiques" pour séparer le faisceau THz du faisceau laser juste derrière le plasma. Si cela est possible, de forts champs THz peuvent être obtenus juste dans le voisinage du plasma sans besoin de fortement focaliser le faisceau THz ce qui est limité par la diffraction.

Pour contrôler les effets plasmoniques durant la génération de rayonnement THz, nous nous intéressons à la lumière "structurée". Par exemple, nous nous attendons à contrôler les effets résonnants par contrôle de la polarisation du faisceau à deux couleurs : le champs électrique d'un faisceau laser de polarisation azimutale est orienté perpendiculairement au gradient de densité électronique, alors qu'il est orienté parallèlement dans le cas d'une polarisation radiale. Comme nous avons montré qu'un fort gradient électronique le long du champ électrique était nécessaire pour exciter des résonances plasmoniques, passer de l'une à l'autre des polarisations permet de contrôler ces effets résonants. De plus, en considérant des techniques modernes de structuration spatiale des faisceaux laser, nous pouvons structurer le plasma afin de passer de l'une à l'autre des résonances plasmoniques. Au delà du contrôle spectral, nous espérons guider et confiner les faisceaux THz. Toutes ces considérations sont applicables aux plasmas issus des gaz, liquides ou solides. Pour ces matériaux, nous devons conserver le traitement numérique complet en étendant la réponse du matériel par la prise en compte de la dynamique des électrons liés et l'ionization collisionnelle.

Contents

1. Introduction to terahertz sources

Contents

The main purpose of the thesis is the theoretical investigation of terahertz (THz) generation in laser-induced microplasmas. In this manuscript, THz radiation is defined as electromagnetic radiation ranging from 300 GHz to 30 THz (see Fig. 1.0.1). The corresponding photon energy ranges from 1.24 meV[1] to 124 meV. This photon energy is much smaller than the electron binding energies in atoms and molecules or electronic band gaps of semiconductors or insulators, that have typical values in the order of several eV. Fundamental modes that can be excited by THz waves are found in the rotational motion of molecules, vibrational motion of crystal lattices or precession of spins. The exploration and excitation of such states is the common idea behind all applications that are going to be presented in Sec. 1.1. In turn, these applications pose various requirements on the THz sources.

[1] 1 meV$= 10^{-3}$ eV

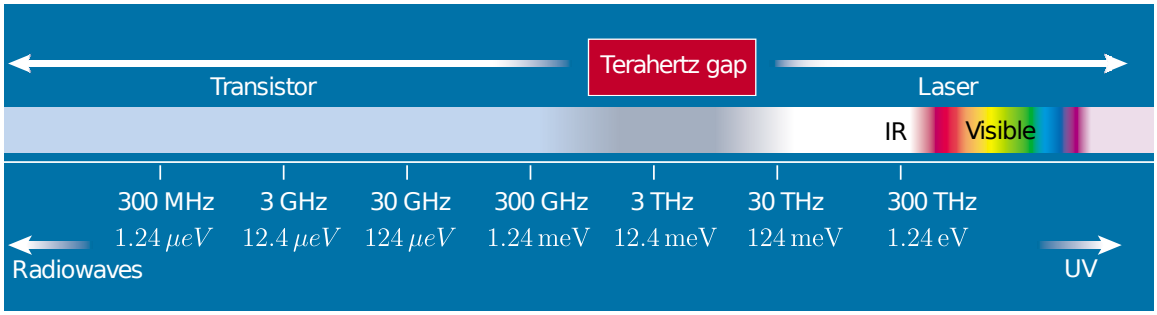

Figure 1.0.1.: Schematic representation of the electromagnetic spectrum between radiowaves and UV including THz frequencies that are labeled by the red box. This spectral region is difficult to access and thus often called the "Terahertz gap" [1].

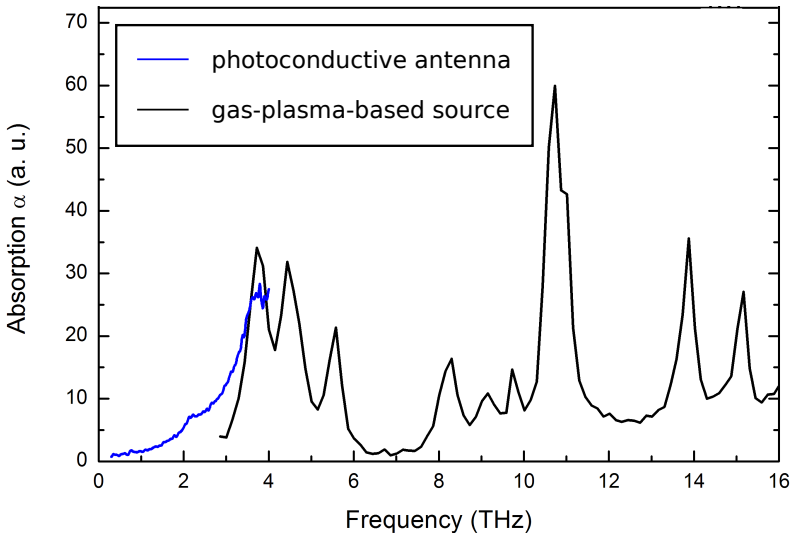

Figure 1.1.1.: Absorbtion spectra of TNT with many features in the THz domain obtained by THz time-domain (TD) spectroscopy [3]. Source: DTU Lyngby / ISL [4].

The frequency interval of 300 GHz to 30 THz corresponds to oscillation periods from 3 ps down to 30 fs. Thus, in order to produce THz radiation, processes faster than 3 ps, but slower than 30 fs are needed. To fulfill this requirement is quite challenging: Typical sources of electromagnetic radiation in the range from GHz to PHz are either electronic devices or lasers. But, electronic devices barely reach response times below 3 ps ($\hat{=}$ 1.38 meV) [2] and lasers typically cannot produce radiation with oscillation periods above 30 fs ($\hat{=}$ 138 meV) since their active media are usually based on electronic transitions. This problem is often referred to as the "THz gap" [1] that should reflect the lack of proper sources in the THz spectral range (see Fig. 1.0.1). In Sec. 1.2, an overview of common solutions to this problem is presented.

A particular and rather new way to bridge the THz gap are THz sources based on laser-induced gas-plasmas. The broad spectrum of laser-induced-gas-plasma schemes is discussed in Sec. 1.3. Particular attention is paid to the strengths and limitations of these sources, motivating to investigate laser-induced microplasmas as THz sources in this thesis.

1.1. Applications

Most of applications exploit linear "optical" properties of matter in the THz frequency range, either for characterization or identification. One can divide those applications into two classes: Some applications need tunable small spectral bandwidth sources; other require pulsed broadband THz sources, ideally covering the whole THz range. When using small spectral bandwidth sources, typically the reflectivity, transmittance or absorption by a sample is measured. Here, it is sufficient to access the amplitude of a THz wave, e.g., by using a bolometer. In order to get phase informations as well, detection techniques like Fourier-transform spectrometry [5] or electro-optic sampling [3] have been developed. These techniques require THz pulses. Broadband THz pulses have also other advantages as will be elaborated in Sec. 1.1.1.

Moreover, recent development of intense THz sources provides the possibility to control matter by exploring nonlinear interaction with THz radiation. Typically, resonant excitation is provided by small bandwidth radiation, whereas non-resonant excitation is often exploited by broadband few-cycle THz pulses. Selected examples are presented in Sec. 1.1.2.

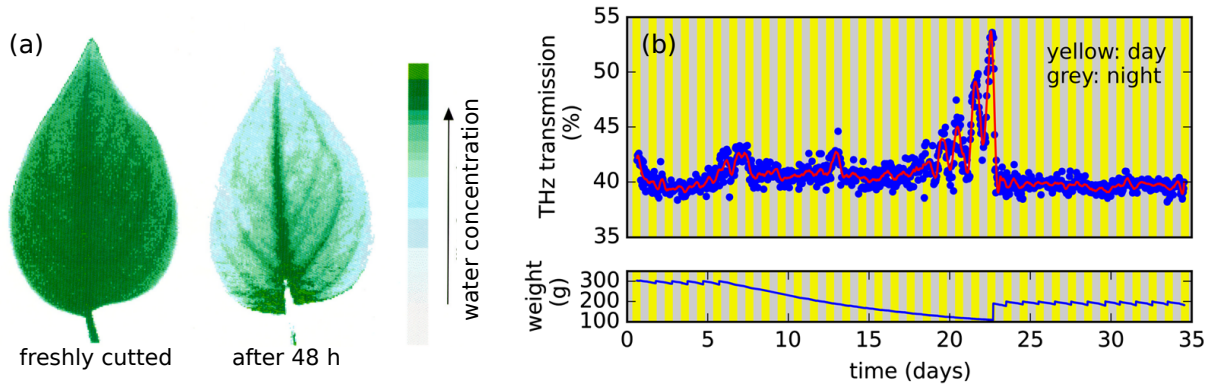

Figure 1.1.2.: (a) Imaging of water content in a freshly cut leaf and after 48 hours by using THz-TD spectroscopy [10]. (b) THz transmission of a rye leaf during 35 days measured by THz-TD spectroscopy. Below, the weight of the pot containing the rye plant that visualizes the amount of available water in the earth. Higher THz transmission can be associated with a smaller water concentration [11].

1.1.1. Exploiting linear interaction of matter with THz pulses

Linear "optical" properties of matter are characterized by the frequency-dependent complex dielectric function ϵ. It determines the phase velocity of the THz wave and its attenuation during the propagation [6]. Specific dielectric linear properties of materials in the THz frequency range give rise to the following applications.

Spectroscopic identification Many materials have resonant features of ϵ in the THz frequency range. The dielectric function is intimately linked to the amount of energy absorbed by a sample (absorption α). This fact can be exploited to identify drugs-of-abuse, pharmaceuticals, explosives and other hazardous substances [7]. For example, Fig. 1.1.1 (black line) presents the THz absorption spectrum of trinitrotoluol (TNT). The diversity of spectral features can be used to identify TNT with a high selectivity. Moreover, THz spectra can give an inside about DNA, amino and protein structures [8, 9]. All these applications can profit from broadband THz spectra that cover a large amount of spectral features.

Biological and medical applications In biology THz sources find a wide range of applications besides spectroscopy. The main reason is that THz waves are very sensitive to water content, one of the main constituents of biological tissues. For frequencies of 1-100 THz the penetration depth in water is less than 1 µm due to linear absorption caused by vibrational and rotational transition [12]. Absorption measurements can identify and spatially resolve different tissues by their water concentrations. For example, structural informations as water distribution in leaf veins can be provided [see Fig. 1.1.2(a)] and in-vivo transmission measurements through plant leaves can be used for optimization of irrigation strategies [see Fig. 1.1.2(b)].

In medicine, THz waves provide a tool for detection of diseases [12]. Unlike X-rays, THz radiation is usually harmless to a living organism [13]. THz imaging can resolve tissues that contain polar molecules. 2D imaging by spatial scanning or even 3D tomography with THz waves have been already demonstrated [14]. In particular depending on the availability of cheap and compact THz sources, THz imaging techniques might be utilized in clinical routine as a complementary diagnostics tool of breast or skin cancer [15].

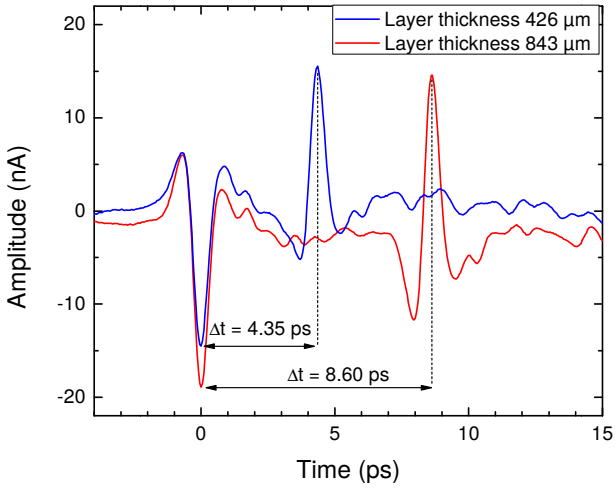

Figure 1.1.3.: Wall thickness measurements on two points of the same high-density polyethylene bottle by measuring the delay-time of the reflected THz pulse according to [16].

Industrial process and quality control

THz waves can penetrate through several materials as polymers, paper or textiles that are opaque for infrared radiation (IR) and visual frequencies [16]. The delay time between the THz pulses that are reflected at the front and rear surface of a layer determines its thickness (see Fig. 1.1.3). Also for control of coating thickness for drugs, THz based thickness measurements are of interest since the coating thicknesses plays an important role for the release of the drug inside the human body. Unlike traditional methods using x-rays coherent tomography or thermography, even in-situ indestructible measurements of multi-layer systems are possible [17]. Moreover, reflective measurements allow for identification of defects like for example sub-surface cracks in polymers.

The resolution of the layer thickness is determined by the THz pulse duration. Decreasing the pulse duration from few ps to 100 fs or shorter could increase the resolution from the 1 μm up to date to 0.1 μm. Thus, there is a demand for broadband sources capable of delivering shorter THz pulses. Moreover, the signal-to-noise ratio of the measurement is proportional to the average power $\mathfrak{P}^{\mathrm{av}}_{\mathrm{THz}} = \mathfrak{E}_{\mathrm{THz}}\nu_{\mathrm{rep}}$ of the THz source, where $\mathfrak{E}_{\mathrm{THz}}$ is the THz pulse energy and ν_{rep} the repetition rate. Therefore, high THz average powers are needed, in particular to accelerate the measurement processes or to insure a better accuracy. This conclusion holds for all applications which explore the sample by a linear interaction with THz pulses, i.e., all the applications that have been presented above. For industrial process and quality control measurements, typical THz average powers of $\mathfrak{P}^{\mathrm{av}}_{\mathrm{THz}} = 50\,\mu\mathrm{W}$ are needed [16, 17].

1.1.2. Control over matter

All the applications presented so far are based on linear interaction which does not require strong THz fields. However, over the past years the achievable THz peak electric and magnetic fields increased considerably. For ps-long THz pulses, electric fields around 1 MV/cm and magnetic fields around 0.33 T can nowadays be reached at many laboratories. Consequently, the number of investigations involving nonlinear interaction of THz radiation with matter, in particular, control over matter by THz radiation, is rapidly increasing.

Low-frequency electromagnetic fields in the THz domain are favorable for excitation of matter: The reason is that charged particles, for example electrons, can gain a substantial energy in the

THz electric field because the THz-oscillation period is large. After half of the THz cycle the electron that is accelerated by the THz electric field gains the maximum energy $\frac{q_e^2 E_0^2}{2m_e\omega_{\mathrm{THz}}^2}$, where q_e is the electron charge, E_0 the amplitude of the electric field oscillation, m_e the electron mass and ω_{THz} the angular THz frequency. Already for $E_{\max} = 0.15$ MV/cm and the THz frequency $\nu_{\mathrm{THz}} = \omega_{\mathrm{THz}}/(2\pi) = 1$ THz, the electron gains an energy of 1 eV. This idea has been used in [18] where electrons were accelerated by the longitudinal electric field of a 10-μJ single-cycle THz pulse. Only 0.1 MV/cm-THz-electric-field amplitude was sufficient to let the electron gaining 7 keV of energy within a waveguide along the distance of 3 mm.

THz pulses can even control the ionic motion: In [19], THz pulses with MV/cm-strong electric fields have been used to switch the polarization of ferroelectric crystals. Here, few-cycle THz pulses were coupled resonantly to the ionic motion in lithium niobate changing the conformation of the crystal structure and herewith the ferroelectric polarization. Many other examples of nonresonant and resonant control over matter and even light by THz radiation are given in [20].

The broad range of possibilities of matter control by THz radiation that has been presented above suggests that there is still a large number of unexplored applications that are limited by the availability of THz sources providing higher field amplitudes. Furthermore, the availability of operating systems beyond the laboratory rooms will strongly depend on the compactness of THz sources that can provide 0.1-1 MV/cm electric field amplitudes.

1.1.3. Demands on THz sources

Based on the insights in previous examples, the demands on THz sources can be formulated as follows:

1. The requirements with respect to the THz spectrum differ strongly from application to application. However, as has been shown above, many applications require pulsed broadband THz sources, ideally covering the whole THz range from 0.3 to 30 THz.

2. Most THz applications perform measurements of linear "optical" properties. The THz average power $\mathfrak{P}_{\mathrm{THz}}^{\mathrm{av}} = \mathfrak{E}_{\mathrm{THz}}\nu_{\mathrm{rep}}$ is important to provide a reasonable signal-to-noise-ratio. However, average powers of $\mathfrak{P}_{\mathrm{THz}}^{\mathrm{av}} \sim 0.1 - 50$ μW are often sufficient [16, 17, 21]. On the one hand those can be reached by sufficiently high THz pulse energies $\mathfrak{E}_{\mathrm{THz}}$, on the other hand by high repetition rates ν_{rep}.

3. As will be shown in the next section, many THz sources are driven by ultra-short laser pulses which have a strong impact on the compactness and costs of THz sources. Thus, it is advantageous to keep the driving laser pulse energy $\mathfrak{E}_\mathrm{L}$ for a given THz average power $\mathfrak{P}_{\mathrm{THz}}^{\mathrm{av}}$ small. Thus, a large ratio $\mathfrak{P}_{\mathrm{THz}}^{\mathrm{av}}/\mathfrak{E}_\mathrm{L} = \nu_{\mathrm{rep}}\eta_{\mathrm{THz}}$ with laser-to-THz conversion efficiency $\eta_{\mathrm{THz}} = \mathfrak{E}_{\mathrm{THz}}/\mathfrak{E}_\mathrm{L}$ is intended and requires, besides a high repetition rate ν_{rep}, a reasonably large laser-to-THz conversion efficiency η_{THz}.

4. When controlling matter or light by THz radiation, i.e., within a nonlinear interaction regime, strong THz field amplitudes are needed. Electric fields of the order $0.1-1$ MV/cm and magnetic fields of the order 33-330 mT or above are required for current experiments.

1.2. Conventional sources

In the following an overview on modern THz sources is given with the noted exception of laser-induced-gas-plasma-based THz sources that are discussed separately in the subsequent section. First, a non-laser-driven THz source, the quantum cascade laser, is introduced. Then, three

laser-driven types of pulsed THz sources are presented. Finally, the abilities of conventional THz sources are summarized.

1.2.1. Quantum cascade lasers

Until 1994 it was not possible to exploit the laser principle to bridge the THz gap [22]. The reason is the technological difficulty to construct an active medium operating at THz frequencies. Lasers emitting radiation in visual and near-infrared spectral region contain active bulk or gaseous media providing electronic transitions with eV energies. At THz frequencies nowadays only cascades of engineered quantum states can provide meV transitions [24].

Fig. 1.2.1(a) illustrates the energy band diagram of the active medium in the so-called quantum cascade laser (QCL). It consists of periodically arranged structures that can be divided into an active region and a relaxation region in Fig. 1.2.1(a). The active region contains semiconductor layers with different band gaps. A sequence of three layers can form a potential trap for the electrons with a localized quantum state. Three potential traps with spatially overlapping wavefunctions lead to a three level system as needed to create population inversion. The transition from level 3 to 2 for example can lead to stimulated emission of THz radiation. After reaching the state 1, the electron enters the relaxation region that has the main function to avoid space-charge creation. The active medium is pumped by an electrostatic field that leads to a potential that decreases from left to right in Fig. 1.2.1(a). Thus after leaving the relaxation region, the electron goes into the 3^{rd} level of the next three level system.

QCLs operate in the frequency bands from 1 to 5 THz and from 10 to 30 THz [25]. Since they are based on the laser principle only single-frequency or small-bandwidth pulsed operation is possible [26, 27, 28]. Ultra-broadband THz radiation in the context of QCLs covers spectral bandwidths of only $\Delta\nu = 1$ THz and can be achieved only with advanced mode control techniques [29, 30]. Typically, operation below 5 THz needs cooling by hundreds of Kelvin below the room temperature and results in $\mathfrak{P}^{\text{av}}_{\text{THz}} \leq 100$ mW [31]. However, operation at room temperature is possible providing moderate output powers around $\mathfrak{P}^{\text{av}}_{\text{THz}} \approx 5\ \mu$W and tunable single-frequency THz emission from 2.06 to 4.35 THz. Even when focusing the THz radiation down to the diffraction limit, THz electric fields reach only few kV/cm below 5 THz. Above 10 THz, $\mathfrak{P}^{\text{av}}_{\text{THz}} \geq 1$ W has been achieved and peak electric fields can reach tens of kV/cm.

Tunable small spectral bandwidths of QCLs are convenient for spectroscopy where narrow resonances have to be resolved. However, emission frequencies from 5 THz to 10 THz cannot be accessed by QCLs due to strong absorption and dispersion in the active medium. Below

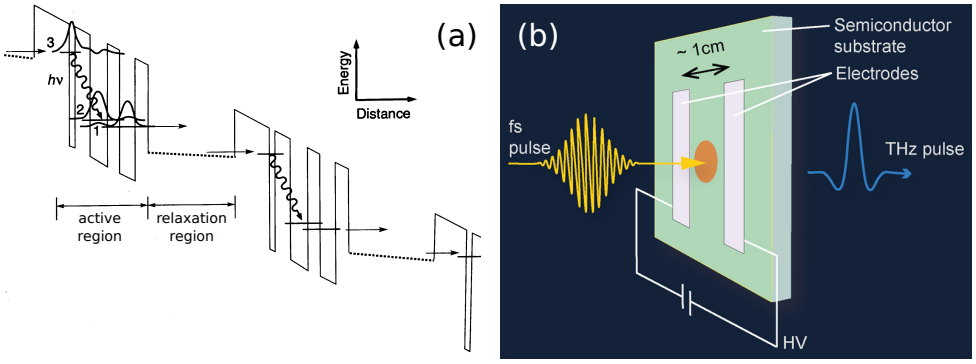

Figure 1.2.1.: (a) Energy band diagram of the QCL active medium that has been realized for the first time in [22]. (b) Illustration of a photoconductive switch/antenna [23].

5 THz, devices at room temperature deliver moderate powers of $\mathfrak{P}^{\mathrm{av}}_{\mathrm{THz}} \approx 5\ \mu\mathrm{W}$, but require low operation temperatures to achieve higher powers limiting the compactness and availability of such QCLs. At least above 10 THz, providing tens of kV/cm electric field amplitudes in single-frequency operation QCLs are used preferably for resonant control over matter.

1.2.2. Photoconductive switches

As sketched in Fig. 1.2.1(b), a photoconductive switch (PCS) consists of two principal components: a semiconductor and a pair of electrodes. High voltage (HV) is applied to the electrodes. No charge carriers are circulating until a fs-laser pulse reaches the semiconductor. By creating electron-hole pairs, a time-varying conductance is induced. Then, a current starts to flow between and within the electrodes. The electrodes are acting as THz wave emitting antennas. Their design is important to reach a high emission efficiency. Finally, the electron-hole pairs recombine and again no current flow is possible. Since the current flow is changing typically within a picosecond corresponding to 1 THz, the emitted radiation is in the THz range.

THz emission from PCS has been demonstrated the first time in 1984 [32]. Nowadays, several PCS-based THz sources driven by only nJ 50-fs-long 1550-nm laser pulses are commercially available providing emission between 0.3 and 3 THz [33]. They can reach moderate average powers $\mathfrak{P}^{\mathrm{av}}_{\mathrm{THz}} = 50\,\mu\mathrm{W}$, $\nu_{\mathrm{rep}} = 100$ MHz and laser-to-THz conversion efficiency $\eta_{\mathrm{THz}} = 4 \cdot 10^{-4}$. Focusing leads to electric fields up to 1 kV/cm. In general, THz amplitudes cannot be increased beyond several kV/cm [34]. The analysis in [35] shows that $\mathfrak{E}_{\mathrm{THz}}$ saturates with the laser pulse energy $\mathfrak{E}_{\mathrm{L}}$. Increasing emitted THz pulse energy by increasing the HV is possible up to certain limits. Above a threshold value HV arcing effect of GaAs at the electrodes leads to the damage of the PCS.

Generation of THz waves above 3 THz remains a big challenge for PCSs. Usually the THz pulse duration and thus the spectral bandwidth is limited by the PCS electronic circuit inertness, in particular induced by the charge carrier recombination time of GaAs that is around 1 ps [35]. Efforts have been made to resolve this problem by shortening the recombination times. THz radiation up to 30 THz has been demonstrated by using low-temperature grown GaAs and 12-fs-short only-4-nJ laser pulses [36]. More recently interdigitated photoconductive antennas made of semi-insulating GaAs have been used to produce THz pulses with frequencies up to 20 THz using 15-to-35-fs-short only-nJ pulses [37]. To the best of the authors knowledge, however, no reasonable THz average powers above 3 THz have been reported, yet.

In summary, compact PCS-based THz sources driven by few-μJ fs-laser pulses providing $\mathfrak{P}^{\mathrm{av}}_{\mathrm{THz}} \approx 50\ \mu\mathrm{W}$ are interesting for applications based on linear THz-pulse-matter-interaction below 3 THz. Generation above 3 THz with PCSs is still inefficient. THz field amplitudes are limited to several kV/cm which restricts the applications to linear interaction regimes.

1.2.3. Optical rectification

Another very popular technique to generate THz radiation is based on optical rectification (OR) in nonlinear crystals [38]. Non-centrosymmetric crystals exhibit a $\chi^{(2)}$-nonlinearity, i.e., a nonlinear polarization that is proportional to the product of the exciting laser field oscillating at the central frequency ω_{L} with itself. This product leads besides frequency doubling to nonlinear down-conversion towards the $(\omega_{\mathrm{L}} + \Delta\omega_{\mathrm{L}}) - \omega_{\mathrm{L}} = \Delta\omega_{\mathrm{L}}$ frequency where $\Delta\omega_{\mathrm{L}}$ is limited by the spectral bandwidth of the laser. When the laser pulse has an appropriate bandwidth, frequencies $\omega_{\mathrm{THz}} = \Delta\omega_{\mathrm{L}}$ in the THz spectral range are produced.

Under certain assumptions, in particular disregarding dispersion effects, one would expect a quadratic growth of the THz pulse energy $\mathfrak{E}_{\mathrm{THz}}$ with laser pulse energy $\mathfrak{E}_{\mathrm{L}}$ and thus a linearly increasing conversion efficiency η_{THz}. However, two-photon absorption and depletion of the pump laser pulse limit $\mathfrak{E}_{\mathrm{THz}}$ [39]. Moreover, due to linear dispersion[2] $\omega(k)$, the group velocity $v_{\mathrm{g,L}} = \partial_k \omega(k_{\mathrm{L}})$ of the laser pulse and the phase velocity $v_{\mathrm{ph,THz}} = \omega_{\mathrm{THz}}(k_{\mathrm{THz}})/k_{\mathrm{THz}}$ of the THz wave are different. After a certain propagation length in the nonlinear crystal, the driving nonlinear polarization and the THz pulse are out of phase [see also Sec. 1.2.4]. This phase mismatch limits the maximum laser-to-THz conversion efficiency. Moreover, the phase velocity of the THz wave is frequency dependent. Thus, it is challenging to obtain phase-matching for a broad range of frequencies and THz generation by OR is always a trade-off between $\mathfrak{E}_{\mathrm{THz}}$ and spectral bandwidth $\Delta\nu_{\mathrm{THz}}$ [3].

Using ZnTe crystals the phase mismatch can be reasonable [34]. Here, THz pulses below 3 THz with average powers of $\mathfrak{P}^{\mathrm{av}}_{\mathrm{THz}} \approx 150$ μW have been created by 30-fs-short laser pulses with $\mathfrak{E}_{\mathrm{L}} = 48$ mJ at low repetition rates $\nu_{\mathrm{rep}} = 100$ Hz [34]. Experimental results provided THz peak electric fields of 69 kV/cm and could be even increased by one order of magnitude with a stronger focusing. $\mathfrak{P}^{\mathrm{av}}_{\mathrm{THz}}$ and thus the peak electric field is limited for a fixed crystal diameter by the damage threshold of 1 MW/cm^2 for ZnTe [40]. Moreover, the conversion efficiency has been shown to saturate to $\eta_{\mathrm{THz}} = 3 \cdot 10^{-5}$ [34, 41], in particular due to the two-photon absorption of the pump pulse and free-carrier absorption of the THz wave in ZnTe [42, 43].

As an alternative the use of $LiNbO_3$ crystals having low THz absorption, higher nonlinear coefficients as well as higher damage threshold has been proposed. However, linear dispersion in $LiNbO_3$ is strong. To resolve this problem, the phase-matching of laser pulse group velocity and THz phase velocity by introducing a pulse front tilt to the laser have been experimentally demonstrated [44]. This technique could increase the efficiency to $\eta_{\mathrm{THz}} = 10^{-3}$ [45]. THz pulses below 3 THz were generated with $\mathfrak{P}^{\mathrm{av}}_{\mathrm{THz}} = 2$ mW at $\nu_{\mathrm{rep}} = 1$ kHz for 85-fs-long driving laser pulses with $\mathfrak{E}_{\mathrm{L}} = 4$ mJ. Tightest focusing produced 1 MV/cm THz fields. For a similar driving configuration, the conversion efficiency could be boosted to $\eta_{\mathrm{THz}} = 10^{-2}$ using cryogenic cooling that reduces the absorption of the pump in the crystal [46].

Another attractive alternative turned out to be the organic crystal DSTMS as it provides nonlinear coefficients one order of magnitude larger than $LiNbO_3$ and good phase-matching. The use of DSTMS could increase the efficiency to $\eta_{\mathrm{THz}} = 10^{-1}$ [47]. THz pulses below 5 THz were emitted with several tens of mW average power at $\nu_{\mathrm{rep}} = 100$ Hz for 65-fs-long driving laser pulses with $\mathfrak{E}_{\mathrm{L}} = 3$ mJ. THz peak electric fields of 3.6 MV/cm have been reported and are even in principle further up-scalable when increasing the driving laser pulse energy and the crystal surface that has been already 20×20 mm^2-large in [47].

In principle for OR, the up-scaling of the THz pulse energy by increasing the THz-generating-solid surface proportionally to the driving laser pulse energy while keeping the intensity constant is realizable. This is a great plus of these approaches that makes record-breaking peak electric field amplitudes possible by focusing the generated THz pulses down to the diffraction limit. However, compact THz sources should not be driven by mJ-laser pulses, but require μJ-laser pulses. A proof of principles in [48] has shown that high-repetition rate compact fs-fiber lasers can drive OR in DSTMS creating pulsed THz radiation ranging from 0.2 to 8 THz that is suitable for THz-TD spectroscopy. However, no THz average powers and efficiencies that could compete with PCSs have been reported up to date. The reason might be that the scalability to lower driving laser pulse energies is limited for OR, because it is efficient only in the collimated-laser regime. Decreasing the driving laser beam size in the nonlinear crystal would decrease η_{THz}.

[2] Here, ω is the angular frequency and k is the wavenumber. The indices "L" and "THz" indicate whether the value for the driving laser or for the THz wave is meant, correspondingly.

THz source	spectral range [THz]	$\Delta\nu_{\mathrm{THz}}$	$\mathfrak{P}^{\mathrm{av}}_{\mathrm{THz}}$	max E_{THz}	η_{THz}	ν_{rep}
QCL	$1 \leq \nu_{\mathrm{THz}} \leq 5$	< 1 THz	100 mW	1 kV/cm	-	-
	$10 \leq \nu_{\mathrm{THz}} \leq 30$		1 W	10 kV/cm	-	-
PCS	$0.3 \leq \nu_{\mathrm{THz}} \leq 3$	< 3 THz	50 μW	1 kV/cm	10^{-4}	100 MHz
OR	$0.3 \leq \nu_{\mathrm{THz}} \leq 8$	< 8 THz	10 mW	1 MV/cm	10^{-2}	1 kHz
DFG	$\nu_{\mathrm{THz}} \geq 10$	< 10 THz	10 mW	100 MV/cm	10^{-3}	1 kHz

Table 1.1.: Characteristics of conventional broadband THz sources that are presented in Sec. 1.2.

In summary, OR is a widely used approach to generate mW-average-power pulsed THz radiation. Efficiencies beyond $\eta_{\mathrm{THz}} = 10^{-3}$ can be reached by using cryogenic cooling or wide-surface organic crystals, however, only at kHz repetition rates. Tight focusing of the THz pulse leads to peak electric fields above 1 MV/cm. This, however, requires at least mJ-driving-laser pulses. Thus, OR based THz sources are not compact. Moreover, the upper emission frequency is limited to 3 - 8 THz.

1.2.4. Difference frequency generation

The limitation of OR with respect to maximum THz-emission frequency can be resolved by using difference frequency generation (DFG). DFG is also based on the $\chi^{(2)}$-nonlinearity. However, the driving laser spectrum is rather broad, either because a very short laser pulse is used or two laser pulses with different frequencies ω_2, ω_1 such that $\omega_{\mathrm{THz}} = \omega_2 - \omega_1$ is sufficiently large. Like for OR, phase matching is required: the phase mismatch $\Delta k L_{\mathrm{c}} = [k(\omega_2) - k(\omega_1) - k(\omega_{\mathrm{THz}})]L_{\mathrm{c}}$ with crystal length L_{c} must be small. We refind OR as the border case for $\omega_{\mathrm{THz}} \to 0$ since $\Delta k L_{\mathrm{c}} \to [v^{-1}_{\mathrm{gr,L}} - v^{-1}_{\mathrm{ph,THz}}]\omega_{\mathrm{THz}} L_{\mathrm{c}}$, where the phase mismatch is defined by the group velocity of the laser pulse and the phase velocity of the THz wave.

To obtain phase matching for DFG, mostly thin GaSe crystals are used. The first proof of principles in [49] has shown that 10-fs-short pulses in GaSe can produce tunable broadband emission from 8 to 50 THz. Adjusting the incidence angles fixes the phase-matching to specific frequencies and makes the tuning possible. For small incident angles even emission from 0.1 to 5 THz has been generated. Pulsed THz emission from 10 to 72 THz with $\Delta\nu_{\mathrm{THz}} = 10$ THz has been reported in [50]. A 4-mJ-strong laser pulse has been used to produce two spectrally tunable driving pulses at $\nu_{\mathrm{rep}} = 1$ kHz. Resulting 1.7-to-19-mW-average-power THz radiation was tightly focused to create 100 MV/cm-strong field-amplitudes at high emission frequencies that are rather in the IR than THz spectral range.

Same as for QCL, DFG in inorganic crystals is not able to produce radiation between 5 and 8 THz due to strong THz absorption. DSTMS crystals resolved this problem. Tunable 1-THz-small-band THz emission from 4 to 18 THz has been produced by using 3 mJ driving laser pulses with 1 kHz repetition rate [51]. Resulting 1.9-mW-average-power THz pulses were focused leading to 3.7 MV/cm THz-field amplitudes.

In summary, DFG resolves the problem of OR to access THz frequencies beyond 8 THz providing otherwise similar characteristics with OR. However, the frequency window between 5 and 8 THz remains difficult to access and only organic crystals can leverage DFG to bridge this gap by tunable small band THz radiation.

1.2.5. Summarizing the abilities of conventional THz sources

Tab. 1.1 summarizes the characteristics of conventional PCSs, QCLs or OR/DFG-based broadband THz sources[3] that comply with many requirements of THz application: Together, they can cover almost the whole THz gap. OR- and DFG-based sources provide up to 10 THz broad radiation below 8 THz and above 10 THz, respectively. They produce THz average powers around 10 mW that are sufficient to create THz peak electric field amplitudes $\max E_{\mathrm{THz}} = 1$ MV/cm and larger. Such a strong THz fields are required for nonlinear interaction of THz waves with matter (see Sec. 1.1.2). For linear interaction, strong THz fields are not desirable and moderate average powers of few μW are already sufficient (see Sec. 1.1.1). Those applications could profit above all from compact broadband THz sources. These requirements can be fulfilled below 3 THz by conventional PCSs which provide conversion efficiencies around 10^{-4} already for only nJ-driving-laser-pulse energies and operate at high repetition rates of 100 MHz.

Except for PCSs-based pulsed sources below 3 THz and some few-μJ-weak QCLs working at room temperature, THz sources are usually driven by mJ-lasers that strongly limit their compactness and availability. Moreover, none of the conventional sources provides moderate or high-power THz pulses closing the whole THz gap at one blow.

1.3. Laser-induced gas-plasma-based terahertz sources

An alternative approach to THz sources that might overcome certain limitations of conventional emitters are laser-induced gas-plasma-based terahertz sources. Here, a laser pulse ionizes an initially neutral gas creating a plasma. The plasma electrons interact with the laser pulse giving rise to several mechanisms for THz generation, as will be shown in this section [55, 56, 57]. Ionization of atoms typically sets in at intensities below 10^{14} W/cm^2. As simple estimations suggest, when focusing a 100-fs-laser pulse down to 1 μm focal beam width, already 100 nJ laser pulse energy are sufficient to reach this intensity and create free electrons[4]. Three main groups of approaches are presented in the following: using single-color, DC-biased[5] single-color and multi-color fs-laser-induced gas-plasmas. The focus lies on important experiments and corresponding propositions to explain the observed THz radiation as well as the interesting features of the emitted THz radiation.

1.3.1. Single-color fs-laser-induced gas-plasma

1.3.1.1. The first THz emission reported from a gas-plasma

By definition single-color (1C) laser pulses have one frequency peak. THz emission from gas-plasma induced by such laser pulses has been reported the first time by Hamster et al. in 1994 [55]. By focusing a 120-fs-long 50-mJ-strong laser pulse into gaseous helium, a THz pulse was emitted in the laser propagation direction. Bolometric measurement of the THz pulse energy revealed $\mathfrak{E}_{\mathrm{THz}} = 1$ nJ resulting in a laser-to-THz conversion efficiency (in the following

[3] Many other propositions have been made to bridge the THz gap for intense THz sources. A record-braking 300-μJ-strong THz pulse has been produced by coherent synchrotron radiation by electrons in magnetic fields within 1-2 THz spectral range [52]. Linear mode conversion of laser wake fields in inhomogeneous plasmas has been shown to support THz radiation below 9 THz and GV/m-strong THz fields [53]. In [54], FEL-based THz sources have been demonstrated emitting at 1.2-100 THz pulses with $\mathfrak{E}_{\mathrm{THz}} = 1 - 50$ μJ. These ultra-intense THz sources are good candidates and already partially exploited to study the physics of intense THz fields. However, they need large laser or accelerator facilities. The down-scaling to compact devices with moderate output powers by keeping the efficiency cannot be done straightforwardly reducing the driving power.

[4] The required laser pulse energy is $\mathfrak{E}_{\mathrm{L}} \sim 10^{14}\,\mathrm{W/cm^2} \cdot (1\,\mu\mathrm{m})^2 \cdot 100\,\mathrm{fs} = 100$ nJ.

[5] DC-biased $\hat{=}$ exposed by a constant electric field

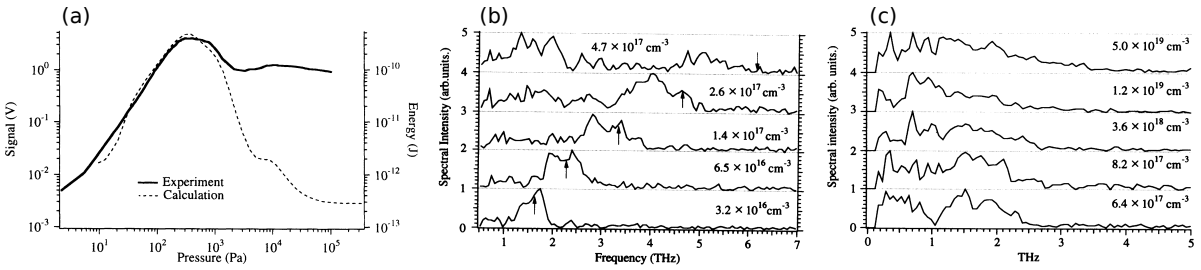

Figure 1.3.1.: (a) Bolometer signal voltage detecting the THz power emitted by a laser-induced helium-plasma depending on the gas pressure from [55]. (b-c) Corresponding THz power spectrum measured by an FTIR-spectrometer for different initial atom densities n_a. The arrows in (b) indicate the value of the plasma frequency ν_p for a singly ionized gas.

only conversion efficiency) of $\eta_\mathrm{THz} = 2 \cdot 10^{-8}$. As Fig. 1.3.1(a) shows, $\mathfrak{E}_\mathrm{THz}$ and thus η_THz depend on the gas-pressure p that in turn is proportional to the initial atom density n_a. $\mathfrak{E}_\mathrm{THz}$ increases quadratically with p up to its maximum value at $p \approx 170$ Pa and then tends to saturate. Corresponding THz spectra in Fig. 1.3.1(b-c) indicate two regimes. In (b), the spectral peaks appear close to the plasma frequency $\nu_\mathrm{p} = \sqrt{q_\mathrm{e}^2 n_\mathrm{e}/(m_\mathrm{e}\epsilon_0)}/(2\pi)$ with free electron density $n_\mathrm{e} = n_\mathrm{a}$ for a singly ionized gas[6]. This observation stays valid as long as $\nu_\mathrm{p} t_\mathrm{L} < 1$ ($p < 170$ Pa, $n_\mathrm{e} < 4.6 \cdot 10^{17}$ cm^{-3}) for $t_\mathrm{L} = 120$ fs indicating a resonant regime of excitation. For $\nu_\mathrm{p} t_\mathrm{L} > 1$ in (c), the spectrum almost does not change with the electron density indicating a non-resonant regime.

Two mechanisms have been proposed to explain the associated THz radiation driven by the time t and position $\mathbf{r} = (x, y, z)^\mathrm{T}$-dependent transverse linearly x-polarized electric laser field $E_{\mathrm{L},x}(\mathbf{r}, t)$: On the one hand, electrons can be pushed by the cycle-averaged ponderomotive force

$$\langle \mathbf{F}_\mathrm{pond}(\mathbf{r}, t)\rangle_t = -\frac{q_e^2}{4 m_\mathrm{e}\omega_\mathrm{L}^2} \nabla \langle E_{\mathrm{L},x}(\mathbf{r}, t)^2\rangle_t \tag{1.3.1}$$

where $< \, . \, >$ indicates the averaging over one laser cycle[7]. Due to the cycle averaging, the fast oscillations at $2\omega_\mathrm{L}$ vanish. However, the ponderomotive force oscillating at $2\omega_\mathrm{L}$ should not be neglected. Due to the product with a fast oscillating electron density it can also drive a low frequency current (see Sec. 4.1 for more details). On the other hand, in [55] the force $\propto (\nabla n_\mathrm{e} \cdot \mathbf{e}_\mathrm{pol})\mathbf{e}_\mathrm{pol}$ where $\mathbf{e}_\mathrm{pol}$ is the laser polarization direction was claimed to be able to excite the plasma at THz frequencies[8]. In our systematic theory in Sec. 2.5.2, we will regain this term.

The response of the plasma, in particular to the ponderomotive force, has been modeled in [55] by means of a local harmonic oscillator that has a resonance at the plasma frequency. According to this model, if the excitation spectrum is broad enough to excite the oscillations at the plasma frequency, the far-field emission is peaked there. This approach could not explain the experimental results above $p = 10^3$ Pa, in particular the strength of the signal in Fig. 1.3.1(a) above $p = 10^3$ Pa which corresponds to the spectra peaked at low-frequencies in Fig. 1.3.1(c). We will find in Chap. 4 a similar spectral behavior in microplasmas. Also, the quadratic increase and the saturation of the signal with the gas pressure in Fig. 1.3.1(a) will be retrieved and their potential origin clarified (see Chap. 4).

[6] Here, q_e is the electron charge, m_e the electron mass and ϵ_0 the electric permittivity.
[7] Vectors are typed bold.
[8] This term seems to be forgotten since the often cited [58].

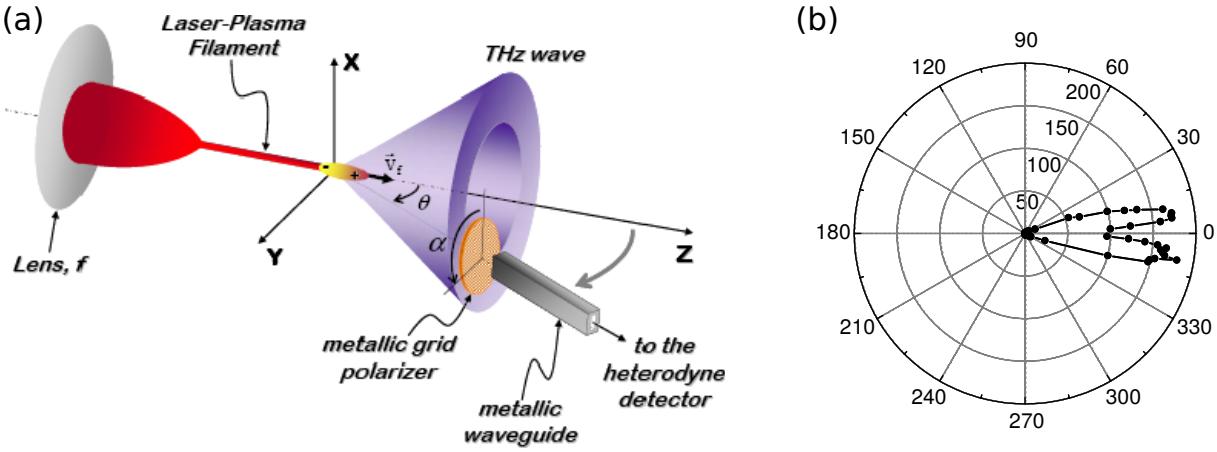

Figure 1.3.2.: (a) THz generation scheme in a 1C laser induced air-filament from [59]: a 4-mJ 150-fs-long laser pulse (red) is focused into air using a 2 m focal lens leading to filament formation. As indicated by the blue cone in (a) and confirmed by the measured radiation profile in (b), THz radiation is emitted within a cone that is oriented in the laser propagation direction.

1.3.1.2. Single-color fs-laser-induced filament

One decade later, THz generation in 1C-laser-induced gas-plasmas has been extended to filaments [59, 60], motivated by the need to produce THz emission remotely. In [59], a 150-fs-long 4-mJ-strong laser pulse generates a filament in air [see Fig. 1.3.2(a)]. This filament and in particular the self-generated plasma, leads to THz radiation. As displayed in Fig. 1.3.2(b), conical THz emission in the laser propagation direction was observed. The polarization of the THz emission has been determined to be radial, i.e., the projection of the THz electric field vector into the xy-plane has only a radial component.

Based on theoretical investigations in [58], a model has been proposed in [59] to describe the corresponding THz emission. Here, the longitudinal[9] electric field E_z in the plasma driven by the longitudinal ponderomotive force is governed by [59]

$$\left(\partial_t^2 + \nu_\mathrm{e}\partial_t + \omega_\mathrm{p}^2\right) E_z(z,t) = -\frac{q_\mathrm{e}\omega_\mathrm{p}^2}{2\epsilon_0 m_\mathrm{e}\omega_\mathrm{L}^2 c}\left(\frac{2\nu_\mathrm{e}}{c} - \partial_z\right) I_\mathrm{L}(z,t)\,, \tag{1.3.2}$$

where ν_e is the electron collision frequency, $\omega_\mathrm{p} = 2\pi\nu_\mathrm{p}$ the angular plasma frequency[10], c the vacuum speed of light and I_L the intensity envelope of the laser pulse. The validity of Eq. (1.3.2) requires that the current J_z is computed via $J_z = -\epsilon_0\partial_t E_z$ assuming implicitly $(\nabla \times \mathbf{B})_z = 0$. In addition, in order to determine the whole spatio-temporal structure of J_z, a second strong assumption is made: the plasma is assumed to be transversally infinitely thin. Then, the computation of the far-field radiation emitted by the current gives THz far-field spectra and radiation patterns. This model turned out to match well the conical radiation pattern. The emission angle follows $\theta \propto \sqrt{\lambda_\mathrm{THz}/L_\mathrm{p}}$ for $\lambda_\mathrm{THz}/L_\mathrm{p} \ll 1$, where λ_THz is the emitted THz wavelength and L_p the length of the filament-plasma. Thus, for a filament that is typically much longer than the THz wavelength, the emission angle is very small. This mechanism was referred to as transition-Cherenkov (TC) mechanism. The name comes from the characteristic conical

[9] In the laser propagation direction z the component of a vector is referred to as "longitudinal".
[10] Here, ν_e and ω_p are treated as a constant.

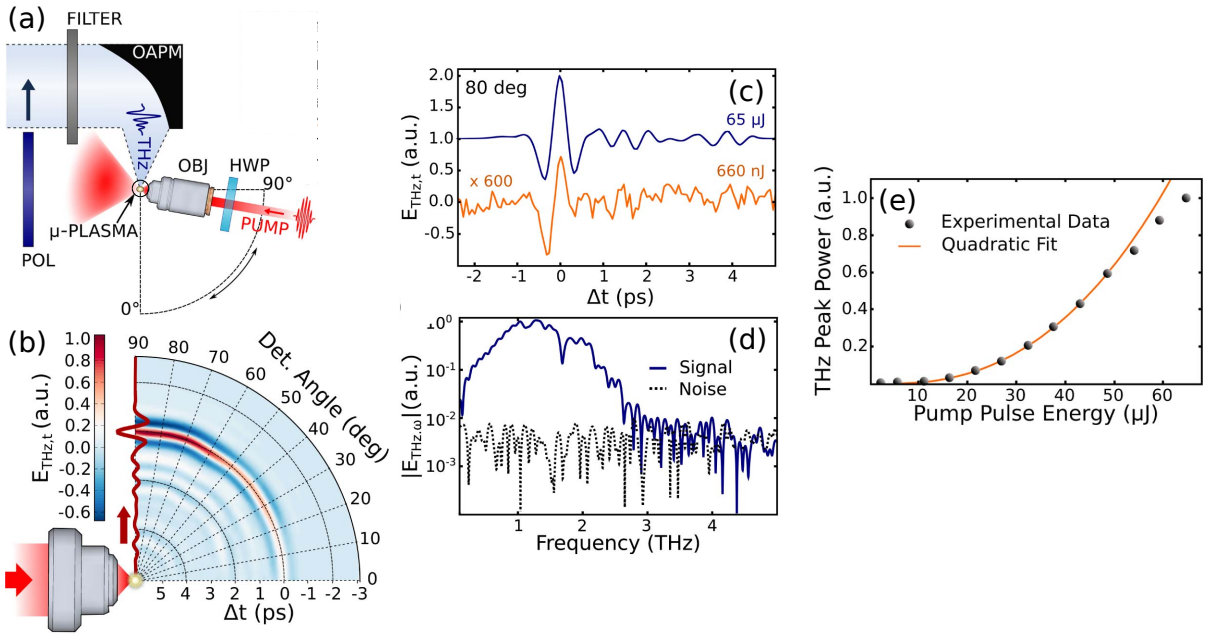

Figure 1.3.3.: (a) Schematic view of the set-up that was realized to characterize a THz-emitting microplasma in [61]: The 100-fs pump laser (PUMP) is passing through a half wave plate (HWP) and is focused by high numerical aperture objective (OBJ) into ambient air; the THz radiation is focused by an off-axis parabolic mirror (OAPM) before passing through a THz polarizer (POL). (b) Angularly and temporally resolved THz signal $E_{\mathrm{THz,t}}$ that was measured by means of electro-optic sampling. THz radiation is emitted within an emission cone of 80°. (c) Reconstructed THz electric field $E_{\mathrm{THz,t}}$ at the detection angle $\varphi = 80°$ and laser pulse energies $\mathfrak{E}_{\mathrm{L}} = 65\ \mu$J, $\mathfrak{E}_{\mathrm{L}} = 660$ nJ. (d) Spectral amplitude for $\mathfrak{E}_{\mathrm{L}} = 65\ \mu$J and $\varphi = 80°$. (e) THz peak power scaling with $\mathfrak{E}_{\mathrm{L}}$ at $\varphi = 80°$.

radiation profile. While Cherenkov radiation usually requires the force moving at superluminal velocity, this is not necessary for an emission zone of a finite length (see Chap. 4).

In terms of the plasma response to the excitation by the ponderomotive force, the model based on Eq. (1.3.2) from [59] is very similar to the previously discussed propositions in [55]. Both predict, for a sufficiently short laser pulse, oscillations of the current at the plasma frequency ω_{p} and the resulting far-field radiation to be peaked at ω_{p}. However, using Eq. (1.3.2) and then assuming a transverse shape of the plasma for the description of THz emission violates energy conservation: This can be easily seen for the collision-less case. For $\nu_{\mathrm{e}} = 0$, an initially excited plasma would oscillate with a constant amplitude at ω_{p} after the excitation forever. Thus, the energy within the plasma would stay constant. But, THz radiation emission requires a depletion of this energy, because no external energy source is available after the excitation by the laser pulse. This simple consideration shows that the model should be completed (see Chap. 2).

1.3.1.3. Single-color fs-laser-induced microplasma

Two decades after the first investigations of Hamster et al. in [55], the first proof of principles has been made that gas-plasma based THz generation is indeed accessible with compact driving lasers. In 2015, Buccheri and Zhang [61] generated THz radiation by strongly focusing a sub-μJ laser pulse into air. Their experimental set-up is sketched in Fig. 1.3.3(a). A microplasma is

created in the focal region and emits conical THz radiation with a large opening angle $\theta \approx 80°$ as can be seen from Fig. 1.3.3(b). Similar emission patterns but with a smaller θ have been observed in filaments which are much longer than a microplasma [cf. Sec. 1.3.1.2]. This observation is in agreement with the model in [59] where the opening angle of the emission cone increases when the plasma length decreases. As can be seen in the reconstructed THz electric field in Fig. 1.3.3(c), ps-long THz pulses have been created. The corresponding far-field spectrum in Fig. 1.3.3(d) reveals no sharp spectral features like one could expect from oscillations at the plasma frequency. The spectrum is rather similar to what has been observed in Fig. 1.3.1(c) close to the ambient pressure where $1.2 \cdot 10^{19}$ cm$^{-3} \leq n_e = 2.7 \cdot 10^{19}$ cm$^{-3} \leq 5 \cdot 10^{19}$ cm^{-3} for a singly ionized gas. For few-tens-of-μJ laser pulses, the THz power is shown in Fig. 1.3.3(e) to scale quadratically with the laser pulse energy $\mathfrak{E}_L$, consistent with a linear increase of the conversion efficiency. For $\mathfrak{E}_L > 50\,\mu$J, the scaling of the power becomes rather linear and the conversion efficiency saturates.

In summary, it has been shown that already few-μJ laser pulse energies are sufficient to produce THz emission from gas-plasmas like the microplasma in [61]. The first gas-plasma based experiments on THz generation in [55] revealed only conversion efficiencies around 10^{-8} with mJ-driving-laser-pulse energies. The experimental set-ups win over their simplicity and provide first proofs of principle that gas-plasma based THz sources can provide broadband THz pulses below 6 THz and can be compact. However, the modeling of the THz radiation is incomplete at this stage: On the one hand, besides longitudinal ponderomotive forces, transverse ponderomotive forces [62], thermal pressure [63] and many other effects can lead to excitation of the plasma at THz frequencies (see Sec. 2.5.2, 4.1). Thus, for 1C-driving-laser pulses the dominating THz generation mechanism is still controversial. On the other hand, the modeling of the plasma response should be completed. Moreover, the conversion efficiencies and spectral bandwidth as observed from 1C-laser-induced microplasmas need a substantial improvement in order to compete with traditional THz sources. The efforts to resolve these problems will be elaborated in the rest of the manuscript.

1.3.2. DC-biased single-color fs-laser-induced gas-plasma

Another approach to generate THz radiation by using 1C-fs-laser-induced gas-plasmas originates from the principle that has been already successfully realized in PCSs (see Sec. 1.2.2): Applying a static electric field (DC-bias) during a fs-laser pulse induces a conductivity in a medium, a low frequency current can be generated. In PCSs, the current in the metallic antenna attached to the photo-conductive medium emits THz waves. In gas-plasmas, the plasma itself acts as antenna. Löffler at al. were the first in 2000 [56] who produced THz emission from a DC-biased gas-plasma [see Fig. 1.3.4(a)].

Later, it has been shown experimentally that DC-bias can increase the THz pulse energy in 1C-fs-laser-induced filaments [64]. As the measurement (markers) and the quadratic fit (red dashed line) in Fig. 1.3.4(b) show, $\mathfrak{E}_{THz}$ scales quadratically with the applied constant electric field E_s having an off-set for $E_s = 0$. This off-set is interpreted as the signal originating from the ponderomotive excitation that has been discussed in Sec. 1.3.1.2. The THz emission profile in Fig. 1.3.4(c) reveals a forward directed emission which has a light asymmetry. This asymmetry could be the result of the interference between the radially polarized THz wave originating from the ponderomotive excitation and the linearly polarized emission coming from the DC bias. Using a 50-fs-long 2.4-mJ laser pulse and $E_s = 5$ kV/cm within a 2-cm long filament, the THz pulse energy has been estimated to be $\mathfrak{E}_{THz} = 0.05$ nJ resulting in $\eta_{THz} = 2 \cdot 10^{-8}$. In [64], the authors estimate that potential improvements like higher bias-voltage or longer interaction

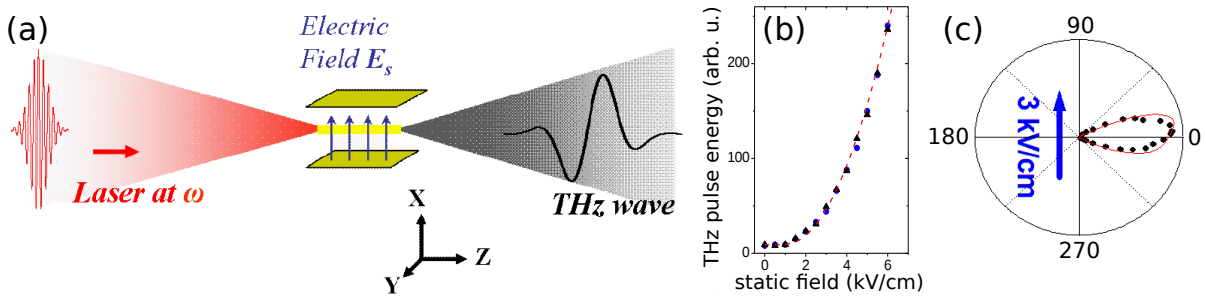

Figure 1.3.4.: (a) Schematic figure of the scheme with DC-bias [64]: A static electric field E_s is applied normally to the propagation direction of the ionizing laser pulse and leads to an excitation of the gas-plasma that emits a THz wave. (b) measured THz pulse energy (marker) and a quadratic fit (line) depending on the applied static electric field E_s. (c) Radiation profile measured (marker) and computed (line) from a DC-biased filament with $E_\mathrm{s} = 3$ kV/cm.

lengths could further increase the THz pulse energy to hundreds of nJ. However, a significant increase of E_s beyond tens of kV/cm is not possible due to creation of an electron avalanche leading to sparks between the electrodes. Consequently, THz pulse energies around hundreds of nJ from DC-biased 1C-fs-laser-induced filaments have not been reported up to date.

However, the limit for E_s can be increased by using higher gas pressures. Higher gas pressures lead to a reduction of the mean free path of the electrons. Thus, they are slower when colliding with neutrals and ions. Consequently, the impact-ionization probability is reduced and no avalanche is formed. In stronger focused configurations where no filament is created, THz pulse energy has been shown to be independent on the gas pressure between 1 and 46 bar [65]. Because of that, it was possible to increase the static field to $E_\mathrm{s} = 200$ kV/cm and the emitted THz field. Using a 390-μJ strong fs-laser pulse, THz electric fields of 0.5 kV/cm have been reported in nitrogen and 1 kV/cm in air [66]. Furthermore, the THz electric field has been shown to be proportional to $\mathfrak{E}_\mathrm{L}$ without any indication for a saturation behavior [56, 65, 66, 67]. As a direct comparison with GaAs PCSs in [65] shows, THz field amplitudes accessible with DC-biased gas-plasmas could beat the one based on PCSs when extrapolating the driving laser pulse energy to 10-100 mJ.

Same as for the non-biased 1C-laser pulses, the THz generation mechanism for DC-biased 1C-fs-laser-induced gas-plasmas is controversial. Originally, in [56] the THz emission was associated with acceleration of laser-induced charge careers and their deceleration or recombination. In [64], the role of screening has been pointed out[11]: After the electrons get accelerated by the external static electric field, a charge is created at the boundaries of the plasma and screens the external electric field inside the gas-plasma. Assuming instantaneous ionization of the electrons followed by the screening after the time ω_p^{-1}, the current amplitude can be estimated to $\sim \epsilon_0 E_\mathrm{s} \omega_\mathrm{p}$. In [64], the response of the plasma has been claimed to be determined by the Fourier spectrum of the current $\mathfrak{F}\{J_x\}$ following locally

$$\mathfrak{F}\{J_x\}(\omega) = \frac{\epsilon_0 E_\mathrm{s} \omega_\mathrm{p}^2}{\omega^2 - \omega_\mathrm{p}^2 + \mathrm{i}\nu_\mathrm{e}\omega}\,. \tag{1.3.3}$$

Similar to the procedure in [59], the assumption of an infinitely thin plasma wire can be used

[11] The model in [68] omits the screening resulting in an unlimited acceleration of the electrons.

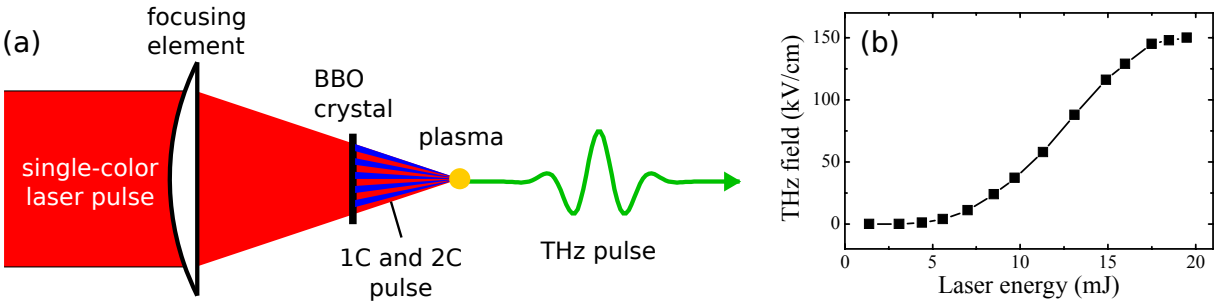

Figure 1.3.5.: (a) Illustration of the typical two-color THz generation scheme [69]. Measured THz peak electric field depending on the laser pulse energy from [57].

to compute the resulting hypothetical THz far-field spectrum. However, as pointed out in Sec. 1.3.1.2, such an oscillating current cannot treat the plasma response correctly. In particular, it does not account for the energy dissipation to the radiating field.

In summary, using an external static electric field can significantly enforce the THz generation compared to unbiased 1C-fs-laser-induced gas-plasmas. Using mJ-strong laser pulses, DC-biased gas-plasma sources might compete with PCSs in terms of achievable THz peak electric fields. The modeling, however, does not account for screening effects and plasma response correctly. It will be extended in Chap. 2 and applied in Sec. 4.4 to describe THz emission from 1C-laser-driven DC-biased microplasmas.

1.3.3. Two-color fs-laser-induced gas-plasma

Two-color (2C) fs-laser pulses are by definition laser pulses with two frequency peaks. In the following, the focus relies on 2C-laser pulses which have typically one fundamental harmonic (FH) frequency peak at ω_L and one second harmonic (SH) frequency peak at $2\omega_L$. The standard 2C-THz-generation scheme consists of a focused 1C-laser pulse with pulse energy $\mathfrak{E}_L$ and a β-barium-borate (BBO) crystal that is placed just before the focus [see Fig. 1.3.5(a)]. In the BBO crystal, a $\chi^{(2)}$-nonlinear process leads to creation of the SH field and both harmonics co-propagate towards the common focal spot. Close to the focus the resulting 2C-laser pulse ionizes the gas creating an electron plasma that emits a THz pulse.

Initially, THz emission from 2C-laser pulses has been reported by Cook and Hochstrasser in 2000 [70]. A 65-fs 150-μJ laser pulse has been used to produce THz radiation with frequency components < 4 THz in air. However, only few-pJ THz pulses leading to THz peak electric fields below 1 kV/cm could be demonstrated resulting in $\eta_{THz} = 10^{-8}$, that is not an substantial improvement compared to 1C configurations in Sec. 1.3.1-1.3.2. Later, 10 kV/cm THz peak electric field have been reported for $\mathfrak{E}_L = 400\,\mu$J [66] and 150 kV/cm for $\mathfrak{E}_L = 20\,$mJ in saturation [57] [see Fig. 1.3.5(b)]. Using 50-fs-long 30-mJ laser pulses in argon, efficiencies of $\eta_{THz} = 10^{-4}$ and spectral bandwidth of 75 THz were achieved in [71]. The gas pressure turned out to be important to maximize the THz pulse energy increasing with p up to $p = 1$ bar and then decreasing for higher gas pressures [see Fig. 1.3.6(a)] [66, 71]. Finally, exploring the λ_L-dependence of the THz generation by 2C-laser pulses [72], impressing 4.4 MV/cm THz peak electric field amplitude have been reported reaching 20-THz-spectral bandwidth for 60-fs 400-μJ-strong driving laser pulses leading to $\mathfrak{E}_{THz} = 0.6\,\mu$J and thus $\eta_{THz} \geq 10^{-3}$ for $\lambda_L = 1.8\ \mu$m [see Fig. 1.3.6(b)] [73].

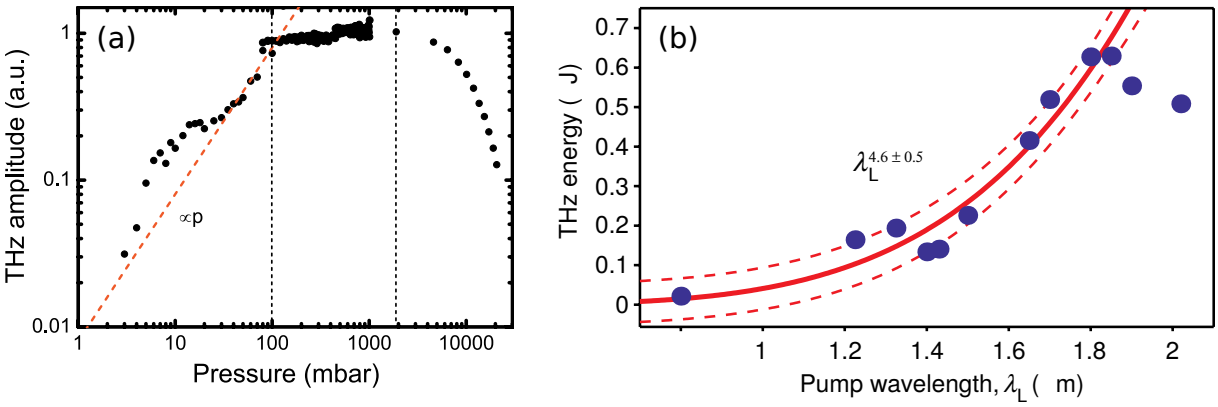

Figure 1.3.6.: (a) Air-pressure dependence of the 2C-laser-induced THz peak electric field that was measured in [66]. Fundamental-pump-wavelength λ_L dependence of the THz-pulse energy in nitrogen that has been reported in [73]. The blue dots specify the measured values. The red solid line is $\propto \lambda_L^{4.6}$ and the dashed red lines specify the tolerance curves $\propto \lambda_L^{4.1}$and $\propto \lambda_L^{5.1}$.

Initially, the THz emission from 2C-laser pulses has been attributed to the four-wave-mixing (FWM) process [70]. FWM is based on the $\chi^{(3)}$-nonlinearity of the neutral gas where the mixing of three frequencies results in a down-conversion to the zero-frequency since $\omega_L + \omega_L - 2\omega_L = 0$. Due to the finite pulse duration of the FH and SH pulse not only excitation at the 0-frequency but also at THz frequencies is realized (cf. Sec. 1.2.3). For intensities sufficiently far below 10^{14} W/cm^2, gases as air or argon get only weakly ionized and FWM contributes significantly to THz generation (see Sec. 2.2.1 and [72, 74]). However, another THz generation mechanism referred to as the ionization current (IC) or photo-current mechanism is held responsible for the large THz peak amplitudes as observed in [57, 66, 73]: During the interaction of the laser electric field $\mathbf{E}$ with an electron that is bounded within a neutral atom, the electron can be ionized and subsequently accelerated in the laser electric field. Assuming at the time point t a macroscopic electron density $n_e(t)$, the resulting local macroscopic current[12] writes [75]

$$\partial_t \mathbf{J}_{IC}(t) = \underbrace{\frac{q_e^2 n_e(t)}{m_e}}_{=\iota_{IC}} \mathbf{E}_L(t) \,, \tag{1.3.4}$$

where the term on the right hand side ι_{IC} can be considered as the IC source.

At intensities above 10^{14} W/cm^2, the atoms are ionized in the tunnel ionization regime that yields the typical step-like increase of the electron density as can be seen from Fig. 1.3.7(a). The evaluation of Eq. (1.3.4) for a 2C-laser pulse leads to currents that can have a non-zero value after the interaction which indicates a DC component of the current[13] [see Fig. 1.3.7(b)]. The amplitude of the low-frequency current is determined by ι_{IC}. For 2C-laser pulses, it can provide a significant excitation at THz frequencies whereas for similar 1C-laser pulses ι_{IC} yields almost no low-frequency components [see Fig. 1.3.7(c)].

The model Eq. (1.3.4), treats electrons as test particles in an external electric laser field. But, accelerated electrons emit in particular THz electric field waves that vice versa can drive

[12] Throughout the manuscript, the current density is referred to as a current for sake of brevity.

[13] This low-frequency component of the current can be considered as the source for a 'zero-order' Brunel harmonic [76, 77].

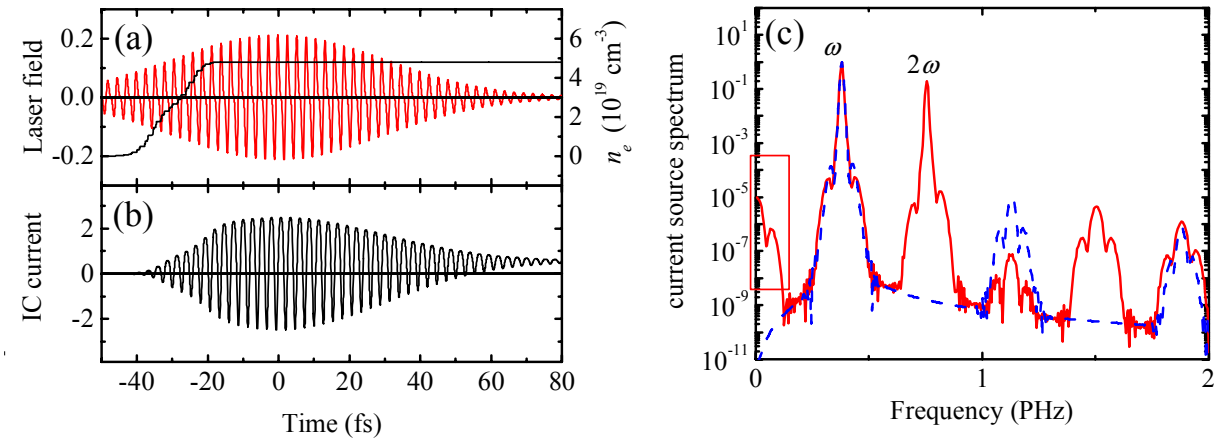

Figure 1.3.7.: (a) An example from [57], where in (a) an exemplary electric field (red) and resulting step-like increasing electron density (black) is presented. (b) shows the corresponding ionization current and (c) the spectrum of the current source ι_{IC} for a 2C-laser pulse (solid red line) and 1C-laser pulse (dashed blue line).

the electron current [78]. Moreover, it is tempting to add a constant electric field E_{s} to the laser field in ι_{IC} to describe DC-biased 1C-laser-induced gas-plasmas (see Sec. 1.3.2)[14]. But, this would lead to an unterminated acceleration of the electrons. In reality, one expects that displaced electrons impose a total charge density and thus, a restoring electric field. Such a screening should appear whenever ι_{IC} has a DC frequency component, independently whether DC-biased 1C-laser pulses or 2C-laser pulses are considered. Thus, a self-consistent treatment of the electron current and electric field is in general necessary.

In summary, 2C-fs-laser-induced gas-plasmas provide currently the most successful gas-plasma-based-THz source. Using mJ-strong laser pulses, THz pulses can be created with efficiencies up to 10^{-3} leading to MV/cm-large THz peak electric fields. Thus, the 2C-fs-laser-induced gas-plasma sources can compete with conventional THz sources that have been presented in Sec. 1.2 in terms of average power, efficiency and peak THz fields. In terms of spectral properties, 2C-fs-laser-induced gas-plasma sources can produce even broader frequency spectra than conventional sources covering the whole THz gap at one blow. However, mJ-laser-driven THz sources are still not compact. Their scalability to lower pulse energies is an open issue and leads to the main motivation of this work.

1.4. Motivation of this work

There is a large demand for THz sources driven by a wide range of applications ranging from spectroscopic identification of explosives to industrial quality control of polymers (see Sec. 1.1). Many of them can profit from compact broad-band pulsed THz sources covering the whole THz gap between 0.3 and 30 THz. Conventional sources like PCSs or DFG-based sources (see Sec. 1.2) cannot bridge the THz gap at one blow. Alternatively, fs-laser-induced gas-plasma-based THz sources can be used (see Sec. 1.3). Those have been shown to provide broad-band THz pulses emitting radiation even beyond the THz gap. Like conventional sources, they can reach THz average powers at mW-level and THz peak electric fields of 1 MV/cm. The high performance relies on mJ-driving lasers that dictate the size and costs of the THz source.

[14] This model has been used in [68] to model DC-biased 1C-laser-induced gas-plasmas.

Applications exploiting linear properties of THz-matter interaction require often only few-μW average power and do not require MV/cm peak electric field amplitudes. This poses the question, if the driving laser pulses could be down-scaled to the μJ-level. Smaller driving lasers are not only compact, they also can operate at much higher repetition rates. While mJ-lasers typically operate at 1 kHz, μJ-lasers can easily operate at 100 MHz. This means that μJ-laser-based THz sources could produce the same THz average powers like mJ-laser-based THz sources, but are allowed to have efficiencies two orders of magnitude below.

The hope that μJ-laser-driven gas-plasma-based sources can reach this expectations is founded by recent experiments [61]. Here, THz emission from a strongly focused 1C-laser pulse has been observed. Even laser-pulse energies below 1 μJ have been sufficient to create a microplasma in focus. However, this compact THz source did not reach the performance in terms of spectral bandwidth covering the hole THz gap and laser-to-THz conversion efficiencies $\eta_{\mathrm{THz}} \geq 10^{-4}$ like it is known from mJ-lasers-driven gas-plasma-based sources. This poses the question if it is actually possible to improve the performance of fs-laser-induced microplasmas.

This work is dedicated to the theoretical investigation of THz generation in fs-laser-induced microplasmas. The major goal is to understand the mechanisms of THz generation. This requires a model that gives

1. a unified description of the major THz generation mechanisms,
2. a Maxwell-consistent theory of the plasma response.

Such a model is derived in Chap. 2. To investigate fs-laser-induced microplasmas by solving the model equations, we provide

3. numerical tools for Maxwell-consistent modeling of the microplasma,
4. a numerical tool for tight focusing of laser pulses.

The presentation of those tools is a part of Chap. 3. Then, we want to

5. identify the major THz generation mechanisms in microplasmas,
6. understand the plasma response and emission properties,
7. propose ways to increase the laser-to-THz conversion efficiency.

This is done for single-color driving lasers in Chap. 4 and for two-color driving lasers in Chap. 5.

2. Theory of THz emission from laser induced microplasmas

Contents

First, the ionization model that is used to compute the ion densities is presented. We argue why linear and nonlinear polarization of the neutral atoms can be neglected. Afterwards, the fundamental equations of the theory are presented: the Maxwell equations and the Vlasov equation for the electrons. Then, the velocity moments of the Vlasov equation are computed leading to the continuity, Euler and energy equations. A multiple scale expansion is performed based on these equations, the two lowest order sets of equations are detailed and some properties of them are discussed before considering the limitations of the multiple scale expansion. Finally, we define what we consider as the far-field power spectrum from the gas-plasma and show how to compute the far-field power spectrum from a current consistently with the Maxwell's equations.

2.1. The ionization model

The ionization model is based on a semi-classical approach: We use the results from quantum mechanics on field ionization in order to determine the density of free electrons, i.e., electrons that are detached from the parent-ion. Then, the motion of free electrons interacting with the laser is described classically (see Sec. 2.3). In this section, we repeat the results from the theory of field ionization for peak intensities $I_\mathrm{L} > 10^{14}$ W/cm^2.

Two regimes of field ionization are distinguished and prevail in low and high intensity regime, respectively [79]. The Keldysh parameter $\gamma = \omega_\mathrm{L}\sqrt{(2m_\mathrm{e}I_\mathrm{p})}/|q_\mathrm{e}E_\mathrm{L}^{(0)}|$, where I_p is the ionization potential and $E_\mathrm{L}^{(0)}$ is the electric field amplitude, determines the dominant regime. For $\gamma \gg 1$, the multi-photon regime dominates. Here, the electron absorbs a number of photons such that the total energy of the absorbed photons is higher than the ionization potential. For $\gamma \ll 1$, the tunneling regime prevails. Here, the dipole energy $\mathbf{r}_\mathrm{e}\mathbf{E}(t)$, where $\mathbf{r}_\mathrm{e}$ is the position of the electron relative to the parent ion and $\mathbf{E}$ is the time varying-electric field, cancels the Coulomb potential of the ion $V_\mathrm{bound}(\mathbf{r}_\mathrm{e})$, such that the total potential decreases for a short moment and the electron escapes from the parent ion. Assuming a laser wavelength $\lambda_\mathrm{L} = 2\pi c/\omega_\mathrm{L} = 0.8\,\mu\mathrm{m}$ and the first-level ionization potential of argon with $I_\mathrm{p} = 15.759$ eV [80], $\gamma = 1$ is reached for an intensity $I_\mathrm{L}^{(0)} = c\epsilon_0(E_\mathrm{L}^{(0)})^2/2 = 1.3 \cdot 10^{14}$ W/cm^2. Since we are working with intensities $I_\mathrm{L} \in [10^{14}, 10^{16}]$ W/cm^2, we consider the tunneling mechanism to model field ionization. In this regime, the ionization rate can be written as a monotonically increasing function of the modulus of the instantaneous electric field. Because of that, a step-like increase of the electron density, one at each extremum of the electric field, is characteristic for tunneling ionization and has been indeed observed in experiments [81, 82]. This step-like increase is crucial for THz generation in two-color-laser-induced gas-plasmas (see Sec. 1.3.3). More rigorous quantum-mechanical approaches report qualitatively similar results like those obtained from quasi classical approaches [83], at least for many cycle laser pulses.

In this work, the ionization rate $W^{(Z)}$ is computed according to the quasistatic ADK theory [84, 85]:

$$W^{(Z)}[E] = I_\mathrm{p}\left|C_{n^\star_{(Z)},l^\star_{(Z)}}\right| f(l_{(Z)}, m_{(Z)}) \exp\left(-\frac{2E_0^{(Z)}}{3|E[E_\mathrm{at}]|}\right)\left(\frac{2E_0^{(Z)}}{|E[E_\mathrm{at}]|}\right)^{2n^\star_{(Z)}-m_{(Z)}-1}, \tag{2.1.1}$$

where

$$E_0^{(Z)} = (2I_\mathrm{p}^{(Z)}[27.2116\,\mathrm{eV}])^{3/2} \tag{2.1.2}$$

$$f(l,m) = \frac{(2l+1)(l+|m|)!}{2^{|m|}|m|!(l-|m|)!} \tag{2.1.3}$$

$$n^\star_{(Z)} = \frac{Z}{\sqrt{2I_\mathrm{p}^{(Z)}}} \tag{2.1.4}$$

$$C_{n^\star_{(Z)},l^\star_{(Z)}} = \frac{2^{2n^\star_{(Z)}}}{n^\star_{(Z)}\Gamma(n^\star_{(Z)}+l^\star_{(Z)}+1)\Gamma(n^\star_{(Z)}-l^\star_{(Z)})} \tag{2.1.5}$$

$$\Gamma(x) = \int_0^\infty t^{x-1}\exp(-t)\,dt \tag{2.1.6}$$

$$l^\star_{(Z)} = n^\star_{(Z)} - 1, \tag{2.1.7}$$

Hereby, Z is the charge of the created ion, $l_{(Z)}$ is the angular momentum and $m_{(Z)}$ the magnetic quantum number of the electronic state. The electric field in Eq. (2.1.1) is given in units of $E_\mathrm{at} = 5.1422 \cdot 10^{11}$ V/m and the ionization potential in units of 27.2116 eV. The ionization potentials are taken from [80]. In principle one has to account for $m = -l \ldots l$. However, since the ionization rate for $m = 0$ is much larger than for other m, we are used to consider $m = 0$ [84].

The density $n_{\mathrm{ion}}^{(Z)}$ for a Z charged ion is determined by the set of equations

$$\partial_t n_{\mathrm{ion}}^{(Z)} = \underbrace{W^{(Z)} n_{\mathrm{ion}}^{(Z-1)} - W^{(Z+1)} n_{\mathrm{ion}}^{(Z)}}_{=S^{(Z)}} \tag{2.1.8}$$

for $Z = 0, 1, 2, 3, \ldots$, the initial neutral density is $n_{\mathrm{ion}}^{(0)}(t = -\infty) = n_{\mathrm{n}}(t = -\infty) = n_{\mathrm{a}}$ and formally $n_{\mathrm{ion}}^{(-1)} = 0$, $W^{(0)} = 0$. The atoms can be at most K times ionized and thus $W^{(K+1)} = 0$. For sake of brevity, we introduce the ion source $S^{(Z)}$ by

$$S^{(Z)} = W^{(Z)} n_{\mathrm{ion}}^{(Z-1)} - W^{(Z+1)} n_{\mathrm{ion}}^{(Z)} \,. \tag{2.1.9}$$

The electron source is defined by

$$S = \sum_Z Z S^{(Z)} \,. \tag{2.1.10}$$

2.2. Assumption of a polarization-free gas plasma

Before building the theory, we argue why the nonlinear and linear polarization from bound electrons can be neglected for THz generation and the laser pulse propagation in the case of microplasmas. We exploit mainly the fact that we are dealing with strongly focused laser beams leading to intensities above 10^{14} W/cm^2. This fact results in high ionization degrees and short interaction distances of the laser with the gas-plasma. Later in Sec. 5.2.5, we will argue that also for the propagation of the THz waves, linear dispersion is of minor role for several-hundreds-of-μm-short plasmas, i.e. microplasmas.

Here in the first part, we exclude one of two key effects of the nonlinear polarization: The THz generation by four-wave-mixing (FWM). Then in the second part, both linear and non-linear polarization response of the neutrals are shown to be negligible compared to the electron-response and thus of minor importance for laser propagation effects.

2.2.1. Influence of the neutral polarization on the THz generation

We consider as an example an argon gas and an x-linearly polarized two-color driving laser with the local electric field $E_{\mathrm{L}}(t) = E_{\mathrm{L}}^{(0)} \left[\sqrt{1-\xi}\cos(\omega_{\mathrm{L}} t) + \sqrt{\xi}\cos(2\omega_{\mathrm{L}} t + \phi)\right] \exp\left(-t^2/t_0^2\right)$, where $\lambda_{\mathrm{L}} = 2\pi c/\omega_{\mathrm{L}} = 800$ nm, $t_0 = 50$ fs. The laser amplitude $E_{\mathrm{L}}^{(0)}$, fraction of energy in the SH field ξ and the angle ϕ are kept free. The photon-energy corresponding to $\lambda_{\mathrm{L}} = 800$ nm is 1.5 and 3 eV for the FH and SH wavelength, respectively. The first-level ionization potential of argon is $I_{\mathrm{p}} = 15.759$ eV [80], much larger than the laser photon energy. We assume that the considered laser frequencies are far away from any material resonance. In this case, the nonlinear polarization caused by $\mathbf{E}_{\mathrm{L}}$ leading to a down-conversion from $2\omega_{\mathrm{L}}$, ω_{L} to THz frequencies follows the scheme $\omega_{\mathrm{L}} + \omega_{\mathrm{L}} - 2\omega_{\mathrm{L}} = 0$ and can be described by the following expression [38]

$$P_{\mathrm{NL}}(t) \approx \epsilon_0 \chi_{\mathrm{Ar}}^{(3)} E_{\mathrm{L}}^3(t) \,. \tag{2.2.1}$$

The nonlinear polarization can be rewritten as a current [6] $J_{\mathrm{NL}} = \partial_t P_{\mathrm{NL}}$. This is a very useful definition in order to compare the contributions from the nonlinear polarization with the IC-mechanism. There, the current J_{IC} is driven according to Eq. (1.3.4) in the linear polarization case by the IC source $\iota_{\mathrm{IC}} = q_{\mathrm{e}}^2 n_{\mathrm{e}} E_{\mathrm{L}}/m_{\mathrm{e}} = \partial_t J_{\mathrm{IC}}$. Analogous, we can define the nonlinear current source ι_{NL} by

$$\iota_{\mathrm{NL}} = \partial_{tt}\left(\epsilon_0 \chi_{\mathrm{Ar}}^{(3)} E_{\mathrm{L}}^3(t)\right) \,. \tag{2.2.2}$$

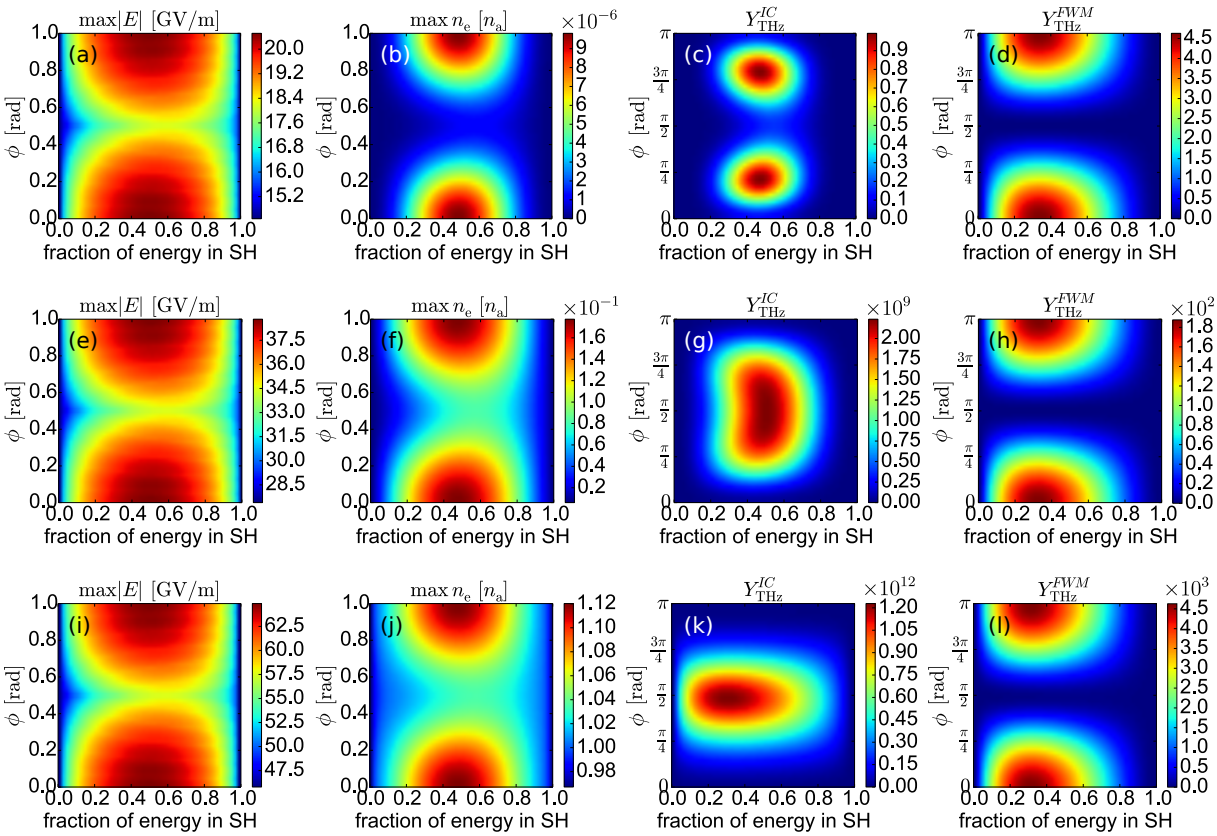

Figure 2.2.1.: Peak electric field amplitudes $\max|E_\mathrm{L}|$, maximum electron density $\max n_\mathrm{e}$ in an argon-plasma as well as the IC-THz-yield $Y_\mathrm{THz}^\mathrm{IC}$ and FWM-THz-yield $Y_\mathrm{THz}^\mathrm{FWM}$ in arbitrary but comparable units. The dependence on phase ϕ and fraction of SH energy ξ is shown for three different laser field strengths of a two-color laser pulse: $E_\mathrm{L}^{(0)} = 14.5$ GV/m (a-d), $E_\mathrm{L}^{(0)} = 27.4$ GV/m (e-h) and $E_\mathrm{L}^{(0)} = 45.8$ GV/m (i-l). The laser pulse duration is $t_0 = 50$ fs. The initial atom density is $n_\mathrm{a} = 2.7 \cdot 10^{19}$ cm^{-3}.

Assuming that the currents J_IC and J_NL are present within a small volume, a point-source, the emitted THz radiation is proportional to the time derivative of the current and thus to the nonlinear source terms ι_IC and ι_NL. This motivates to introduce the THz yield of the current source by

$$Y_\mathrm{THz}^\mathrm{(IC/FWM)} = \int_0^{2\pi\times 60\,\mathrm{THz}} |\hat{\iota}_\mathrm{IC/NL}(\omega)|^2 \, d\omega \,, \tag{2.2.3}$$

where the "$\hat{}$" indicates the Fourier transform with respect to time as it is introduced in App. A. Moreover, we have extended the integration beyond the THz-gap[1] in order to be consistent with considerations in Chaps. 4-5.

Now, we consider the THz yield for different laser field amplitudes. In [86], we find the nonlinear refractive index $n_2 = 10.4 \cdot 10^{-20}\,\mathrm{cm}^2/\mathrm{W}$ for argon that can be converted into $\chi_\mathrm{Ar}^{(3)} \approx 2n_2 n^2 c\epsilon_0/3 = 1.8{\cdot}10^{-26}\ \mathrm{m}^2/\mathrm{V}^2$ following [38]. Hereby, n is the linear refractive index with $n \approx 1$. The neutral density n_n and ion-densities $n_\mathrm{ion}^{(Z)}$ for a Z times charged ion are computed according

[1] The following conclusions, however, do not change if integrating only up to 30 THz in Eq. (2.2.3).

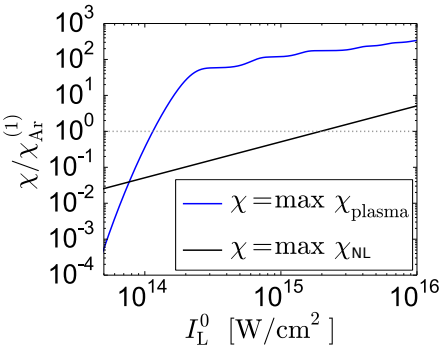

Figure 2.2.2.: Intensity-dependent contributions of the plasma-response and Kerr-response to the susceptibility for a single-color laser pulse with $t_0 = 50$. In both cases the maximum value for all times is taken. The gray dotted line is the linear susceptibility $\chi_{\mathrm{Ar}}^{(1)}$ for a neutral argon gas with $n_{\mathrm{a}} = 2.7 \cdot 10^{19}\,\mathrm{cm}^{-3}$.

to Sec. (2.1) and the electron density is approximated here by $n_{\mathrm{e}} \approx \sum Z n_{\mathrm{ion}}^{(Z)}$. Fig. 2.2.1(b) shows that for peak electric fields around 20 GV/m [see Fig. 2.2.1(a)], the ionization degree is far below full single ionization. Naturally, it becomes maximum, when the electric field becomes maximum. This happens when half of the energy is in the SH and $\phi = 0, \pi$. As can be seen in Fig. 2.2.1(c-d), in such a case of weak ionization, more THz radiation is expected from the FWM process than from the IC mechanism[2]. However, when reaching electric field amplitudes around 40 GV/m corresponding to an intensity of 10^{14} W/cm^2, about 10 % of the atoms are ionized and $Y_{\mathrm{THz}}^{(\mathrm{IC})}$ dominates $Y_{\mathrm{THz}}^{(\mathrm{FWM})}$ already by 7 orders of magnitude [see Fig. 2.2.1(e-h)]. The difference becomes more and more dramatic when increasing the laser field amplitude [see Fig. 2.2.1(i-l)]. For $E_{\mathrm{L}}^{(0)} = 45.8$ GV/m that is a typical value for examples that are going to be considered in Chap. 5, $Y_{\mathrm{THz}}^{(\mathrm{IC})}$ dominates $Y_{\mathrm{THz}}^{(\mathrm{FWM})}$ by 9 orders of magnitude. Thus, we can neglect the nonlinear polarization as the source of THz radiation for $I_{\mathrm{L}}^{(0)} \geq 10^{14}$ W/cm^2.

2.2.2. Influence of the neutral polarization on the laser propagation

The propagation of a laser pulse through a gas-plasma can deviate from propagation in vacuum first of all because of the neutral atoms and electrons response. This response can be characterized by the frequency dependent susceptibility [6, 38]. In the following, we estimate the linear and nonlinear susceptibility of the neutrals and the susceptibility of the electrons for different intensities. Hereby, we consider laser pulses from Sec. 2.2.1 with $\xi = 0$, i.e., single-color laser pulses.

The susceptibility of the electrons for $\omega_{\mathrm{p}}(t) = \sqrt{q_{\mathrm{e}}^2 n_{\mathrm{e}}(t)/(m_{\mathrm{e}}\epsilon_0)} \ll \omega_{\mathrm{L}}$ and neglecting the damping of the electron current can be defined by

$$\chi_{\mathrm{plasma}}(t) = -\frac{\omega_{\mathrm{p}}^2(t)}{\omega_{\mathrm{L}}^2}\,. \tag{2.2.4}$$

[2]The THz yield is π-periodic with respect to ϕ. Moreover, $Y_{\mathrm{THz}}^{(\mathrm{FWM})}$ becomes as expected maximal when maximizing $(1-\xi)\sqrt{\xi}$ at $\xi = 1/3$ and for $\phi \in \{0, \pi\}$ [87]. For $Y_{\mathrm{THz}}^{(\mathrm{IC})}$, the situation is more complicated: For high ionization degrees $Y_{\mathrm{THz}}^{(\mathrm{IC})}$ becomes maximal when $\phi = \pi/2$ in agreement with the common literature [71, 88, 89]. For low ionization degrees, $Y_{\mathrm{THz}}^{(\mathrm{IC})}$ becomes maximal at some $\phi \neq \pi/2$. As anticipated from Fig. 2.2.1, this deviation arises from the fact that $\phi = \pi/2$ minimizes the peak electric field and thus the electron density. The influence of the phase angle ϕ on the THz generation is detailed in Chap. 5.

The nonlinear polarization in Eq. (2.2.1) contains besides THz-components for two-color pulses also components at ω_L and thus influences the laser propagation. We define[3]

$$\chi_\mathrm{NL}(t) = \chi^{(3)}_\mathrm{Ar} E^2_\mathrm{L}(t)\,. \tag{2.2.5}$$

Moreover, the linear susceptibility of the neutral argon is $\chi^{(1)}_\mathrm{Ar} = 2.65 \cdot 10^{-4}$ for $\lambda_\mathrm{L} \in [0.5, 2]\,\mu$m measured at 15 °C [90, 91].

Figure 2.2.2 presents the maximum values of χ_plasma (solid blue line) and χ_NL (solid black line) normalized to $\chi^{(1)}_\mathrm{Ar}$ depending on the laser peak intensity $I^{(0)}_\mathrm{L}$. Obviously the response of the plasma dominates for $I^{(0)}_\mathrm{L} \geq 10^{14}$ W/cm^2 over the neutral response[4]. Thus, in a strong focusing geometry where the intensity quickly increases before the focus leading to high degrees of ionization over short propagation distances, the response of the neutral atoms can be neglected and the electron-plasma response mainly determines the laser propagation. Hence, the linear and nonlinear susceptibility of neutral atoms are disregarded in our model.

2.3. Maxwell and Vlasov equations

We assume the validity of the macroscopic Maxwell's equations [6] that are the divergence-equations[5]

$$\nabla \cdot \mathbf{E}(\mathbf{r}, t) = \frac{\rho(\mathbf{r}, t)}{\epsilon_0} \tag{2.3.1}$$

$$\nabla \cdot \mathbf{B}(\mathbf{r}, t) = 0 \tag{2.3.2}$$

and curl-equations

$$\nabla \times \mathbf{E}(\mathbf{r}, t) = -\partial_t \mathbf{B}(\mathbf{r}, t) \tag{2.3.3}$$

$$\nabla \times \mathbf{B}(\mathbf{r}, t) = \frac{1}{c^2}\partial_t \mathbf{E}(\mathbf{r}, t) + \mu_0 \mathbf{J}\,. \tag{2.3.4}$$

Here, $\mathbf{E}$ and $\mathbf{B}$ are the macroscopic electric and magnetic vector fields[6], $\mathbf{J}$ is the macroscopic current density and ρ is the macroscopic charge density[7]. Here, all fields are functions of position vector $\mathbf{r} = (x, y, z)^\mathrm{T}$ and time t. The current will include only the contribution by the electrons, because the ions are assumed to be fixed[8].

The electron-plasma is governed by the non-relativistic Vlasov equation describing the distribution function f_e of the electrons depending on the electron position $\mathbf{r}$ and electron velocity $\mathbf{v}$

$$\partial_t f_\mathrm{e}(\mathbf{r}, \mathbf{v}, t) + \mathbf{v} \cdot \nabla_\mathbf{r} f_\mathrm{e}(\mathbf{r}, \mathbf{v}, t) + \frac{\mathbf{F}}{m_\mathrm{e}} \cdot \nabla_\mathbf{v} f_\mathrm{e}(\mathbf{r}, \mathbf{v}, t) = S[n^{(Z)}_\mathrm{ion}, \mathbf{E}]\delta(\mathbf{v}) + C[f_\mathrm{e}, f^{(Z)}_\mathrm{ion}]\,, \tag{2.3.5}$$

[3] Often, instead of $E_\mathrm{L}(t)$, the envelope of the electric field without fast oscillations is included in the definition because one is only interested in the polarization at ω_L. However, for the response of the electron-plasma a linear susceptibility cannot be introduced in this sense because of the fast variation of the electron density due to ionization. For consistency, we introduce both susceptibilities using the fast oscillating field E_L.

[4] This conclusion holds also for air as shown in App. B.

[5] Hereby, $\nabla = (\partial_x, \partial_y, \partial_z)^\mathrm{T}$.

[6] Vectors are typed in bold.

[7] For sake of brevity, $\mathbf{E}$, $\mathbf{B}$, $\mathbf{J}$ and ρ are also called electric field, magnetic field, current and charge density.

[8] For example, Argon ions have a mass that is more than 10^4 times larger than the mass of electrons. Thus, ions are assumed to be fixed.

where $\mathbf{v}$ is the electron-velocity coordinate[9]. The electrons are pushed by the electromagnetic force

$$\mathbf{F} = q_\mathrm{e} \left[\mathbf{E}(\mathbf{r}, t) + \mathbf{v} \times \mathbf{B}(\mathbf{r}, t)\right], \tag{2.3.6}$$

with the negative elementary charge of the electron $q_\mathrm{e} = -1.602 \cdot 10^{-19}$ C. The ionization of atoms is taken into account by the source term S that is specified in Sec. 2.1. We assume that each electron is born with zero velocity by writing the delta-distribution $\delta(\mathbf{v})$ on the right side of Eq. (2.3.5). The term $C[f_\mathrm{e}, f_\mathrm{ion}^{(Z)}]$ in Eq. (2.3.5) describes elastic collisions, i.e., C has the property to conserve the density and the total energy of the particles. Inelastic collisions are neglected[10]. We are interested in the damping of the electron current due to collisions. Non-relativistic electron-electron collisions do not change the electron current[11] and thus we will account for electron-ion collisions only.

Finally, defining the macroscopic current density $\mathbf{J}$ as the 1st velocity moment of the electron distribution function f_e,

$$\mathbf{J}(\mathbf{r}, t) = q_\mathrm{e} \int \mathbf{v} f_\mathrm{e}(\mathbf{r}, \mathbf{v}, t) d^3\mathbf{v}\,, \tag{2.3.7}$$

allows for coupling to the macroscopic Maxwell equations. In addition, introducing the electron density n_e as the 0th moment of the electron distribution function f_e, the total charge density reads

$$\rho(\mathbf{r}, t) = q_\mathrm{e} \left(\underbrace{\int f_\mathrm{e}(\mathbf{r}, \mathbf{v}, t) d^3\mathbf{v}}_{=n_\mathrm{e}(\mathbf{r},t)} - \sum_Z Z n_\mathrm{ion}^{(Z)}(\mathbf{r}, \mathbf{v}, t) \right). \tag{2.3.8}$$

2.4. Moments of the Vlasov equation

In the following, the 0th, 1st, and 2nd velocity moments of the distribution function f_e leading to continuity and Euler equation, respectively, as well as the equation for the total energy of the electrons will be re-derived. For sake of brevity, the functional arguments are skipped.

2.4.1. Continuity equation

Here, the 0th velocity moment of Eq. (2.3.5) is computed. With the definition of the electron density in Eq. (2.3.8), the first term on the left hand side provides

$$\int \partial_t f_\mathrm{e}\, d^3\mathbf{v} = \partial_t \int f_\mathrm{e}\, d^3\mathbf{v} = \partial_t n_\mathrm{e}\,. \tag{2.4.1}$$

[9] Now, we distinguish between $\nabla_\mathbf{r} = (\partial_x, \partial_y, \partial_z)^\mathrm{T} = \nabla$ and $\nabla_\mathbf{v} = (\partial_{v_x}, \partial_{v_y}, \partial_{v_z})^\mathrm{T}$.

[10] This includes recombination of the electron with its parent ion just after the ionization process that is in particular the source of high harmonic generation, but not probable for intensities $\gtrsim 10^{14}$ W/cm^2 [92]. Avalanche ionization is neglected because of the relatively small atomic densities $\leq 10^{20}$ cm^{-3}, high ionization degrees and laser pulse duration in the fs-domain. In weakly ionized gases and ps-long laser pulses avalanche ionization cannot be neglected [93]. Recombinations are neglected since they appear only at ps-time scales and the electron current is already damped before a significant number of electrons recombines [58].

[11] This can be seen as follows: Assume two non-relativistic electrons 'a' and 'b' with momenta $\mathbf{p}_\mathrm{a}$ and $\mathbf{p}_\mathrm{b}$ before the collision event and $\mathbf{p}'_\mathrm{a}$ and $\mathbf{p}'_\mathrm{b}$ after the collision event. Momentum conservation gives $\mathbf{p}_\mathrm{a} + \mathbf{p}_\mathrm{b} = \mathbf{p}'_\mathrm{a} + \mathbf{p}'_\mathrm{a}$. Since all the electrons have the same mass and charge and in the non-relativistic regime, a corresponding equality holds for the electron velocities. Thus, the electron current is conserved.

Using integration by part for the second term gives

$$\int \mathbf{v} \cdot \nabla_{\mathbf{r}} f_{\mathrm{e}} d^3\mathbf{v} = \nabla_{\mathbf{r}} \cdot \int \mathbf{v} f_{\mathrm{e}} d^3\mathbf{v} = \nabla_{\mathbf{r}} \cdot (n_{\mathrm{e}}\mathbf{u}) \,, \tag{2.4.2}$$

where the (electron) fluid velocity $\mathbf{u}$ is defined by

$$\mathbf{u} = \frac{1}{n_{\mathrm{e}}} \int \mathbf{v} f_{\mathrm{e}} d^3\mathbf{v} \,. \tag{2.4.3}$$

Since the ions are assumed to be fixed, according to Eq. (2.3.7) the total current density reads

$$\mathbf{J} = q_{\mathrm{e}} n_{\mathrm{e}} \mathbf{u} \,. \tag{2.4.4}$$

The 0^{th} moment of the force term vanishes because

$$\int \mathbf{F} \cdot \nabla_{\mathbf{v}} f_{\mathrm{e}} d^3\mathbf{v} = -\int f_{\mathrm{e}} \nabla_{\mathbf{v}} \cdot \mathbf{F} d^3\mathbf{v} = 0 \,, \tag{2.4.5}$$

when using integration by parts and $f_{\mathrm{e}}(|\mathbf{v}| = \infty) = 0$ as well as $\nabla_{\mathbf{v}} \cdot \mathbf{F} = q_{\mathrm{e}} \nabla_{\mathbf{v}} \cdot (\mathbf{E} + \mathbf{v} \times \mathbf{B}) = 0$. Moreover, it is easy to see that

$$\int S\delta(\mathbf{v}) d^3\mathbf{v} = S \,. \tag{2.4.6}$$

Finally, the 0^{th} moment of the term C has to vanish because elastic collisions conserve the particle density. Adding up all the terms leads to the continuity equation

$$\partial_t n_{\mathrm{e}} + \nabla_{\mathbf{r}} \cdot (n_{\mathrm{e}}\mathbf{u}) = S \,. \tag{2.4.7}$$

2.4.2. Euler equation

In analogy to Sec. 2.4.1, the 1^{st} velocity moment of all terms in Eq. (2.3.5) is computed. First, we have

$$\int \mathbf{v} \partial_t f_{\mathrm{e}} d^3\,\mathbf{v} = \partial_t \left(n_{\mathrm{e}}\mathbf{u}\right) \,. \tag{2.4.8}$$

Rewriting the moment of the second term gives

$$\int \mathbf{v} \left(\mathbf{v} \cdot \nabla_{\mathbf{r}} f_{\mathrm{e}}\right) d^3\mathbf{v} = \nabla_{\mathbf{r}} \cdot \int f_{\mathrm{e}} \mathbf{v} \otimes \mathbf{v} d^3\mathbf{v} \,, \tag{2.4.9}$$

where $\otimes$ denotes the usual outer product, and the divergence operator applied to a matrix-valued function yields the divergence for each row of the matrix. By defining the expression for the velocity spread of the electrons

$$\mathrm{var}\,\mathbf{v} = \frac{1}{n_{\mathrm{e}}} \int f_{\mathrm{e}} (\mathbf{v} - \mathbf{u}) \otimes (\mathbf{v} - \mathbf{u}) \, d^3\mathbf{v} \tag{2.4.10}$$

as well as using the electron density from Eq. (2.3.8) and fluid velocity from Eq. (2.4.3) results in

$$\int \mathbf{v} \left(\mathbf{v} \cdot \nabla_{\mathbf{r}} f_{\mathrm{e}}\right) d^3\mathbf{v} = \nabla_{\mathbf{r}} \cdot \left(n_{\mathrm{e}}\mathbf{u} \otimes \mathbf{u} + n_{\mathrm{e}} \mathrm{var}\,\mathbf{v}\right) \,. \tag{2.4.11}$$

We assume instantaneous thermalization of the plasma, which renders $\mathrm{var}\,\mathbf{v}$ proportional to the identity matrix:

$$\mathrm{var}\,\mathbf{v} = \mathrm{diag}(1,1,1) \frac{1}{3n_{\mathrm{e}}} \int |\mathbf{v} - \mathbf{u}|^2 \, f_{\mathrm{e}} \, d^3\mathbf{v} \,. \tag{2.4.12}$$

Again via integration by parts, we find

$$\begin{aligned}\int \mathbf{v}\left(\frac{\mathbf{F}}{m_\mathrm{e}}\cdot\nabla_\mathbf{v} f_\mathrm{e}\right) d^3\mathbf{v} &= -\int f_\mathrm{e}\nabla_\mathbf{v}\cdot\left(\mathbf{v}\otimes\frac{\mathbf{F}}{m_\mathrm{e}}\right) d^3\mathbf{v}\\ = -\int f_\mathrm{e}\left(\frac{\mathbf{F}}{m_\mathrm{e}}+\mathbf{v}\frac{\nabla_\mathbf{v}\cdot\mathbf{F}}{m_\mathrm{e}}\right) d^3\mathbf{v} &= -\frac{q_\mathrm{e}n_\mathrm{e}}{m_\mathrm{e}}\left(\mathbf{E}+\mathbf{u}\times\mathbf{B}\right)\end{aligned} \tag{2.4.13}$$

for the 1st moment of the force term. The contribution from the ionization source term S vanishes. In order to handle the 1st velocity moment of the collision term, the electron-ion collision frequency ν_ei is introduced via

$$\int \mathbf{v}C\, d^3\mathbf{v} = -n_\mathrm{e}\nu_\mathrm{ei}\mathbf{u}\,. \tag{2.4.14}$$

This term is responsible for the damping of the electron current, as will be clear later. Note that in Eq. (2.4.14) we make again the assumption of instantaneous thermalization and thus electron-ion collisions are isotropic, i.e., a scalar collision frequency ν_ei is sufficient.

In summary, the 1st moment of Eq. (2.3.5) is giving the Euler equation

$$\partial_t\left(n_\mathrm{e}\mathbf{u}\right)+\nabla_\mathbf{r}\cdot\left(n_\mathrm{e}\mathbf{u}\otimes\mathbf{u}+n_\mathrm{e}\mathrm{var}\,\mathbf{v}\right)=\frac{q_\mathrm{e}n_\mathrm{e}}{m_\mathrm{e}}\left(\mathbf{E}+\mathbf{u}\times\mathbf{B}\right)-n_\mathrm{e}\nu_\mathrm{ei}\mathbf{u}\,. \tag{2.4.15}$$

2.4.3. Energy equation

Finally, the energy density of electrons $\mathcal{E}$ is considered. It is defined by

$$\mathcal{E}=\frac{m_\mathrm{e}}{2}\int|\mathbf{v}|^2 f_\mathrm{e}\, d^3\mathbf{v}\,. \tag{2.4.16}$$

Again, first the 2nd velocity momenta of all terms in Eq. (2.3.5) are computed:

$$\int|\mathbf{v}|^2\,\partial_t f_\mathrm{e}\, d^3\mathbf{v}=\frac{2}{m_\mathrm{e}}\partial_t\mathcal{E}\,. \tag{2.4.17}$$

Next we have

$$\int|\mathbf{v}|^2\ \mathbf{v}\cdot\nabla_\mathbf{r} f_\mathrm{e}\, d^3\mathbf{v}=\nabla_\mathbf{r}\cdot\int|\mathbf{v}|^2\,\mathbf{v}f_\mathrm{e}\, d^3\mathbf{v}\,, \tag{2.4.18}$$

which is already of 3rd order in the velocity and therefore, as we will see below, not relevant for our multiple scale analysis in the next section. Furthermore,

$$\int|\mathbf{v}|^2\frac{\mathbf{F}}{m_\mathrm{e}}\cdot\nabla_\mathbf{v} f_\mathrm{e}\, d^3\mathbf{v}=-\int f_\mathrm{e}\nabla_\mathbf{v}\cdot\left(|\mathbf{v}|^2\frac{\mathbf{F}}{m_\mathrm{e}}\right) d^3\mathbf{v}=-2\int f_\mathrm{e}\,\mathbf{v}\cdot\frac{\mathbf{F}}{m_\mathrm{e}}\, d^3\mathbf{v}=-\frac{2q_\mathrm{e}n_\mathrm{e}}{m_\mathrm{e}}\mathbf{u}\cdot\mathbf{E}\,,$$

where we used integration by parts, Eq. (2.4.5), and $\mathbf{v}\cdot(\mathbf{v}\times\mathbf{B})=0$. The ionization source S gives no contribution, and the assumption of elastic collisions dictates

$$\int|\mathbf{v}|^2 C\, d^3\mathbf{v}=0. \tag{2.4.19}$$

Using these results and the Euler equation (2.4.15), the free electron energy density is governed by

$$\begin{aligned}&\partial_t\mathcal{E}+\frac{m_\mathrm{e}}{2}\nabla_\mathbf{r}\cdot\int|\mathbf{v}|^2\,\mathbf{v}f_\mathrm{e}\, d^3\mathbf{v}-m_\mathrm{e}n_\mathrm{e}\nu_\mathrm{ei}\left|\mathbf{u}\right|^2\\ &=m_\mathrm{e}\mathbf{u}\cdot\left[\partial_t\left(n_\mathrm{e}\mathbf{u}\right)+\nabla_\mathbf{r}\cdot\left(n_\mathrm{e}\mathbf{u}\otimes\mathbf{u}+n_\mathrm{e}\mathrm{var}\,\mathbf{v}\right)\right].\end{aligned} \tag{2.4.20}$$

It is possible to recast the electron energy density in terms of $\mathbf{u}$ and $\operatorname{var}\mathbf{v}$:

$$\begin{aligned}\int |\mathbf{v}|^2 f_\mathrm{e}\, d^3\mathbf{v} &= \int |\mathbf{u}|^2 f_\mathrm{e}\, d^3\mathbf{v} + \int |\mathbf{v}-\mathbf{u}|^2 f_\mathrm{e}\, d^3\mathbf{v} \\ &= n_\mathrm{e} |\mathbf{u}|^2 + \mathrm{tr}\left(n_\mathrm{e} \operatorname{var}\mathbf{v}\right) ,\end{aligned} \tag{2.4.21}$$

where tr denotes the trace of the matrix. Then, we can identify kinetic and thermal energy density as

$$\mathcal{E}_\mathrm{kin} = \frac{m_\mathrm{e}}{2} n_\mathrm{e} |\mathbf{u}|^2 , \qquad \mathcal{E}_\mathrm{th} = \frac{m_\mathrm{e}}{2} \mathrm{tr}\left(n_\mathrm{e} \operatorname{var}\mathbf{v}\right) , \tag{2.4.22}$$

respectively. Finally, we can exploit our assumption of instantaneous thermalization in Eq. (2.4.12) and relate $(\operatorname{var}\mathbf{v})_2$ via Eq. (2.4.22) to the thermal energy density

$$\epsilon^2 : \quad (\operatorname{var}\mathbf{v})_2 = \mathrm{diag}(1,1,1)\, \frac{2\mathcal{E}_{\mathrm{th},2}}{3 m_\mathrm{e} n_0} . \tag{2.4.23}$$

2.5. Multiple scale expansion

In the following, Eqs. (2.4.7), (2.4.15) and (2.4.20) are simplified by means of a multiple scale analysis. The general idea behind this approach is that electron velocities are small compared to the speed of light, and thus velocity momenta become less important with increasing order. What exactly "small" means in this context is discussed at the end of this section. We introduce a scaling parameter $\epsilon \ll 1$, and expand the relevant quantities

$$\begin{aligned} &n_e = \sum_{i=0}^{\infty} \epsilon^i n_i, \quad \mathbf{u} = \sum_{i=1}^{\infty} \epsilon^i \mathbf{u}_i, \quad \mathcal{E} = \sum_{i=2}^{\infty} \epsilon^i \mathcal{E}_i, \\ &\operatorname{var}\mathbf{v} = \sum_{i=2}^{\infty} \epsilon^i \left(\operatorname{var}\mathbf{v}\right)_i , \quad \int |\mathbf{v}|^2 \mathbf{v} f_\mathrm{e}\, d^3\mathbf{v} = \sum_{i=3}^{\infty} \epsilon^i \left(\int |\mathbf{v}|^2 \mathbf{v} f_\mathrm{e}\, d^3\mathbf{v} \right)_i . \end{aligned} \tag{2.5.1}$$

Each summation in Eq. (2.5.1) starts at the order of the respective power in $\mathbf{v}$. This insures as will be seen later, that the k^{th} moment is driven by terms of order ϵ^k and higher, only. Furthermore, the collision frequency ν_ei and the ionization source S are set to the order ϵ^0. Thus, the ion densities $n_\mathrm{ion}^{(Z)}$ are also at the order ϵ^0. Eqs. (2.4.3) and (2.5.1) imply that the lowest order current is of the order ϵ^1. These scalings and the linearity of Maxwell's equations (2.3.3)-(2.3.4) implies that all the macroscopic quantities in Maxwell's equations start at the order ϵ^1:

$$\mathbf{E} = \sum_{i=1}^{\infty} \epsilon^i \mathbf{E}_i, \ \mathbf{B} = \sum_{i=1}^{\infty} \epsilon^i \mathbf{B}_i, \ \mathbf{J} = \sum_{i=1}^{\infty} \epsilon^i \mathbf{J}_i, \ \rho = \sum_{i=1}^{\infty} \epsilon^i \rho_i . \tag{2.5.2}$$

Plugging Eqs. (2.5.1), (2.5.2) into Eqs. (2.4.7), (2.4.15) and (2.4.20) and separating the dif-

ferent orders of ϵ gives[12]:

$$\epsilon^0: \quad \partial_t n_0 = S \tag{2.5.3}$$

$$\epsilon^1: \quad \partial_t n_1 + \nabla \cdot (n_0 \mathbf{u}_1) = 0 \tag{2.5.4}$$

$$\epsilon^1: \quad \partial_t (n_0 \mathbf{u}_1) + n_0 \nu_{\mathrm{ei}} \mathbf{u}_1 = \frac{q_\mathrm{e} n_0}{m_\mathrm{e}} \mathbf{E}_1 \tag{2.5.5}$$

$$\epsilon^2: \quad \partial_t (n_0 \mathbf{u}_2) + \partial_t (n_1 \mathbf{u}_1) + n_0 \nu_{\mathrm{ei}} \mathbf{u}_2 + n_1 \nu_{\mathrm{ei}} \mathbf{u}_1 + \nabla_\mathbf{r} \cdot [n_0 \mathbf{u}_1 \otimes \mathbf{u}_1 + n_0 (\mathrm{var}\, \mathbf{v})_2] = \frac{q_\mathrm{e}}{m_\mathrm{e}} (n_0 \mathbf{E}_2 + n_1 \mathbf{E}_1 + n_0 \mathbf{u}_1 \times \mathbf{B}_1) \tag{2.5.6}$$

$$\epsilon^2: \quad \partial_t \mathcal{E}_2 = m_\mathrm{e} \nu_{\mathrm{ei}} n_0 |\mathbf{u}_1|^2 + m_\mathrm{e} \mathbf{u}_1 \cdot \partial_t (n_0 \mathbf{u}_1) \,. \tag{2.5.7}$$

We introduce the total energy per electron E_tot by

$$E_\mathrm{tot} = \frac{\mathcal{E}_2}{n_0} \,. \tag{2.5.8}$$

Following [94], we assume for the electron-ion collision frequency ν_{ei}

$$\nu_{\mathrm{ei}}[\mathrm{s}^{-1}] = \frac{3.9 \times 10^{-6} \sum_Z Z^2 n_\mathrm{ion}^{(Z)} [\mathrm{cm}^{-3}] \lambda_{\mathrm{ei}}}{E_\mathrm{tot}[\mathrm{eV}]^{3/2}} \,, \tag{2.5.9}$$

where λ_{ei} is the Coulomb logarithm.

The model is complete. In the following, we summarize the model equations by replacing fluid velocities by current densities. Moreover, we regroup the equations into hierarchic sets of equations. First, the lowest order set of equation is presented. Then, the next higher order set of equation is considered.

2.5.1. The lowest order set of equation

Using Eqs. (2.1.8)-(2.1.9) and Eq. (2.5.1), (2.5.3), we have

$$\begin{aligned} \epsilon^0: &\quad \partial_t n_\mathrm{ion}^{(Z)} = S^{(Z)}[n_\mathrm{ion}^{(Z)}, \mathbf{E}_1] \\ \epsilon^0: &\quad n_0 = \sum_Z Z n_\mathrm{ion}^{(Z)} \,. \end{aligned} \tag{2.5.10}$$

Hereby, we assume that the ionization source term S depends only on the lowest order electric field $\mathbf{E}_1$. The definition of the current in Eq. (2.4.4) gives $\mathbf{J}_1 = q_\mathrm{e} n_0 \mathbf{u}_1$. Eq. (2.5.5) determines the current evolution by

$$\epsilon^1: \quad \partial_t \mathbf{J}_1 + \nu_{\mathrm{ei}}[n_\mathrm{ion}^{(Z)}, n_0, \mathcal{E}_2] \mathbf{J}_1 = \frac{q_\mathrm{e}^2}{m_\mathrm{e}} n_0 \mathbf{E}_1 \,, \tag{2.5.11}$$

where the electron-ion collision frequency ν_{ei} is specified by Eq. (2.5.9). In particular, ν_{ei} depends on the total electron energy $E_\mathrm{tot} = \mathcal{E}_2 / n_0$. Using Eq. (2.5.7), $\mathbf{J}_1 = q_\mathrm{e} n_0 \mathbf{u}_1$ and Eq. (2.5.11), we gain an expression for the evolution of the electron energy density

$$\epsilon^2: \quad \partial_t \mathcal{E}_2 = \mathbf{E}_1 \cdot \mathbf{J}_1 \,. \tag{2.5.12}$$

[12] From now on again $\nabla = \nabla_\mathbf{r} = (\partial_x, \partial_y, \partial_z)^\mathrm{T}$.

Linearity of the Maxwell's equations (2.3.3)-(2.3.4) implies

$$\nabla \times \mathbf{E}_1(\mathbf{r},t) = -\partial_t \mathbf{B}_1(\mathbf{r},t) \tag{2.5.13}$$

$$\nabla \times \mathbf{B}_1(\mathbf{r},t) = \frac{1}{c^2}\partial_t \mathbf{E}_1(\mathbf{r},t) + \mu_0 \mathbf{J}_1\,. \tag{2.5.14}$$

Herewith, the lowest order set of equation is complete. It describes the evolution of the lowest order quantities $n_{\mathrm{ion}}^{(Z)}$, n_0, $\mathbf{J}_1$, $\mathbf{E}_1$ $\mathbf{B}_1$ and $\mathcal{E}_2$. Now, the initial and boundary conditions of the problem have to be fixed: For this, we define the laser electric and magnetic fields $\mathbf{E}_{\mathrm{L}}$ and $\mathbf{B}_{\mathrm{L}}$ that have to fulfill the Maxwell's equations (2.3.3)-(2.3.4) in vacuum ($\mathbf{J}_1 = 0$). Before the electric field $\mathbf{E}_1$ is large enough to ionize the gas, we have $\mathbf{E}_1 = \mathbf{E}_{\mathrm{L}}$ and $\mathbf{B}_1 = \mathbf{B}_{\mathrm{L}}$. From the moment on where $n_0 \neq 0$ and thus $\mathbf{J}_1 \neq 0$, we have in general $\mathbf{E}_1 \neq \mathbf{E}_{\mathrm{L}}$ and $\mathbf{B}_1 \neq \mathbf{B}_{\mathrm{L}}$.

Before coming to the next higher order set of equation, we interpret the role of the lowest order set of equations and put them into the usual context of THz generation. The 0^{th} order electron density n_0 in Eq. (2.5.10) describes the electrons that are produced locally due to ionization. The 1^{st} order current $\mathbf{J}_1$ in Eq. (2.5.11) is driven by the 1^{st} order electric field $\mathbf{E}_1$ which has to be computed consistently with the Maxwell equations (2.5.13)-(2.5.14). The electric field $\mathbf{E}_1$ does not equal to the electric laser field $\mathbf{E}_{\mathrm{L}}$. In particular, it contains the THz electric field that we are interested in. This is the fundamental difference compared to the IC-current $\mathbf{J}_{\mathrm{IC}}$ in Eq. (1.3.4) from Sec. (1.3.3) that was initially proposed in [57, 66]. Herewith, the lowest order set of equations gives a framework for the description of the ionization current mechanism that is usually explored for two-color laser pulses. Such a Maxwell-consistent treatment has been explored in [95, 96], but only for 1D and 2D geometries. In 3D geometry, only the unidirectional pulse propagation equation is frequently employed to describe THz generation by two-color laser pulses in weakly focused geometries [72, 75, 97]. Besides a Maxwell-consistent treatment of the current and the electric field, the present model takes into account the evolution of the electron-ion collision frequency ν_{ei} that is normally assumed to be constant in studies on THz generation. According to Eq. (2.5.9), ν_{ei} increases with the ion densities and decreases for more energetic electrons. Eq. (2.5.12) computes the required electron energy density $\mathcal{E}_2$.

2.5.2. Next higher order set of equations

Here, we consider one higher order set of equations. We suppose that n_0, $\mathbf{J}_1$, $\mathbf{E}_1$, $\mathbf{B}_1$ and $\mathcal{E}_2$ are known from the solution or approximation of the equations in the previous section. Then, according to Eq. (2.5.4), the 1^{st} order electron density n_1 is determined by

$$\epsilon^1: \quad \partial_t n_1 + \frac{1}{q_{\mathrm{e}}}\nabla \cdot \mathbf{J}_1 = 0 \tag{2.5.15}$$

The definition of the current in Eq. (2.4.4) gives $\mathbf{J}_2 = q_{\mathrm{e}} n_1 \mathbf{u}_1 + q_{\mathrm{e}} n_0 \mathbf{u}_2$. Then, Eq. (2.5.6) determines the current evolution by

$$\epsilon^2: \quad \partial_t \mathbf{J}_2 + \nu_{\mathrm{ei}} \mathbf{J}_2 = \frac{q_{\mathrm{e}}^2}{m_{\mathrm{e}}} n_0 \mathbf{E}_2 + \boldsymbol{\iota}_2\,, \tag{2.5.16}$$

where we define the source term $\boldsymbol{\iota}_2$ by

$$\boldsymbol{\iota}_2 = \frac{q_{\mathrm{e}}^2}{m_{\mathrm{e}}} n_1 \mathbf{E}_1 + \frac{q_{\mathrm{e}}}{m_{\mathrm{e}}} \mathbf{J}_1 \times \mathbf{B}_1 - \frac{\mathbf{J}_1}{q_{\mathrm{e}} n_0}\left(\nabla \cdot \mathbf{J}_1\right) - \left(\mathbf{J}_1 \cdot \nabla\right)\frac{\mathbf{J}_1}{q_{\mathrm{e}} n_0} - \frac{2 q_{\mathrm{e}}}{3 m_{\mathrm{e}}} \nabla \mathcal{E}_{\mathrm{th},2}\,, \tag{2.5.17}$$

with

$$\mathcal{E}_{\mathrm{th},2} = \mathcal{E}_2 - \underbrace{|\mathbf{J}_1|^2/(2m_\mathrm{e}q_\mathrm{e}^2 n_0)}_{=\mathcal{E}_{\mathrm{kin},2}} . \tag{2.5.18}$$

Hereby, $\mathcal{E}_{\mathrm{th},2}$ carries the role of $(\mathrm{var}\,\mathbf{v})_2$ after the substitution by using Eq. (2.4.23). Moreover, we obtain another set of Maxwell's equations

$$\nabla \times \mathbf{E}_2(\mathbf{r},t) = -\partial_t \mathbf{B}_2(\mathbf{r},t) \tag{2.5.19}$$

$$\nabla \times \mathbf{B}_2(\mathbf{r},t) = \frac{1}{c^2}\partial_t \mathbf{E}_2(\mathbf{r},t) + \mu_0 \mathbf{J}_2 . \tag{2.5.20}$$

Compared to the previous set of equations that also governs the evolution of the laser fields, here, the initial and boundary conditions are very simple: All the fields equal to zero in the beginning.

We elaborate the physical meaning of the present terms. The 1st order electron density in Eq. (2.5.15) accounts for the outflow of the current $\mathbf{J}_1$. The 2nd order current $\mathbf{J}_2$ is driven by the electric field $\mathbf{E}_2$ at the same order and can be damped similar to the lowest order set of equations. But now, in addition the current is driven by the current source term $\boldsymbol{\iota}_2$. The 2nd, 3rd and 4th terms of $\boldsymbol{\iota}_2$ in Eq. (2.5.17) have been already established by the ad-hoc model in [58]: in particular, they contain as shown in App. D the ponderomotive source. Now in addition, the first term $\propto n_1 \mathbf{E}_1$ describes the action of the electric field $\mathbf{E}_1$ on n_1 ("the missing electrons that have been displaced by the action of $\mathbf{E}_1$"). Furthermore, the last term accounts for the diffusion of the electrons[13]. Thus, we unified various well known THz generation mechanisms and can treat them consistent with the Maxwell's equations at the same level.

2.5.3. Evolution equations for the electric field

In the following, we isolate the laser fields from the electromagnetic fields due to the laser-plasma interaction. For this, the homogeneous set of equations in Sec. 2.5.1 is transformed into an inhomogeneous problem, but with trivial initial-boundary conditions, same as for the set of equations in Sec. 2.5.2. The 1st order fields originating from the laser-gas-plasma interaction excluding the laser fields are introduced by

$$\begin{aligned} \tilde{\mathbf{E}}_1 &= \mathbf{E}_1 - \mathbf{E}_\mathrm{L} \\ \tilde{\mathbf{B}}_1 &= \mathbf{B}_1 - \mathbf{B}_\mathrm{L} . \end{aligned} \tag{2.5.21}$$

Since $\mathbf{E}_\mathrm{L}$, $\mathbf{B}_\mathrm{L}$ solve the Maxwell's equations (2.5.13)-(2.5.14) for $\mathbf{J} = 0$, the current is transformed as $\tilde{\mathbf{J}}_1 = \mathbf{J}_1$. Then, the Maxwell's equations (2.5.13)-(2.5.14) are not affected by this transformation. The current Eq. (2.5.11) transforms as follows

$$\partial_t \mathbf{J}_1 + \nu_\mathrm{ei}\mathbf{J}_1 = \frac{q_\mathrm{e}^2}{m_\mathrm{e}} n_0 \tilde{\mathbf{E}}_1 + \boldsymbol{\iota}_1 \tag{2.5.22}$$

$$\boldsymbol{\iota}_1 = \frac{q_\mathrm{e}^2}{m_\mathrm{e}} n_0 \mathbf{E}_\mathrm{L} . \tag{2.5.23}$$

[13] A similar term has been made responsible for THz emission in [63]. Here, no assumption of instantaneous thermalization of the electron-velocity-phase-space has been made. Instead, a phenomenological relaxation time for the thermalization was introduced. However, in Sec. 4.1 using our model will show that the last term in Eq. (2.5.17) is negligible compared to the other terms for our laser pulse parameters.

In analogy to the current Eq. (2.5.16), we introduced the lowest order current source term $\boldsymbol{\iota}_1$. Looking at Eq. (2.5.22) and Eq. (2.5.16) we see, that we expressed the current equations at both orders in the same manner.

Now it is possible to write down the evolution equation for the 1st and 2nd order of $\mathbf{E}$ in the same form. The Maxwell's equations and current Eq. (2.5.22), (2.5.16) give

$$\partial_{tt}\tilde{\mathbf{E}}_1 + \nu_\mathrm{e}\partial_t\tilde{\mathbf{E}}_1 + \underbrace{\frac{q_\mathrm{e}^2 n_0}{m_\mathrm{e}\epsilon_0}}_{=\omega_\mathrm{p}^2(\mathbf{r},t)}\tilde{\mathbf{E}}_1 + c^2\nabla\times\nabla\times\tilde{\mathbf{E}}_1 + c^2\nu_\mathrm{e}\int\nabla\times\nabla\times\tilde{\mathbf{E}}_1\,dt = -\frac{\boldsymbol{\iota}_1}{\epsilon_0} \tag{2.5.24}$$

$$\partial_{tt}\mathbf{E}_2 + \nu_\mathrm{e}\partial_t\mathbf{E}_2 + \omega_\mathrm{p}^2(\mathbf{r},t)\mathbf{E}_2 + c^2\nabla\times\nabla\times\mathbf{E}_2 + c^2\nu_\mathrm{e}\int\nabla\times\nabla\times\mathbf{E}_2\,dt = -\frac{\boldsymbol{\iota}_2}{\epsilon_0}\,, \tag{2.5.25}$$

where we introduce the time- and space-dependent generalization of the usual plasma frequency ω_p. It is important to note that the left side of Eq. (2.5.25) is of the same shape for both $\tilde{\mathbf{E}}_1$ and $\mathbf{E}_2$. The only difference lies in the source terms $\boldsymbol{\iota}_1$ and $\boldsymbol{\iota}_2$. Those depend strongly on the driving laser field $\mathbf{E}_\mathrm{L}$. Thus, it is important to study the source terms for different types of incoming laser fields, in particular its strength and spectral properties. This will be done mainly in Chaps. 4, 5.

2.5.4. Estimating the validity of the multiple scale expansion

The multiple scale expansion assumes that the amplitude of the quantities decreases with increasing order of ϵ. Here, typical ratios between $|n_1|$ and n_0 as well as $|\mathbf{J}_2|$ and $|\mathbf{J}_1|$ are estimated. We consider two different aspects: First, the lowest order electric field is considered to be dominated by the laser field $\mathbf{E}_\mathrm{L}$. The electron current $\mathbf{J}_1$ is then non-resonantly driven at the laser frequency ω_L. This will give an upper bound for the amplitude of the laser field. Second, we consider one resonant excitation scenario which will give an upper bound for the time scale at which the multiple scale expansion is valid.

2.5.4.1. Upper bound for the laser field amplitude

It is reasonable to assume that the lowest order electric field is dominated by the driving laser field $\mathbf{E}_\mathrm{L}$ since we are dealing with gases that are transparent for the laser and no field enhancement can be expected. This assumption is expressed by $|\mathbf{E}_1| \sim E_\mathrm{L}^{(0)}$ that means that the magnitude of $|\mathbf{E}_1|$ is of the order of the laser electric field amplitude $E_\mathrm{L}^{(0)}$. Then, Eq. (2.5.23) gives

$$|\boldsymbol{\iota}_1| \sim \frac{q_\mathrm{e}^2 n_0}{m_\mathrm{e}} E_\mathrm{L}^{(0)}\,. \tag{2.5.26}$$

Since $\mathbf{E}_1$ is dominated by $\mathbf{E}_\mathrm{L}$ that oscillates at the laser frequency ω_L, the amplitude of $\mathbf{J}_1$ can be estimated by using Eq. (2.5.22) and replacing $\partial_t \to \omega_\mathrm{L}$ to be

$$|\mathbf{J}_1| \sim \frac{q_\mathrm{e}^2 n_0 E_\mathrm{L}^{(0)}}{m_\mathrm{e}\omega_\mathrm{L}}\,. \tag{2.5.27}$$

This estimation translates in terms of the fluid velocity $u_1 = \mathbf{J}/(q_\mathrm{e}n_0)$ into

$$\frac{|\mathbf{u}_1|}{c} \sim \frac{q_\mathrm{e}E_\mathrm{L}^{(0)}}{cm_\mathrm{e}\omega_\mathrm{L}} = a_0\,, \tag{2.5.28}$$

where we define the normalized laser electric field amplitude a_0. For $a_0 \ll 1$, the regime is non-relativistic. For $\lambda_\mathrm{L} = 0.8\,\mu\mathrm{m}$, the relativistic case with $a_0 = 1$ is reached when $E_\mathrm{L}^{(0)} = 40$ GV/cm corresponding to intensity $I_\mathrm{L}^{(0)} = 2.13 \cdot 10^{18}$ W/cm^2. Thus, for our intensities below 10^{16} W/cm^2, $a_0 \ll 1$ and we indeed work in the non-relativistic regime.

We now estimate the ratio between $|n_1|$ and n_0. Even in the strongest focusing geometry the focal spot size is limited due to the diffraction limit (see Sec. 3.3.2.2). Thus, it is reasonable to assume that the typical length over which the current can vary is $\lambda_\mathrm{L}/(2\pi)$. Same as $\mathbf{J}_1$, n_1 oscillates mainly at ω_L and using Eq. (2.5.15) and replacing $\partial_t \to \omega_\mathrm{L}$ as well as $\partial_{x/y/z} \to 2\pi/\lambda_\mathrm{L}$

$$\frac{|n_1|}{n_0} \sim \frac{1}{q_\mathrm{e} n_0} \frac{2\pi |\mathbf{J}_1|}{\omega_\mathrm{L} \lambda_\mathrm{L}} \sim \frac{|\mathbf{u}_1|}{c} \sim a_0 \,. \tag{2.5.29}$$

Thus in a gas-plasma in the non-relativistic regime, $|n_1| \ll n_0$ should be well fulfilled.

Next, we estimate the ratio between $|\mathbf{J}_2|$ and $|\mathbf{J}_1|$ that should be at the order of the ratio between the driving source terms $|\boldsymbol{\iota}_2|$ and $|\boldsymbol{\iota}_1|$. Therefore, we estimate an upper bound for $\mathcal{E}_\mathrm{th,2}$. Using Eq. (2.5.18), (2.5.12) and (2.5.11) we get an expression for $\mathcal{E}_\mathrm{th,2}$:

$$\partial_t \mathcal{E}_\mathrm{th,2} = \mathcal{E}_\mathrm{kin,2} \left(2\nu_\mathrm{ei} + \frac{\partial_t n_0}{n_0} \right) . \tag{2.5.30}$$

Integration of this equation results in the estimation

$$\mathcal{E}_\mathrm{th,2} \lesssim \frac{m_\mathrm{e} |\mathbf{J}_1|^2}{2 q_\mathrm{e}^2 n_0} \left(2\nu_\mathrm{ei} t_0 + 1 \right) , \tag{2.5.31}$$

where t_0 is the laser pulse duration and we used the definition of $\mathcal{E}_\mathrm{kin,2}$ in Eq. (2.5.18). Now, we replace in Eq. (2.5.17) all spatial derivatives by $\partial_{x/y/z} \to 2\pi/\lambda_\mathrm{L}$. Moreover, we assume that $1/\nu_\mathrm{ei} > t_0 > 1/\omega_\mathrm{L}$. Then, after some algebra, we find

$$|\boldsymbol{\iota}_2| \lesssim a_0 |\boldsymbol{\iota}_1| \,. \tag{2.5.32}$$

Thus, we can conclude that the ratio of $|\boldsymbol{\iota}_2|$ over $|\boldsymbol{\iota}_1|$ and thus of $|\mathbf{J}_2|$ over $|\mathbf{J}_1|$ and $|\mathbf{E}_2|$ over $|\mathbf{E}_1|$ is typically much smaller than a_0, rendering the multiple scale approach valid for non-relativistic laser pulses.

2.5.4.2. Upper bound for the valid time-scale

Above, we considered frequency components of $\mathbf{J}_1$ that are close to the laser frequency ω_L. However, also other frequency components can be excited, in particular oscillations at the plasma frequency ω_p. Oscillations at ω_p can survive for a long time and this poses an additional limitation to the multiple scale expansion as will be shown in the following.

Just to see this limitation, we assume a simple 1D system with $\partial_y = \partial_z = 0$, $\nu_\mathrm{e} = 0$ and a preformed plasma with an x-dependent electron density $n_0 = n_0(x)$ and thus a space dependent plasma-frequency $\omega_\mathrm{p}(x) = \sqrt{q_\mathrm{e}^2 n_0(x)/(m_\mathrm{e}\epsilon_0)}$. We imagine that at the time point $t = 0$ a constant electric field E_s is applied along the x-axis. This translates into the initial conditions $E_{1,x}(x, t = 0) = E_\mathrm{s}$, $\partial_t E_{1,x}(x, t = 0+) = 0$, where $0+$ indicates the state just after $t = 0$. Eq. (2.5.14) and the translational invariance in y and z leading to $(\nabla \times \mathbf{B}) \cdot \mathbf{e}_x = 0$ give

$$J_{1,x}(x,t) = -\epsilon_0 \partial_t E_{1,x}(x,t) \,. \tag{2.5.33}$$

Then, using Eq. (2.5.11) results in

$$\partial_{tt} E_{1,x}(x,t) + \omega_p^2(x) E_{1,x}(x,t) = 0\,, \tag{2.5.34}$$

with the solution

$$E_{1,x}(x,t) = E_\mathrm{s} \cos\left[\omega_\mathrm{p}(x)t\right]\,, \tag{2.5.35}$$

which fulfills our initial conditions. Thus, we consider an extreme situation, where oscillations at ω_p are not damped by losses, neither radiative losses nor losses by current damping and thus the oscillations can survive for a long time.

Now, we compare n_0 with n_1. In order to evaluate Eq. (2.5.15) and to compute n_1, we need $\nabla \cdot \mathbf{J}_1 = \partial_x J_{1,x}$. Using the solution for $E_{1,x}$ and Eq. (2.5.33) gives

$$J_{1,x}(x,t) = \epsilon_0 \omega_\mathrm{p} E_\mathrm{s} \sin\left(\omega_\mathrm{p}(x)t\right)\,, \tag{2.5.36}$$

and thus

$$\partial_x J_{1,x} = \epsilon_0 \omega_\mathrm{p} E_\mathrm{s} \left(\frac{\partial_x \omega_\mathrm{p}}{\omega_\mathrm{p}} \sin(\omega_\mathrm{p} t) + (\partial_x \omega_\mathrm{p}) t \cos(\omega_\mathrm{p} t) \right)\,. \tag{2.5.37}$$

Please note, that the amplitude of $J_{1,x}$ is limited to $\epsilon_0 \omega_\mathrm{p} E_\mathrm{s}$ whereas the amplitude of $\partial_x J_{1,x}$ increases with t and is according to our solution using the multiple scale expansion not limited. The reason is that the current in Eq. (2.5.36) oscillates at the plasma frequency that changes in space. As the time goes on, the current at two positions gets more and more off-phase leading to an increasing gradient.

Then, Eq. (2.5.15) gives

$$n_1(x,t) = -\frac{\epsilon_0 E_\mathrm{s}}{q_\mathrm{e}} (\partial_x \omega_\mathrm{p}) t \sin(\omega_\mathrm{p} t)\,. \tag{2.5.38}$$

comparing n_1 with n_0 gives

$$\left|\frac{n_1}{n_0}\right| \leq \left|\frac{\epsilon_0 E_\mathrm{s}}{q_\mathrm{e} n_0} (\partial_x \omega_\mathrm{p}) t\right|\,, \tag{2.5.39}$$

where the "equal"-case is reached for $t = \pi/2 + k\pi$ and $k \in \mathbb{N}$. However, the multiple scale expansion assumes $|n_1| \ll |n_0|$ and thus the time scale, where the solution is valid is limited to

$$t \ll \left|\frac{q_\mathrm{e} n_0}{\epsilon_0 E_\mathrm{s} \partial_x \omega_\mathrm{p}}\right| \sim \left|\frac{2 q_\mathrm{e} L_\mathrm{typ} n_0}{\epsilon_0 E_\mathrm{s} \omega_\mathrm{p}}\right| = 2\sqrt{\frac{m_\mathrm{e}}{\epsilon_0}} \frac{L_\mathrm{typ}}{E_\mathrm{s}} \sqrt{n_0}\,, \tag{2.5.40}$$

where we now introduce the typical length L_typ by $L_\mathrm{typ}^{-1} = \max\left|(\partial_x n_0)/n_0\right| = 2\max\left|(\partial_x \omega_\mathrm{p})/\omega_\mathrm{p}\right|$. Thus, the smaller the plasma density gradients and the smaller the exciting electric field E_s, the longer the multiple scale expansion is valid. Moreover, the larger the electron density, the longer the multiple scale expansion is valid, too[14].

In is interesting to note that during the development of the multiple scale expansion, we never used the Gauss law in Eq. (2.3.1) and also the divergence equation for the magnetic field in Eq. (2.3.2). However, both are automatically valid at each order since they can be derived from the other Maxwell's equations and the continuity equation. Here, we can just verify this conclusion: For example, it can be easily seen that $\nabla \cdot \mathbf{E}_1 = \rho_1/\epsilon_0 = q_\mathrm{e} n_1/\epsilon_0$ is fulfilled when taking our solutions in Eq. (2.5.35), (2.5.38).

[14]This result might appear surprising. However, n_1 is only proportional to ω_p and thus to $\sqrt{n_0}$ according to Eq. (2.5.38). So, the ratio between n_1 and n_0, which is important for the validity of the multiple scale expansion, is proportional to $n_0^{-1/2}$ which makes the surprising result plausible.

Now, we have to compare $\boldsymbol{\iota}_2$ with $\boldsymbol{\iota}_1 = q_\mathrm{e}^2 n_0 / m_\mathrm{e} E_\mathrm{s}$. The 2$^{\mathrm{nd}}$ order source term is x-polarized and writes for the collision-less case using Eq. (2.5.17)

$$\iota_{2,x} = \frac{q_\mathrm{e}^2}{m_\mathrm{e}} n_1 E_{1,x} - \frac{J_{1,x}}{q_\mathrm{e} n_0} \partial_x J_{1,x} - J_{1,x} \partial_x \left(\frac{J_{1,x}}{q_\mathrm{e} n_0} \right) . \tag{2.5.41}$$

By plugging in the previously computed n_1, $E_{1,x}$ and $J_{1,x}$ gives after some algebra for $t \gg \omega_\mathrm{p}^{-1}$

$$\left| \frac{\iota_{2,x}}{\iota_{1,x}} \right| \leq \left| \frac{\epsilon_0 E_\mathrm{s}}{q_\mathrm{e} n_0} (\partial_x \omega_\mathrm{p}) t \right| , \tag{2.5.42}$$

an analogical expression to Eq. (2.5.39). Thus, Eq. (2.5.40) stays the only necessary condition that has to be fulfilled to render the multiple scale expansion valid.

According to Eq. (2.5.40), assuming $L_\mathrm{typ} = 1\,\mu\mathrm{m}$ and $\max n_0 = 3 \cdot 10^{25}\ \mathrm{m}^{-3}$, renders the multiple scale expansion valid if $t \times E_\mathrm{s} \ll 3.6\,\mathrm{ps} \times \mathrm{GV/m}$. The considered laser peak electric fields in this work are at the level of 40 GV/m - 400 GV/m. Like this, the electric fields due to laser-plasma interaction stay below the GV/m-level (see in Chap. 4). Thus, the multiple scale expansion is valid at ps time scales. In this section, we neglected the damping of the current. However, typical damping times around 100 fs lead to an attenuation of the current before the multiple scale approach becomes invalid.

2.6. Far-field emission from a current

When the current $\mathbf{J}$ in the gas-plasma is known, e.g., because it has been determined by means of a simplified model like for the IC-mechanism in Sec. (1.3.3), then the emission by this current in the far-field can be computed by means of the Maxwell equations (2.3.3)-(2.3.4). Using them, in the temporal Fourier space (see App. A) the magnetic field fulfills the wave equation

$$\Delta \hat{\mathbf{B}}(\mathbf{r}, \omega) + \frac{\omega^2}{c^2} \hat{\mathbf{B}}(\mathbf{r}, \omega) = -\mu_0 \nabla \times \hat{\mathbf{J}}(\mathbf{r}, \omega) , \tag{2.6.1}$$

where ω is the angular frequency coordinate. Solutions of Eq. (2.6.1) can be written as [6]

$$\hat{\mathbf{B}}(\mathbf{r}, \omega) = \mu_0 \int\limits_{V_\mathrm{plasma}} \nabla_{\mathbf{r}'} \times \hat{\mathbf{J}}(\mathbf{r}', \omega)\, G^{3\mathrm{D}}(\mathbf{r} - \mathbf{r}', \omega)\, d^3\mathbf{r}' \tag{2.6.2}$$

with the Green function

$$G^{3\mathrm{D}}(\mathbf{r}, \omega) = \frac{\exp\left(\pm \mathrm{i} \frac{\omega}{c} |\mathbf{r}| \right)}{4\pi |\mathbf{r}|} . \tag{2.6.3}$$

The $\pm$ indicates whether the incoming or the outgoing wave is considered. Here, we have to consider outgoing waves and use the " + " sign. Integration by parts in Eq. (2.6.2) gives the far field approximation ($|\mathbf{r}| \gg |\mathbf{r}'|$)

$$\hat{\mathbf{B}}_\mathrm{far}(\mathbf{r}, \omega) \approx -\mathrm{i}\mu_0 \frac{\omega}{c} \frac{\mathbf{r}}{|\mathbf{r}|} \times \int\limits_{V_\mathrm{plasma}} \hat{\mathbf{J}}(\mathbf{r}', \omega)\, G^{3\mathrm{D}}(\mathbf{r} - \mathbf{r}', \omega)\, d^3\mathbf{r}' . \tag{2.6.4}$$

The corresponding electric field in the far field, in particular outside the plasma volume, can then be computed from $c^2\nabla\times\hat{\mathbf{B}}_{\rm far}=-\mathrm{i}\omega\hat{\mathbf{E}}_{\rm far}$ as

$$\hat{\mathbf{E}}_{\rm far}(\mathbf{r},\omega)\approx -c\frac{\mathbf{r}}{|\mathbf{r}|}\times\hat{\mathbf{B}}_{\rm far}(\mathbf{r},\omega)\,. \tag{2.6.5}$$

We define the far-field power spectrum[15] $P^{\rm 3D}_{\rm far}$ following the usual definition [6] by

$$P^{\rm 3D}_{\rm far}(r,\theta,\varphi,\omega)=\frac{2}{\mu_0}\Re\left[\hat{\mathbf{E}}_{\rm far}(r,\theta,\varphi,\omega)\times\hat{\mathbf{B}}^{\star}_{\rm far}(r,\theta,\varphi,\omega)\right]\cdot\mathbf{e}_r\,, \tag{2.6.6}$$

where $\Re$ denotes the real part[16]. Here, we switched to standard (ISO) spherical coordinates (r,θ,ϕ) according to

$$x=r\sin(\theta)\cos(\phi)\quad y=r\sin(\theta)\sin(\phi)\quad z=r\cos(\theta) \tag{2.6.7}$$

for convenience. Then, the detection angle is given by (θ,φ) and the detector distance by r. The vector $\mathbf{e}_r=\mathbf{r}/|\mathbf{r}|$ is the unit vector in $\mathbf{r}$-direction and normal to the radiation sphere. Using Eq. (2.6.4)-(2.6.5), the far-field power spectrum is given by

$$P^{\rm 3D}_{\rm far}(r,\theta,\varphi,\omega)=2\frac{c}{\mu_0}\left|\hat{\mathbf{B}}_{\rm far}(r,\theta,\varphi,\omega)\right|^2\,. \tag{2.6.8}$$

The integral of $P^{\rm 3D}_{\rm far}$ over the radiation sphere gives the angularly integrated power spectrum

$$\tilde{P}^{\rm 3D}_{\rm far}(\omega)=\int_{-\frac{\pi}{2}}^{\frac{\pi}{2}}\int_{0}^{2\pi}P^{\rm 3D}_{\rm far}(r,\theta,\varphi,\omega)\,r^2\sin\theta\,d\varphi\,d\theta\,, \tag{2.6.9}$$

where the r-independence of $\tilde{P}^{\rm 3D}_{\rm far}$ is ensured in the far-field due to energy conservation. Performing moreover the integral over ω we get the total radiated energy

$$\mathfrak{E}^{\rm 3D}_{\rm THz}=\int_0^{\omega_{\rm m}}\tilde{P}^{\rm 3D}_{\rm far}(\omega)d\omega\,, \tag{2.6.10}$$

where we count the THz signal up to the angular frequency $\omega_{\rm m}$.

Far-field emission from a current in 2D Special care has to be taken when it comes to evaluating Eq. (2.6.4) for 2D geometries with translational invariance in, e.g., y-direction[17]. Then, the integration over y can be performed analytically leading to the 2D Green function valid in the far field. We substitute $K=\frac{\omega}{c}\sqrt{x^2+z^2}\gg 1$ and $\theta=\frac{\omega}{c}|\mathbf{r}|-K$ in Eq. (2.6.3) and approximate

[15] The far-field power spectrum corresponds to the spectral pointing flux.

[16] The "2" has been introduced since later we want to integrate only over positive frequencies.

[17] Such a configuration is used in Chap. 4, where we perform for sake of computational costs particle-in-cell (PIC) simulations only in 2D. There, for a better comparison with PIC simulations, the simplified model that need to compute the far-field emission from a current is also evaluated in 2D.

as follows

$$G^{\mathrm{2D}}(x,z) = \int_{-\infty}^{\infty} \frac{\exp\left(\mathrm{i}\frac{\omega}{c}|\mathbf{r}|\right)}{4\pi|\mathbf{r}|}\, dy = \int_{0}^{\infty} \frac{\exp\left(\mathrm{i}\theta + \mathrm{i}K\right)}{2\pi\sqrt{\theta^2 + 2K\theta}}\, d\theta$$
$$\approx \int_{0}^{\infty} \frac{\exp\left(\mathrm{i}\theta + \mathrm{i}K\right)}{2\pi\sqrt{2K\theta}}\, d\theta = \frac{\exp\left(\mathrm{i}\frac{\omega}{c}\sqrt{x^2+z^2} + \mathrm{i}\frac{\pi}{4}\right)}{\sqrt{8\pi\frac{\omega}{c}\sqrt{x^2+z^2}}}\,. \tag{2.6.11}$$

Here, we used that for all y, $\theta/K \to 0$ for $r_\perp = \sqrt{x^2+z^2} \to \infty$. Moreover, we have used that $\int_0^\infty \sin(x) = \int_0^\infty \cos(x) = \sqrt{\pi/2}$ [98].

For 2D geometry with translational invariance in y-direction, we use polar coordinates (r,φ) to parametrize the (x,z) plane according to

$$x = r\cos(\phi) \quad y = r\sin(\phi) \quad . \tag{2.6.12}$$

Moreover, in 2D geometry, the THz energy density is defined analogous to the energy in 3D by

$$\mathfrak{E}^{\mathrm{2D}}_{\mathrm{THz}} = \int_0^{\omega_\mathrm{m}} \underbrace{\int_0^{2\pi} \tilde{P}^{\mathrm{2D}}_{\mathrm{far}}(r,\varphi,\omega)\, r\, d\varphi}_{=\bar{P}^{\mathrm{2D}}_{\mathrm{far}}(\omega)}\, d\omega\,. \tag{2.6.13}$$

3. Numerical tools

Contents

This chapter presents numerical tools that serve for the analysis of THz generation in fs-laser-induced microplasmas in Chap. 4 and Chap. 5. Sec. 3.1 summarizes some fundamentals of Particle-In-Cell (PIC) codes which solve the fundamental equations given in Sec. 2.3, that are the Vlasov equation coupled to the Maxwell equations. The lowest order set of equations from the multiple scale expansion of these last ones, given in Sec. 2.5.1, is solved by a fluid code. It is described and benchmarked by a 3D PIC simulation in Sec. 3.2. Finally, both numerical codes require a tool to introduce tightly focused laser pulses into electromagnetic codes. We have developed such an algorithm and present it in Sec. 3.3.

3.1. Fundamentals of Particle-In-Cell simulations

Particle-in-cell (PIC) codes compute the electromagnetic fields $\mathbf{E}$, $\mathbf{B}$ and the electron distribution function $f_e(\mathbf{r}, \mathbf{v}, t)$ by numerically solving the Maxwell's equations and the equations of motion for electrons, respectively[1]. First, we present the particle method used to solve the non-relativistic Vlasov equation and then two different solvers for the numerical solution of the Maxwell's equations. Finally, we explain how these two kinds of discretization schemes are coupled in PIC codes.

3.1.1. Modeling the plasma dynamics

We assume for the moment that we are looking for the approximation to the solution of the homogeneous Vlasov equation, i.e., for $S = 0$ and $C = 0$ in Eq. (2.3.5). Here, we do not detail the theory of the PIC codes described in [101], but give a brief description of its algorithm. PIC codes model the plasma with the so-called macro-particles. These macro-particles are characterized

[1] In this work, we utilize the PIC codes OCEAN [99] and CALDER [100] that even can treat relativistic electrons. In OCEAN and CALDER, an additional Vlasov equation for the ion species is discretized. Optionally the ions can be fixed as done for our study.

by the same physical quantities like real particles, for example mass and charge. But, they have a statistical weight w_i in such a way that one macro-particle models the dynamics of several real particles. The discretization of the electron distribution function is then

$$f_\mathrm{e}(\mathbf{r},\mathbf{v},t) \approx \sum_i w_i S[\mathbf{r}-\mathbf{r}_i(t),\mathbf{v}-\mathbf{v}_i(t)]\,, \tag{3.1.1}$$

where w_i is the weight of the macro-particle i, $\mathbf{v}_i$ and $\mathbf{r}_i$ are the velocity and position of the macro-particle i and S the weight function. It is typically chosen as a delta-functions in the $\mathbf{v}$-coordinate and a polynomial spline $\tilde{S}$ in the $\mathbf{r}$-coordinate such that $S(\mathbf{r},\mathbf{v}) = \tilde{S}(\mathbf{r})\delta(\mathbf{v})$.

The dynamics of a macro-particle i is governed by the equations of motion

$$\partial_t \mathbf{r}_i(t) = \mathbf{v}_i(t) \tag{3.1.2}$$

$$\partial_t \mathbf{v}_i(t) = \frac{q_\mathrm{e}}{m}\left\{\mathbf{E}[\mathbf{r}_i(t),t] + \mathbf{v}_i(t)\times\mathbf{B}[\mathbf{r}_i(t),t]\right\}\,. \tag{3.1.3}$$

The equations of motions can be solved numerically for a sequence of discrete time-steps with time-resolution δt.

In order to find an approximation to the full inhomogeneous Vlasov equation including ionization and collisions, one splits the evolution of the electron distribution function into several phases. First, one can generate macro-particles accounting for field ionization. Both, the PIC code CALDER and OCEAN account for ionization following the scheme described in [100]. Hereby, the macro-particles are born at the position of the parent ion similarly to what happens to real particles. Then, the macro-particles are pushed by the electromagnetic forces solving the equations of motions. And finally, the momenta of the macro-particles may be modified due to collisions. The PIC code CALDER is capable to account for electron-ion and electron-electron collisions following the scheme that is described in [102].

3.1.2. Maxwell solver

The PIC codes that are used in this work, OCEAN and CALDER, solve the Maxwell equations with different schemes: The Yee scheme in CALDER and the directional splitting (DS) scheme in OCEAN. Both belong to the group of finite-difference-time-domain (FDTD) methods. The idea of both schemes as well as their advantages and drawbacks are summarized in the following.

3.1.2.1. The Yee scheme

The Yee scheme has been proposed in 1966 [103] and is probably the most exploited scheme for the solution of Maxwell's equations up to date. It discretizes the Maxwell equations (2.3.3)-(2.3.4) using the symmetric discrete derivative in space and time: For a differentiable function $f(x)$, the derivative $f'(x)$ can be approximated by $f'(x) \approx [f(x+\delta x/2) - f(x-\delta x/2)]/\delta x$ up to an error $\propto \delta x^2$ by means of Taylor expansion. For demonstration of the idea, we consider a simple example in 1D with translational invariance in x, y such that $\partial_x \equiv 0 \equiv \partial_y$. Imagine, we want to propagate an x-linearly polarized electric field E_x and a y-polarized magnetic field B_y along the z-axis. Then, Eq. (2.3.3) gives $\partial_t B_y = -\partial_z E_x$ that can be discretized up to a second order error in time and space by

$$B_y(z,t) \approx B_y(z,t-\delta t) - \frac{\delta t}{\delta z}\left[E_x(z+\delta z/2, t-\delta t/2) - E_x(z-\delta z/2, t-\delta t/2)\right]\,. \tag{3.1.4}$$

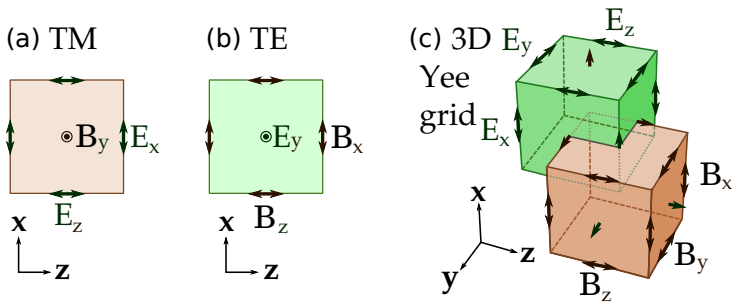

Figure 3.1.1.: Distribution of the electromagnetic field sampling points according to the Yee scheme in three cases [104]: two types of meshes in 2D and the 3D Yee grid.

Thus, we can compute the magnetic field at the new time-step using the electric and magnetic fields from the past. Similar, Eq. (2.3.4) gives $\partial_t E_x = c^2 \partial_z B_y - \mu_0 J_x$ and in discretized version

$$E_x(z+\delta z/2, t+\delta t/2) \approx E_x(z+\delta z/2, t-\delta t/2) - c^2 \delta t \Big[\mu_0 J_x(z+\delta z/2, t) - \frac{B_y(z+\delta z, t) - B_y(z-\delta z, t)}{\delta z} \Big]. \quad (3.1.5)$$

Thus, we can compute the electric field at the new time-step using the magnetic and electric field as well as the current from the past. This kind of subsequent computation of the magnetic and electric fields that are known at time steps separated by $\delta t/2$ is called the leap-frog method. In both discretized equations, besides the shift in time, the spatial grid of the electric and magnetic fields are also shifted, namely by $\delta z/2$.

This idea can be straightforwardly extended to 2D and 3D [105]. In 2D, e.g., with translational invariance in y ($\partial_y \equiv 0$), the Maxwell's equations separate into two independent sets of equations[2]: one for the fields E_x, B_y and E_z (TM) and one for B_x, E_y and B_z (TE)[3]. The corresponding Yee-meshes are presented in Fig. 3.1.1(a-b). In both cases the y-polarized magnetic/electric field is shifted by half of the spatial mesh, i.e., $\delta x/2$ and $\delta z/2$. This ensures the possibility to access to the symmetric and thus 2^{nd} order discrete spatial derivatives as required for the discretization of the Maxwell's equations. In 3D, the situation is similar: As shown in Fig. 3.1.1(c), the electric field components are located at the edges of the green cube and the magnetic field components normal to the surface of this green cube. When considering the red cube that is shifted by $\delta x/2$, $\delta y/2$ and $\delta z/2$, the magnetic fields appear along the edges whereas the electric fields appear normal to the surfaces.

An advantage of the Yee scheme is the possibility to choose the spatial sampling distances δx, δy and δz independently of each other. This can save computational resources, for example when the electromagnetic fields are slowly varying in one transverse direction, but quickly varying in the others (e.g. in Sec. 5.3). However, the time resolution δt is constrained by $c\delta t \leq \sqrt{1/(\delta x^2 + \delta y^2 + \delta z^2)}$ (Courant-Friedrichs-Lewy condition) in order to ensure stability of the scheme [105]. This can make it slower than other schemes, especially in 3D. Moreover, as will be shown in Sec. 3.2.1, different sampling point positions for different fields can pose an additional difficulty, in particular when coupling the Yee scheme to nonlinear differential equations. Furthermore, due to a finite size of the computation box, the Yee scheme requires

[2] This is true as long as the current does not introduce an asymmetry that is not the case in our problems.

[3] The name "TM" decrypts as "transverse magnetic", since the magnetic field is zero in the laser propagation direction z. The name "TE" decrypts as "transverse electric", since the electric field is zero in the laser propagation direction z.

boundary conditions that let the electromagnetic fields propagate out of the numerical box. The electromagnetic codes that are considered in this work and are based on the Yee scheme utilize absorbing boundary conditions [106]. Unfortunately, these boundary conditions are not perfect such that some reflections of the electromagnetic fields occur at the box boundaries[4]. Finally, the Yee scheme exhibits numerical dispersion that will be compared in Sec. 3.1.2.3 with the numerical dispersion of the directional splitting scheme presented next.

3.1.2.2. The directional splitting scheme

An alternative to the Yee scheme is the directional splitting (DS) scheme [101, 107]. The Maxwell equations can be written in the form $\partial_t \mathbf{F} + \mathbb{A}\partial_x \mathbf{F} + \mathbb{B}\partial_y \mathbf{F} + \mathbb{C}\partial_z \mathbf{F} = \epsilon_0^{-1}(\mathbf{J}^{\mathrm{T}}, 0, 0, 0)^{\mathrm{T}}$ with $\mathbf{F} = (\mathbf{E}^{\mathrm{T}}, \mathbf{B}^{\mathrm{T}})^{\mathrm{T}}$ and some constant matrices $\mathbb{A}$, $\mathbb{B}$ and $\mathbb{C}$. The idea is to split the solution into three steps: First advancing the fields in x by solving $\partial_t \mathbf{F} + \mathbb{A}\partial_x \mathbf{F} = \epsilon_0^{-1}(\mathbf{J}^{\mathrm{T}}, 0, 0, 0)^{\mathrm{T}}$ for a small time step δt, then in y by solving $\partial_t \mathbf{F} + \mathbb{B}\partial_y \mathbf{F} = \epsilon_0^{-1}(\mathbf{J}^{\mathrm{T}}, 0, 0, 0)^{\mathrm{T}}$ and finally in z by solving $\partial_t \mathbf{F} + \mathbb{C}\partial_z \mathbf{F} = \epsilon_0^{-1}(\mathbf{J}^{\mathrm{T}}, 0, 0, 0)^{\mathrm{T}}$. However, this gives in general only a 1^{st} oder accuracy. In 2D, for $\mathbf{J} = 0$ the scheme can be upgraded by switching the order of advections [108]. Practically, also in 3D the permutation of the three steps that are mentioned above leads to a significant improvement. Another disadvantage of the scheme is that the spatial resolution is fixed for each direction to $\delta x = \delta y = \delta z$. Compared to the Yee scheme, the DS scheme allows to use a larger time step to insure its stability. The CFL condition is fulfilled if $\delta t = \delta x/c$. So, with equal spatial resolution this makes the computations faster compared to the Yee scheme. Another advantage of the DS scheme is that every field is discretized on the same mesh. Moreover, particular boundary conditions are not required since the scheme naturally splits forward and backward propagating waves.

3.1.2.3. Numerical dispersion of the schemes

The finite difference time domain solvers, i.e., the Yee and the DS scheme, are affected by numerical dispersion. This means that electromagnetic waves that should propagate with the speed of light c in vacuum, propagate with a different phase velocity which is frequency and wave-propagation-direction dependent. To evaluate the numerical dispersion of the Yee and the DS scheme, we consider a 2D plane wave of the form $\mathbf{E} = E_0 \exp[\mathrm{i}(\omega t - k_x x - k_z z)]$ and analogous for $\mathbf{B}$ with angular frequency ω and wavenumbers k_x, k_z. These plane waves are solutions of the discretized equations of the Yee scheme and the DS scheme. However, this imposes a relation between $\mathbf{k} = (k_x, k_z)$ and $\omega(\mathbf{k})$ [105, 107].

For the Yee scheme, we consider $\delta x = \delta z = \delta$ and the largest possible time step $\delta t = \delta/\sqrt{2}$. It is common to introduce the phase velocity $v_{\mathrm{ph}}(k_x, k_z) = \omega(k_x, k_z)/|\mathbf{k}|$. Then, according to [105] we have

$$\frac{v_{\mathrm{ph}}^{\mathrm{Yee}}(k_x, k_z)}{c} = \frac{2\sqrt{2}}{\sqrt{(k_x\delta)^2 + (k_z\delta)^2}} \sin^{-1}\left(\sqrt{\frac{\sin^2(k_x\delta/2)}{2} + \frac{\sin^2(k_z\delta/2)}{2}}\right). \tag{3.1.6}$$

This normalized phase velocity is presented in Fig. (3.1.2)(a). Obviously, the Yee scheme is dispersion free if the electromagnetic wave propagates at an angle of 45° to the z axis and is dispersive along the x and z axes.

[4] We observe reflected electromagnetic fields with an amplitude about 10^{-4} of the incoming wave.

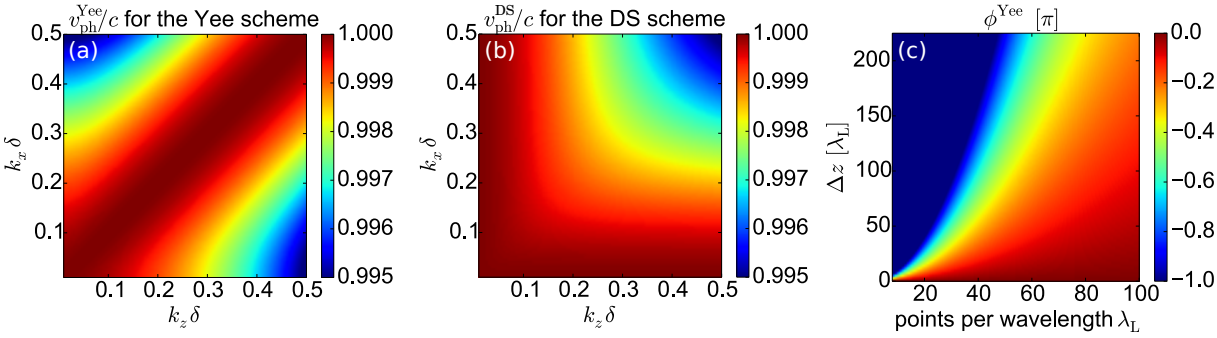

Figure 3.1.2.: Normalized phase velocity of electromagnetic waves that are propagated by the Yee scheme (a) and the directional splitting scheme (b). Phase error ϕ^{Yee} between the FH and SH plane waves after a distance Δz depending on the resolution (c).

For the DS scheme, we always have $\delta x = \delta z = c\delta t = \delta$ and following [107]

$$\frac{v_{\mathrm{ph}}^{\mathrm{DS}}(k_x, k_z)}{c} = \frac{1}{\sqrt{(k_x\delta)^2 + (k_z\delta)^2}} \cos^{-1}\left(\frac{\cos(k_x\delta) + \cos(k_z\delta) + \cos(k_x\delta)\cos(k_z\delta) - 1}{2}\right) . \quad (3.1.7)$$

Fig. (3.1.2)(b) shows that for the DS scheme the numerical dispersion is large at an angle of 45° and the scheme is dispersion free for propagation along the x and z axes.

What is the role of the numerical dispersion for simulations of THz generation in gas-plasmas? In Fig. 2.2.1(c,g,k) of Sec. 2.2.1, we have seen that the THz yield of the ionization current (IC) mechanism is very sensitive to the phase ϕ between the FH and SH electric fields. During the propagation of the FH and SH waves through a medium with linear dispersion, this phase changes. As pointed out above, the DS scheme is dispersion free along the propagation axis z. But, we should estimate the effect of the numerical dispersion on the propagation of the FH and SH field in the Yee scheme. We consider the FH plane wave $\propto \cos(\Psi_1)$ and the SH plane wave $\propto \cos(\Psi_2)$ with $\Psi_1 = \omega_{\mathrm{L}} t - k_z(\omega_{\mathrm{L}})\Delta z$ and $\Psi_2 = 2\omega_{\mathrm{L}} t - k_z(2\omega_{\mathrm{L}})\Delta z + \varphi$ after the propagation distance Δz. Now, k_z is considered to be dependent on ω_{L}. Without numerical dispersion, i.e., when $k_z(\omega) = \omega/c$, it can be easily verified that $\varphi = \Psi_2 - 2\Psi_1$. However, due to the numerical dispersion of the Yee scheme the following error ϕ^{Yee} is created

$$\begin{aligned}\phi^{\mathrm{Yee}} &= \Psi_2 - 2\Psi_1 - \varphi = 2\omega_{\mathrm{L}}\Delta z \left(\frac{1}{v_{\mathrm{ph}}^{\mathrm{Yee}}\left(k_x = 0, k_z(\omega_{\mathrm{L}})\right)} - \frac{1}{v_{\mathrm{ph}}^{\mathrm{Yee}}\left(k_x = 0, k_z(2\omega_{\mathrm{L}})\right)}\right) \\ &\approx 2\omega_{\mathrm{L}}\Delta z \left(\frac{1}{v_{\mathrm{ph}}^{\mathrm{Yee}}\left(k_x = 0, \omega_{\mathrm{L}}/c\right)} - \frac{1}{v_{\mathrm{ph}}^{\mathrm{Yee}}\left(k_x = 0, 2\omega_{\mathrm{L}}/c\right)}\right) . \end{aligned} \quad (3.1.8)$$

This error is presented in Fig. 3.1.2(c) depending on the propagation distance Δz and resolution in terms of number of sampling points per fundamental laser wavelength. The error can be considered modulo π since the effect of φ is π-periodic. When propagating by less that $50\lambda_{\mathrm{L}}$, the error is only in the order of few percent for 50 sampling points per wavelength. However, in order to propagate $\Delta z = 200\lambda_{\mathrm{L}}$ while keeping the same error, the resolution should be increased.

We conclude that special care should be taken for two-color laser pulses: The phase difference between the FH and SH fields according to Eq. (3.1.8) introduced by the numerical dispersion should not dominate the phase difference that is induced by real propagation effects (see

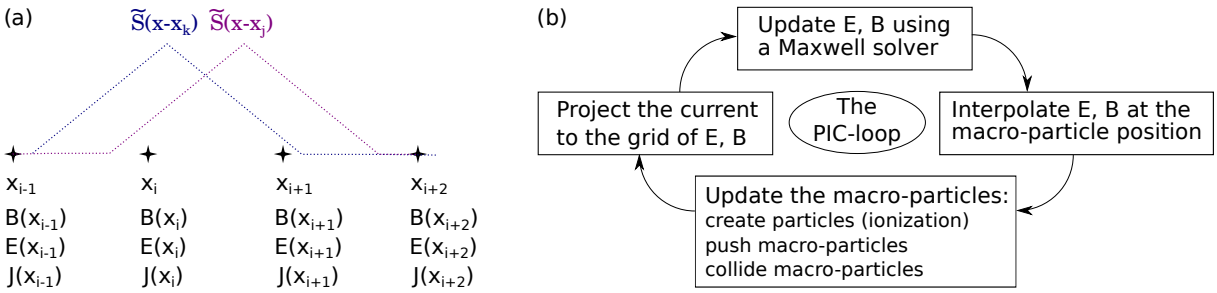

Figure 3.1.3.: (a) Schematic representation of the discretization in PIC simulations with four electromagnetic grid points and two macro-particles. (b) The PIC-loop scheme.

Chap. 5). This problem appears particularly in the Yee scheme[5], since the DS scheme is dispersion free along the laser propagation axis[6].

3.1.3. The PIC loop

On the one hand Sec. 3.1.2 has shown, that the Maxwell equations are typically discretized by FDTD methods that describe the approximative electromagnetic fields on a grid at discrete spatial positions. In the spatial cell within the volume $V = \delta x \delta y \delta z$ each field component is known at one single position. On the other hand in PIC codes, the Vlasov equation is discretized in terms of macro-particles as has been sketched in Sec. 3.1.1. Those represent a big number of real particles. The macro-particles have a continuously valued position and velocity coordinate, i.e. they can be located not at the position of the electromagnetic fields. Fig. 3.1.3(a) illustrates an example in 1D with two macro-particles with a spline order one shape $\tilde{S}$. How are the electromagnetic fields and macro-particles coupled in PIC codes?

PIC codes are organized in the so-called PIC loop that is sketched in Fig. 3.1.3(b). Hereby, the coupled system of Maxwell's and the Vlasov equations is solved iteratively advancing in time by one time step per loop iteration. The functionality of these two components which update $\mathbf{E}$, $\mathbf{B}$ and the macro-particles in particular pushing them by the electromagnetic force has been already signified above. In addition to these two blocks, two intermediate blocks have to be added [101]. On the one hand, after the electromagnetic fields have been updated, one has to interpolate $\mathbf{E}$, $\mathbf{B}$ at the continuously valued position $\mathbf{r}_k(t)$ of the macro-particles obtaining

$$\mathbf{E}(\mathbf{r}_k(t)) = V \sum_i \mathbf{E}(\mathbf{r}_i, t) \tilde{S}[\mathbf{r}_i - \mathbf{r}_k(t)] \,, \quad \mathbf{B}(\mathbf{r}_k(t)) = V \sum_i \mathbf{B}(\mathbf{r}_i, t) \tilde{S}[\mathbf{r}_i - \mathbf{r}_k(t)] \,. \tag{3.1.9}$$

On the other hand after the macro-particles have been updated, the charge contribution from each macro-particle has to be projected onto the grid positions $\mathbf{r}_i$ of the electromagnetic solver:

$$\rho(\mathbf{r}_i, t) = q_\mathrm{e} \sum_k w_k \tilde{S}_i[\mathbf{r}_i - \mathbf{r}_k(t)] \,. \tag{3.1.10}$$

The current density is then computed using a charge conserving algorithm detailed in [109].

[5] One could inject the laser at the angle of 45° in order to suppress this effect. However, then the focal plane where the laser fields are usually prescribes would be not parallel to the numerical box boundaries anymore. This would make the computation of the laser boundary fields according to Sec. 3.3 computationally significantly heavier since one could not resort to FFTs.

[6] One could argue that also the DS scheme introduces an error for waves that are propagating not parallel to z that appear for strongly focused beams. However, for those beams the interaction of the laser with the plasma is limited to only few tens of laser wavelengths (see Sec. 3.3.4.1) such that numerical dispersion stays weak.

3.2. Fluid code ARCTIC: solving the lowest order set of multiple scale equations

When electrons perform a rather collective motion such that only the lowest order velocity moments of the electron distribution function f_e are significant, a fluid description of the plasma is sufficient. In Chap. 2, a fluid model has been derived and estimated to be able to describe THz generation in fs-laser induced microplasmas. Here, we present our discretization scheme for the lowest order set of fluid equations given in Sec. 2.5.1 that governs in particular the IC mechanism for THz generation (see Sec. 1.3.3 and Chap. 5). The corresponding code is called ARCTIC[7]. The Maxwell's equations are discretized by means of the Yee scheme (see Sec. 3.1.2.1). In the following section, we discuss the discretization of the material equations. Moreover, the results of a benchmark against the PIC code OCEAN in 3D is presented.

3.2.1. Discretization of the material equations

The material equations given in Sec. 2.5.1 are local in space, i.e., they contain only time derivatives. Preferably, we want to keep the 2^{nd} order accuracy of the Yee scheme in time when coupling the material equations to the Maxwell's equations. Same as for the Yee scheme, we use the fact that for a differentiable function $f(t)$, the derivative $f'(t)$ can be approximated by the symmetric difference quotient $f'(t) \approx [f(t+\delta t/2) - f(t-\delta t/2)]/\delta t$ up to a 2^{nd} order error, i.e., $\propto \delta t^2$. Moreover, we can approximate $f(t) \approx [f(t+\delta t/2) + f(t-\delta t/2)]/2$, also up to a 2^{nd} order error. Then, the ionization rate equations (2.1.8) can be approximated by $n_{\text{ion}}^{(Z)}(t \pm \delta t/2)$ according to

$$\begin{aligned}\frac{n_{\text{ion}}^{(Z)}(t+\delta t/2) - n_{\text{ion}}^{(Z)}(t-\delta t/2)}{\delta t} \approx & W^{(Z)}[\mathbf{E}_1(t)] \frac{n_{\text{ion}}^{(Z-1)}(t+\delta t/2) + n_{\text{ion}}^{(Z-1)}(t-\delta t/2)}{2} \\ & - W^{(Z+1)}[\mathbf{E}_1(t)] \frac{n_{\text{ion}}^{(Z)}(t+\delta t/2) + n_{\text{ion}}^{(Z)}(t-\delta t/2)}{2}, \end{aligned} \tag{3.2.1}$$

Obviously, Eq. (3.2.1) allows to compute the "new" ion density $n_{\text{ion}}^{(Z)}(t+\delta t/2)$ from the "new" ion density $n_{\text{ion}}^{(Z-1)}(t+\delta t/2)$, the old ion densities $n_{\text{ion}}^{(Z)}(t-\delta t/2)$ and $n_{\text{ion}}^{(Z-1)}(t-\delta t/2)$ and the electric field $\mathbf{E}_1(t)$ at an intermediate time step (see App. E). If we assume that the old ion densities at $t - \delta/2$ and the electric field $\mathbf{E}_1(t)$ are known, then the new ion densities can be computed iteratively: First we compute the neutral density $n_{\text{ion}}^{(0)}(t+\delta t/2)$ since formally $n_{\text{ion}}^{(-1)}(t+\delta t/2) = 0$ and then we compute $n_{\text{ion}}^{(Z)}(t+\delta t/2)$ for $Z \geq 1$. Note that $n_{\text{ion}}^{(Z)}$ and thus the electron density $n_0 = \sum_Z Z n_{\text{ion}}^{(Z)}$ are computed at times delayed by $\delta t/2$ from the electric field $\mathbf{E}_1$ [see also Fig. 3.2.1(a)] following the leap frog method (see Sec. 3.1.2.1): Here, $\mathbf{E}_1$ and $\mathbf{B}_1$ are shifted by half a time step and the current $\mathbf{J}_1$ is sampled in time same as $\mathbf{B}_1$.

Thus, when discretizing the current equation (2.5.11), we have to operate with the temporal sampling of the current $\mathbf{J}_1$ that is already determined by the Yee scheme. Following the same

[7] ARCTIC is the "small brother" of the PIC code OCEAN [99]. The PIC code OCEAN has two versions: one based on the Yee scheme and one on the the DS scheme. In this work, we use only the version utilizing the DS scheme. However, the code ARCTIC is based on the implementation of the Yee scheme version of the PIC code OCEAN that has been implemented by Rachel Nuter.

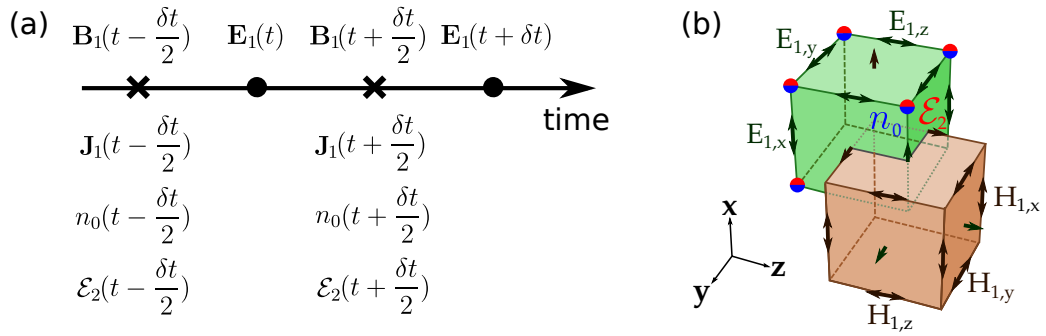

Figure 3.2.1.: Schematic representation of the discretization in ARCTIC: in time (a) following the leap frog scheme, in space (b) by extending the Yee scheme from Sec. 3.1.2.1.

approach like for the ion densities in Eq. (3.2.1) we get

$$\frac{\mathbf{J}_1(t+\delta t/2)-\mathbf{J}_1(t-\delta t/2)}{\delta t}+\nu_{\mathrm{ei}}\left[\bar{n}_{\mathrm{ion}}^{(Z)}(t),\bar{n}_0(t),\bar{\mathcal{E}}_2(t)\right]\frac{\mathbf{J}_1(t+\delta t/2)+\mathbf{J}_1(t-\delta t/2)}{2}$$
$$\approx\frac{q_{\mathrm{e}}^2\bar{n}_0(t)}{m_{\mathrm{e}}}\mathbf{E}_1(t) \tag{3.2.2}$$

using the abbreviation

$$\bar{n}_{\mathrm{ion}}^{(Z)}(t)=\frac{n_{\mathrm{ion}}^{(Z)}(t+\delta t/2)+n_{\mathrm{ion}}^{(Z)}(t-\delta t/2)}{2}, \tag{3.2.3}$$

and analogous for $\bar{n}_0$ and $\bar{\mathcal{E}}_2$. For the energy equation (2.5.12) we approximate

$$\frac{\mathcal{E}_2(t+\delta t/2)-\mathcal{E}_2(t-\delta t/2)}{\delta t}\approx\mathbf{E}_1(t)\cdot\frac{\mathbf{J}_1(t+\delta t/2)+\mathbf{J}_1(t-\delta t/2)}{2}\,. \tag{3.2.4}$$

Since $\nu_{\mathrm{ei}}[\mathcal{E}_2]$ is a "complicated" nonlinear function [see Eq. (2.5.9)], the system of equations (3.2.2)-(3.2.4) cannot give explicit expressions for the "new" current $\mathbf{J}_1(t+\delta t/2)$ and energy density $\mathcal{E}_2(t+\delta t/2)$. We approximate the solution using the fix-point iteration method that is detailed in App. F: First, Eq. (3.2.2) gives an approximation of $\mathbf{J}_1(t+\delta t/2)$ by approximating $\mathcal{E}_2(t+\delta t/2)\approx\mathcal{E}_2(t-\delta t/2)$. Then Eq. (3.2.4) uses this approximative value of the "new" current to create a better approximation to $\mathcal{E}_2(t+\delta t/2)$. The procedure is continued until the difference between two iterations is smaller than a parameter. Already few iterations can reduce the error in terms of final thermal energy from 10^{-3} for one iteration to machine precision (cf. App. F).

Up to now we ignored that the spatial grid points of different components of $\mathbf{E}_1$ are located at different positions in the Yee scheme. So, we place n_0 and $\mathcal{E}_2$ according to Fig. 3.2.1(b) just in-between of two neighboring points of $E_{1,x}$, $E_{1,y}$ and $E_{1,z}$ and linearly interpolate at the position of n_0 and $\mathcal{E}_2$ when needed. This procedure conserves the 2^{nd} order error in space. Thus, it does not pose any problem to the approximation of the new ion densities according to Eq. (3.2.1). However, when iterating between Eq. (3.2.2) and Eq. (3.2.4) in order to determine the new current and energy density, the ion, electron and energy density have to be interpolated at the grid of $\mathbf{J}_1$ in Eq. (3.2.2) and the current has to be interpolated in Eq. (3.2.4) at the grid of $\mathcal{E}_2$ introducing a spatial averaging. So, practically the number of iteration has to be kept small in order not to smooth the macroscopic quantities too much. Usually, we use only one iteration accepting an error around 10^{-3} in terms of energy density[8].

[8]For few-cycle pulses two iteration are used since one turned out to be unstable, in particular simulation.

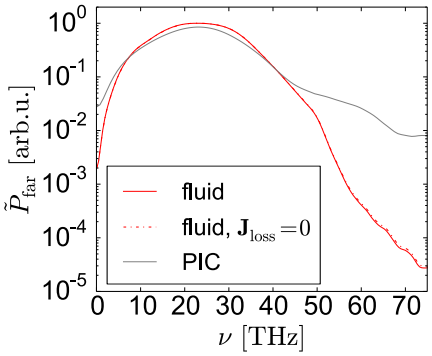

Figure 3.2.2.: Angularly integrated THz far field spectrum obtained from the fluid model (red solid line) and a PIC simulation (gray line) in 3D for the following parameter: Two-color 0.17-μJ Gaussian laser pulse ($E_\omega = 40$ GV/m, $E_{2\omega} = 20$ GV/m, $t_0 = 50$ fs, $\mathbf{e}_{\rm FH} = \mathbf{e}_{\rm SH} = \mathbf{e}_x$ according to Eq. 5.1.1) focused down to $w_0 = \lambda_{\rm FH} = 0.8$ μm in argon with initial neutral density $n_{\rm a} = 3 \cdot 10^{19}$ cm^{-3} (see Chap. 5 for details). In addition, fluid simulations without the loss current ($\mathbf{J}_{\rm loss} = 0$) are shown (dashed red line).

Before presenting a benchmark of the fluid code ARCTIC against the PIC code OCEAN, we comment on the losses due to ionization. During the ionization process, the energy is transfered from the electromagnetic field to the liberated electrons. Our PIC codes account for this by introducing the loss current

$$\mathbf{J}_{\rm loss} = \frac{\mathbf{E}}{|\mathbf{E}|^2} \sum_Z I_{\rm p}^Z W^{(Z)} n_{\rm ion}^{(Z-1)} \,. \tag{3.2.5}$$

For consistency, we introduce in ARCTIC the same current but with $\mathbf{E} \to \mathbf{E}_1$. This current is added to the current $\mathbf{J}_1 \to \mathbf{J}_1 + \mathbf{J}_{\rm loss}$. We always keep track of the ionization losses that turn out to be negligible for many-cycle-laser pulses and can have an impact for few-cycle pulses (see next section and Chap. 4).

3.2.2. Benchmark: Drude-fluid vs. PIC in 3D

Here, we benchmark the code ARCTIC by the PIC code OCEAN in full 3D. The driving laser pulse is defined by its transverse vacuum electric field at focus according to Eq. (5.1.1) in Chap. 5 and introduced with the algorithm described in Sec. 3.3. Laser and gas parameters used in the benchmark are given in the caption of Fig. 3.2.2. Since we use a two-color laser pulse, the IC-current mechanism is expected to be well described by the lowest order set of equations from Sec. 2.5.1 solved by ARCTIC. The resulting angularly integrated THz far-field spectra are presented in Fig. 3.2.2. A very good agreement between the fluid based model (solid red line) and the PIC result (solid gray line) down to the PIC noise level is observed. In addition, the fluid spectra with (solid red line) and without (dashed red line) the loss current $\mathbf{J}_{\rm loss}$ reveal almost no visible difference. Thus, ionization losses could be in principle neglected in this example.

The fluid simulations have been performed with the spatial resolution of $\delta z = 8$ nm (100 points per $\lambda_{\rm L}$), $\delta x = 16$ nm, $\delta y = 32$ nm and temporal resolution $\delta t = 25$ as. The resolution in the laser propagation z direction has been selected to be very fine because of the numerical dispersion of the Yee scheme that introduces a spurious phase shift between the FH and SH electric fields. The resolution along the main transverse laser polarization direction x has been chosen to be finer than along y in order to resolve higher field gradients that appear when the plasma is oscillating

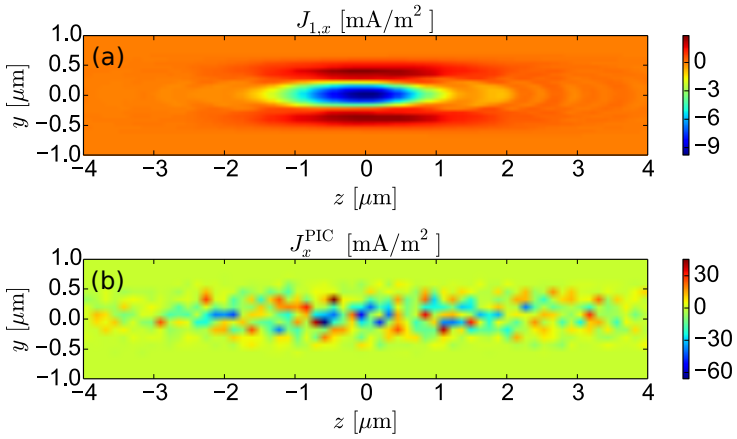

Figure 3.2.3.: Snapshot of the x-polarized current 150 fs after the laser has passed the focus: from the fluid simulation with ARCTIC (a) and PIC simulation with OCEAN (b).

with the local plasma frequencies (cf. Sec. 2.5.4.1 and Sec. 5.1.2.2). We will see in Chap. 5 that the plasma in our benchmark simulation is less than 10 μm-long corresponding to $12.5\lambda_{\mathrm{L}}$. Thus, according to Fig. 3.1.2(c) in Sec. 3.1.2.3, for a resolution of 100 points per wavelength the artificial phase shift introduced by the numerical dispersion is negligible[9]. The simulation with the PIC code OCEAN has been performed with the spatial resolution of $\delta x = \delta y = \delta z = 32$ nm and temporal resolution $\delta t = 106$ as. Because in OCEAN the Maxwell solver is based on the direction splitting (DS) scheme, the numerical dispersion along the x, y, z - axes is null and the resolution in the laser propagation direction is less critical (see Sec. 3.1.2.3). As a consequence, also the time step could be increased compared to the fluid simulation (Courant-Friedrichs-Lewy condition).

The PIC and fluid codes are parallelized by means of domain decomposition. Thus, we measure the computational resources in number of used CPU's times the computation hours, in short CPUh. The PIC simulation for Fig. 3.2.2 required 58900 CPUh, while the fluid simulation consumed 9700 CPUh, which corresponds to a speed-up factor of 6. When using the same resolution even a speed-up by two orders of magnitude is reached.

Besides the speed-up, in the fluid code ARTIC the fields inside the plasma are significantly less noisy than in PIC simulations. Snapshots of the transverse currents in laser polarization direction 150 fs after the laser pulse has passed the focus are presented in Fig. 3.2.3 for the benchmark simulations. The noise of the PIC simulation with 10 macro-particles per cell in (b) is almost 10 times stronger than the "real" current in the fluid simulation in (a). This noise originates from the spread of the electron distribution function due to thermal heating (see Chap. 4) and is proportional to $1/\sqrt{N}$ where N is the number of the macro-particles[10]. Thus, in order to reduce the noise to the signal level, one would need more than $10 \cdot 10^2 = 1000$ macro-particles per cell. This is not feasible in 3D. Thus, for PIC simulations, just the angularly integrated far-field spectra give reliable result in the THz domain due to averaging between all the macro-particles within the plasma, while the fields in the plasma are too noisy to inspect their spatial structure.

[9] We verified by various simulations in vacuum that this artificial phase-shift is indeed negligible obtaining an artificial phase shift in focus of only 0.01π in our benchmark simulation.

[10] This statement becomes plausible considering equally weighted macro-particle in a cell with the random scalar velocity v_i and a Gaussian distribution function with the expectation values $u_i = u$ and the variance $\Delta v_i = \Delta v$. The sum of the velocities $\sum_i v_i$ determining the current in the PIC simulation has also the Gaussian distribution function with the expectation values u, but with the variance $\Delta v/\sqrt{N}$ for $N \to \infty$.

3.3. A technique to introduce arbitrarily shaped laser pulses

Investigation of laser matter interaction with electromagnetic codes requires to implement sources for the electromagnetic fields. In the case of PIC codes like CALDER [110], PICLS [111] or OCEAN [99], it is common practice to prescribe external electric and magnetic fields at the numerical box boundaries and let the laser propagate towards the medium inside the box. Very often, the paraxial approximation [112, 113] is used to calculate the required fields at the boundaries. However, the paraxial approximation is valid only if the angular spectrum of the laser pulse is sufficiently narrow. Thus, it is not possible to use this approximation for strongly focused pulses. For several beam types, e.g. Gaussian, higher order approximations have been presented [114, 115, 116, 117], but they are rather complicated and therefore not easy to implement. Moreover, for more exotic beam shapes, like vector beams or even sampled experimental profiles, it may be even impossible to find an explicit analytical solution. In [118], a focusing geometry with perfectly reflecting mirrors is exploited to introduce a tightly focused laser pulse into an electromagnetic code. Here, the spatial profile of the laser is automatically pre-defined by the focusing geometry and thus restricted to specific shapes.

In the following, we consider a simple and efficient algorithm for a Maxwell consistent calculation of the electromagnetic fields at the boundaries of the computational domain[11]. We call them Laser Boundary Conditions (LBCs). Our algorithm describes any kind of laser pulses, in particular tightly focused, arbitrarily shaped and polarized ones. Sec. 3.3.1 details the problem we want to solve. In Sec. 3.3.2, the theory of laser propagation in vacuum is reviewed. Sec. 3.3 describes in detail our algorithm for the computation of Maxwell consistent LBCs, and in Sec. 3.3.4 we present two illustrative examples: A tightly focused Gaussian beam and a longitudinal needle beam. Sec. 4.5 summarizes the results.

3.3.1. Schematic presentation of the laser injection

In numerical studies of laser matter interaction, it is common practice to define the laser by its propagation in vacuum, for example, by position and shape of the pulse at focus. Here, we choose to prescribe the pulse in a plane $\mathcal{P}$ parallel to a boundary of the rectangular numerical box, i.e., typically in the focal plane (see Fig. 3.3.1). The laser (red) is passing through the plane $\mathcal{P}$, where the fields[12] $\mathbf{E}_0$, $\mathbf{B}_0$ are prescribed for all times t. The goal is to calculate the fields $\mathbf{E}_\mathrm{B}$, $\mathbf{B}_\mathrm{B}$ at the laser boundary from $\mathbf{E}_0$, $\mathbf{B}_0$. As we will see in Sec. 3.3, choosing $\mathcal{P}$ parallel to a numerical box boundary allows us to resort to Fast Fourier Transforms (FFTs) in the numerical computation of the LBCs. It is of course possible to prescribe the fields in any plane and use the general solution given in the next section to calculate the LBCs. However, in this case one cannot exploit the advantage of an efficient computation with FFTs (Sec. 3.3) and will have to evaluate the spatial Fourier integrals directly, for example by performing discrete sums.

3.3.2. Laser field propagation in vacuum

Let $\mathbf{E}_0(\mathbf{r}_\perp, t) = \mathbf{E}(\mathbf{r}_\perp, z = z_0, t)$ and $\mathbf{B}_0(\mathbf{r}_\perp, t) = \mathbf{B}(\mathbf{r}_\perp, z = z_0, t)$ be the electromagnetic fields in the plane $\mathcal{P}$, where $\mathbf{r}_\perp = (x, y)^\mathrm{T}$. In the following, we want to compute $\mathbf{E}$, $\mathbf{B}$ in the whole space and for all times in vacuum, i.e., the laser fields[13] from Sec. 2.5. We will see that not all components of $\mathbf{E}_0$, $\mathbf{B}_0$ can be prescribed independently. Moreover, we will comment on how to handle evanescent fields, and finally discuss the paraxial limit.

[11] The algorithm has been published in [119].

[12] Vectors are typed in bold.

[13] For sake of clarity and since we only deal with vacuum electromagnetic fields here, during the whole Sec. 3.3.2 we set $\mathbf{E} = \mathbf{E}_\mathrm{L}$, $\mathbf{B} = \mathbf{B}_\mathrm{L}$.

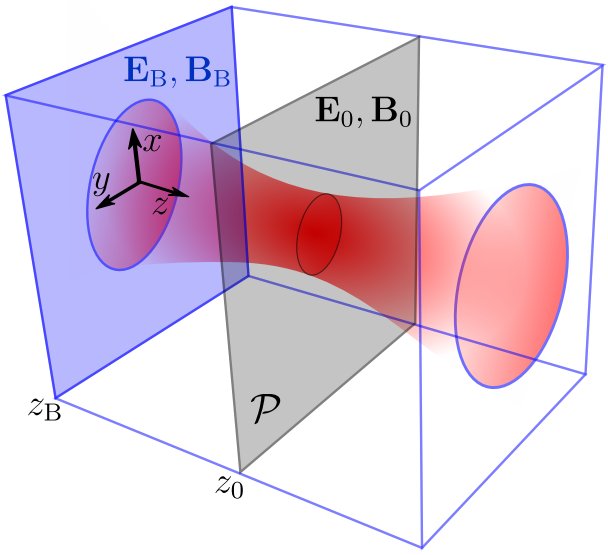

Figure 3.3.1.: Schematic picture of the laser (red) injection problem into the computational domain: Electric and magnetic fields $\mathbf{E}_0$, $\mathbf{B}_0$ are prescribed in the plane $\mathcal{P}$ [here the (x, y)-plane at $z = z_0$]. The fields $\mathbf{E}_\mathrm{B}$, $\mathbf{B}_\mathrm{B}$ at the laser boundary (blue) are unknown and have to be calculated.

3.3.2.1. Propagation of electromagnetic fields and their interdependencies

Electromagnetic fields in vacuum are governed by Maxwell's equations (2.3.1)-(2.3.4) for $\mathbf{J} = 0$ and $\rho = 0$. In frequency or temporal Fourier space they read (for the definition of the Fourier transforms see App. A.)

$$\nabla \cdot \hat{\mathbf{E}}(\mathbf{r}, \omega) = 0 \qquad \nabla \times \hat{\mathbf{E}}(\mathbf{r}, \omega) = \mathrm{i}\omega \hat{\mathbf{B}}(\mathbf{r}, \omega) \tag{3.3.1}$$

$$\nabla \cdot \hat{\mathbf{B}}(\mathbf{r}, \omega) = 0 \qquad \nabla \times \hat{\mathbf{B}}(\mathbf{r}, \omega) = -\mathrm{i}\omega \frac{1}{c^2} \hat{\mathbf{E}}(\mathbf{r}, \omega)\,. \tag{3.3.2}$$

Here, ω is the frequency variable, c is the vacuum speed of light, and "$\hat{}$" denotes the Fourier transform with respect to time t. The wave equation[14] for the electric field $\mathbf{E}$ in frequency space reads (analogous for the magnetic field $\mathbf{B}$)

$$\Delta \hat{\mathbf{E}}(\mathbf{r}, \omega) + \frac{\omega^2}{c^2} \hat{\mathbf{E}}(\mathbf{r}, \omega) = 0\,. \tag{3.3.3}$$

Written in spatial Fourier space (with wavevector $\mathbf{k}$ as spatial Fourier variables) Eq. (3.3.3) would reduce to an algebraic equation and lead to the vacuum dispersion relation $\mathbf{k}^2 = \omega^2/c^2$. However, we want to describe propagation of $\mathbf{E}_0$ along z. To this end, we keep the z variable and perform the Fourier transform with respect to the transverse variables $\mathbf{r}_\perp$ only. Transforming Eq. (3.3.3) to transverse spatial Fourier space, where $\mathbf{k}_\perp = (k_x, k_y)^\mathrm{T}$ is the transverse wavevector, gives

$$k_z^2(\mathbf{k}_\perp, \omega) \bar{\mathbf{E}}(\mathbf{k}_\perp, z, \omega) + \partial_z^2 \bar{\mathbf{E}}(\mathbf{k}_\perp, z, \omega) = 0\,, \tag{3.3.4}$$

where $k_z(\mathbf{k}_\perp, \omega) = \sqrt{\omega^2/c^2 - k_x^2 - k_y^2}$, and "$\bar{}$" denotes the temporal and transverse spatial Fourier domain. The fundamental solutions of Eq. (3.3.4) are the forward (+) and backward

[14] We treat laser fields and thus always assume $\omega \neq 0$.

(−) propagating, plane or evanescent waves (analogous for the magnetic field $\mathbf{B}$)

$$\bar{\mathbf{E}}^{\pm}(\mathbf{k}_\perp, z, \omega) = \bar{\mathbf{E}}_0^{\pm}(\mathbf{k}_\perp, \omega) e^{\pm \mathrm{i} k_z(\mathbf{k}_\perp, \omega)(z - z_0)} \,. \tag{3.3.5}$$

It is important to note that $\mathbf{E}_0^{\pm}$, $\mathbf{B}_0^{\pm}$ cannot be chosen arbitrarily. In fact, only two out of six vector components (for forward and backward direction, respectively) are independent. For example, we can choose to prescribe $\mathbf{E}_{0,\perp}^{\pm}$ in the plane $\mathcal{P}$. Then, by exploiting Eqs. (3.3.1) and (3.3.5), we get

$$\bar{\mathbf{E}}_\perp^{\pm}(\mathbf{k}_\perp, z, \omega) = \bar{\mathbf{E}}_{0,\perp}^{\pm}(\mathbf{k}_\perp, \omega) e^{\pm \mathrm{i} k_z(\mathbf{k}_\perp, \omega)(z - z_0)} \tag{3.3.6}$$

$$\bar{E}_z^{\pm}(\mathbf{k}_\perp, z, \omega) = \mp \frac{\mathbf{k}_\perp \cdot \bar{\mathbf{E}}_\perp^{\pm}(\mathbf{k}_\perp, z, \omega)}{k_z(\mathbf{k}_\perp, \omega)} \tag{3.3.7}$$

$$\bar{\mathbf{B}}^{\pm}(\mathbf{k}_\perp, z, \omega) = \frac{1}{\omega k_z(\mathbf{k}_\perp, \omega)} \mathbb{R}^{\pm}(\mathbf{k}_\perp, \omega) \bar{\mathbf{E}}^{\pm}(\mathbf{k}_\perp, z, \omega) \,, \tag{3.3.8}$$

with the matrix

$$\mathbb{R}^{\pm}(\mathbf{k}_\perp, \omega) = \begin{pmatrix} \mp k_x k_y & \mp \left[k_z^2(\mathbf{k}_\perp, \omega) + k_y^2\right] & 0 \\ \pm \left[k_z^2(\mathbf{k}_\perp, \omega) + k_x^2\right] & \pm k_x k_y & 0 \\ -k_y k_z(\mathbf{k}_\perp, \omega) & k_x k_z(\mathbf{k}_\perp, \omega) & 0 \end{pmatrix} . \tag{3.3.9}$$

The third column of $\mathbb{R}^{\pm}$ in Eq. (3.3.9) is composed of zeros, because the magnetic field is determined by the transverse electric field components $\bar{\mathbf{E}}_{0,\perp}^{\pm}$ only. Obviously, we are imposing $k_z \neq 0$, which is implicitly assumed when stating that the laser is passing through the plane $\mathcal{P}$. Thus, the laser pulse must not have any components propagating parallel to $\mathcal{P}$. In complete analogy, one could prescribe the transverse magnetic fields $\mathbf{B}_{0,\perp}^{\pm}$ in the plane $\mathcal{P}$ and exploit Eqs. (3.3.2) to compute $\mathbf{B}^{\pm}$ and $\mathbf{E}^{\pm}$ in the whole space.

We have thus shown that laser fields fulfilling Maxwell's equation in vacuum also fulfill Eqs. (3.3.6)-(3.3.9). To prove the Maxwell consistency/equivalence of our approach for laser pulses, we also have to show that the electromagnetic fields fulfilling Eqs. (3.3.6)-(3.3.9) fulfill Maxwell's equations: Because of Eqs. (3.3.6) and (3.3.7) the electric field $\bar{\mathbf{E}}$ has the $\exp\left(\pm \mathrm{i} k_z(\mathbf{k}_\perp, \omega) z\right)$ dependence in z and thus fulfills

$$k_z^2(\mathbf{k}_\perp, \omega) \bar{\mathbf{E}}(\mathbf{k}_\perp, z, \omega) + \partial_z^2 \bar{\mathbf{E}}(\mathbf{k}_\perp, z, \omega) = 0 \,. \tag{3.3.10}$$

This is equivalent to the Helmholtz equation in position space:

$$\Delta \hat{\mathbf{E}}(\mathbf{r}, \omega) + \frac{\omega^2}{c^2} \hat{\mathbf{E}}(\mathbf{r}, \omega) = 0 \,. \tag{3.3.11}$$

In complete analogy, Eq. (3.3.7) ensures that the electric field fulfills

$$\nabla \cdot \hat{\mathbf{E}}(\mathbf{r}, \omega) = 0 \,, \tag{3.3.12}$$

and plugging Eq. (3.3.7) into Eq. (3.3.8) gives

$$\nabla \times \hat{\mathbf{E}}(\mathbf{r}, \omega) = \mathrm{i}\omega \hat{\mathbf{B}}(\mathbf{r}, \omega) \,. \tag{3.3.13}$$

Applying the divergence operator on Eq. (3.3.13) we immediately get

$$\nabla \cdot \hat{\mathbf{B}}(\mathbf{r}, \omega) = 0 \,. \tag{3.3.14}$$

Finally, replacing the Δ-operator in Eq. (3.3.11) with the $-\nabla\times\nabla\times$-operator (possible because $\nabla\cdot\hat{\mathbf{E}}=0$) and using Eq. (3.3.13) we get

$$\nabla\times\hat{\mathbf{B}}(\mathbf{r},\omega)=-\mathrm{i}\omega\frac{1}{c^2}\hat{\mathbf{E}}(\mathbf{r},\omega)\,. \tag{3.3.15}$$

Eqs. (3.3.12)-(3.3.15) show that $\hat{\mathbf{E}}$, $\hat{\mathbf{B}}$ in position space defined by Eqs. (3.3.6)-(3.3.9) fulfill the vacuum Maxwell's equations in temporal frequency space.

In App. G, we give an alternative method to compute Maxwell consistent laser fields based on the vector potential in the Lorentz gauge. Such description can be advantageous in specific cases, for example radially polarized doughnut beams [120], where only one component of the vector potential is sufficient to describe the whole laser pulse.

3.3.2.2. Eliminating evanescent fields and the paraxial limit

For $k_x^2+k_y^2>\omega^2/c^2$, $k_z(\mathbf{k}_\perp,\omega)$ becomes imaginary and Eq. (3.3.5) describes evanescent waves, with exponentially growing or decaying amplitude in z direction. In free space propagation, evanescent waves violate energy conservation and are thus unphysical and do not exist. In order to get rid of evanescent waves, the spatial Fourier spectrum of $\mathbf{E}_0$ and $\mathbf{B}_0$ has to be filtered in transverse spatial Fourier space, such that it contains only components with $k_x^2+k_y^2<\omega^2/c^2$. This condition is nothing else then ensuring the Abbe diffraction limit [112] for the fields prescribed at $z=z_0$, which, for instance, forbids to focus a beam to an arbitrary small transverse size.

In contrast, if the spatial Fourier spectrum of $\mathbf{E}_0$ and $\mathbf{B}_0$ is nonzero only for $k_x^2+k_y^2\ll\omega^2/c^2$, one can expand k_z as a Taylor series and approximate

$$k_z(\mathbf{k}_\perp,\omega)\approx\frac{|\omega|}{c}-\frac{c}{2|\omega|}\left(k_x^2+k_y^2\right)\,. \tag{3.3.16}$$

Then, Eqs. (3.3.6)–(3.3.8) simplify to

$$\bar{\mathbf{E}}_\perp^\pm(\mathbf{k}_\perp,z,\omega)\approx\bar{\mathbf{E}}_{0,\perp}^\pm(\mathbf{k}_\perp,\omega)e^{\pm\mathrm{i}\left[\frac{|\omega|}{c}-\frac{c}{2|\omega|}\left(k_x^2+k_y^2\right)\right](z-z_0)} \tag{3.3.17}$$

$$\bar{E}_z^\pm(\mathbf{k}_\perp,z,\omega)\approx 0 \qquad \bar{B}_x^\pm(\mathbf{k}_\perp,z,\omega)\approx\mp\frac{1}{c}\bar{E}_y^\pm(\mathbf{k}_\perp,z,\omega) \tag{3.3.18}$$

$$\bar{B}_z^\pm(\mathbf{k}_\perp,z,\omega)\approx 0 \qquad \bar{B}_y^\pm(\mathbf{k}_\perp,z,\omega)\approx\pm\frac{1}{c}\bar{E}_x^\pm(\mathbf{k}_\perp,z,\omega)\,, \tag{3.3.19}$$

which is well known as the paraxial or Fresnel approximation [113]. The paraxial approximation as it is presented above is valid if the spatial Fourier spectrum is sufficiently narrow. In position space the transverse electric fields have to vary slowly along transverse coordinates over distances $2\pi c/\omega$.

3.3.3. Implementing the laser boundary conditions

Now, we describe the practical implementation of LBCs based on the solution of Maxwell's equations as derived in the previous Section. In the following, the laser pulse will propagate in the forward direction (+) along z, i.e., we inject the laser pulse from the left side of the box (see Fig. 3.3.1). In the plane $\mathcal{P}$ at $z=z_0$ we prescribe the electric field $\mathbf{E}_{0,\perp}(\mathbf{r}_\perp,t)$ that can be an arbitrary function in space and time, for example a Gaussian profile in t and $\mathbf{r}_\perp$. Then, we want to calculate the fields $\mathbf{E}_\mathrm{B}(\mathbf{r}_\perp,t)$ and $\mathbf{B}_\mathrm{B}(\mathbf{r}_\perp,t)$ at the boundary $z=z_\mathrm{B}$ on the numerical grid for all times. Let us consider an equidistant rectangular grid x^i, y^j, indices i, j running from 1

to N_x, N_y, respectively, and with spatial resolution δx, δy. We evaluate $\mathbf{E}_{0,\perp}$ at the grid points x^i, y^j for equidistant times t^n, n is running from 1 to N_t, with temporal resolution δt:

$$\mathbf{E}_{0,\perp}^{ijn} = \mathbf{E}_{0,\perp}(x^i, y^j, t^n)\,. \tag{3.3.20}$$

The following algorithm computes the electric and magnetic fields $\mathbf{E}_{\mathrm{B}}^{ij}(t)$ and $\mathbf{B}_{\mathrm{B}}^{ij}(t)$ at the boundary $z = z_{\mathrm{B}}$ for any given time $t \in [t^1 - \frac{z_{\mathrm{B}}-z_0}{c}, t^{N_t} - \frac{z_{\mathrm{B}}-z_0}{c}]$:

1. Calculate $\hat{\mathbf{E}}_{0,\perp}^{ijn}$ via discrete Fourier transforms (DFTs) in time [121]:

$$\omega^n = \frac{2\pi}{N_t \delta t}\left(-\frac{N_t}{2} + n\right) \tag{3.3.21}$$

$$\hat{\mathbf{E}}_{0,\perp}^{ijn} = \frac{\delta t}{2\pi}\sum_{l=1}^{N_t} \mathbf{E}_{0,\perp}^{ijl} e^{\mathrm{i}\omega^n t^l}\,, \qquad n = 1, \ldots, N_t\,. \tag{3.3.22}$$

2. Calculate $\bar{\mathbf{E}}_{0,\perp}^{ijn}$ via two-dimensional DFTs in transverse space:

$$k_x^i = \frac{2\pi}{N_x \delta x}\left(-\frac{N_x}{2} + i\right) \qquad k_y^j = \frac{2\pi}{N_y \delta y}\left(-\frac{N_y}{2} + j\right) \tag{3.3.23}$$

$$\bar{\mathbf{E}}_{0,\perp}^{ijn} = \frac{\delta x \delta y}{(2\pi)^2}\sum_{l,m=1}^{N_x,N_y} \hat{\mathbf{E}}_{0,\perp}^{lmn} e^{-\mathrm{i}(k_x^i x^l + k_y^j y^m)}\,, \qquad i,j = 1, \ldots, N_{x,y}\,. \tag{3.3.24}$$

3. Calculate transverse electric field components at the boundary ($z = z_{\mathrm{B}}$):

$$k_z^{ijn} = \Re\sqrt{\frac{(\omega^n)^2}{c^2} - (k_x^i)^2 - (k_y^j)^2} \tag{3.3.25}$$

$$\bar{\mathbf{E}}_{\mathrm{B},\perp}^{ijn} = \begin{cases} \bar{\mathbf{E}}_{0,\perp}^{ijn} e^{\mathrm{i}k_z^{ijn}(z_{\mathrm{B}}-z_0)} & \text{for } k_z^{ijn} > 0 \\ 0 & \text{for } k_z^{ijn} = 0 \end{cases}. \tag{3.3.26}$$

   Here, $\Re$ denotes the real part of a complex number. Note that we have set $k_z^{ijn} \equiv 0$ and $\bar{\mathbf{E}}_{\mathrm{B},\perp}^{ijn} \equiv 0$ for indices i, j, n with $(k_x^i)^2 + (k_y^j)^2 \geq (\omega^n)^2/c^2$, in order to suppress evanescent waves (see Sec. 3.3.2.2).

4. Calculate the longitudinal electric field component at $z = z_{\mathrm{B}}$:

$$\bar{E}_{\mathrm{B},z}^{ijn} = \begin{cases} -\frac{k_x^i \bar{E}_{\mathrm{B},x}^{ijn} + k_y^j \bar{E}_{\mathrm{B},y}^{ijn}}{k_z^{ijn}} & \text{for } k_z^{ijn} > 0 \\ 0 & \text{for } k_z^{ijn} = 0 \end{cases}. \tag{3.3.27}$$

5. Calculate the magnetic field at $z = z_{\mathrm{B}}$:

$$\mathbb{R}^{ijn} = \begin{pmatrix} -k_x^i k_y^j & (k_x^i)^2 - \frac{(\omega^n)^2}{c^2} \\ \frac{(\omega^n)^2}{c^2} - (k_y^j)^2 & k_x^i k_y^j \\ -k_y^j k_z^{ijn} & k_x^i k_z^{ijn} \end{pmatrix} \tag{3.3.28}$$

$$\bar{\mathbf{B}}_{\mathrm{B}}^{ijn} = \begin{cases} \frac{1}{\omega^n k_z^{ijn}} \mathbb{R}^{ijn} \bar{\mathbf{E}}_{\mathrm{B},\perp}^{ijn} & \text{for } k_z^{ijn} > 0 \\ 0 & \text{for } k_z^{ijn} = 0 \end{cases}. \tag{3.3.29}$$

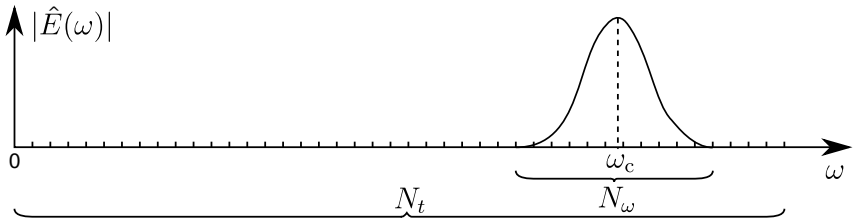

Figure 3.3.2.: Sketch of the electric field amplitude for a multi-cycle laser pulse in frequency domain. The spectrum is significantly different from zero only in $N_\omega \ll N_t$ frequency points.

6. Calculate $\hat{\mathbf{E}}_{\mathrm{B}}^{ijn}$ and $\hat{\mathbf{B}}_{\mathrm{B}}^{ijn}$ via two-dimensional inverse DFTs:

$$\hat{\mathbf{E}}_{\mathrm{B},\perp}^{ijn} = \frac{(2\pi)^2}{N_x N_y \delta x \delta y} \sum_{l,m=1}^{N_x,N_y} \bar{\mathbf{E}}_{\mathrm{B}}^{lmn} e^{\mathrm{i}(k_x^l x^i + k_y^m y^j)} \tag{3.3.30}$$

$$\hat{\mathbf{B}}_{\mathrm{B},\perp}^{ijn} = \frac{(2\pi)^2}{N_x N_y \delta x \delta y} \sum_{l,m=1}^{N_x,N_y} \bar{\mathbf{B}}_{\mathrm{B}}^{lmn} e^{\mathrm{i}(k_x^l x^i + k_y^m y^j)} . \tag{3.3.31}$$

7. Calculate $\mathbf{E}_{\mathrm{B}}^{ij}(t)$ and $\mathbf{B}_{\mathrm{B}}^{ij}(t)$ for any given time $t \in [t^1 - \frac{z_{\mathrm{B}}-z_0}{c}, t^{N_t} - \frac{z_{\mathrm{B}}-z_0}{c}]$:

$$\mathbf{E}_{\mathrm{B},\perp}^{ij}(t) = \frac{2\pi}{N_t \delta t} \sum_{n=1}^{N_t} \hat{\mathbf{E}}_{\mathrm{B}}^{ijn} e^{-\mathrm{i}\omega^n t} \tag{3.3.32}$$

$$\mathbf{B}_{\mathrm{B},\perp}^{ij}(t) = \frac{2\pi}{N_t \delta t} \sum_{n=1}^{N_t} \hat{\mathbf{B}}_{\mathrm{B}}^{ijn} e^{-\mathrm{i}\omega^n t} . \tag{3.3.33}$$

The DFTs in steps 1, 2, and 6 can be calculated efficiently by means of FFTs. There are various FFT libraries available, one of the most popular and efficient implementations is the FFTW [122]. One has to take into account the particular definitions of spatial and temporal Fourier transform in App. A, as well as the conventions of the particular FFT library. For the FFTW [122], one has to use the forward transform (flag `FFTW_FORWARD`) in step 2, and the backward transform (flag `FFTW_BACKWARD`) in steps 1 and 6. Then, in the worst case scenario of three-dimensional simulations, the computational bottlenecks are the $N_x \cdot N_y$ one-dimensional FFTs (step 1) and the $8 \cdot N_\omega$ two-dimensional FFTs (steps 2, 6), respectively.

The Fourier sums in step 7 allow to compute $\mathbf{E}_{\mathrm{B}}^{ij}(t)$ and $\mathbf{B}_{\mathrm{B}}^{ij}(t)$ for any given time t by means of discrete Fourier interpolation. In fact, most of the discrete frequencies ω^n will have a negligible contribution to the spectrum when we are dealing with not-too-short laser pulses, i.e., a pulse envelope modulated with the laser frequency ω_{L} (see Fig. 3.3.2). By taking only $N_\omega \ll N_t$ significant summands into account when evaluating the Fourier sums Eqs. (3.3.32) and (3.3.33) reduces significantly both memory consumption and execution time. Nevertheless, there is a priori no restriction on the temporal bandwidth of the laser pulse[15], because the solution of the Maxwell's equations is performed in frequency space (see Sec. 3.3.2.1).

When using DFTs to approximate continuous Fourier transforms as in the proposed algorithm above, one has to be careful with respect to sampling rates and the inevitable periodic boundary conditions. The initial datum $\mathbf{E}_{0,\perp}$ has to be well resolved in space and time, and one has to check that the beam fits well in the transverse numerical box for all relevant z (e.g., the beam width

[15]The zero-frequency fields have to be always zero.

may be larger at the boundary $z = z_\mathrm{B}$ due to diffraction). Finally, one should not forget that Eqs. (3.3.32) and (3.3.33) should be evaluated for times t in the interval $[t^1 - \frac{z_\mathrm{B}-z_0}{c}, t^{N_t} - \frac{z_\mathrm{B}-z_0}{c}]$ only, otherwise a pulse train will be injected due to periodicity in time.

In a practical implementation, steps 1-6 will be performed by a pre-processor before launching the main simulation. Then, only the relevant (nonzero) contents of the arrays $\hat{\mathbf{E}}_\mathrm{B}^{ijn}$ and $\hat{\mathbf{B}}_\mathrm{B}^{ijn}$ (see remark above) will be passed to the main code and step 7 will be calculated at each time step of the main simulation.

Before going on with examples, we want to make a last remark concerning the grid structure of particular Maxwell solvers. For solvers like the Directional Splitting scheme (see Sec. 3.1.2.2), $\mathbf{E}$ and $\mathbf{B}$ are discretized on the same equidistant grid and the above algorithm can be applied directly. For other solvers, like the Yee scheme (see Sec. 3.1.2.1), the fields are described on grids shifted by $\delta x/2$, $\delta y/2$, $\delta z/2$, respectively. In such case, a straightforward workaround is to run the pre-processor on several transversely shifted grids, in order to compute the desired field components for laser injection.

There are cases of practical relevance as laser injection at inclined incidence where it is insufficient to compute the fields $\mathbf{E}_\mathrm{B}(\mathbf{r}_\perp, t)$ and $\mathbf{B}_\mathrm{B}(\mathbf{r}_\perp, t)$ in a plane only. In these cases the discrete Fourier sums in Eqs. (3.3.30), (3.3.31) can be evaluated directly without taking advantage of FFTs. Instead of calculating the boundary fields at grid points x^i, y^j one would calculate them at any desired x and y coordinate within the spatial window of validity, in complete analogy to step 7.

3.3.4. Examples

3.3.4.1. Tightly focused Gaussian pulse

Here, we are going to simulate a tightly focused Gaussian pulse and its interaction with an initially neutral gas, that is going to be ionized during the interaction. The electromagnetic fields resulting from LBCs in paraxial approximation Eqs. (3.3.17)-(3.3.19), as they are often applied in PIC codes, will be compared with LBCs according to the Maxwell consistent approach Eqs. (3.3.6)-(3.3.8). For sake of computational costs, we restrict ourselves to the two-dimensional case, where $\partial_y \equiv 0$ accounts for translational invariance in transverse y direction. For both cases, a linearly polarized Gaussian pulse is prescribed in the focal plane $z = z_0$ by

$$\mathbf{E}_{0,\perp}(x,t) = E_0 e^{-\left(\frac{x}{w_0}\right)^2 - \left(\frac{t}{t_0}\right)^2} \cos(\omega_\mathrm{L} t)\mathbf{e}_x \,, \tag{3.3.34}$$

with the laser wavelength $\lambda_\mathrm{L} = 2\pi c/\omega_\mathrm{L} = 0.8\,\mu$m, pulse duration $t_0 = 20$ fs, peak intensity $I_0 = \epsilon_0 c|E_0|^2/2 = 5 \times 10^{14}$ W/cm^2 and beam width $w_0 = 0.35\,\mu$m giving $E_0 = 61.4$ GV/m. The particular choice of the beam width w_0 implies that non-negligible parts of $\bar{\mathbf{E}}_{0,\perp}(k_x, \omega)$ are evanescent. These evanescent fields are suppressed in the calculation of $\mathbf{E}_\mathrm{B}(\mathbf{r}_\perp, t)$ and $\mathbf{B}_\mathrm{B}(\mathbf{r}_\perp, t)$ at the boundary $z = z_\mathrm{B}$ fully compatible with Abbe's diffraction limit (see Sec. 3.3.2.2). This leads to a 10% larger full-width-at-half-maximum (FWHM) beam width and smaller electric field at focus.

We solve Maxwell's equations numerically using the PIC code OCEAN ([99], Sec. 3.1). A spatial resolution of $\delta x = \delta z = 0.25\, c/\omega_\mathrm{L} = 32$ nm and temporal resolution of $\delta t = 0.25\,/\,\omega_\mathrm{L} = 0.1$ fs were employed. The domain consists of 2000×400 cells with 10000 macro-particles per cell, and third order interpolation was used. In all simulations we consider an argon atmosphere at ambient pressure having initially $n_0 = 3 \times 10^{19}\,\mathrm{cm}^{-3}$ neutral atoms. Figure 3.3.3 compares snapshots of transverse (E_x) and longitudinal (E_z) electric field components for paraxial (a-c) and Maxwell consistent (d-f) LBCs when the pulse is at focus. Distortions in the fields produced

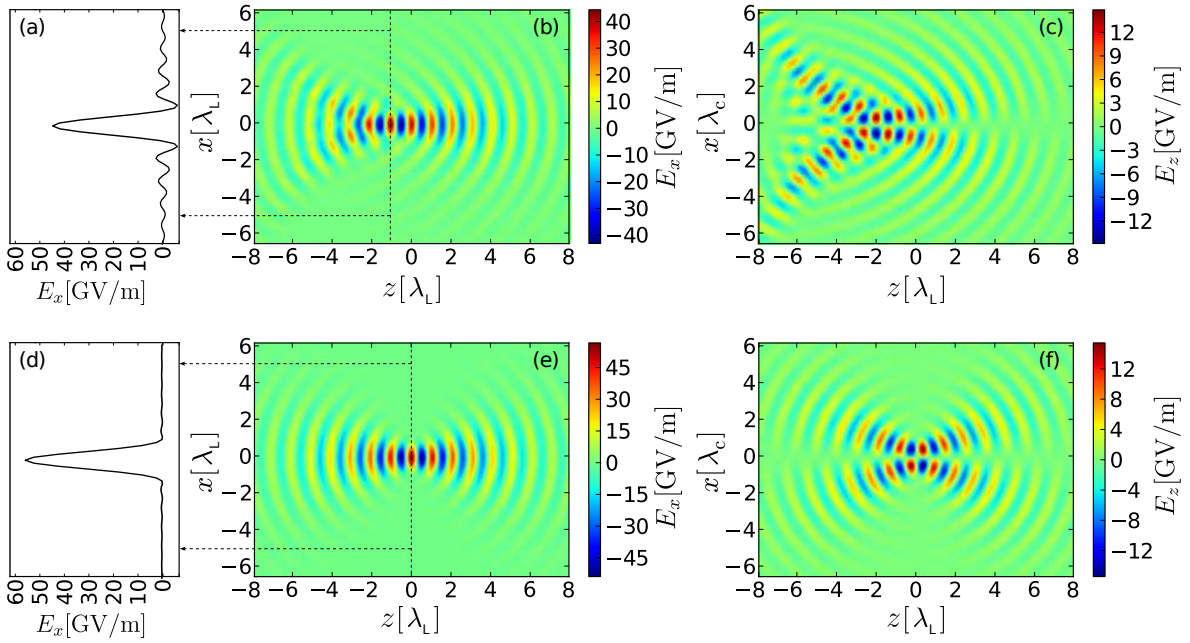

Figure 3.3.3.: Comparison of LBCs in paraxial approximation Eqs. (3.3.17)-(3.3.19) (a-c) and according to the Maxwell consistent approach Eqs. (3.3.6)-(3.3.8) (d-f). Snapshots of transverse fields E_x (b,e) and longitudinal fields E_z (c,f) of a tightly focused Gaussian pulse reveal strong distortions in case of the paraxial LBCs. Calculations were performed using the PIC code OCEAN ([99], Sec. 3.1), assuming an argon atmosphere at ambient pressure. In (a) and (d) line-outs of the transverse electric field E_x at focus are presented, revealing strong side-wings in the beam profile for the paraxial LBCs. The laser pulse propagates from left to right.

by the paraxial LBCs [see Fig. 3.3.3(b,c)] are clearly visible, even the focus (position of smallest beam width) is shifted by more than 1 μm from the expected position at $z_0 = 0\,\mu$m. Both transverse and longitudinal field amplitudes are not symmetric with respect to the focus. This effect is also present in vacuum and is not caused by pulse propagation through the plasma. As the line-out at focus in Fig. 3.3.3(a) shows, non-negligible side-wings appear outside the main lobe. In contrast, the Maxwell consistent LBCs produce symmetric fields [see Fig. 3.3.3(e,f)] with respect to the focus at $z_0 = 0$, and the line-out in Fig. 3.3.3(d) shows no side-wings in the beam profile. The maximum transverse electric field amplitude for the paraxial LBCs is significantly lower than that achieved with the Maxwell consistent LBCs. For both LBCs, the longitudinal field amplitude reaches about 30% of the transverse field amplitude, a direct consequence of the steep transverse gradients in the beam profile.

The code OCEAN fully accounts for ionization according to the quasistatic ADK theory (see [123, 84, 85], Sec. 2.1). Here, we use the ionization data from [124][16]. It is instructive to inspect the electron plasma generated by the tightly focused laser pulses for paraxial and Maxwell consistent LBCs. The resulting distributions of the electron density n_e after the laser pulse has passed through the interaction region are shown in Fig. 3.3.4. The electron density profiles are even qualitatively different for paraxial and Maxwell consistent LBCs: The paraxial LBCs give a fish-like shape, where before the focus (negative z) the peak electron density appears off-axis [see Fig. 3.3.4(a)], and only up to 60% of the argon atoms get ionized. In contrast, the Maxwell

[16] In Chaps. 4, 5, we are using ionization data from [80] that report a slightly lower ionization potential for argon. However, the results almost do not change when using [124] instead of [80].

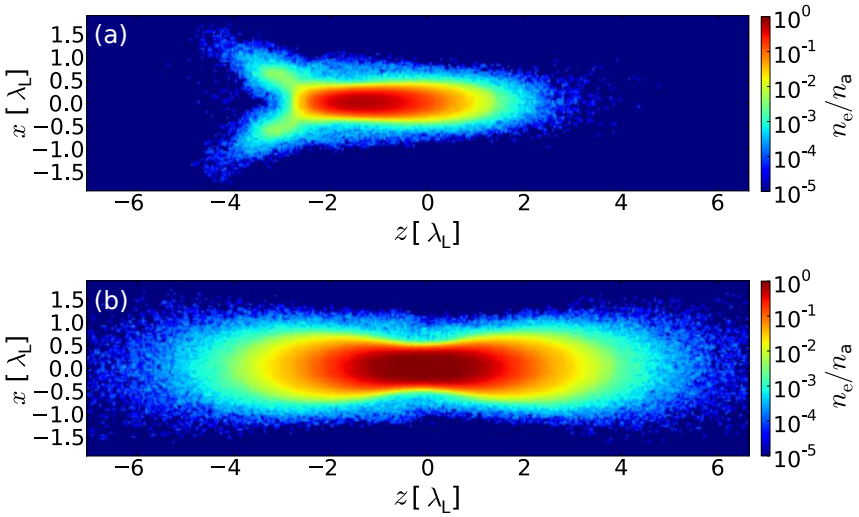

Figure 3.3.4.: Electron densities n_e produced by the tightly focused Gaussian laser pulses shown in Fig. 3.3.3 (see text for details). The profile produced by paraxial LBCs (a) is even qualitatively different than the one produced by Maxwell consistent LBCs (b). Electron densities are scaled to the initial neutral density $n_a = 3 \times 10^{19}\,\mathrm{cm}^{-3}$. The laser pulse propagates from left to right.

consistent LBCs produce a cigar like shape with the peak electron density on the optical axis [see Fig. 3.3.4(b)], and at focus a fully ionized plasma is produced. These deviations in the plasma profile are far from negligible, and have a noticeable impact on THz generation especially by two-color laser pulses and might have a significant impact on back-reflected radiation or energy deposition in different media. The observed sensitivity towards the LBC for tight focusing is not limited to ultrashort low energy pulses interacting with gaseous media, but should be equally important for solid targets and higher pulse energies.

3.3.4.2. Longitudinal needle beam

In order to demonstrate generality and ease of use of the proposed Maxwell consistent LBCs, let us have a look at a (at the first glance) more complicated example. In [125], the authors describe the "creation of a needle of longitudinally polarized light" by tight focusing of a radially polarized Bessel-Gaussian beam. The radial component of the electric field of such beam at focus reads

$$\begin{aligned}\mathbf{E}_{0,\perp}(r,t) = &\int_0^\alpha T(\theta)\sqrt{\cos\theta}\sin(2\theta)e^{-\left(\frac{\sin\theta}{\sin\alpha}\right)^2} J_1\left(2\frac{\sin\theta}{\sin\alpha}\right) J_1\left(\frac{\omega_L}{c} r\sin\theta\right) d\theta \\ &\times E_0\cos(\omega_L t)\mathbf{e}_r\,.\end{aligned} \tag{3.3.35}$$

Here, the electric field is written in cylindrical coordinates (r, ϕ, z), and $\mathbf{e}_r$ is the radial unit vector. The beam profile is given as an integral over the angle θ, where α denotes the acceptance angle of the focusing optic. Following [125], we assume a numerical aperture NA $= 0.95$, corresponding to $\alpha \approx 0.4\pi$. $J_1(x)$ denotes the corresponding Bessel function. The transmission function $T(\theta)$ takes into account a binary-phase optical element, which may further increase the relative longitudinal field strength as well as the length of the needle, however, to the detriment of the optical efficiency. Here, we consider a five-belt optical element and following [125] we

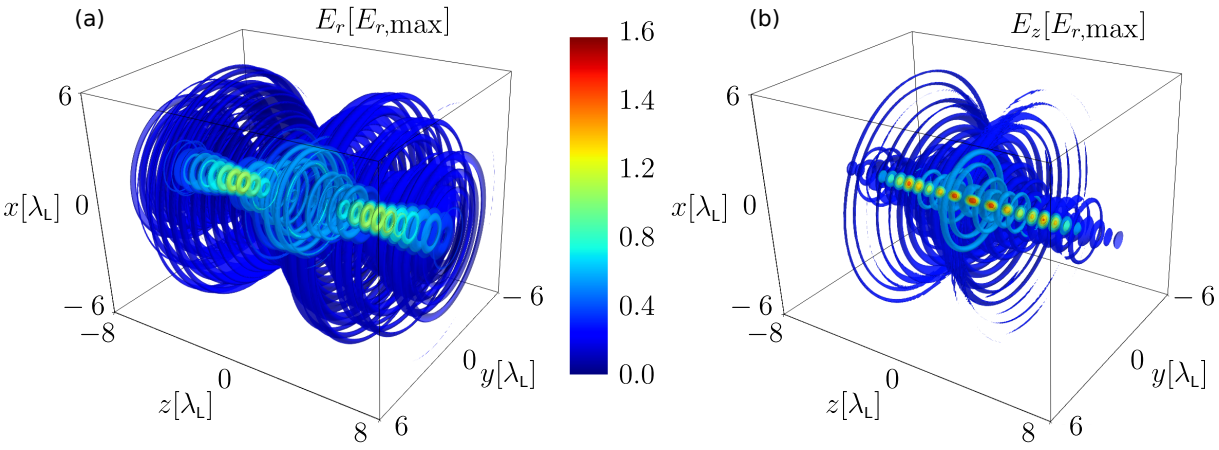

Figure 3.3.5.: The absolute values of the radial and longitudinal electric fields E_r (a) and E_z (b) of a longitudinal needle beam in the focal region. The fields are normalized to the maximum $E_{r,\max}$ of the radial field E_r in the whole space.

define the transmission function T as

$$T(\theta) = \begin{cases} 1 & \text{for } 0 \le \theta < \theta_1,\ \theta_2 \le \theta < \theta_3,\ \theta_4 \le \theta < \alpha \\ -1 & \text{for } \theta_1 \le \theta < \theta_2,\ \theta_3 \le \theta < \theta_4 \end{cases}, \tag{3.3.36}$$

with $\theta_1 = 0.0275\pi$, $\theta_2 = 0.121\pi$, $\theta_3 = 0.19\pi$, and $\theta_4 = 0.26\pi$. The function T takes the values "1" and "-1" in the corresponding intervals for θ specified in Eq. (3.3.36). As in the previous example, we consider a laser wavelength of $\lambda_L = 0.8\,\mu$m.

Figure 3.3.5 presents radial and longitudinal electric fields of the longitudinal needle beam from simulations using OCEAN [99] and Maxwell consistent LBCs. A spatial resolution of $\delta x = \delta y = \delta z = 32$ nm with $600 \times 3072 \times 3072$ cells and a temporal resolution of $\delta t = 0.1$ fs have been applied. In agreement with [125] we find a longitudinal field amplitude that exceeds the radial one in the focal region along several laser wavelengths ($\sim 8\lambda_L$). The maximum longitudinal field amplitude is about 1.6 times larger than the radial one, which achieves its maximum out of focus at $z = \pm 4\lambda_L$. This allows the longitudinal field to dominate in the focal plane by a factor of 2.5. Because of the strong longitudinal field that requires a broad transverse spatial Fourier spectrum the paraxial approximation cannot be applied for the needle beam and Maxwell consistent LBCs are indispensable.

3.3.5. Conclusion

Injecting laser pulses into Maxwell solvers requires to prescribe the electromagnetic fields at the boundaries of the numerical box. Often, these fields are calculated by using the paraxial approximation. We have shown that for tightly focused beams this approach does not give accurate results. Instead, Maxwell's equations in vacuum have to be solved rigorously in order to find the proper fields at the boundaries. We proposed an easy to implement algorithm to achieve this goal, which allows to calculate the laser boundary conditions (LBCs) from transverse electric or magnetic field components defined in a plane, e.g., the focal plane. The presented algorithm can be parallelized in a straight forward manner and may be used with simulations tools employing domain decomposition.

We successfully employed our approach to simulate a tightly focused Gaussian pulse. An accurate handling of the laser injection turns out to be crucial: Electron density profiles from ionization of neutral argon atoms due to field ionization are shown to be strongly dependent on the LBCs. Consequently, the LBCs may have significant impact on features like back-reflected radiation or energy deposition in the medium. Furthermore, our algorithm offers a simple way to simulate more complex pulse configurations or even sampled experimental beam profiles.

In summary, two types of electromagnetic codes coupling to different types of material equations have been presented: PIC codes that approximate the solution to the fundamental equation of the theory in Chap. 2, the Vlasov equation of electrons, and a fluid code that solves the lowest order of the multiple-scale expansion. We have created a tool to introduce accurately arbitrarily shaped, in particular tightly focused, one- and two-color laser pulses into electromagnetic codes. In the following, these numerical tools will be utilized to investigate THz generation in fs-laser induced microplasmas.

4. Single-color fs-laser-induced microplasmas

Contents

As has been pointed out in Sec. 1.3.1.3, a promising approach towards miniaturization of THz sources has been investigated experimentally in [61]: A pulsed single-color (1C) fs-laser is strongly focused into a gas (e.g., air or argon). Intensities of 10^{14}–10^{16} W/cm^2 in the focal region are reached with µJ driving pulses focused down to Abbe's diffraction limit. In the focal region, the neutral gas is ionized. A few-micrometer-thick and few-tens-of-micrometer-long microplasma is created. The excitation of the plasma by the ionizing laser pulse leads to THz radiation that can be measured in the far field.

The major goal of this chapter is to investigate theoretically and numerically the THz radiation from such a microplasma[1]. For 1C-driving pulses, THz emission can be caused by excitation of plasma currents via ponderomotive and radiation pressure sources [58]. These excitation sources are included in the 2$^{\text{nd}}$ order set of equations in Sec. 2.5.2. This idea has been applied to explain THz emission for filaments ([59, 60], see Sec. 1.3.1.2), and is usually referred to as transition-Cherenkov (TC) mechanism: The ponderomotive force of the driving laser pulse produces a longitudinal current structure, which propagates approximately with the speed of light. The interference of radiation from distinct points along the propagation axis leads to a conical emission. The name transition-Cherenkov mechanism comes from this characteristic radiation profile. For 1C-laser pulses, the prevailing mechanism is still under discussion and depends on both, laser and gas properties (see Sec. 1.3.1). Throughout this chapter, we assume the laser pulses to interact with argon gas at ambient pressure (initial atom density $n_{\text{a}} = 3 \cdot 10^{19}$ cm^{-3}, $p \approx 1$ bar) when nothing else is written.

The chapter is organized in the following way. In Sec. 4.1, the model from Chap. 2 is analyzed for the one-dimensional (1D) case to understand the main processes occurring in the laser gas interaction: ionization, heating, collisions, and in particular excitation of plasma waves at THz frequencies. We also estimate the laser pulse parameters where either the excitation via the ionization current (IC) mechanism ($\mathbf{J}_1$) or TC mechanism (current in $\mathbf{J}_2$) dominates. However, not every excited current leads to THz emission. In Sec. 4.2, the analysis is extended to the two-dimensional (2D) case. The important role of non-radiative plasma wave excitations is

[1] The investigations have been published in [126].

discussed. In Sec. 4.3, symmetry properties of the system are studied. Then, we provide a simplified 2D/3D model for THz radiation in the 1C case. By means of this simplified approach, the scaling of the THz conversion efficiency with various pulse parameters is discussed. All the results are benchmarked by rigorous particle-in-cell (PIC) simulations (cf. Sec. 3.1) using the codes OCEAN [99] and CALDER [100]. Finally in Sec. 4.4, we investigate DC-biased 1C-fs-laser-induced microplasmas (cf. Sec. 1.3.2). The excitation of the plasma by applying an additional constant electric field can be modeled by the IC mechanism that is included in the lowest order set of equations in Sec. 2.5.1. The idea of [65] to boost the laser-to-THz conversion efficiency by the DC-bias at high gas-pressures is explored for microplasmas by means of the fluid code ARCTIC (cf. Sec. 3.2).

4.1. Comparing mechanisms of THz excitation

In the following section, the excitation of plasma currents in the THz range is analyzed for various laser pulse durations and intensities. To this end, we restrict ourselves to a 1D configuration, where translational invariance is assumed in the x and y directions while the laser pulse propagates along z. The translational invariance in the x and y directions implies that no emission from z-polarized currents that emit normal to the z-axis can be modeled. However, we can study their excitation. We assume a laser pulse propagating through vacuum for $z \leq 0$ and entering the gas at $z = 0$. The incoming linearly polarized laser pulse is prescribed as

$$\mathbf{E}_\mathrm{L}(t, z=0) = E_\mathrm{L}^0 \sin(\omega_\mathrm{L} t) \exp\left(-t^2/t_0^2\right) \mathbf{e}_x \,, \tag{4.1.1}$$

where t_0 characterizes the pulse duration, E_L^0 is the electric field amplitude, and $\mathbf{e}_x$ the unit vector in x direction. The corresponding intensity can be calculated as $I_\mathrm{L}^0 = \epsilon_0 c \left(E_\mathrm{L}^0\right)^2/2$ where ϵ_0 is the vacuum permittivity. The electric laser field $\mathbf{E}_\mathrm{L}$ in Eq. (4.1.1), solves the vacuum Maxwell's equations (with the corresponding magnetic field) as we have defined in Chap. 2. It is important to select a sine pulse (and not a cosine pulse) to have no zero-frequency component in the laser field $\mathbf{E}_\mathrm{L}$, in particular for pulses down to the single-cycle level. Otherwise, the THz yield would be strongly overestimated.

One advantage of our multiple scale model presented in Sec. 2.5 is that the orders ϵ^1 and ϵ^2, i.e., in particular Eq. (2.5.11) and Eq. (2.5.16), can be analyzed separately. Let us start with order ϵ^1. We have seen in Sec. 2.5.3, that the current $\tilde{\mathbf{J}}_1 = \mathbf{J}_1$ in Eq. (2.5.22) is driven by the electric laser field $\mathbf{E}_\mathrm{L}$ and the interaction field $\tilde{\mathbf{E}}_1 = \mathbf{E}_1 - \mathbf{E}_\mathrm{L}$. As suggested in previous works [57, 75, 88], we could neglect the effect of $\tilde{\mathbf{E}}_1$ when computing $\mathbf{J}_1$. By doing so, electrons are treated as test particles driven by the laser electric field. As a consequence, there is no feedback of the radiation (electric field $\tilde{\mathbf{E}}_1$) emitted by the current $\mathbf{J}_1$ on $\mathbf{J}_1$ itself. However, such back-coupling has an important impact in particular in the THz frequency range [78], and therefore this approximation can only serve as a very rough estimation for $\mathbf{J}_1$ at THz frequencies. But fortunately, this back-coupling has a negligible impact on the main spectral component of $\mathbf{J}_1$, namely at the laser frequency ω_L, when laser propagation effects are negligible, thus in particular for the short propagation distances (~ 10 µm) and underdense plasmas that we are interested in. In the following, we will compute the laser field $\mathbf{E}_\mathrm{L}$ for vacuum propagation, and neglect plasma dispersion and nonlinear propagation effects. We therefore approximate $\mathbf{E}_1 \approx \mathbf{E}_\mathrm{L}$ and Eq. (2.5.11) for the 1st order current gives

$$\partial_\tau \mathbf{J}_1 + \nu_\mathrm{ei} \mathbf{J}_1 \approx \boldsymbol{\iota}_1 \,, \tag{4.1.2}$$

with the first-order nonlinear source term $\boldsymbol{\iota}_1 = q_\mathrm{e}^2 n_0 \mathbf{E}_\mathrm{L}/m_\mathrm{e}$. The current density $\mathbf{J}_1$ is transverse,

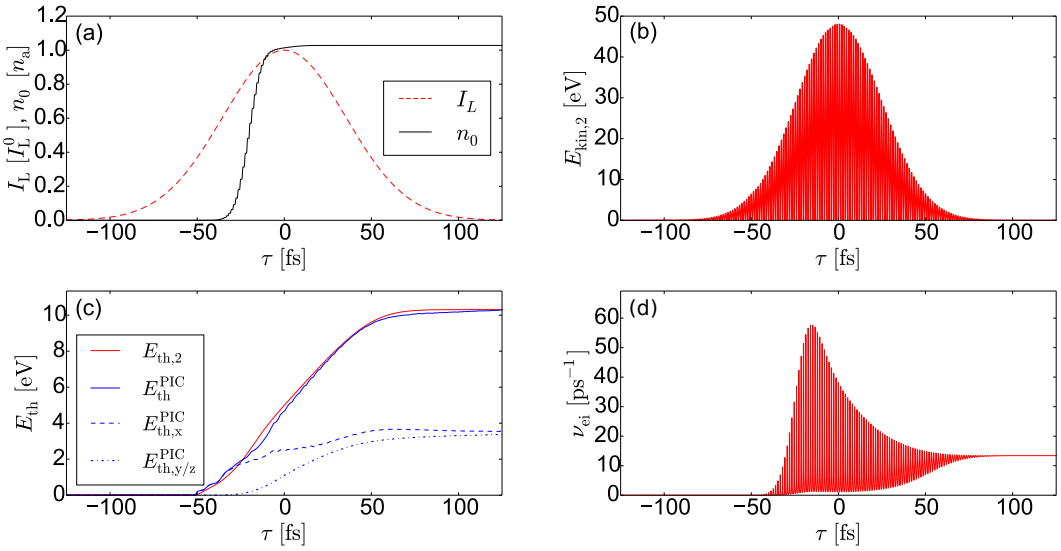

Figure 4.1.1.: Example of a $t_0 = 50\,\mathrm{fs}$, $I_\mathrm{L}^0 = 4\times10^{14}\,\mathrm{W/cm^2}$ laser pulse at $\lambda_\mathrm{L} = 800\,\mathrm{nm}$ in argon gas with initial atom density $n_\mathrm{a} = 3\times10^{19}\,\mathrm{cm^{-3}}$ in 1D configuration. Because we neglect laser propagation effects, the problem depends on the co-moving time $\tau = t - z/c$ only. In (a) the laser intensity I_L (dashed red line) and the resulting electron density n_0 (solid black line) according to our model are shown. The electron kinetic energy is presented in (b). Figure (c) presents the thermal energy E_th as captured by the model (solid red line) for $\lambda_\mathrm{ei} = 3.5$, in excellent agreement with the thermal energy $E_\mathrm{th,2}^\mathrm{PIC}$ obtained from a PIC simulation (solid blue line). In (d) the collision frequency ν_ei according to Eq. (2.5.9) is shown.

as the electric field $\mathbf{E}_\mathrm{L}$. For technical convenience, we switched to the co-moving pulse frame by introducing the new time variable $\tau = t - z/c$. The collision frequency ν_ei has to be computed from Eqs. (2.5.9) and the electron energy is determined by the energy equation (2.5.12). The electron density $n_0 = \sum Z n_\mathrm{ion}^{(Z)}$ follows from the ion densities $n_\mathrm{ion}^{(Z)}$ that are solution of the rate equations [Eq. (2.1.8)] given in Sec. 2.1.

4.1.1. Laser heating

Let us have a look at a first illustrative example showing some basic processes, namely the ionization and laser heating, captured by the ϵ^1 model. We consider a laser pulse with $t_0 = 50\,\mathrm{fs}$, $I_\mathrm{L}^0 = 4\times10^{14}\,\mathrm{W/cm^2}$, $\lambda_\mathrm{L} = 800\,\mathrm{nm}$ in argon gas with the initial atom density $n_\mathrm{a} = 3\times10^{19}\,\mathrm{cm^{-3}}$, corresponding to about 1 bar pressure. The laser pulse profile is shown in Fig. 4.1.1(a) (dashed red line). The gas atoms are getting ionized and the electron density n_0 in Fig. 4.1.1(a) (solid black line) is growing step-wise near time points corresponding to extrema of $\mathbf{E}_\mathrm{L}$. In this particular case the final electron density n_0 reaches the initial gas density n_a, thus the atoms undergo complete single ionization. The electron kinetic energy $E_\mathrm{kin,2}$ reaches about 48 eV, and oscillates at $2\omega_\mathrm{L}$ [see Fig. 4.1.1(b)]. According to our model, the thermal energy $E_\mathrm{th,2}$ of the electrons increases up to 10 eV [solid red line in Fig. 4.1.1(c)]. As shown by Eq. (2.5.30), the heating of the electrons is driven by two mechanisms. Firstly, we have the contribution of electron-ion collisions $\propto \nu_\mathrm{ei}$. Secondly, the ionization term $\propto \partial_t n_0$ increases the thermal energy as well, consistent with results published in [127]: Electrons which are born at a time point in the laser cycle displaced from the peak electric field acquire a dephasing energy. This mechanism

is important for fs-laser pulses but becomes negligible for longer pulses ($> 100\,\mathrm{fs}$)[2], where the heating from electron-ion collisions dominates. The evolution of the collision frequency ν_{ei} is shown in Fig. 4.1.1(d). It features a maximum near the peak intensity of the driving pulse and decreases finally to $13\,\mathrm{ps}^{-1}$ corresponding to a collision time of 77 fs. Oscillations at $2\omega_{\mathrm{L}}$ appear due to the dependency on $E_{\mathrm{kin},2}$.

The prediction of the thermal energy by our model is now confronted with a 1D PIC simulation accounting for electron-ion and electron-electron collisions by means of the code CALDER [102]. The input laser pulse [same as shown in Fig. 4.1.1(a)] propagates over 10 µm in argon, without noticeable deformation. Thus, the thermal energies extracted from this simulation depend only on the retarded time τ as well. The PIC electron thermal energy $E_{\mathrm{th}}^{\mathrm{PIC}}$ shown in Fig. 4.1.1(c) (solid blue line) is in excellent agreement with the model. As already mentioned above, we expect contributions from two different heating processes, which can be visualized in the PIC results. The dashed blue line in Fig. 4.1.1(c) shows the thermal energy $E_{\mathrm{th},x}^{\mathrm{PIC}}$ in the motion of the electrons along the x-axis, which is the laser polarization direction. The dash-dotted blue line shows the thermal energy $E_{\mathrm{th},y/z}^{\mathrm{PIC}}$ contained in each of the other two degrees of freedom. We note up to the laser pulse peak ($\tau = 0$) that the thermal energy along the laser electric field polarization direction x is larger than the ones in the other direction. Thus, the momentum distribution of the electrons in the PIC simulation is anisotropic. The reason for this anisotropy is the heating by the second term $\propto \partial_t n_0$ on r.h.s in Eq. (2.5.30): The corresponding dephasing energy (see above) is acquired solely along the laser polarization direction leading to a momentum spread of the electron distribution function along x only. In contrast, heating by electron-ion collisions is isotropic. However, the phase space quickly thermalizes in the PIC simulation due to electron-electron and electron-ion collisions leading to an equal distribution of the thermal energy along each direction after 100 fs of the interaction. This fact justifies the assumption of instantaneous thermalization in our model.

4.1.2. Ionization current vs. transition-Cherenkov mechanism

Before discussing THz emission from the ϵ^1 model (IC mechanism), let us proceed with the calculation of $\mathbf{J}_2$ (TC mechanism). In 1D configuration, the current at order ϵ^2 is driven by the purely longitudinal source term $\boldsymbol{\iota}_2 = \iota_{2,z}\mathbf{e}_z$, which according to Eq. (D.6) in App. D contains four contributions

$$\iota_{2,z} = \iota_{2,z}^{\mathrm{pond}} + \iota_{2,z}^{\mathrm{ion}} + \iota_{2,z}^{\mathrm{col}} + \iota_{2,z}^{\mathrm{heat}}\,. \tag{4.1.3}$$

In the co-moving pulse frame, these contributions read (see App. H for details)

$$\begin{aligned} \iota_{2,z}^{\mathrm{pond}} &= \frac{n_0}{2q_{\mathrm{e}}c}\partial_\tau\left|\frac{\mathbf{J}_1}{n_0}\right|^2, \qquad \iota_{2,z}^{\mathrm{ion}} = \frac{(\partial_\tau n_0)}{q_{\mathrm{e}}c}\left|\frac{\mathbf{J}_1}{n_0}\right|^2, \\ \iota_{2,z}^{\mathrm{col}} &= \frac{n_0\nu_{\mathrm{ei}}}{q_{\mathrm{e}}c}\left|\frac{\mathbf{J}_1}{n_0}\right|^2, \qquad \iota_{2,z}^{\mathrm{heat}} = \frac{2\partial_\tau(n_0 E_{\mathrm{th}})}{3m_{\mathrm{e}}q_{\mathrm{e}}c}\,. \end{aligned} \tag{4.1.4}$$

The first term is the ponderomotive source $\iota_{2,z}^{\mathrm{pond}}$. The second source term $\iota_{2,z}^{\mathrm{ion}}$ is a direct consequence of the ionization, and is absent in preformed plasmas. The third source term $\iota_{2,z}^{\mathrm{col}}$ takes the radiation pressure into account. Finally, the fourth source term $\iota_{2,z}^{\mathrm{heat}}$ is caused by diffusion or pressure of the electrons. We note that $\iota_{2,z}^{\mathrm{pond}}$, $\iota_{2,z}^{\mathrm{ion}}$, and $\iota_{2,z}^{\mathrm{col}}$ have already been derived in [58]. In a 1D configuration, the longitudinal component of $\nabla \times \mathbf{B}$ vanishes and Eq. (2.5.20)

[2] According to the estimations of Eq. (2.5.31), the collisional heating dominates for $2\nu_{\mathrm{ei}}t_0 \gg 1$. Inspired by Fig. 4.1.1(d), we take $\nu_{\mathrm{ei}} = 13\ \mathrm{ps}^{-1}$ and obtain $t_0 \gg 38$ fs.

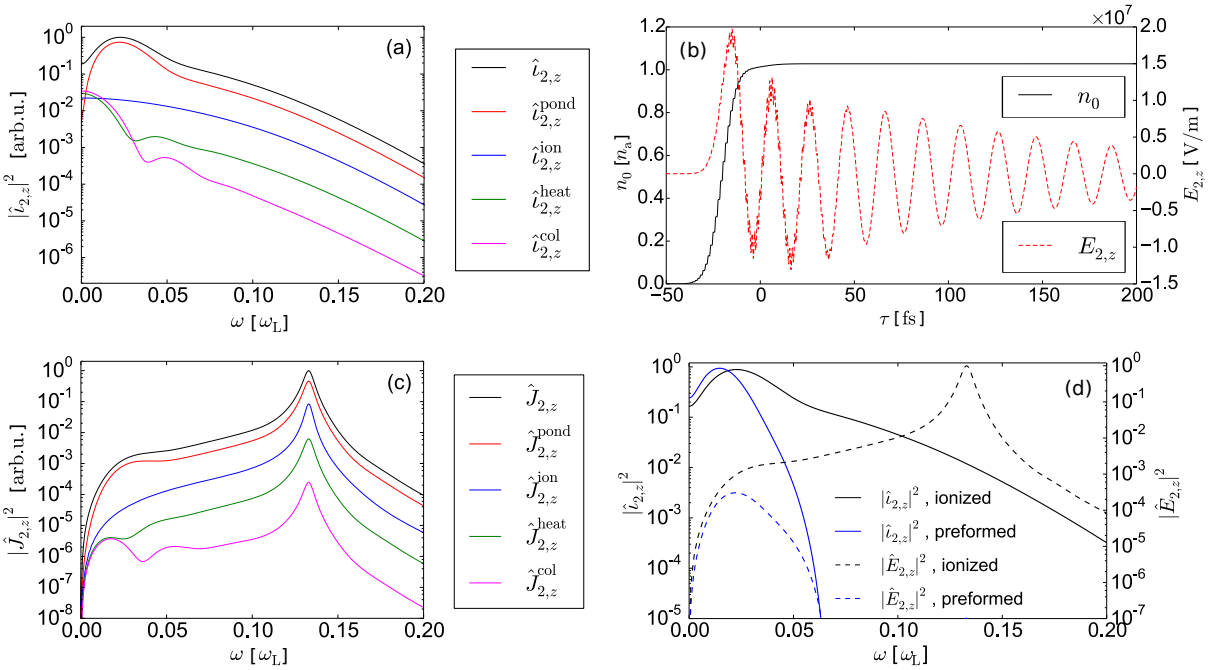

Figure 4.1.2.: In (a) the low-frequency power spectra of the second-order source term $\iota_{2,z}$ (topmost line) and its constituents are shown. The longitudinal electric field $E_{2,z}$ is presented in (b) together with the electron density n_0. In (c) the power spectra of the longitudinal currents corresponding to the source terms in (a) are plotted. In (d), the power spectra of the second-order source term $\iota_{2,z}$ (solid lines) and the electric field $E_{2,z}$ (dashed lines) are shown for an initially neutral gas (black lines) and a preformed plasma (blue lines) with the same electron density as in the gas after ionization. Driving laser and gas parameter are the same as in Fig. 4.1.1.

dictates that the longitudinal electric field $E_{2,z}$ is connected to the longitudinal current $J_{2,z}$ via

$$J_{2,z} = -\epsilon_0 \partial_\tau E_{2,z} \,. \tag{4.1.5}$$

Thus, we can substitute $J_{2,z}$ in Eq. (2.5.16) and end up with the following equation for the longitudinal field $E_{2,z}$:

$$\partial_{\tau\tau} E_{2,z} + \nu_{ei} \partial_\tau E_{2,z} + \left(\frac{q_e^2 n_0}{m_e \epsilon_0} \right) E_{2,z} = -\frac{\iota_{2,z}}{\epsilon_0} \,. \tag{4.1.6}$$

All quantities involved, in particular $\iota_{2,z}$, can be computed from the solution to the 1st order problem.

Let us now come back to the case study of a 50-fs pulse from above. The low-frequency power spectra of the 2nd order source term $\iota_{2,z}$ and its four constituents defined in Eq. (4.1.4) are presented in Fig. 4.1.2(a). Obviously, $\iota_{2,z}$ (black line) is dominated by the ponderomotive source $\iota^{pond}_{2,z}$ (red line). Other contributions are at least one order of magnitude smaller for this driving pulse. The peak excitation happens around $0.022\omega_L$ (i.e., $\nu \approx 8.25\,\mathrm{THz}$). In comparison, the power spectrum of $\iota_{2,z}$ at the plasma frequency $\omega_p \approx \sqrt{(q_e^2 n_a / m_e \epsilon_0)} \approx 0.13\omega_L$ (i.e., $\nu \approx 50\,\mathrm{THz}$) is almost two orders of magnitude smaller[3]. Nevertheless, longitudinal plasma oscillations at

[3]For our 50-fs example pulse the final electron density is $n_0(t \to \infty) \approx n_a$

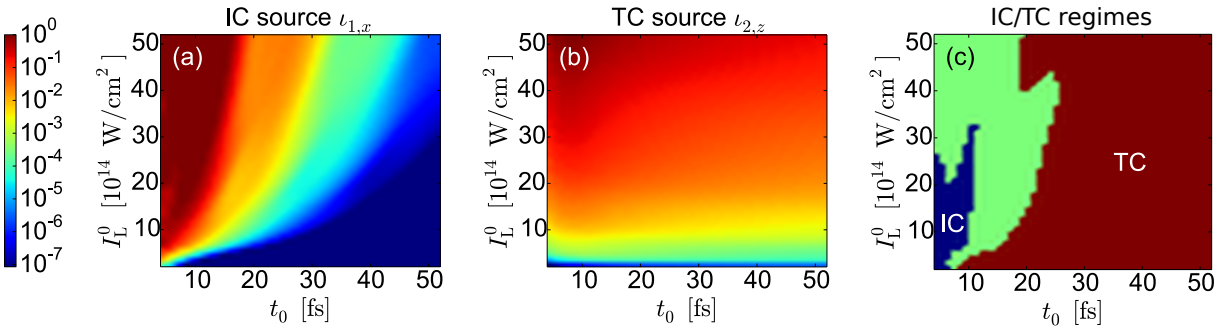

Figure 4.1.3.: In (a) the up to $0.2\omega_L$ ($\nu \leq 75\,\mathrm{THz}$) integrated power spectrum of the source term $\iota_{1,x}$ (IC source) is shown as a function of laser pulse duration t_0 and intensity I_L^0. The same data for $\iota_{2,z}$ (TC source) are shown in (b). These two terms are compared in panel (c): In the blue region the IC source term $\iota_{1,x}$ dominates by at least one order of magnitude, in the red region the same is true for the TC source term $\iota_{2,z}$, and in the green region $\iota_{1,x}$ and $\iota_{2,z}$ are both important. The computations are performed for an argon gas with the initial atom density $n_a = 3 \times 10^{19}\,\mathrm{cm}^{-3}$.

ω_p are excited in $E_{2,z}$ when the electron density n_0 builds up, as can be seen in Fig. 4.1.2(b). This excitation is also visible in the spectrum of the current $J_{2,z}$ shown in Fig. 4.1.2(c). It is interesting to note that for our example the observed strong excitation at the plasma frequency ω_p is intimately linked to ionization. The power spectra of the electric field $E_{2,z}$ in a preformed plasma and an initially neutral gas are compared in Fig. 4.1.2(d). Shooting the same driving pulse into a preformed plasma with constant density $n_0 \equiv n_a$ triggers almost no oscillations at ω_p. For constant n_0, the power spectrum of the second-order source term $\iota_{2,z}$ is more narrow, and in particular its value at ω_p is more than three orders of magnitude lower. Only very short driving pulses fulfill the resonance condition $t_0 \lesssim \pi/\omega_p$ and significantly excite plasma oscillations in a preformed plasma.

In our discussion of plasma currents in the THz spectral range above we completely ignored the first-order current $\mathbf{J}_1$. The reason for this is simply that for our 50-fs 1C-driving pulse, $J_{1,x}$ has no significant THz component. In the spectral range shown in Fig. 4.1.2(c), the power spectrum of $J_{1,x}$ (not shown) is more than ten orders of magnitude lower than that of $J_{2,z}$. Thus, in our example the IC mechanism is not present and THz emission results from the TC mechanism only. However, this may change for other driving pulse parameters, even in 1C configuration. In the following, the IC ($\mathbf{J}_1$) and TC ($\mathbf{J}_2$) mechanisms are compared for laser intensities $I_L^0 = 2 - 50 \times 10^{14}\,\mathrm{W/cm}^2$ and pulse durations $t_0 = 4 - 50\,\mathrm{fs}$. Figures 4.1.3(a,b) show the power spectra of $\iota_{1,x}$ and $\iota_{2,z}$ (IC resp. TC source) integrated up to $0.2\omega_L$ ($\nu \leq 75\,\mathrm{THz}$). Figure 4.1.3(a) reveals that the IC mechanism requires short and intense pulses to play a role, in agreement with [96]. By contrast, the source term $\iota_{2,z}$ of the TC mechanism varies only weakly in the considered parameter range [see Fig. 4.1.3(b)]. Finally, Fig. 4.1.3(c) displays the parameter regions where one of the source terms dominates by at least one order of magnitude. We can conclude that the IC mechanism described by the lowest order of the multiple scale expansion in Sec. 2.5.1 is important for very short pulses only, whereas the TC mechanism which is included in the next higher order set of equations in Sec. 2.5.2 is the key player for sufficiently long 1C-laser pulses.

We now want to cross-check the predictions of Fig. 4.1.3 by means of 1D PIC simulations. To this end, we consider two pulse configurations: A few-cycle pulse with $t_0 = 5\,\mathrm{fs}$, $I_L^0 =$

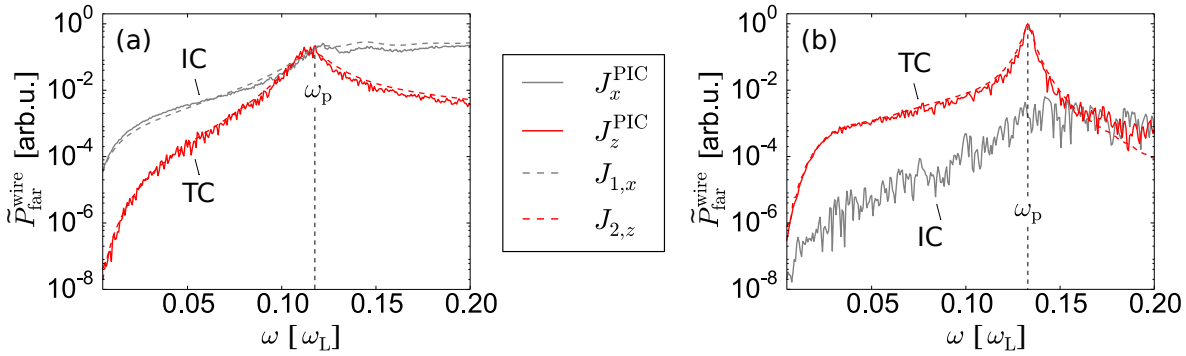

Figure 4.1.4.: Hypothetical far field spectra integrated over all angles computed by assuming an infinitely thin 10 µm long plasma wire (see text) are shown for $I_L^0 = 4 \times 10^{14}$ W/cm^2, $t_0 = 5$ fs (a) and $t_0 = 50$ fs (b). Power spectra are calculated from current densities associated with the IC (x-polarized current), TC (z-polarized current) mechanisms that are obtained from 1D PIC simulations and model according to the legend.

4×10^{14} W/cm^2 to illustrate the IC dominated regime and the multi-cycle pulse with $t_0 = 50$ fs, $I_L^0 = 4 \times 10^{14}$ W/cm^2 already used above as an example for the TC dominated regime. Following [60, 59], we use the 1D results for the current density $\mathbf{J}$ and compute a hypothetical angularly integrated far-field spectrum $\tilde{P}^{wire}_{far}$ by assuming the plasma having a transverse shape of an infinitely thin 10-μm-long wire. The far-field spectrum is computed according to Eq. (2.6.8). Simulation (solid lines) and model results (dashed lines) are presented in Fig. 4.1.4. For the IC mechanism (light gray lines) we use the transverse current J_x^{PIC} from PIC simulation[4] and $J_{1,x}$ from the full ϵ^1 model[5], without approximating $\mathbf{E}_1$ by $\mathbf{E}_L$. For the TC mechanism (dark red lines) we use the longitudinal current J_z^{PIC} from the PIC simulation and $J_{2,z}$ from the simplified ϵ^2 model according to Eq. (4.1.5). Obviously, PIC simulations (solid lines) and the model (dashed lines) are in an excellent agreement. The PIC results confirm that the IC mechanism dominates the TC mechanism for the short pump pulse (a), and vice versa for the longer pulse (b). In the latter case, $\tilde{P}^{wire}_{far}$ produced by J_x^{PIC} is even dominated by the noise of the PIC simulation and the model gives a signal far below the signal from the TC mechanism (not shown).

It is important to note that the IC mechanism requires the full treatment of the equations at order ϵ^1. In contrast, assuming $\mathbf{E}_1 \approx \mathbf{E}_L$ causes almost no loss of accuracy when evaluating the ϵ^2 order of the model: The computation of the nonlinear source $\iota_{2,z}$ for Fig. 4.1.4(b) was performed approximating $\mathbf{J}_1$ according to Eq. (4.1.2) and gives already perfect agreement with the PIC simulation. For the few-cycle pulse in Fig. 4.1.4(a), laser energy loss due to ionization [cf. Eq. (3.2.5)] and electron heating becomes notable: The electric field amplitude decreases during the propagation through the 10-μm-long gas-plasma by 3 %, and the final electron density at $z = 10$ µm is about 11 % smaller than at $z = 0$ µm (not shown). Therefore, in Fig. 4.1.4(a) a full treatment of the model up to order ϵ^2 was necessary to obtain perfect agreement with PIC results.

It is quite tempting to conclude from hypothetical far field spectra obtained from 1D results, as shown in Fig. 4.1.4, on actual THz emission from a real 3D plasma as produced in experiments. While such reasoning can be found in the literature, e.g. in [60], it is generally incorrect. On the one hand, we assume translational invariance in the transverse directions when computing

[4]The simulation has been performed with the code CALDER (see Sec. 3.1) accounting for binary electron-ion and electron-electron collisions with the resolution $\delta t = 5.3$ as, $\delta z = 15.9$ nm and 80000 macro-particles per mesh.

[5]The simulation has been performed with the fluid code ARCTIC (see Sec. 3.2) with $\delta t = 5.3$ as, $\delta z = 15.9$ nm.

the 1D current, on the other hand, we impose later a thin transverse shape of the plasma wire when computing the hypothetical far field. As we will see in the next section, realistic THz emission spectra differ very strongly from Fig. 4.1.4. The reason for this discrepancy is that not all plasma currents lead to emission of radiation, and in particular oscillations at the plasma frequency may not radiate [128].

4.2. Radiating and non-radiating excitations

In the previous section, we have analyzed plasma currents generated by an intense fs-laser pulse in a gas, with particular emphasize on excitations in the THz spectral range. The question we want to answer now is how the radiation produced by these currents looks like. As already indicated in the concluding remarks of Sec. 4.1, one has to be careful with excitations at the plasma frequency, which may not contribute to the radiation spectrum [128]. The reason for this will be elaborated in the following, however, a simple physical picture gives already some insight: The plasma oscillations at ω_p, whenever they are eigen-oscillations of the system, would continue forever (for $\nu_{\mathrm{ei}} = 0$) and their energy would stay inside the plasma. Thus, they cannot contribute to radiation, or otherwise energy conservation is violated.

As we have seen above, the TC mechanism is expected to dominate the THz emission from microplasmas created by multi-cycle 1C-laser pulses as used in [61]. In this section, we focus on the TC mechanism and thus emission from the 2$^{\mathrm{nd}}$ order current $\mathbf{J}_2$. Our starting point is thus Eq. (2.5.25) that we repeat for clarity

$$\partial_{tt}\mathbf{E}_2 + \nu_{\mathrm{ei}}\partial_t\mathbf{E}_2 + \frac{q_e^2 n_0}{m_e\epsilon_0}\mathbf{E}_2 + c^2\nabla\times\nabla\times\mathbf{E}_2 + \nu_{\mathrm{ei}}c^2\int_{-\infty}^{t}\nabla\times\nabla\times\mathbf{E}_2 = -\frac{\boldsymbol{\iota_2}}{\epsilon_0}\,. \tag{4.2.1}$$

This equation is nothing else but the 3D version of Eq. (4.1.6). In contrast to the 1D case studied above (where $\boldsymbol{\iota_2}$ is purely longitudinal and the z-component of $\nabla\times\mathbf{E}_2$ vanishes), in 3D all components of $\mathbf{E}_2$ are non-zero and coupled. Moreover, focusing dynamics of the driving laser pulse render a transformation to the co-moving pulse frame useless.

In order to identify the part of $\mathbf{E}_2$ which actually contributes to the far field, we note that according to Faraday's law in Eq. (2.5.19) a curl-free field ($\nabla\times\mathbf{E}_2 = 0$) does not lead to radiation in the far-field, because no electro-magnetic wave is produced ($\partial_t\mathbf{B}_2 = 0$). By using the Helmholtz decomposition theorem, we can decompose $\mathbf{E}_2 = \mathbf{E}_{2,\mathrm{d}} + \mathbf{E}_{2,\mathrm{r}}$ into a curl-free field $\mathbf{E}_{2,\mathrm{d}}$ with $\nabla\times\mathbf{E}_{2,\mathrm{d}} = 0$ and a divergence-free field $\mathbf{E}_{2,\mathrm{r}}$ with $\nabla\cdot\mathbf{E}_{2,\mathrm{r}} = 0$. In general, both fields are coupled in Eq. (4.2.1) by the terms $\propto n_0$ and $\propto \nu_{\mathrm{ei}}$. By taking the curl of Eq. (4.2.1), we find[6] that $\mathbf{E}_{2,\mathrm{d}}$ decouples from $\mathbf{E}_{2,\mathrm{r}}$ if

$$\mathbf{E}_{2,\mathrm{d}}\times\nabla n_0 = 0\,, \qquad \partial_t\mathbf{E}_{2,\mathrm{d}}\times\nabla\nu_{\mathrm{ei}} = 0 \tag{4.2.2}$$

$$\mathbf{E}_{2,\mathrm{r}}\cdot\nabla n_0 = 0\,, \qquad \partial_t\mathbf{E}_{2,\mathrm{r}}\cdot\nabla\nu_{\mathrm{ei}} = 0\,. \tag{4.2.3}$$

Let us have a look at a simple but illustrative example for the occurrence of such non-radiative curl-free electric fields: In a preformed collisionless plasma ($n_0 = \mathrm{const.}$, $\nu_{\mathrm{ei}} = 0$), the curl-free and divergence-free fields are decoupled (see also [6]). Moreover according to Eq. (D.6), $\boldsymbol{\iota}_2$ reduces to the ponderomotive source[7] $\boldsymbol{\iota}_2^{\mathrm{pond}} = -n_0/2q_e\nabla|\mathbf{J}_1/n_0|^2$. Because $\boldsymbol{\iota}_2^{\mathrm{pond}}$ is obviously curl-free, the solution to Eq. (4.2.1) is also curl-free and Eq. (4.2.1) reduces to a simple oscillator

[6] We use $\nabla\cdot(n_0\mathbf{E}_2) = (\nabla n_0)\cdot\mathbf{E}_2 + n_0\nabla\cdot\mathbf{E}_2$, $\nabla\times(n_0\mathbf{E}_2) = (\nabla n_0)\times\mathbf{E}_2 + n_0\nabla\times\mathbf{E}_2$ and similarly for $\nu_{\mathrm{ei}}\partial_t\mathbf{E}_2$.
[7] Note that for $n_0 = \mathrm{const.}$, $\nu_{\mathrm{ei}} = 0$, we have a cold plasma ($\mathcal{E}_2 = 0$). Moreover, $\nabla\cdot\mathbf{J}_1 = 0$.

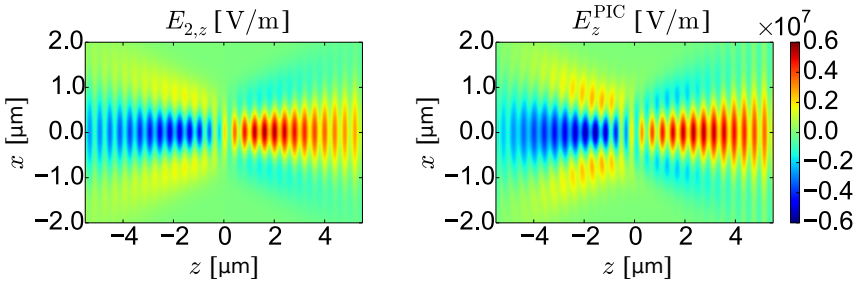

Figure 4.2.1.: Snapshot of the longitudinal electric field $E_{2,z}$ from the model (a) and E_z^{PIC} from the corresponding 2D PIC simulation (b) at the time moment when the laser pulse is at focus. The y-polarized Gaussian laser pulse ($t_0 = 50\,\mathrm{fs}$, $I_{\max} = 4 \times 10^{14}\,\mathrm{W/cm^2}$) is focused to $w_0 = 0.8\,\mu\mathrm{m}$ into a uniform preformed plasma ($n_0 = 3 \times 10^{19}\,\mathrm{cm^{-3}}$).

equation

$$\partial_{tt}\mathbf{E}_2 + \frac{q_\mathrm{e}^2 n_0}{m_\mathrm{e}\epsilon_0}\mathbf{E}_2 = -\frac{n_0}{2q_\mathrm{e}}\nabla\left|\frac{\mathbf{J}_1}{n_0}\right|^2 . \tag{4.2.4}$$

We now consider a 2D (translational invariance in y-direction, $\partial_y \equiv 0$) linearly polarized Gaussian pulse with the vacuum electric field in focus according to

$$\mathbf{E}_{\mathrm{L},\perp}(\mathbf{r}_\perp, z=0, t) = \sqrt{\frac{2I_\mathrm{L}^{(0)}}{c\epsilon_0}}\exp\left(-\frac{|\mathbf{r}_\perp|^2}{w_0^2} - \frac{t^2}{t_0^2}\right)\sin\left(\omega_\mathrm{L} t\right)\mathbf{e}_\mathrm{y}, \tag{4.2.5}$$

where the peak intensity is $I_{\max} = 4 \times 10^{14}\,\mathrm{W/cm^2}$, $t_0 = 50$ fs and $0.8\,\mu$m. Moreover, we assume a uniform preformed plasma with electron density $n_0 = 3 \times 10^{19}\,\mathrm{cm^{-3}}$. This particular 2D configuration has the advantage that in the PIC simulation the electric field of the driving laser appears in the E_y component only, and the longitudinal component E_z is produced by the plasma only. Thus, a direct confrontation of $E_{2,z}$ from the model with E_z^{PIC} is possible. When evaluating the model, the ponderomotive source and the laser field are approximated (see App. I). Nevertheless, a temporal snapshot of the longitudinal electric field at focus (see Fig. 4.2.1)[8] shows an excellent agreement between analytical model (a) and 2D PIC simulation (b). A low-frequency field and a second harmonic (SH) field are clearly visible as a fast and slow modulation pattern along z. Both fields are non-radiating according to our previous argumentation. This is confirmed by inspecting the magnetic field component B_y in the PIC simulation, which is found to be at background noise level (not shown).

For laser-induced plasmas, we have a finite plasma volume with spatially (and temporally) varying electron density ($\nabla n_0 \neq 0$). For the sake of simplicity, we will look for curl-free solutions of Eq. (4.2.1) for $\boldsymbol{\iota}_2 = 0$ only, i.e., after the driving pulse has passed. Then, n_0 is constant in time and the general solution in the collisionless case has the form (see App. J)

$$\mathbf{E}_{2,\mathrm{d}} = A(n_0)\cos\left[\sqrt{\frac{q_\mathrm{e}^2 n_0}{m_\mathrm{e}\epsilon_0}}t + \phi(n_0)\right]\nabla n_0\,, \tag{4.2.6}$$

where A and ϕ are scalar functions depending on the electron density n_0. The solution $\mathbf{E}_{2,\mathrm{d}}$ oscillates at the local plasma frequency $\omega_\mathrm{p}(\mathbf{r}) = \sqrt{q_\mathrm{e}^2 n_0(\mathbf{r})/m_\mathrm{e}\epsilon_0}$, and the electric field vector is

[8] The simulation has been performed with the PIC code OCEAN (cf. Sec. 3.1) with 3200 macro-particles per mesh, $\delta z = \delta x = 31.8$ nm and $\delta t = 100$ as.

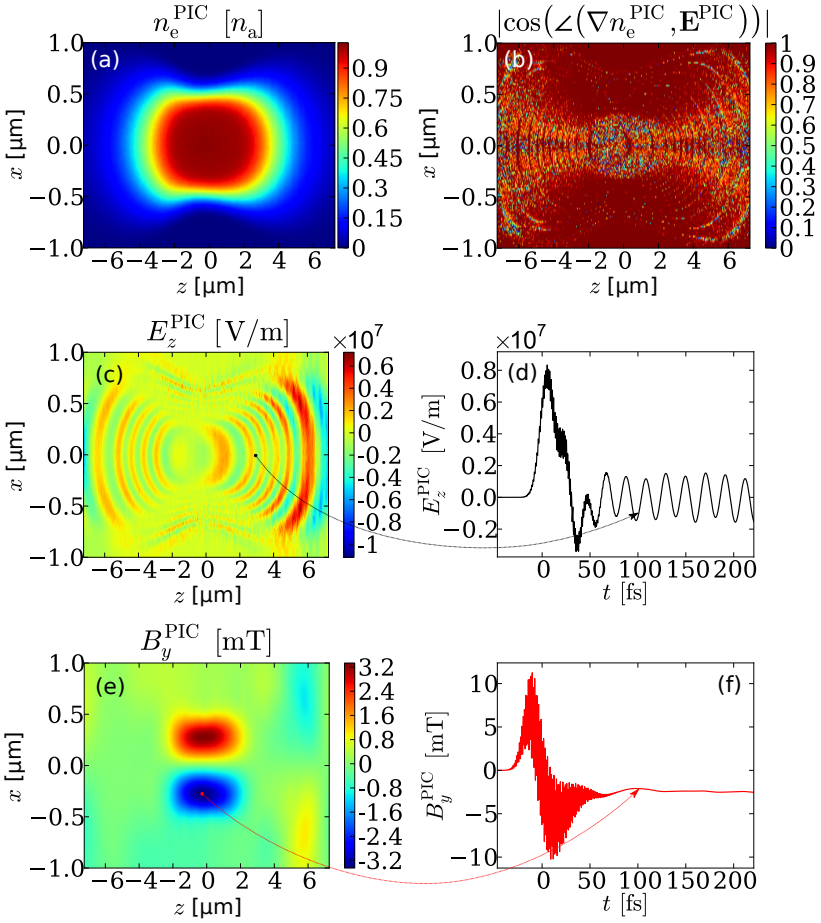

Figure 4.2.2.: The same laser pulse as in Fig. 4.2.1 is focused into argon gas at ambient pressure. A snapshot of the generated plasma (a) and the absolute value of the cosine of the angle between $\mathbf{E}^{PIC}$ and ∇n^{PIC} (b) after the pulse has passed the focus are shown. The corresponding snapshot of the electric field component E_z^{PIC} is depicted in (c). The exemplary time trace of E_z^{PIC} in (d) features oscillations at the local plasma frequency, in agreement with Eq. (4.2.6). The snapshot of B_y^{PIC} in (e) shows the magneto-static field which is present in the interaction region after the laser pulse has passed [see corresponding time trace in (f)]. All temporal snapshots in (a,b,c,e) are taken about 100 fs after the pulse has passed the focus. Recording positions of the time traces shown in (d,f) are indicated by the respective arrows.

always parallel to ∇n_0, thus $\mathbf{E}_{2,d}$ is decoupled from radiating fields $\mathbf{E}_{2,r}$ [c.f. Eq. (4.2.3)]. Those findings are in agreement with [129].

Equation (4.2.6) presents the solution for a non-radiating eigen-oscillation at the plasma frequency in 2D/3D configuration. We now want to show that such fields are really excited in laser-induced microplasmas and inject the same y-polarized laser as in the previous example of a preformed plasma in argon gas with $n_a = 3 \times 10^{19}\,\mathrm{cm}^{-3}$. As above, we use the 2D geometry with translational invariance in y-direction in the PIC simulation and neglect collisions. The resulting electron density profile after the laser pulse has passed through the interaction region is shown in Fig. 4.2.2(a): A 10 μm-long and 1 μm-wide plasma with fully singly ionized argon at focus. In order to check whether the electric field in the PIC simulation after the laser pulse has passed is of the form in Eq. (4.2.6), the absolute value of the cosine of the angle between $\mathbf{E}^{PIC}$ and ∇n_e^{PIC}

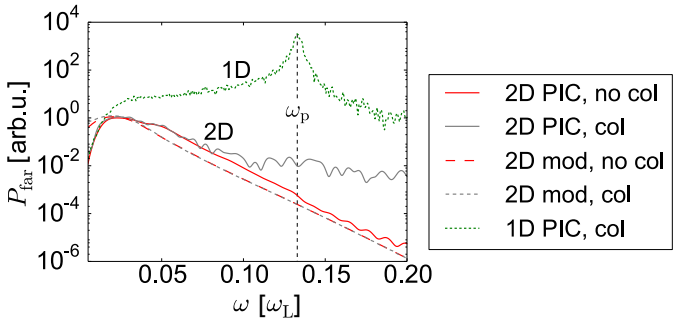

Figure 4.2.3.: The same laser pulse as in Figs. 4.2.1, 4.2.2 is focused into argon gas at ambient pressure. The angle-integrated far field spectra obtained from 2D PIC simulation, model and 1D wire model are presented according to the legend.

is computed[9] and presented in Fig. 4.2.2(b). Obviously, after the laser has left the interaction region the two vectors are (anti-)parallel almost everywhere. Moreover, Figs. 4.2.2(c,d) confirm that after the laser has left the interaction region, the electric field $\mathbf{E}^{\rm PIC}$ oscillates at the local plasma frequency[10]. However, as expected from our previous reasoning, these oscillations occur inside the plasma only, the angle-integrated far field spectrum in Fig. 4.2.3 (solid dark red line) exhibits no feature at the plasma frequency, in direct contradiction to the results from the 1D wire model[11] discussed in the previous section (dotted green line). Moreover, 2D PIC simulations with collisions (solid light gray line) coincide perfectly with PIC simulations without collisions, up to the noise level around 10^{-2}. In particular, collisions do not enhance the far-field amplitude at the plasma frequency.

As previously explained, in the PIC simulation no radiation is emitted due to plasma oscillations after the excitation by the laser pulse. During the laser pulse, the non curl-free $\boldsymbol{\iota}_2^{\rm pond}$ term (as $\nabla n_0 \neq 0$) is able to generate a potentially radiating field $\mathbf{E}_{2,r}$. The investigation of this TC radiation will be presented in the next section and explains the spectrum observed in Fig. 4.2.3.

Besides the non-radiating excitation $\mathbf{E}_{2,\rm d}$, there exists a second non-radiating, magneto-static excitation. The corresponding field $\mathbf{B}_{2,\rm m}$ is linked to a non-radiating, static current $\mathbf{J}_{2,\rm m}$ via

$$\Delta \mathbf{B}_{2,\rm m} = -\mu_0 \nabla \times \mathbf{J}_{2,\rm m}\,. \tag{4.2.7}$$

The PIC simulation above confirms the existence of such a magneto-static excitation as well: The y-component of the magnetic field $\mathbf{B}^{\rm PIC}$ is constant in time after the laser has passed the interaction region. In Fig. 4.2.2(e) a snapshot of this static magnetic field component is shown, together with an exemplary time trace in Fig. 4.2.2(f).

The total non-radiative current created in the microplasma can thus be written as

$$\mathbf{J}_2^{\rm nonrad} = \mathbf{J}_{2,\rm m} - \epsilon_0 \partial_t \mathbf{E}_{2,\rm d}\,. \tag{4.2.8}$$

Interestingly, the second (curl-free) term in Eq. (4.2.8) is exactly what we used in the previous 1D

[9] If the absolute of $\mathbf{E}^{\rm PIC}$ or $\nabla n_{\rm e}^{\rm PIC}$ is smaller than 1% of its average value in the whole box, we set the value to unity since the angle between zero-vectors cannot be defined.

[10] Here, we can validate a posteriori the validity of the multiple scale expansion for this example: we find an electric field corresponding to $\mathbf{E}_2$ driven by $\boldsymbol{\iota}_2$ of the order $10^7\,\mathrm{V/m}$. Similar values have been found in Fig. 4.1.2(b) for 1D configuration. The ratio of 1st and 2nd order electric field is thus about $2\times10^{-3} < 1.4\times10^{-2} = |q_{\rm e}E_{\rm L}^0/m_{\rm e}\omega_{\rm L}c|$, i.e., the upper bound for the ratio established in Sec. 2.5.4.1.

[11] Here, the current has been computed same as in Sec. 4.1.2. Then, by assuming an infinitely thin plasma in x, the far-field power spectrum has been computed according to Sec. 2.6. Since, we compare with 2D PIC simulations here, we have to use the 2D Greens function $G^{\rm 2D}$.

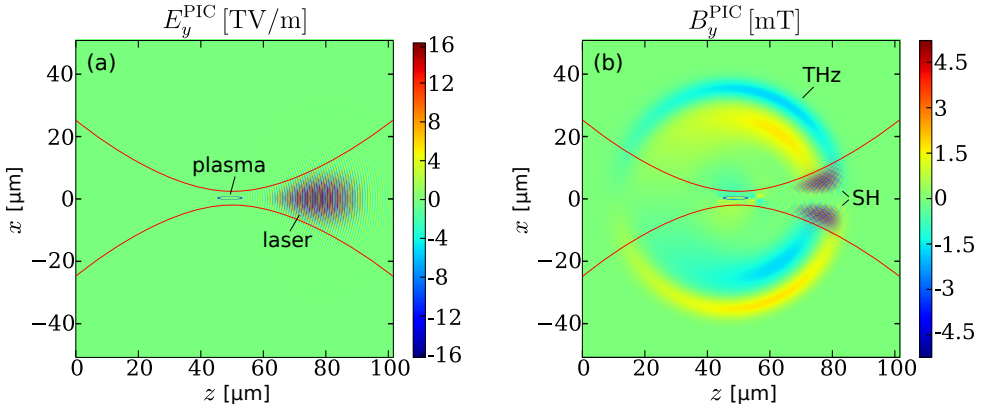

Figure 4.3.1.: Snapshot of the electric field E_y^{PIC} (a) and the magnetic field B_y^{PIC} (b) from the same PIC simulation as presented in Fig. 4.2.2. The figure is a zoom-out of Fig. 4.2.2(e), so the emitted THz and SH waves are visible (denoted as 'SH' and 'THz'). The mean width of the focused laser is indicated by the dark red lines, and the position of the generated plasma is marked as a blue oval.

model [c.f. Eq. (4.1.5)]. In order to compute the hypothetical far field spectra in Fig. 4.1.4, this (curl-free) current density has been multiplied by a narrow transverse electron distribution in order to represent a thin wire. It is obvious that such operation destroys the "curl-free" property of the current and thus introduces an artificial radiation. To judge if a current is radiating, its transverse spatial dependence is of great importance. Therefore, 1D modeling is not suitable for the description of THz emission from plasma currents and we perform 2D modeling for the radiating fields in the next section.

4.3. Terahertz radiation from single-color-fs-laser-induced microplasmas

We have seen in the previous section that one has to be careful when concluding from plasma excitations on THz radiation in the far field. Plasma oscillations can be excited at the local plasma frequency, which do not necessarily emit radiation. Using a 1D plasma model in order to predict THz emission spectra from fs-laser gas interaction, as proposed in [60] and later used, e.g., in [59, 61], may give incorrect results: As shown in Fig. 4.2.3, THz emission spectra obtained from such model deviate strongly from those obtained from PIC simulations. Thus, in order to understand the THz emission spectra, 2D or even 3D models are inevitable.

Throughout this section, we consider the 50-fs y-polarized laser pulse configuration already employed in Figs. 4.2.2 and 4.2.3 as an example. For the sake of computational costs, the following PIC simulations are performed in this 2D configuration [$\partial_y \equiv 0$, $\mathbf{E}_{\mathrm{L}} = \mathbf{E}_{\mathrm{L},y}\mathbf{e}_y$, see Fig. 4.3.1(a)]. Our particular 2D geometry implies, that $\mathbf{E}_1$ and $\mathbf{J}_1$ are y-polarized. Then, according to Eq. (2.5.17), $\iota_{2,y} = 0$. Thus, the radiation driven by such a source is fully described by the magnetic field component $B_{2,y}$, while $B_{2,x} = B_{2,z} = 0$. On the other hand, the driving laser pulse is y-polarized and hence $B_{\mathrm{L},y} = 0 = B_{1,y}$. This natural separation, which is a special feature of the chosen 2D geometry, is very handy when it comes to analyzing the PIC simulation results. In Fig. 4.3.1(b) a snapshot of B_y^{PIC} from the PIC simulation is presented. The beam envelope of the focused laser is shown schematically as red lines. The snapshot is taken about 100 fs after the driving pulse has passed the focus, and the extension of the created plasma is sketched as a blue oval. In fact, zooming in on the region where the plasma is created

would reproduce Fig. 4.2.2(e). In the larger frame of Fig. 4.3.1 emitted THz and also SH waves propagating forward inside a cone are clearly visible. No radiation is emitted on-axis along z in agreement with PIC simulations in [62].

What is the origin of this THz emission? In the framework of the 1D model in Sec. 4.1.2, the excitation at THz frequencies turned out to be driven by the longitudinal ponderomotive source mostly. However, one has to keep in mind that in 2D and 3D, $\boldsymbol{\iota}_2$ has also transverse components, in particular transverse ponderomotive sources that have been made responsible for THz emission in gas jets [62]. To understand what is the driving source polarization direction in microplasmas, we exploit the symmetries of the sources and the radiating currents in the following section. We will see that the thickness of the plasma determines whether transverse currents lead to THz emission. Afterwards, we consider a simple model of THz emission that allows to estimate the laser-to-THz conversion efficiency for various laser pulse energies and focusing conditions.

4.3.1. Determining the radiating current polarization by symmetries

In this section, depending on the transverse spatial symmetry of the incoming driving laser beam, the polarization of the prevailing THz-radiating currents for the TC mechanism (and the IC mechanism) is determined for narrow plasmas. First, we determine the symmetry of the current source $\boldsymbol{\iota}_2$ (TC) that inherits the symmetry to the current $\mathbf{J}_2$ (cf. App. C). Second, we show by using the relation between the current and the far-field emission from Sec. 2.6 that transversally antisymmetric currents in a narrow plasma, i.e., a microplasma, give a negligible contribution to the far-field-THz emission. Using these insights, we conclude about the emitting current polarization depending on the driving laser beam symmetry.

4.3.1.1. Transverse symmetries of the THz-radiating currents

The second order nonlinear source term $\boldsymbol{\iota}_2$ is computed in particular from the lowest order current $\mathbf{J}_1$ [cf. Eq. (2.5.17)]. Thus, we have to consider the symmetries of $\boldsymbol{\iota}_1$ and $\mathbf{J}_1$ before concluding about $\boldsymbol{\iota}_2$ and $\mathbf{J}_2$.

If the electron density profile n_0 is symmetric in the transverse coordinate $\mathbf{r}_\perp$, the symmetry of $\boldsymbol{\iota}_1 \propto n_0 \mathbf{E}_\mathrm{L}$ is determined by the laser electric field $\mathbf{E}_\mathrm{L}$. First, let us consider a symmetric transverse electric laser field [$\mathbf{E}_{\mathrm{L},\perp}(\mathbf{r}_\perp) = \mathbf{E}_{\mathrm{L},\perp}(-\mathbf{r}_\perp)$], for example the usual linearly polarized Gaussian laser beam [cf. Eq. (4.2.5)[12]]. In Sec. 3.3, we have seen that even in vacuum a linearly polarized Gaussian beam has a longitudinal electric field $E_{\mathrm{L},z}$. Eq. (2.3.1) determines this field as $E_{\mathrm{L},z} = -\int \nabla_\perp \cdot \mathbf{E}_{\mathrm{L},\perp}\, dz$: the integration along z does not change the transverse symmetry, but $\nabla_\perp = (\partial_x, \partial_y)^\mathrm{T}$ does. Thus, $E_{\mathrm{L},z}$ is antisymmetric in $\mathbf{r}_\perp$ [$E_{\mathrm{L},z}(\mathbf{r}_\perp) = -E_{\mathrm{L},z}(-\mathbf{r}_\perp)$]. We can conclude that $\boldsymbol{\iota}_{1,\perp}$ is symmetric and $\iota_{1,z}$ is antisymmetric in $\mathbf{r}_\perp$. In App. C, this kind of symmetry has been introduced as the s-symmetry and visualized in Fig. C.1. Furthermore, $\boldsymbol{\iota}_1$ induces its symmetry to $\mathbf{J}_1$. We conclude for a linearly polarized Gaussian laser beam (or in general any laser field with the s-symmetry) that the transverse current $\mathbf{J}_{1,\perp}$ in the gas-plasma is symmetric in $\mathbf{r}_\perp$, and the longitudinal current $J_{1,z}$ is antisymmetric.

On the other hand, when considering a transverse electric field that is antisymmetric in the transverse coordinate [$\mathbf{E}_{\mathrm{L},\perp}(\mathbf{r}_\perp) = -\mathbf{E}_{\mathrm{L},\perp}(-\mathbf{r}_\perp)$], one can analogous conclude that $\mathbf{J}_{1,\perp}$ is antisymmetric in the transverse coordinate and $J_{1,z}$ is symmetric. For example, this kind of a-symmetry is present within a radially polarized needle beam in Sec. 3.3.4.2[13].

[12] The transverse symmetry of the laser electric field (in vacuum) is conserved along the laser propagation direction z.

[13] Please note that if $\mathbf{E}_\mathrm{L}$ has either s- or a-symmetry, the modulus of the laser electric field $|\mathbf{E}_\mathrm{L}| = \sqrt{E_{\mathrm{L},x}^2 + E_{\mathrm{L},y}^2 + E_{\mathrm{L},z}^2}$ is always symmetric with respect to $\mathbf{r}_\perp$. Consequently, also the electron density n_0 (and similarly ν_ei, see App. C) is always symmetric with respect to $\mathbf{r}_\perp$.

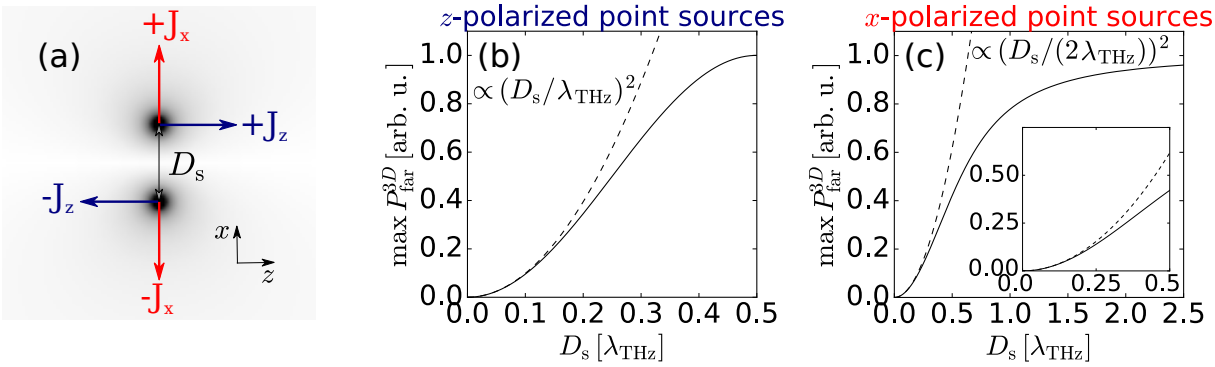

Figure 4.3.2.: (a) Two types of antisymmetric currents with respect to the transverse axis x: transverse antisymmetric currents J_x (red) and longitudinal antisymmetric currents J_z (blue). (b) Maximum of the angularly resolved far-field power spectrum from two longitudinally polarized antisymmetric point-sources that are located according to (a) distance D_s away from each other. The dashed line specifies the function $[2\pi D_\mathrm{s}/\lambda_\mathrm{THz}]^2/4$. (c) The same as in (b) but for a transverse antisymmetric current. The dashed line specifies the function $[2\pi D_\mathrm{s}/(2\lambda_\mathrm{THz})]^2/4$. For transverse currents, the scaling for small D_s is 4 times slower and thus the D_s-axis is extended compared to (b). The inset specifies the behavior for the same D_s-range as in (b). Both far-field spectra are normalized to the maximum of radiation that can be expected for two coherent point-sources, i.e., emitter that are located at the same position and oscillate with the same phase, i.e., in the symmetric case.

Now, the symmetry of $\boldsymbol{\iota}_2$ is determined by Eq. (2.5.17) in Sec. 2.5.2: One can easily show that independently on whether $\mathbf{E}_{\mathrm{L},\perp}$ is symmetric or antisymmetric in $\mathbf{r}_\perp$, the source term ι_2 has the a-symmetry and thus also $\mathbf{J}_2$ has the a-symmetry[14]. This result is true only if $\mathbf{E}_{\mathrm{L},\perp}$ has either the s- or the a-symmetry. If it does not have any of them, i.e. it is the sum of non-zero a- and s-symmetric parts, then $\boldsymbol{\iota}_2$ is in general neither a- nor s-symmetric and thus also $\mathbf{J}_2$ does not have any symmetry.

4.3.1.2. Neglecting the far-field contribution from antisymmetric currents

We have seen previously that transverse currents driven by $\boldsymbol{\iota}_2$ (TC) for a Gaussian laser pulse are antisymmetric in the transverse coordinate $\mathbf{r}_\perp$. In the following, we will see that antisymmetric currents, transverse or longitudinal ones, almost do not emit THz radiation for narrow plasmas. Here, "narrow" means that the thickness of the plasma $D \ll \lambda_\mathrm{THz}$, where $\lambda_\mathrm{THz} = 2\pi c/\omega_\mathrm{THz}$ is the wavelength of the THz emission that we are looking at.

[14]Since $n_1 = -q_\mathrm{e}^{-1} \int \nabla \cdot \mathbf{J}_1 \, dt$ according to Eq. (2.5.15), n_1 is antisymmetric in $\mathbf{r}_\perp$ if $\mathbf{J}_1$ has the s-symmetry and symmetric if $\mathbf{J}_1$ has the a-symmetry. Thus, $n_1\mathbf{E}_1$ has always the a-symmetry independently whether the lowest order fields have the a- or the s-symmetry. For the term $\mathbf{J}_1 \times \mathbf{B}_1$, we find the same result, since for the x-component $(\mathbf{J}_1 \times \mathbf{B}_1)_x = J_{1,y}B_{1,z} - J_{1,z}B_{1,y}$ is always antisymmetric in $\mathbf{r}_\perp$ (analogous for the y-component) and $(\mathbf{J}_1 \times \mathbf{B}_1)_z = J_{1,x}B_{1,y} - J_{1,y}B_{1,x}$ is always symmetric. For the term $\mathbf{J}_1(\nabla \cdot \mathbf{J}_1)$, the same considerations like for $n_1\mathbf{E}_1$ hold and similarly for the 4^th term in Eq. (2.5.17). Since $\mathcal{E}_2$ is symmetric in $\mathbf{r}_\perp$ and following Eq. (2.5.18) also $\mathcal{E}_{2,\mathrm{th}}$ is always symmetric. Because of that, the last source term in Eq. (2.5.17) has the a-symmetry, too.

First, we consider two point sources that are separated by the distance D_s such that[15]

$$\hat{\mathbf{J}}(\mathbf{r},\omega) = J_0 \left[\delta\left(x - \frac{D_\mathrm{s}}{2}, y, z\right) \pm \delta\left(x + \frac{D_\mathrm{s}}{2}, y, z\right)\right] \delta(\omega - \omega_\mathrm{THz}) \mathbf{e}_{x/z}\,, \tag{4.3.1}$$

where J_0 is the amplitude of the current and $\mathbf{e}_{x/z}$ is the unit vector in the x/z-direction. The "+" sign reflects the situation where the currents are symmetric and they are antisymmetric when taking the "-" sign. The two antisymmetric situations are visualized in Fig. 4.3.2(a). Using the results from Sec. (2.6), the far-field power spectrum reads

$$\begin{aligned} P^\mathrm{3D}_\mathrm{far} = \frac{\mu_0\omega^2}{16\pi^2 c|\mathbf{r}|^2}\delta(\omega-\omega_\mathrm{THz}) \left|\mathbf{e}_\mathrm{r}\times\mathbf{e}_{x/z}\right|^2 \Bigg| \exp\left(\mathrm{i}\frac{\omega}{c}\sqrt{\left(x-\frac{D_\mathrm{s}}{2}\right)^2+y^2+z^2}\right) \\ \pm \exp\left(\mathrm{i}\frac{\omega}{c}\sqrt{\left(x+\frac{D_\mathrm{s}}{2}\right)^2+y^2+z^2}\right)\Bigg|^2 \end{aligned} \tag{4.3.2}$$

$$\lesssim \frac{\mu_0\omega^2}{16\pi^2 c|\mathbf{r}|^2}\delta(\omega-\omega_\mathrm{THz}) \begin{cases} 4 & \text{if } + \\ \left(\frac{\omega}{c}D_\mathrm{s}\right)^2 & \text{if } - \end{cases}, \tag{4.3.3}$$

where $\mathbf{e}_\mathrm{r} = \mathbf{r}/|\mathbf{r}|$ is the unit vector normal to the radiation sphere and using Taylor expansions for $D_\mathrm{s}\omega/c \ll 1$. This estimation suggests that antisymmetric currents emit by a factor of $[\lambda_\mathrm{THz}/(\pi D_\mathrm{s})]^2$ weaker than coherently emitting symmetric currents. In Fig. 4.3.2(b) the maximal emission is presented for a z-polarized antisymmetric current evaluating directly Eq. (4.3.2) depending on D_s. The value is normalized to the result for a coherently emitting symmetric source. Indeed, the emission disappears for $D_\mathrm{s} \to 0$ and increases up to 1 when the distance between the sources approaches λ_THz. As presented in Fig. 4.3.2(c), a similar situation is found for an x-polarized antisymmetric source. However, comparing the inset in Fig. 4.3.2(c) with Fig. 4.3.2(b), we find that the emission from transverse antisymmetric currents increases slower with D_s compared to emission from longitudinal antisymmetric currents[16].

In general, for an emitter at $\mathbf{r}'$ in a narrow plasma where

$$\big||\mathbf{r}-\mathbf{r}'| - |\mathbf{r}_\perp + (z-z')\mathbf{e}_z|\big| \le |\mathbf{r}'_\perp| \le D/2 \ll \frac{c}{\omega}\,, \tag{4.3.4}$$

we have for the Green's function in Eq. (2.6.3) by means of the Taylor expansion

$$G^\mathrm{3D}(\mathbf{r}_\perp - \mathbf{r}'_\perp, z-z') \approx G^\mathrm{3D}(\mathbf{r}_\perp + \mathbf{r}'_\perp, z-z') \tag{4.3.5}$$

up to an error $\propto (D\omega/c)^2$. For a current component with $\hat{J}_i(\mathbf{r}'_\perp, z) = -\hat{J}_i(-\mathbf{r}'_\perp, z)$ where $i \in \{x,y,z\}$, we conclude

$$\int\limits_{V_\mathrm{plasma}} \hat{J}_i(\mathbf{r}') G^\mathrm{3D}(\mathbf{r}-\mathbf{r}')\, d^3\mathbf{r}' \approx 0\,, \tag{4.3.6}$$

such that the far field $P^\mathrm{3D}_\mathrm{far}$ vanishes. In 2D geometry, the same argumentation holds when replacing $\mathbf{r}'_\perp \to x'$ and $G^\mathrm{3D} \to G^\mathrm{2D}$.

[15] W.l.o.g., we consider the 3D case here, the 2D case can be treated analogous.

[16] This is because the $|\mathbf{e}_\mathrm{r}\times\mathbf{e}_{x/z}|^2$-term in Eq. (4.3.2) is maximal if $\mathbf{e}_\mathrm{r} = \mathbf{r}/|\mathbf{r}| \perp \mathbf{e}_x$, for example if $\mathbf{e}_\mathrm{r} = \mathbf{e}_y$. However for $\mathbf{r} \perp \mathbf{e}_x$ we have $x = 0$ and the last term in Eq. (4.3.2) is zero such that $P^\mathrm{3D}_\mathrm{far} = 0$ for this emission direction. For a z-polarized current, the $|\mathbf{e}_\mathrm{r}\times\mathbf{e}_{x/z}|^2$-term is also maximal if $\mathbf{e}_\mathrm{r} = \mathbf{e}_y$. But here, also the last term in Eq. (4.3.2) is maximal and thus the maximum of the emission is stronger for a z-polarized antisymmetric current than for an x-polarized antisymmetric current.

The plasmas considered in this chapter are narrow. The electron density profile in Fig. 4.2.2(a) reveals that the plasma is only 1 μm thick, i.e., $2|\mathbf{r}'_\perp| = D_\mathrm{s} \leq D = 1\,\mu$m. In Fig. 4.2.3, we have seen that THz emission is produced for $\omega_\mathrm{THz} \approx 0.02\omega_\mathrm{L}$ and thus for $\lambda_\mathrm{L} = 0.8\,\mu$m we have $\lambda_\mathrm{THz} \approx 40\mu$m. According to previous estimations, antisymmetric currents will radiate $[\lambda_\mathrm{THz}/(\pi D_\mathrm{s})]^2 =$ 162-times weaker than symmetric currents. Thus, for our microplasmas antisymmetric currents are practically not radiating compared to symmetric ones. From the previous section, we know that for $\mathbf{E}_{\mathrm{L},\perp}(-\mathbf{r}_\perp) = \mathbf{E}_{\mathrm{L},\perp}(\mathbf{r}_\perp)$ we have $J_{1,z}(-\mathbf{r}_\perp) = -J_{1,z}(\mathbf{r}_\perp)$ and $\mathbf{J}_{2,\perp}(-\mathbf{r}_\perp) = -\mathbf{J}_{2,\perp}(\mathbf{r}_\perp)$. Thus, for a strongly focused linearly polarized Gaussian laser beam, only transverse currents $\mathbf{J}_{1,\perp}$ contribute to far-field emission via IC mechanism and only longitudinal currents $J_{2,z}$ contribute via TC mechanism. This later mechanism dominated for many-cycle 1C-laser pulses[17].

4.3.2. A simplified model of THz emission

Even if solving the full model up to order ϵ^2 in Sec. 2.5.2, is already much cheaper in terms of computational costs compared to full PIC simulations, it is still too heavy for quick estimations and parameter scans. Therefore, we consider in the following further simplifications for the computation of the THz emission in the far field.

Firstly, we will approximate the source term $\boldsymbol{\iota}_2$ by the ponderomotive source $\boldsymbol{\iota}_2^\mathrm{pond}$. Hereby we neglect three terms in Eq. (D.6): In 1D, the 2$^\mathrm{nd}$ and 3$^\mathrm{rd}$ term have been shown to be much smaller than the ponderomotive source in Sec. 4.1.2. The last summand in Eq. (D.6) is zero since in our particular 2D configuration $\nabla \cdot \mathbf{J}_1 = 0$. As has been shown in Sec. 4.3.1.2, for Gaussian beam profiles and transversely narrow plasmas, only the longitudinal component of the current $J_{2,z}$ contributes to the far-field THz emission. We assume that transverse ponderomotive sources do not couple to radiating longitudinal currents and approximate the longitudinal ponderomotive source term according to App. I by

$$\iota_{2,z}^\mathrm{pond} = -\frac{q_\mathrm{e}^3 n_0 I_\mathrm{L}^\mathrm{2D}(x,z,t)}{2m_\mathrm{e}^2\omega_\mathrm{L}^2\epsilon_0 c}\left\{\left[\frac{z\left(-1+\frac{4\mathbf{r}_\perp^2}{w^2(z)}\right)}{z_\mathrm{R}^2+z^2}+\frac{4\tau}{ct_0^2}\right]\times[1+\cos(2\omega_\mathrm{L}\tau)]+2\frac{\omega_\mathrm{L}}{c}\sin(2\omega_\mathrm{L}\tau)\right\}, \tag{4.3.7}$$

where I_L^2D is the optical intensity (see App. I), $\tau = t - z/c$ and $z_\mathrm{R} = w_0^2\omega_\mathrm{L}/(2c)$.

Secondly, we will not solve the full wave equation (4.2.1) to obtain $\mathbf{E}_2$, but neglect the term proportional to n_0. Then, for the collision-less case ($\nu_\mathrm{ei} = 0$), the simplified equation reads

$$\partial_{tt}\mathbf{E}_2 + \cancel{\frac{q_\mathrm{e}^2 n_0}{m_\mathrm{e}\epsilon_0}\mathbf{E}_2} + c^2\nabla\times\nabla\times\mathbf{E}_2 = -\frac{\boldsymbol{\iota}_2}{\epsilon_0}. \tag{4.3.8}$$

With this approximation, the curl-free part $\mathbf{E}_{2,\mathrm{d}}$ and divergence-free part $\mathbf{E}_{2,\mathrm{r}}$ of the solution $\mathbf{E}_2$ decouple, and we disregard in particular the following three effects:

1. Plasma-frequency oscillations in the curl-free $\mathbf{E}_{2,\mathrm{d}}$ defined by Eq. (4.2.6) are neglected.
2. For the divergence free $\mathbf{E}_{2,\mathrm{r}}$, both dispersion and absorption are neglected.
3. The coupling between $\mathbf{E}_{2,\mathrm{d}}$ and $\mathbf{E}_{2,\mathrm{r}}$ is neglected.

[17] For $\mathbf{E}_{\mathrm{L},\perp}(-\mathbf{r}_\perp) = \mathbf{E}_{\mathrm{L},\perp}(\mathbf{r}_\perp)$ we have $\mathbf{J}_{1,\perp}(-\mathbf{r}_\perp) = -\mathbf{J}_{1,\perp}(\mathbf{r}_\perp)$ and $\mathbf{J}_{2,\perp}(-\mathbf{r}_\perp) = -\mathbf{J}_{2,\perp}(\mathbf{r}_\perp)$. Thus, for antisymmetric laser beams, e.g. for a radially polarized needle beam, only longitudinal currents contribute to far-field emission via IC mechanism and via TC mechanism when the plasma is thin.

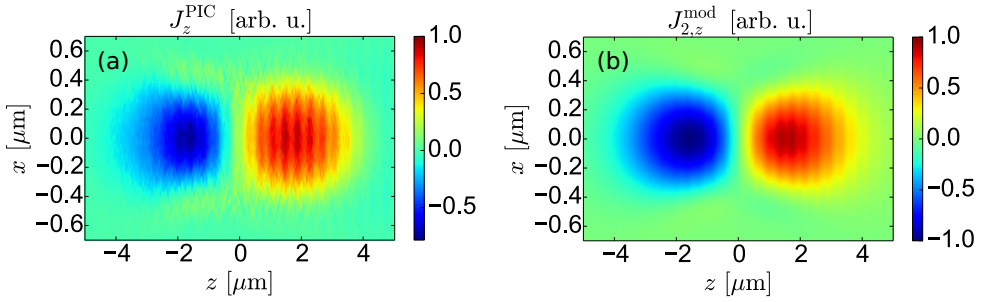

Figure 4.3.3.: Snapshot of the longitudinal current J_z^{PIC} from the PIC simulation (a) and $J_{2,z}^{\mathrm{mod}}$ according to the simplified ϵ^2-model (b), just after the laser pulse has left the focus. The laser pulse parameter are as in Fig. 4.2.2(c,d) $I_{\mathrm{L}}^{(0)} = 4 \cdot 10^{14}$ W/cm^2, $t_0 = 50$ fs, $w_0 = 0.8\,\mu$m. But now $n_{\mathrm{a}} = 7.5 \cdot 10^{17}$ cm^{-3} ($p = 0.028$ bar).

The first point is not problematic for the description of the THz far-field spectra, because such plasma oscillations do not lead to radiation as they are curl-free. The second point is critical and has to be accounted for, in particular for larger and more dense plasmas as we will see below. The third point can be in principle important: The coupling can lead to resonant excitation as in plasma wave-guides, similar to what is frequently exploited in the case of meta-materials [130]. However, as will be shown in Sec. 5.4.5, for smallest microplasmas longitudinal excitations do not provide those effects.

It is interesting to note that using Eq. (4.3.8) instead of Eq. (4.2.1) is equivalent to solving the simplified current equation $\partial_t \mathbf{J}_2 = \boldsymbol{\iota}_2$, or

$$\partial_t \mathbf{J}_2 + \nu_{\mathrm{ei}} \mathbf{J}_2 = \boldsymbol{\iota}_2 \,, \tag{4.3.9}$$

when taking into account collisions. In this light, the approximation is not exactly new and has already been applied for the current $\mathbf{J}_1$ and the IC mechanism [57, 75, 88]. By using Eq. (4.3.9), we can easily compute the current $\mathbf{J}_2$ from $\boldsymbol{\iota}_2$, and then $\mathbf{B}_2$ in the far field following the results from Sec. 2.6 [Eq. (2.6.4), (2.6.6) and G^{2D} from Eq. (2.6.11)].

To crosscheck this model, we compare the longitudinal current $J_{2,z}$ from the simplified model with the current J_z^{PIC} from a PIC simulation. Since our model does not account for the non-radiating plasma oscillation, here we choose a lower gas pressure $p = 0.028$ bar. Then, the gas is fully singly ionized in focus, same as for the previously discussed example with the higher pressure. This results in the plasma oscillation period $t_{\mathrm{p}} = 2\pi/\omega_{\mathrm{p}} = 129$ fs, i.e., sufficiently longer than the laser pulse duration. Thus, we can observe the longitudinal current just before the plasma starts to evolve at the local plasma frequency. The resulting longitudinal currents are compared in Fig. 4.3.3 showing a good agreement between the model and the PIC simulation. It is interesting to note the antisymmetry with respect to z: According to our model, $J_{2,z}$ is just an integral of $\iota_{2,z}^{\mathrm{pond}}$ over time. By looking at the approximation for the longitudinal ponderomotive source $\iota_{2,z}^{\mathrm{pond}}$ in Eq. (4.3.7), we find that the only antisymmetric term is the one $\propto z/(z_{\mathrm{R}}^2 + z^2)$. It has its extrema of $\pm 1/(2z_{\mathrm{R}})$ for $z = \pm z_{\mathrm{R}} = \pm 2.5\,\mu$m, in agreement with our observations of the extrema in Fig. 4.3.3[18]. This term is the result of the strong focusing since it is important for $1/z_{\mathrm{R}} = 1/2.5\,\mu\mathrm{m} > 1/ct_0 = 1/15\,\mu$m. Otherwise, in weaker focusing geometry, the term $\propto 4\tau/(ct_0^2)$ which is the analog of the longitudinal ponderomotive force in 1D according to Sec. 4.1.2 becomes dominant. In the following, we concentrate again on higher gas pressures.

[18] There, the extrema are slightly shifted towards $z = 0$ in particular because of the product with n_0.

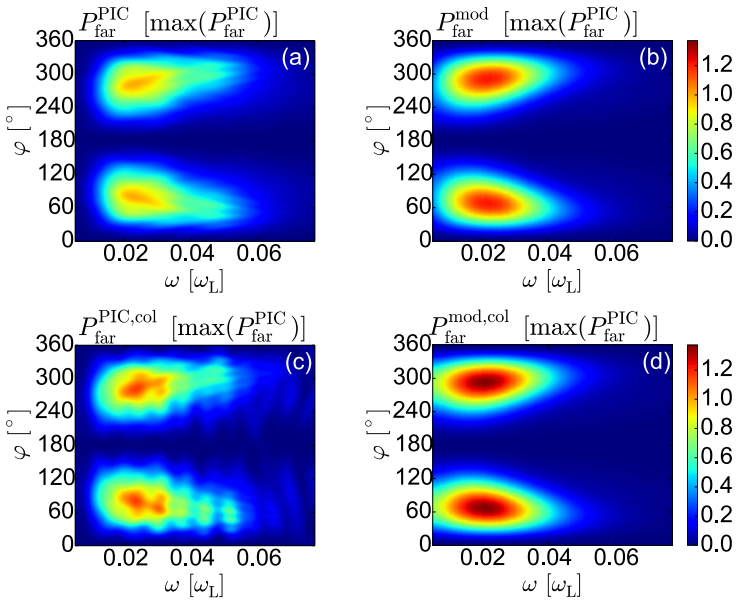

Figure 4.3.4.: Far field THz power spectra as a function of frequency ω_{THz} and detection angle φ for the laser pulse of Figs. 4.2.2, 4.2.3 and 4.3.1. In (a) the result of the PIC simulation and in (b) those of the simplified model (see text) are presented. In (c) and (d) analogous results accounting for collisions are shown. The color scale allows for quantitative comparison of the amplitudes, which are normalized to $\max(P^{\mathrm{PIC}}_{\mathrm{far}})$.

Before confronting the modeled far-field emission with PIC results, we have to take the second point above into account, namely the incorrect treatment of THz dispersion. For frequencies below the plasma frequency ω_{p} the plasma becomes opaque. For given ω_{p} and ν_{ei}, it is possible to compute the penetration depth of the electromagnetic field as

$$s_{\mathrm{p}} = \frac{c}{2\omega_{\mathrm{THz}}} \Im \left\{ \sqrt{\frac{\omega_{\mathrm{THz}}^2 + \mathrm{i}\nu_{\mathrm{ei}}\omega_{\mathrm{THz}}}{\omega_{\mathrm{THz}}^2 + \mathrm{i}\nu_{\mathrm{ei}}\omega_{\mathrm{THz}} - \omega_{\mathrm{p}}^2}} \right\} , \tag{4.3.10}$$

where the symbol $\Im$ denotes the imaginary part of a complex quantity. For singly ionized argon gas, the penetration depth s_{p} is about 0.5 µm for $\omega_{\mathrm{THz}} \approx 0.02\omega_{\mathrm{L}} \ll 0.13\omega_{\mathrm{L}} \approx \omega_{\mathrm{p}}$. This is about half the thickness of the plasma in the example of Fig. 4.2.2(a). For driving pulse configurations which produce larger plasmas or cause multiple ionization, the penetration depth may become significantly smaller than the plasma width. Then, the plasma emits mainly from a thin layer at its surface, where radiation at frequencies below ω_{p} can still exit due to optical tunneling. The frequency dependent thickness of this layer is related to the penetration depth in Eq. (4.3.10). In order to mimic this effect in our simplified model, we do not take into account contributions from the whole plasma when calculating the far field THz power spectrum as described above. Instead, we only take contributions from the current density $\mathbf{J}_2$ in a thin layer at the plasma surface, i.e., from positions $\mathbf{r}$ and frequencies ω_{THZ} with distance to the transparent outer area less than $1.2s_{\mathrm{p}}$. The empirical factor 1.2 was chosen by equaling the THz pulse energy obtained with model and PIC simulation in Fig. 4.3.4, and is kept constant for the rest of the chapter. Of course, this approach implies a strong simplification of the situation, however, as we will see below, it leads to reasonable agreement with PIC simulations with respect to the spectral and angular distribution of the THz emission.

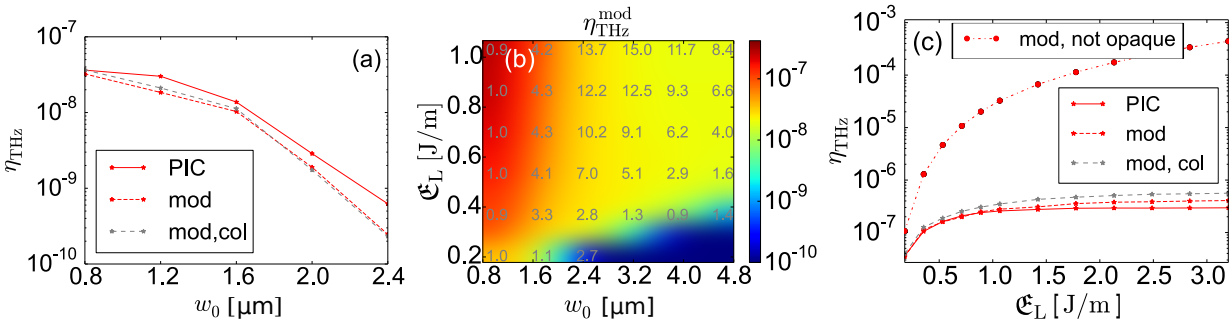

Figure 4.3.5.: Scaling of the conversion efficiency η_{THz} with focal spot-size and pulse energy, for fixed laser wavelength $\lambda_{\mathrm{L}} = 0.8\,\mu\mathrm{m}$, pulse duration $t_0 = 50\,\mathrm{fs}$ and argon gas density $n_{\mathrm{a}} = 3 \times 10^{19}\,\mathrm{cm}^{-3}$. In (a), PIC results (solid dark red line) and the simplified model (dashed dark red line) for a laser pulse energy of $\mathfrak{E}_{\mathrm{L}} = 0.18\,\mathrm{J/m}$ are shown. The dashed light gray line shows model results accounting for collisions. In (b), the model is evaluated in the $(w_0, \mathfrak{E}_{\mathrm{L}})$-plane. Ratios of PIC and model conversion efficiencies are indicated in gray. In (c), η_{THz} as a function of the pulse energy is shown for tight focusing ($w_0 = 0.8\,\mu\mathrm{m}$). Results from PIC simulations and the simplified model with and without collision are in good agreement. The dashed-dotted dark red line shows model results when the opaqueness of the plasma is ignored (see text).

In Fig. 4.3.4(a), we present the angle resolved far field power spectrum $P_{\mathrm{far}}^{\mathrm{PIC}}$ for the PIC simulation of Figs. 4.2.2, 4.2.3 and 4.3.1. The exact definition is provided in Sec. 2.6. For comparison, Fig. 4.3.4(b) shows the power spectrum $P_{\mathrm{far}}^{\mathrm{mod}}$ obtained from our simplified model. We find good qualitative and even quantitative agreement, both spectra feature a broad peak around $0.022\omega_{\mathrm{L}}$ (i.e., 8.24 THz). Simulation and simplified model predict the strongest radiation under an angle of $\varphi \approx 70°$ with respect to the optical axis. Because the length of the plasma is about 10 µm only, THz emission due to the TC mechanism is expected at such large angles (cf. [60, 59] and Sec. 5.2.1). Comparing the power spectrum $P_{\mathrm{far}}^{\mathrm{PIC}}$ with results from PIC simulation accounting for collisions, as shown in Fig. 4.3.4(c), confirms that collisions are of minor importance for the THz emission.

4.3.3. Scaling with the laser pulse energy and the focusing conditions

Let us finally discuss scaling properties of the THz conversion efficiency $\eta_{\mathrm{THz}} = \mathfrak{E}_{\mathrm{THz}}/\mathfrak{E}_{\mathrm{L}}$ where $\mathfrak{E}_{\mathrm{L}}$ is the THz pulse energy density in 2D (see Sec. (2.6) for details) containing frequencies below $0.2\omega_{\mathrm{L}}$ (75 THz) and $\mathfrak{E}_{\mathrm{L}}$ is the energy density of the incoming laser pulse. In the following, we will use the term "energy" also in the 2D case for the sake of readability, even if we mean "energy density". Moreover, we fix the laser wavelength $\lambda_{\mathrm{L}} = 0.8$ µm, pulse duration $t_0 = 50\,\mathrm{fs}$ and neutral argon gas density $n_{\mathrm{a}} = 3 \times 10^{19}\,\mathrm{cm}^{-3}$.

The conversion efficiency η_{THz} for $\mathfrak{E}_{\mathrm{L}} = 0.18\,\mathrm{J/m}$ as a function of the focal beam width w_0 is presented in Fig. 4.3.5(a). The simplified model is in good agreement with the PIC simulations. It turns out that strong focusing leads to the highest conversion efficiency η_{THz} for the chosen pulse energy. Strong focusing is also preferable for higher pulse energies as shown by the $(w_0, \mathfrak{E}_{\mathrm{L}})$-parameter scan in Fig. 4.3.5(b). The results of the parameter scan are presented for the model. The ratio between the PIC and the model conversion efficiencies is indicated by the gray numbers, showing reasonable agreement within one order of magnitude.

For all focusing conditions in Fig. 4.3.5(b), the conversion efficiency η_{THz} first increases with the driving laser pulse energy, and then saturates for higher energies around $10^{-6} - 10^{-7}$. This behavior, which translates into linear growth of the THz energy with the laser energy, is a direct consequence of the opaqueness of the plasma for THz radiation. Figure 4.3.5(c) shows a line-out of Fig. 4.3.5(b) for tight focusing ($w_0 = 0.8\,\mu\mathrm{m}$) and corroborates this statement. Both PIC results (solid red line) and model (dashed red line) are in good agreement. The red circle symbols correspond to results from our simplified model when the opaqueness of the plasma is ignored, i.e., the current density $\mathbf{J}_2$ in the whole plasma volume is taken into account. In particular for larger pulse energies, where the plasma is much wider than the penetration depth s_{p}, conversion efficiencies are overestimated by several orders of magnitude. This clearly shows that it is crucial to take the opacity of the plasma into account when the plasma width exceeds the penetration depth.

4.4. DC-biased microplasmas

As has been shown in Sec. 4.3.3, the laser-to-THz conversion efficiency η_{THz} for smallest microplasmas is slightly above 10^{-8} and saturates with the laser pulse energy to around 10^{-6}. Applying a constant electric field $\mathbf{E}_{\mathrm{s}}$ (DC-bias or bias field) to the gas-plasma increased η_{THz} in filaments [64] as well as in mJ-laser driven gas-plasmas [65] (cf. Sec. 1.3.2). Hereby, in addition to the laser pulse the DC-bias itself drives the electrons leading to a THz emitting free-electron current. In this section, we explore the THz emission originating from the DC bias applied to 1C-laser-induced microplasmas.

To model a gas-plasma in a constant electric field, two different models have been proposed. In [68], the THz emitting current $\mathbf{J}$ has been suggested to be computed from $\partial_t \mathbf{J} = q_{\mathrm{e}}^2 n_{\mathrm{e}}/m_{\mathrm{e}}\mathbf{E}_{\mathrm{s}}$ in analogy to the IC current ([57], cf. Sec. 1.3.3). Then, the electrons are treated as test particles. However, for DC-biased gas-plasmas, this proceeding leads to a catastrophic failure: after the ionization, i.e., when n_{e} is constant in time, the current $\mathbf{J}$ grows to infinity. Descriptively, the constant electric field would continue to accelerate the electrons forever.

This problem is resolved by the model that was proposed in [64] (cf. Sec. 1.3.2). First, it assumes a translational invariant system perpendicular to the bias field. Employing the Amperes law (2.3.4), this allows to compute the current $\mathbf{J}$ consistently with the electric field by $\mathbf{J} = -\epsilon_0 \partial_t \mathbf{E}$. Second, the current is assumed to be driven by the electric field such that $\partial_t \mathbf{J} = q_{\mathrm{e}}^2 n_{\mathrm{e}}/m_{\mathrm{e}}\mathbf{E}$. Third, it assumes that $\mathbf{E} = \mathbf{E}_{\mathrm{s}}$ for $t < 0$, and then at $t = 0$ free electrons are created by ionization such that $\mathbf{E}$ evolves in time and for $t > 0$ in general $\mathbf{E} \neq \mathbf{E}_{\mathrm{s}}$. This results in an electric field $\propto \cos(\omega_{\mathrm{p}} t)$ and current $\propto \sin(\omega_{\mathrm{p}} t)$ that oscillate at the plasma frequency ω_{p} (cf. Sec. 2.5.4.2). Accounting for collisions, this oscillation would be damped to zero, resulting in a field free region inside the plasma, i.e., the external electric field is screened by the electrons. However, since the system is assumed to be translational invariant normal to the oscillating current, no radiation emission can be described by this model. The attempt to truncate the current by assuming it to have a particular shape results in an unphysical overestimation of the THz emission at the plasma frequency as discussed in Sec. 4.2. Thus, we should account for the plasma shape and the current that is driven by a self-consistent electric field within a single framework.

This can be done by solving the lowest order set of equations that is presented in Sec. 2.5.1. Here, the total electric field $\mathbf{E}_1$ including the external electric field $\mathbf{E}_{\mathrm{s}}$ excites the electron current $\mathbf{J}_1$. The displacement of the electrons creates the charge $\rho_1 = \epsilon_0 \nabla \cdot \mathbf{E}_1$ and thus a restoring electric field screens $\mathbf{E}_{\mathrm{s}}$. Besides charge separation, the current $\mathbf{J}_1$ leads also to THz emission since we do not assume the system to be translational invariant normal to $\mathbf{E}_{\mathrm{s}}$.

As we have seen in the previous section, already 1C-fs-laser-induced microplasmas without an external electric field lead to THz emission. There, the current $\mathbf{J}_2$ is excited mainly by ponderomotive forces that are included in the 2$^{\text{nd}}$ order set of equations in Sec. 2.5.2. The total current is just the sum $\mathbf{J}_1+\mathbf{J}_2$ of currents from both effects (and similarly for other fields). In this section, the effect of the bias-field described by the IC mechanism is considered separately from the TC mechanism including the ponderomotive effects. This is a particular advantage of the multiple scale expansion that separates different effects. To solve the IC-mechanism-describing lowest order set of equations in Sec. 2.5.1, we use the code ARCTIC[19] (cf. Sec. 3.2).

Firstly, we consider the influence of the bias-field polarization: Initially proposed set-ups envisaged an excitation by a transverse bias-field. However, the orientation of $\mathbf{E}_\text{s}$ can be adjusted to be longitudinal [131] or even helical [68]. In Sec. 4.4.1, we consider the transverse and longitudinal variant and compare them with respect to efficiency, emission patterns and spectral properties for smallest microplasmas. Secondly, the scaling properties of the conversion efficiency are considered: the gas pressure dependence of η_THz is investigated and the possibility to increase the bias-voltage for high gas-pressures is exploited. Through this section, we also comment on the role of the screening and the validity of the lowest order multiple scale expansion (cf. Sec. 2.5) which is used for the description of the DC-biased fs-laser-induced microplasma.

In the following we restrict again to the 2D case with translational invariance in y. Through the section the same Gaussian y-polarized laser pulse with $t_0 = 50\,\text{fs}$, $I_\text{max} = 4\times10^{14}\,\text{W/cm}^2$ and $w_0 = 0.8\,\mu\text{m}$ is considered as in the largest part of Sec. 4.3. The gas is argon and by default the initial atom density is $n_\text{a} = 3\times10^{19}\,\text{cm}^{-3}$ ($p\approx1$ bar).

4.4.1. DC-bias polarization dependence

Let us consider a microplasma exposed by a longitudinal bias-field first, i.e., the excitation of the low-frequency current takes place in the z-direction. In this sense, the reaction of the gas-plasma to the excitation is expected to behave similarly to what we have seen from excitation by longitudinal ponderomotive forces in Sec. 4.3. And indeed, the snapshot of the magnetic field $B_{1,y}$ at time 100 fs after the laser pulse has left the focus displayed in Fig. 4.4.1(a) reveals THz waves emitted almost normal to the laser propagation direction z. The resulting THz far-field spectrum normal to the laser propagation direction in Fig. 4.4.1(c) is peaked at 5 THz and does not have any signature at the plasma frequency, that is around 49 THz for the considered gas-plasma in focus. This behavior is very similar to what has been observed in Fig. 4.2.3 for the same 1C-fs-laser-induced microplasma without an external bias[20]. As the focal electric field time trace in Fig. 4.4.1(e) shows, the external bias field of 30 kV/cm is screened rapidly as expected [64]. Contrary to what is expected from [64], almost no oscillation at the plasma frequency are present in focus. However, the oscillations of the electric field at the local plasma frequency are strong where the electron density gradient is large as can be seen in Fig. 4.4.2(a,b,c). The snapshots of the longitudinal and transverse electric fields in Fig. 4.4.2(a,b) reveal a spatial modulation pattern qualitatively similar to what has been presented for the un-biased microplasma in Fig. 4.2.2(c): Since the electric fields and currents oscillate at the local plasma frequency,

[19] The equations had to be slightly modified to include an external bias-field into ARCTIC. To this end, we substitute $\check{\mathbf{E}}_1 = \mathbf{E}_1 - \mathbf{E}_\text{s}$, $\check{\mathbf{B}}_1 = \mathbf{B}_1$, $\check{\mathbf{J}}_1 = \mathbf{J}_1$. Now, the ionization rate $W[|\mathbf{E}_1|]$, the current driving term in Eq. (2.5.11), and energy equation (2.5.12) are computed by setting $\mathbf{E}_1 = \check{\mathbf{E}}_1 + \mathbf{E}_\text{s}$. Since the static electric field is a solution of the vacuum Maxwell's equations, we can solve the Maxwell's equations simply by substituting $\mathbf{E}_1 \to \check{\mathbf{E}}_1$, $\mathbf{B}_1 \to \check{\mathbf{B}}_1$, $\mathbf{J}_1 \to \check{\mathbf{J}}_1$.

[20] Moreover, as can be seen in Fig. 4.4.1(a), a relatively strong magnetic field is present around the plasma (small blue oval). This magnetic field is magneto-static or more precise quasi-magneto-static since we consider collisions that damp out the current and thus slowly decrease the magnetic field. A similar magneto-static field has been already observed in the same 1C-fs-laser-induced microplasma without an external bias in Fig. 4.2.2(e).

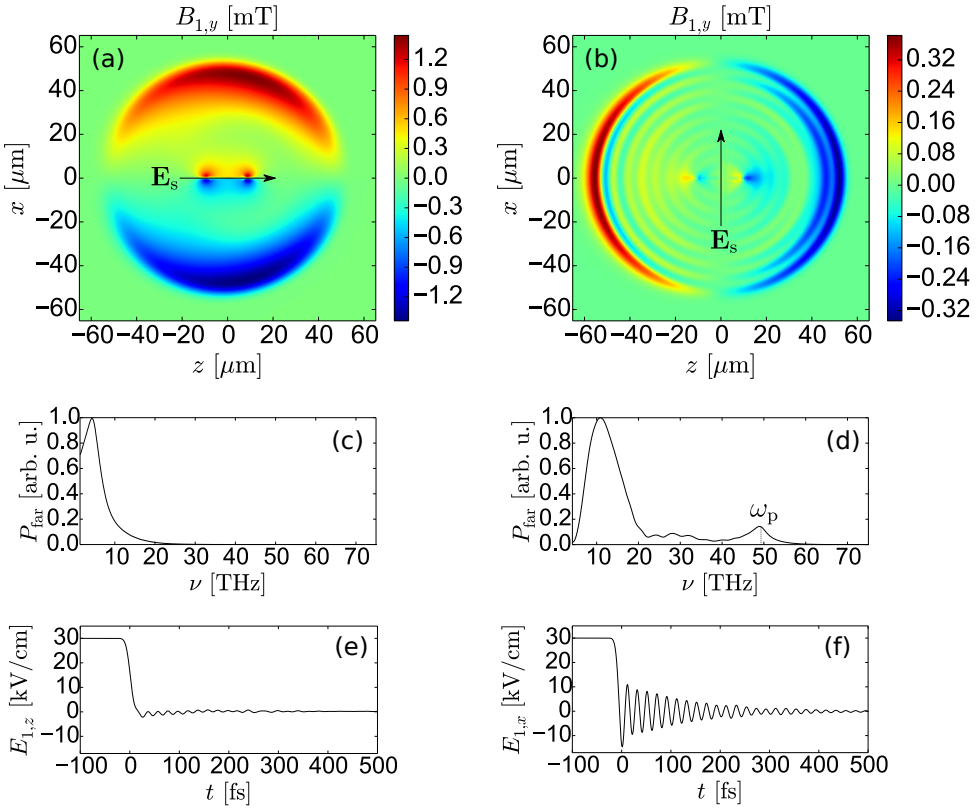

Figure 4.4.1.: DC-biased argon gas with initial neutral density $n_a = 3 \times 10^{19}\,\mathrm{cm}^{-3}$ ($p \approx 1$ bar). The driving Gaussian laser pulse is y-polarized with $t_0 = 50\,\mathrm{fs}$, $I_{max} = 4 \times 10^{14}\,\mathrm{W/cm}^2$ and $w_0 = 0.8\,\mu\mathrm{m}$. The snapshots of the magnetic field $B_{1,y}$ around the DC-biased laser-induced microplasma (blue oval) 150 fs after the laser pulse has left the focus at $z = 0$ are presented in (a-b). The constant electric field is z-polarized in (a) and x-polarized in (b) with the modulus $|\mathbf{E}_s| = 30$ kV/cm. The far-field spectrum at $\mathbf{r} = (0.5, 0, 0)^T$ mm corresponding to the snapshot in (a) is presented in (c). The far-field spectrum at $\mathbf{r} = (0, 0, 0.5)^T$ mm corresponding to the snapshot in (b) is presented in (d). A time trace of the electric field in the polarization direction of the DC field in focus is presented in (e) corresponding to figures (a,c) and in (f) corresponding to (b,d). The system is assumed to be translational invariant in y ($\partial_y \equiv 0$). The computations were performed with ARCTIC (see Sec. 3.2) and the resolution $\delta x = 32$ nm$= \delta z$ and $\delta t = 75$ as.

the oscillations get off-phase to each other shaping this characteristic field pattern. Albeit the presence of these oscillations, no THz emission is observed at the local plasma frequency for a longitudinal DC-bias.

Now, we consider a transverse external bias-field as it has been applied for example in [64]. According to Fig. 4.4.1(b), THz waves are mostly emitted along z. Compared to the previous case, the field amplitude decreased by around a factor 4. The far-field spectrum in the laser propagation direction in Fig. 4.4.1(d) is now significantly broadened and has besides a low-frequency peak at 10 THz a peak around the focal plasma frequency $\nu_p = 49$ THz. Such a double peak structure has been already observed in the very first experimental work [70], even if for a different set-up. Also the screening dynamics change: Now in agreement to [64],

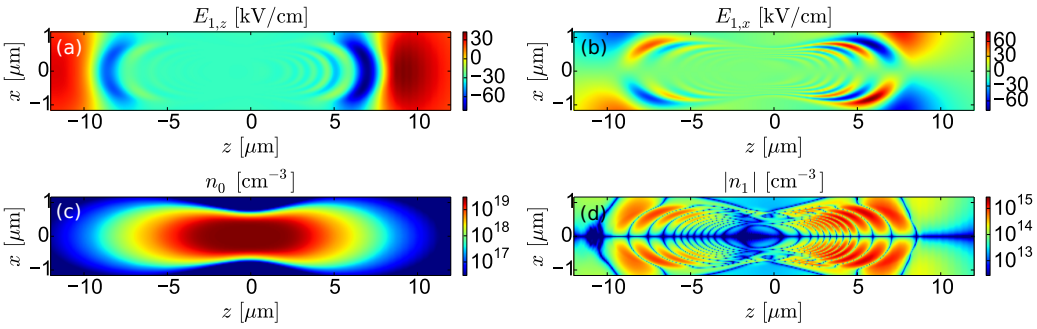

Figure 4.4.2.: Snapshots of the electric field $E_{1,z}$ (a), $E_{1,x}$ (b) as well as the electron densities n_0 (c) and n_1 (d) 100 fs after the laser pulse has passed through the focus. The laser and gas parameter are the same as in Fig. 4.4.1(a).

strong oscillations at the local plasma frequency are visible even in focus [see Fig. 4.4.1(f)]. They disappear mostly due to the damping of the current, i.e., the oscillations at the plasma frequency are partially non-radiative for a transverse DC-bias.

This difference in the spectral emission properties is also found for two-color fs-laser-induced microplasmas in Chap. 5, in particular in full 3D configurations. We interpret them in Sec. 5.4 by a simple plasmonic model.

Before investigating the conversion efficiencies from DC-biased microplasmas, a comment on the validity of the multiple scale expansion that is the base for our investigation is in order. Throughout this section, the lowest order of the multiple scale expansion in Sec. 2.5.1 is exploited. According to Sec. 2.5.4, we have to ensure that the lowest order quantities are large compared to the quantities at the next higher order. This should be in particular true for the electron densities n_0 and $n_1 = \rho_1/q_e = \epsilon_0/q_e \nabla \cdot \mathbf{E}_1$. Here, n_1 can be identified as the displaced electron density, in particular due to the external electric field. Figs. 4.4.2(c-d) compare the electron densities for the configuration in Fig. 4.4.1(a) 100 fs after the laser pulse has left the focus. The colorbar reveals that n_1 is almost 4 orders of magnitude smaller than n_0 justifying the validity of the multiple scale expansion.

In summary, we have seen that the orientation of the current with respect to the plasma shape can have a dramatic impact on the THz radiation properties. A longitudinal DC-bias creates conical emission at large opening angles. A transverse DC-bias leads to forward and backward THz radiations. The microplasma acts almost like a point source of THz emission. The THz pulse energy from the longitudinal excitation is more that 10-times larger than from the transverse excitation. The transverse excitation leads to a spectral broadening up to the focal plasma frequency. Thus DC-biased microplasmas can emit THz radiation with a controllable directionality and spectrum.

4.4.2. Scaling with gas pressure and bias-voltage

Unfortunately, the laser-to-THz conversion efficiency due to the DC-bias in the previously investigated microplasma is below 10^{-8}. Thus, in contrast to the DC-biased filaments [64] or mJ-laser driven gas-plasmas [56], no substantial enhancement of the conversion efficiency can be reported for microplasmas at ambient pressure. However, we can exploit the idea from [65] to increase the bias voltage at high gas pressures since high gas pressures are necessary to increase the threshold for high voltage arcing between the electrodes (cf. Sec. 1.3.2).

To this end, we concentrate on the set-up from Fig. 4.4.1(a) with a longitudinal bias-field. The red stars in Fig. 4.4.3(a) represent the gas-pressure-dependent conversion efficiency obtained

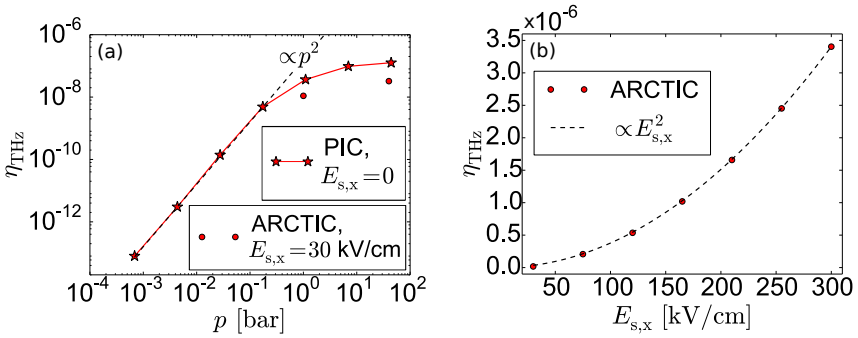

Figure 4.4.3.: (a) Laser-to-THz conversion efficiency from PIC simulations (stars) as a function of the argon-gas pressure p for the laser pulse of Fig. 4.4.1(a) without DC bias. In addition, the dashed line specifies the $\propto p^2$ scaling that one expects when neglecting the opacity of the plasma. For the same laser pulse, the circles specify the conversion efficiencies for $p = 1$ bar and $p = 40$ bar from the DC bias field $E_{s,x} = 30$ kV/cm only, i.e. without ponderomotive excitation, obtained from the fluid code ARCTIC. (b) Conversion efficiency for the same laser pulse and $p = 40$ bar for different bias-fields. The dashed line specifies the quadratic fit.

from PIC simulations with CALDER [110] without an external bias field. For low gas pressures we observe a quadratic increase of η_{THz}. The same dependence has been found in [55] experimentally for low gas pressures. This is in agreement with the simplified model in Sec. 4.3.2 where the THz emitting current is proportional to the electron density n_0 so far the opacity of the plasma is negligible. The two red circles in Fig. 4.4.3(a) specify the conversion efficiency originating from the additional DC-bias field $E_{s,z} = 30$ kV/cm computed by the fluid code ARCTIC. It turns out that the effect of the DC-bias is smaller than the ponderomotive effects for this bias field. Moreover, same as found experimentally in [65], increasing the gas-pressure from 1 bar to 40 bar does not lead to a substantial enhancement for the contribution of the ponderomotive sources (stars) as well as the DC-bias (circles). Besides plasma opacity for THz frequencies, the reason of the saturation is laser defocusing which results in lower electric field amplitudes and electron densities. Fig. 4.4.4(c) presents the electron density profile after the ionization of the gas for $p = 40$ bar. The plasma profile is strongly deformed compared to Fig. 4.4.2(c) where $p \approx 1$ bar. The peak electron density increases only by a factor of 10 instead of 40.

Increasing the gas pressure does not enhance the laser-to-THz conversion efficiency substantially, but it permits to use higher bias voltages. Similarly to [65], we increase the bias voltage to 300 kV/cm for $p = 40$ bar. The resulting conversion efficiency is presented in Fig. 4.4.3(b). We find in agreement with published experiments a quadratic increase. For the highest bias-voltage we obtain $\eta_{THz} \approx 3.5 \cdot 10^{-6}$. This is an enhancement by almost 2 orders of magnitude compared to unbiased microplasmas.

Before concluding on 1C-fs-laser-induced microplasmas, we again validate the multiple scale expansion. Previously, for $p = 1$ bar and $E_{s,z} = 30$ kV/cm, we obtained $n_0 \sim 10^{-4} n_1$. One might expect that an increase of the bias-field $E_{s,z}$ by a factor 10 would degrade the validity by the same factor. However, as Fig. 4.4.4 shows we still obtain $n_0 \sim (10^{-4} - 10^{-3}) n_1$. As suggested in Sec. 2.5.4.2, the ratio between n_0 and n_1 scales predominantly with $\propto E_{s,z}/\sqrt{n_0}$. Thus an increase of the bias-field by a factor of 10 and an additional increase of the electron density by a factor about 10, increases the ratio between n_0 and n_1 only by a factor about 3.2. In this light, it is reasonable that albeit the increased bias voltage the validity of the multiple-scale expansion is almost not affected since we also increased the gas pressure.

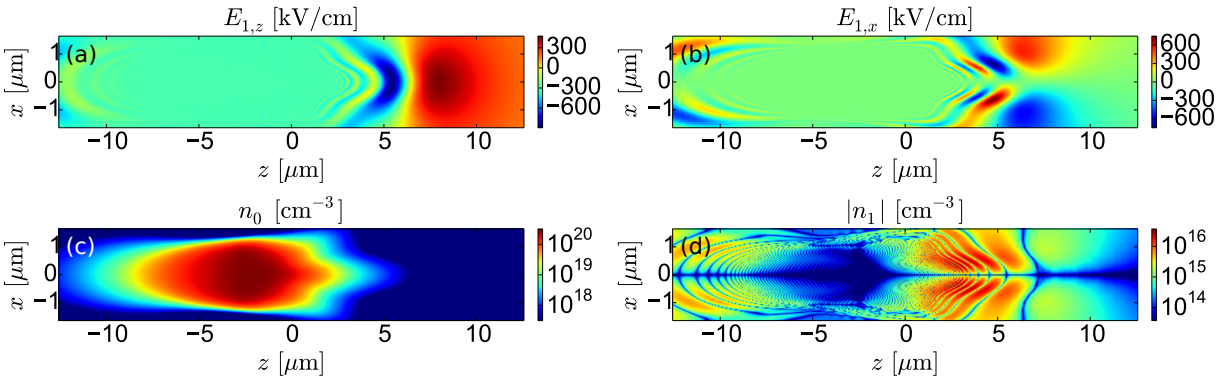

Figure 4.4.4.: Snapshots of the electric field $E_{1,z}$ (a), $E_{1,x}$ (b) as well as the electron densities n_0 (c) and n_1 (d) 100 fs after the laser pulse has passed through the focus. The laser parameter are the same as in Fig. 4.4.1(a). But now, $n_a = 120 \times 10^{19}\,\mathrm{cm}^{-3}$ ($p \approx 40$ bar) and $|\mathbf{E}_s| = 300$ kV/cm.

4.5. Conclusions

For single-color driving pulses in gases at ambient pressure, as used, e.g., in [61], the TC mechanisms is dominant for sufficiently long (50 fs) multi-cycle pulses. The ponderomotive excitation dominates radiation pressure and other convective and diffusive sources. Strong plasma oscillations are excited at the plasma frequency, which are damped due to collisions.

Angularly-resolved far-field spectra confirm the angular THz emission characteristics for the TC mechanism as proposed in [60]. In particular, for microplasmas the THz radiation is predominantly emitted at large angles $> 70°$, as also observed in [61]. The origin of the emission are longitudinal currents. Transverse currents are excited, but do not emit THz radiation due to their antisymmetry with respect to the transverse coordinate and the small transverse size of the microplasma compared to the large THz emission wavelengths.

However, the frequency dependence of the far field power spectra according to the model derived in [60] is not correct: Oscillations at the plasma frequency are present in the microplasma but do not contribute to the far field emission spectrum. This behavior has been analyzed, showing that 1D modeling of the plasma currents is not sufficient to predict correct THz emission spectra. The PIC simulations and model show that for a 50-fs-long single-color laser pulse the THz spectra can cover the frequency range up to 20 THz that is far below the plasma frequency about 50 THz for a fully singly ionized gas am ambient pressure.

The investigation of the THz conversion efficiency suggests that, for low-energy pulses strong focusing is advantageous. Conversion efficiencies of $10^{-6} - 10^{-7}$ have been observed in PIC simulations as well as in our simplified model. For higher laser energies, the conversion efficiency saturates to 10^{-6}, and the THz energy increases linearly with the pump energy. This saturation is intimately linked to the opacity of the plasma at THz frequencies: For higher laser pulse energies, the plasma volume becomes larger and radiates from a thin layer at its surface mostly.

THz radiation from DC-biased single-color fs-laser-induced microplasmas has been shown to be spectrally tunable with a controllable directionality of the THz emission by adjusting the polarization of the static electric field. Same as for un-biased fs-laser-induced microplasmas, longitudinal currents emit far below the plasma frequency, whereas symmetric transverse currents radiate broadband THz emission up to 50 THz. The laser-to-THz conversion efficiency was boosted by 2 orders of magnitude by increasing the bias voltage at high gas pressures such that already for smallest microplasmas efficiencies above 10^{-6} have been obtained.

5. Two-color fs-laser-induced microplasmas

Contents

In Chap. 4, THz radiation from single-color (1C) fs-laser-induced microplasmas has been discussed. In this case, THz emission is produced by longitudinal low-frequency currents driven mainly by the ponderomotive force. The laser-to-THz conversion efficiency for μJ-driving laser pulses has been shown to saturate, even for increasing pulse energies, to around 10^{-6}. DC-biased microplasmas could increase the conversion efficiency beyond 10^{-6}, but only when increasing the bias field that is limited due to high voltage arcing. Moreover, for 50-fs-long laser pulses the emission from unbiased gas-plasmas could range only up to about 15 THz, i.e., not sufficiently broad to cover the whole THz range.

To overcome these limitations, we investigate in this chapter the potential of the ionization current mechanism (IC) in microplasmas. Here, the THz emission is driven by two-color (2C) laser pulses. Effective THz emission by the IC mechanism requires a temporal asymmetry in the driving laser field that can be achieved in a straightforward manner by admixing the second harmonic (SH) to the fundamental harmonic (FH) frequency of the laser pulse [57][1]. This configuration has not been explored experimentally for microplasmas up to date. However, as has been shown in Sec. 1.3.3, it has been already used for larger plasmas to produce broadband THz emission with laser-to-THz conversion efficiencies η_{THz} beyond 10^{-4}.

The major goals of the chapter are to estimate the potential of the IC mechanism in microplasmas, in particular, the scalability of the laser-to-THz conversion efficiency η_{THz} and the

[1] As has been shown in Fig. 2.2.1(c,g,k), the THz yield $Y^{\mathrm{IC}}_{\mathrm{THz}}$, defined as the power in the excitation source $\iota_1 = \iota_{\mathrm{IC}}$ below 60 THz, is almost zero without a fraction of energy in the SH, i.e., the SH field is crucial.

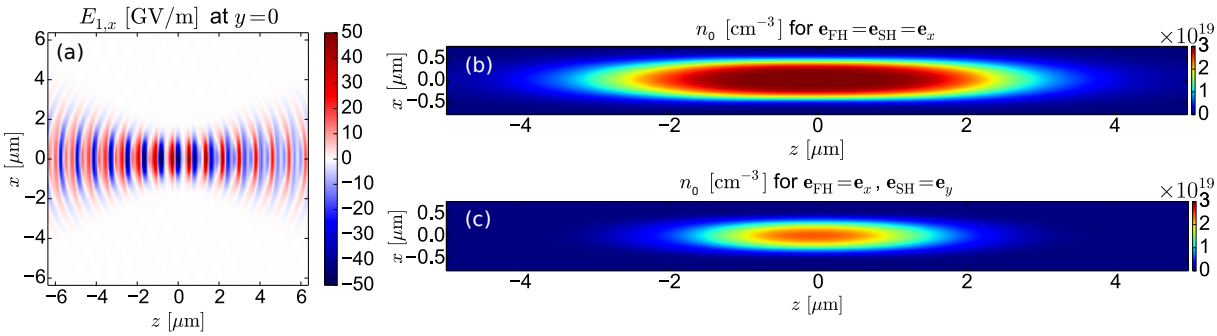

Figure 5.1.1.: Two-color 0.17-μJ Gaussian laser pulse [$E_\omega = 40$ GV/m, $E_{2\omega} = 20$ GV/m, $t_0 = 50$ fs, $\mathbf{e}_{\rm FH} = \mathbf{e}_{\rm SH} = \mathbf{e}_x$ in (a,b) and $\mathbf{e}_{\rm FH} = \mathbf{e}_x$, $\mathbf{e}_{\rm SH} = \mathbf{e}_y$ in (c)] focused down to $w_0 = \lambda_{\rm FH} = 0.8$ μm in argon with initial neutral density $n_{\rm a} = 3 \cdot 10^{19}$ cm^{-3}. (a) Snapshots of the electric field $E_{1,x}$ when the x-polarized laser pulse is in focus. Electron density profile for parallel (b) and perpendicular (c) to each other polarized FH and SH electric fields after the ionization.

spectral properties of the THz emission. To this end, we proceed as follows: Firstly, the major emission properties of the smallest microplasmas are investigated. For this, we recapitulate the influence of the major driving laser pulse parameters with respect to the excitation source. Then, for a selected set of parameters, the emission properties are explored by 3D simulations with the code ARCTIC (see Sec. 3.2). Secondly, we investigate the scalability of the laser-to-THz conversion efficiency $\eta_{\rm THz}$ and elaborate the major differences from the 1C configuration. To estimate the optimal focusing conditions for a given laser pulse energy, a simple model is derived and validated by rigorous simulations with ARCTIC. Thirdly, the exploitation of elliptical beams for THz generation is proposed and their advantages compared to circular beams are discussed. Fourthly, a plasmonic model is proposed to explain important spectral features in the THz emission that are met in all the previously discussed configuration. Finally, the major results are summarized.

5.1. Smallest microplasmas

In the following, the driving laser pulse is defined by its transverse vacuum electric field at focus according to

$$\mathbf{E}_{\rm L,\perp}(\mathbf{r}_\perp, z=0, t) = \exp\left(-\frac{|\mathbf{r}_\perp|^2}{w_0^2} - \frac{t^2}{t_0^2}\right) \times \Big[E_\omega \cos(\omega_{\rm L} t)\, \mathbf{e}_{\rm FH} + E_{2\omega} \cos(2\omega_{\rm L} t + \phi)\, \mathbf{e}_{\rm SH}\Big], \quad (5.1.1)$$

where $\mathbf{r}_\perp = (x, y)^{\rm T}$ and z account for the transverse and longitudinal spatial coordinates, resp., t is the time coordinate, w_0 the vacuum focal beam width, t_0 the pulse duration, E_ω and $E_{2\omega}$ the FH and SH electric field amplitudes, resp., $\omega_{\rm L}$ the FH laser frequency, ϕ the SH relative phase angle, and the unit vectors $\mathbf{e}_{\rm FH}$ and $\mathbf{e}_{\rm SH}$ define the (linear) polarization direction of the FH and SH, respectively. The laser pulse is propagating in the positive z direction, and the origin of the coordinate system is chosen at its vacuum focal point. By defining the tightly focused laser pulse via its properties at the vacuum focus we follow the algorithm described in Sec. 3.3.

Let us start with the smallest microplasma, when a 2C 50-fs x-polarized 0.17-μJ Gaussian pump pulse is focused down to the diffraction limit (here $w_0 = 0.8\,\mu$m) into an argon gas at ambient pressure. A less than 10-μm-long and 1-μm-thick cylindrical microplasma is created

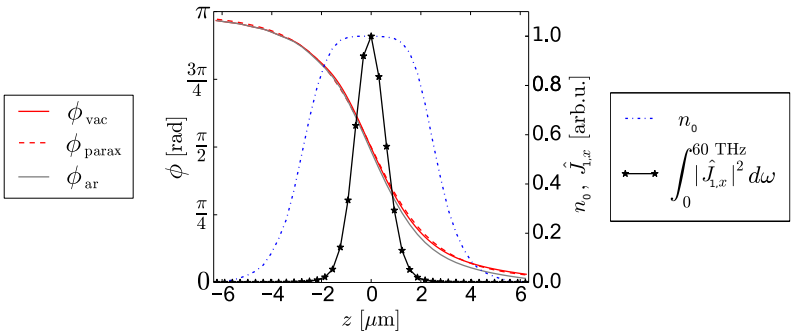

Figure 5.1.2.: Relative phase $\phi(z)$ between the FH and SH field for laser and gas parameter same as in Fig. 5.1.1(a) on the optical axis ($x = y = 0$) as well as the electron density $n_0(z)$ (after the pulse has passed) and the on-axis spectral power of the THz current (< 60 THz). The electron density n_0 and the current power are normalized to one.

[see 5.1.1(b)]. The gas is fully singly ionized at $\mathbf{r} = 0$ in the focal plane, leading to peak electron densities about 3×10^{19} cm^{-3}. Albeit the relatively high electron density, the laser pulse is almost unperturbed by the plasma [see Fig. 5.1.1(a)] because of the small interaction length, and propagates almost as in vacuum. In the following, the THz generation from such a sub-μJ laser pulse is investigated.

5.1.1. Influence of the two-color-pump-pulse parameter on the excitation

Same as for the 1C case in Chap. 4, before studying the THz emission properties from a microplasma it is beneficial to investigate the much easier accessible excitation source, here $\boldsymbol{\iota}_1 = q_e^2 n_0 / m_e \mathbf{E}_L$ [cf. Sec. 2.5.3]. The laser field[2] $\mathbf{E}_L$ approximates well $\mathbf{E}_1$ at the laser frequencies when the laser pulse propagates almost unperturbed through the microplasma. For higher laser pulse energies or weaker focusing (e.g. in the filamentation regime) it would be required to account for nonlinear laser propagation effects. In the following, simply the influence of the laser pulse parameter on the excitation source $\iota_1 = q_e^2 n_0 / m_e \mathbf{E}_L$, mostly in the focal point at $z = 0$, is investigated.

5.1.1.1. Phase angle ϕ between FH and SH

The laser field $\mathbf{E}_L$ is the sum of the FH and SH field, and it is well established that the strongest excitation at THz frequencies takes place usually for the relative angle $\phi = \pi/2$ [cf. Eq. (5.1.1)] between FH and SH [71]. Deviations from that appear only in regimes with low ionization yield [cf. Fig. 2.2.1(b-c) in Sec. 2.2.1], where ϕ strongly influences the free electron density. Since, we concentrate on the case where the gas is typically fully singly ionized[3], $\phi = \pi/2$ at the vacuum focus in most of the simulations is considered.

However, the FH and SH fields are propagating differently, even in vacuum. This makes in particular the relative phase angle ϕ between the two harmonics z-dependent

$$\phi(z) = \psi(z, 2\omega_L) - 2\psi(z, \omega_L), \tag{5.1.2}$$

[2] We shall remember that the laser field has been introduced in Sec. 2.5.1 as the vacuum solution of the Maxwell's equations for the laser.

[3] Adjusting the focusing to full single ionization optimizes the laser-to-THz conversion efficiency as will be shown in Sec. 5.2.

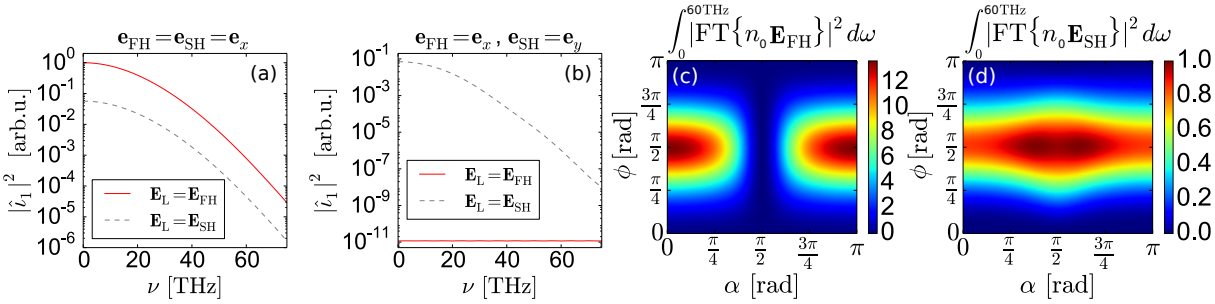

Figure 5.1.3.: Power spectrum of the excitation source $\boldsymbol{\iota}_1 \propto n_0\mathbf{E}_L$ at focus where $\mathbf{E}_L$ is the FH part of the laser field (solid red line) or SH part (gray dashed line) for $\phi = \pi/2$, with laser and gas parameter as in Fig. 5.1.1(a); (a) $\alpha = 0$ (SH field parallel to the FH field); (b) $\alpha = \phi = \pi/2$ (SH field perpendicular to the FH field). THz yield Y^{IC}_{THz} (low-frequency integrated excitation source) driven by the FH (c) and SH (d) field as a function of the angle α between FH and SH field vectors and ϕ. For the computation of n_0 always $\mathbf{E}_L = \mathbf{E}_{FH} + \mathbf{E}_{SH}$ is used.

where ψ is the z-dependent phase at the corresponding frequency. The variation of ϕ along z implies a strong variation of the excitation efficiency of the THz current along z (see Sec. 5.1.1.2 and the following example).

The variation of ψ is determined well in the paraxial approximation by the Gouy phase such that

$$\psi_{parax}(z,\omega) = \psi_{parax}(z=0,\omega) + \arctan\left(\frac{2cz}{w_0^2\omega}\right), \tag{5.1.3}$$

where with our definition in Eq. (5.1.1) $\psi_{parax}(z=0,\omega_L) = 0$ and $\psi_{parax}(z=0,2\omega_L) = \phi(z=0)$. Let us consider the strongest focusing case as presented in Fig. 5.1.1. The dark red dashed line in Fig. 5.1.2 is presenting the corresponding ϕ_{parax}, which almost coincides with both vacuum Maxwell and argon gas Maxwell simulation results. At focus, the optimum value of $\phi = \pi/2$ is retrieved. However, the phase angle ϕ changes from π to 0 over a couple of μm propagation range[4]. Because only $\phi = \pi/2$ leads to an optimum excitation of the THz current, for $z \neq 0$ the excitation is significantly weaker. As a result, the low-frequency current source presented in Fig. 5.1.2 (solid black line with star markers) is significantly shorter than the plasma, indicated by its electron density (dash-dotted blue line).

5.1.1.2. Polarization of FH and SH fields

When in contrast to the configuration with x-polarized FH and SH electric fields, the SH field is perpendicularly polarized to the FH electric field ($\mathbf{e}_{FH} = \mathbf{e}_x, \mathbf{e}_{SH} = \mathbf{e}_y$), the electron density is reduced considerably [see Fig. 5.1.1(b,c)]. The reason is the lower electric field amplitude, because $\sqrt{E_\omega^2 + E_{2\omega}^2} \leq |E_\omega| + |E_{2\omega}|$. As a consequence, the total electron charge Q is reduced by a factor ~ 4.2. Also in this case, the laser pulse is almost unperturbed by the plasma.

In the following, the THz source term $n_0\mathbf{E}$ is analyzed componentwise for $\mathbf{e}_{FH} = \mathbf{e}_x$, $\mathbf{e}_{SH} = \cos(\alpha)\mathbf{e}_x + \sin(\alpha)\mathbf{e}_y$. For the parallel case ($\alpha = 0$), the low-frequency power spectrum of $n_0\mathbf{E}_{FH}$ (red solid line) and $n_0\mathbf{E}_{SH}$ (gray dashed line) is presented in Fig. 5.1.3(a). Here, the excitation is driven by the FH and the SH electric fields. However, the excitation by the FH electric field

[4]We shall note that here we assumed that the focal beam widths of the SH and FH electric fields are the same, namely w_0. But, even if their focal beam widths are different both $\psi_{parax}(z,\omega_L)$ and $\psi_{parax}(z,2\omega_L)$ vary by π along z. Thus, due to its definition in Eq. (5.1.2), ϕ varies always by π along z.

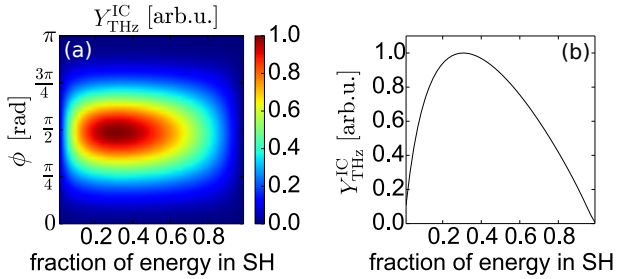

Figure 5.1.4.: THz yield for laser and gas parameter as in Fig. 5.1.1(a). In (a) the dependence on ϕ and the fraction of energy in the SH pulse component is presented. In (b) a line-out of (a) for the optimal angle $\phi = \pi/2$ is shown: The dependency on the SH pulse energy is not so critical. Already for few percent of the total energy in the SH field, the excitation source is reasonably strong.

dominates. For the perpendicular situation ($\alpha = \pi/2$) shown in Fig. 5.1.3(b), solely the SH electric field is responsible for the excitation. The reason is the time-dependence of the electron density n_0 that does not provide a FH frequency component in this case. Thus, the product of n_0 with $\mathbf{E}_{\mathrm{FH}}$ does not lead to a low-frequency component of the source. Since the excitation is driven by the SH electric field, the THz-emitting current has the polarization direction of the SH electric field.

In summary, the polarization of THz radiation should depend on the polarization of the 2C-pump laser fields. When the FH and SH electric fields are parallel to each other, the THz emission is linearly polarized in the same direction. Turning the SH polarization by 90 degrees with respect to the FH polarization should make the THz polarization follow the SH one. Furthermore, as detailed in Fig. 5.1.3(c-d), the optimum configuration for THz production based on the evaluation of the source term is $\phi = \pi/2$ and $\alpha = 0$.

5.1.1.3. Amplitude ratio of FH and SH, pulse duration and laser wavelength

Last but not least we comment on the impact of the FH vs. SH amplitude resp. energy ratio, laser pulse duration t_0 and the laser wavelength λ_{L}. In recent experiments, various fractions of the total pulse energy were converted to the SH frequency. In focused geometries 1 % up to 12 % have been converted [75] and even more than 20 % are in principle possible when focusing the FH and SH beam after its generation in collimated geometry. Our analysis of the strength of THz source term $\boldsymbol{\iota}_1$ depending on the energy ratio is presented in Fig. 5.1.4. Throughout this chapter, we assume that 20 % of the total pulse energy is in the SH field, thus we are very close to the optimum case.

To increase the laser-to-THz conversion efficiency using larger laser wavelengths has been proposed in [73] (see also Sec. 1.3.3). The evaluation of the source term for various laser wavelengths λ_{L} in Fig. 5.1.5(b) confirms indeed that an increase of the THz yield by a factor of 6 when going from $\lambda_{\mathrm{L}} = 0.8\,\mu$m to $\lambda_{\mathrm{L}} = 1.6\,\mu$m might be possible. Moreover, as Fig. 5.1.5(a) shows, this increase is accompanied by a broadening of the excitation spectrum.

In agreement with [132], another possibility to broaden the excitation spectrum is to use shorter driving laser pulses, as the power spectrum of the current source $\boldsymbol{\iota}_1$ in Fig. 5.1.5(c) shows. In Sec. 5.1.3.0.1, another more flexible way to tune the THz spectrum by using incommensurate frequencies will be elaborated [133]. In this work, we will stick to 50-fs 800-nm-FH laser pulses.

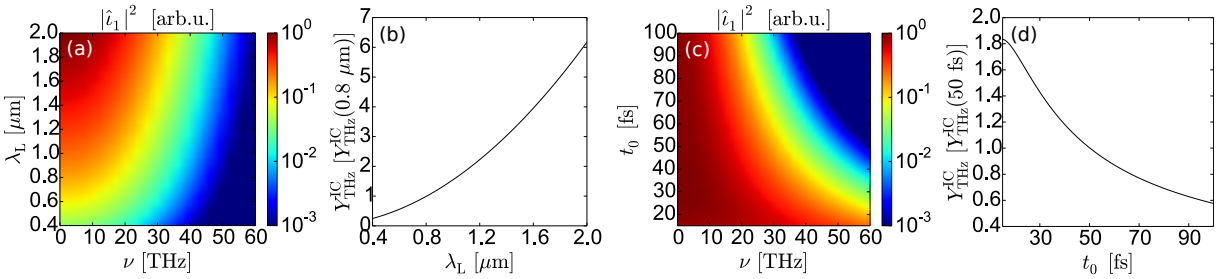

Figure 5.1.5.: In (a) the dependence on λ_L of the power spectrum of $\boldsymbol{\imath}_1$ is illustrated for other laser and gas parameter as in Fig. 5.1.1(a). In (b) the corresponding frequency integrated value, i.e., the THz yield is shown. In (c-d) an analogous parameter scan against the laser pulse duration t_0 is presented. Here, the electric field amplitudes have been kept constant and thus the laser pulse energy depends on t_0.

5.1.2. Emission properties for the two-color scheme

In the following the emission properties for the smallest microplasma, when the 2C 50-fs pump pulse from Fig. 5.1.1 is focused down to the diffraction limit, are investigated. For this, the fluid code ARCTIC is used (cf. Sec. 3.2). In Sec. 3.2.2, ARCTIC is successfully benchmarked against the PIC code OCEAN (cf. Sec. 3.1) exactly for the set-up that is going to be discussed next.

5.1.2.1. Point source radiation profiles

The pulse energy is only 0.17 μJ, and the laser-induced plasma is approximately 8 μm long. For such short interaction length, the laser propagation is practically unaffected and follows almost the vacuum case, where the phase angle ϕ is evolving along z due to the particular frequency dependence of the Gouy phase. The optimum value of $\phi = \pi/2$ is reached only in the focal plane, and the longitudinal variation of ϕ further reduces the effective length of the THz source to approximately 4 μm (cf. Sec. 5.1.1.1). Therefore, the source is small compared to THz wavelengths and the microplasma acts as a point source, i.e., a dipole.

When FH and SH are both x-polarized, the dipole-like THz radiation profile forms a torus with a hole along the x axis as sketched in Fig. 5.1.6(a). Simulations confirm the point-like emission as presented by the angularly resolved THz far-field spectra for three different planes in Fig. 5.1.6(b-d). We regain the characteristic hole of the torus in (b) at $\varphi_{ZX} = 90°, 270°$. Cutting the torus along the ZY plane, like a bagel, we find as expected the φ_{ZY}-independent radiation profile in (c). In (d) in the XY-plane we find a similar emission pattern as in (b) due to the cylindrical symmetry of the emission profile with respect to the x-axis, but shifted by 90 degrees due to the counterclockwise counting of the angles φ_{ZX} and φ_{XY}. Please note that the emission is not exactly toroidal, but slightly forward directed. This can be see from Fig. 5.1.6(c), where the emission at $\varphi_{ZY} = 0°$ appears broader than at $\varphi_{ZY} = 90°$. The laser-to-THz conversion efficiency is $\eta_{THz} = 7.42 \cdot 10^{-7}$ that is already more than one order of magnitude larger than for 1C-driving laser pulses with the same laser-pulse energy.

According to Sec. 5.1.1.2, turning the SH polarization to $\mathbf{e}_{SH} = \mathbf{e}_y$, should provide only an excitation of a y-polarized low-frequency current. Then, since the microplasma acts as a point source, the dipole-like THz radiation profile forms a torus with a hole along the y axis, tilted by 90° compared to the parallel case as sketched in Fig. 5.1.6(e). Simulations confirm the point-like emission as presented by the angularly resolved THz far-field spectra for three different planes in Fig. 5.1.6(f-h). The overall THz energy yield is reduced by a factor ~ 17 compared to the parallel case because of the reduced electron charge and excitation strength (cf. Sec. 5.1.1.2).

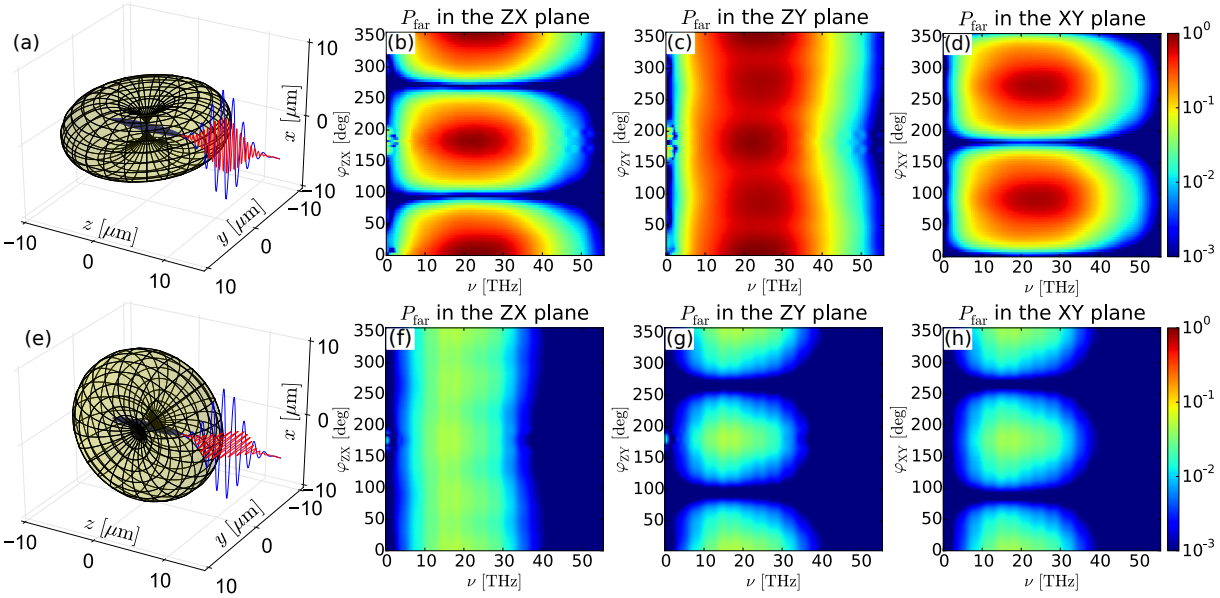

Figure 5.1.6.: The same two-color 0.17-μJ Gaussian laser pulse as in Fig. 5.1.1(a), i.e., both FH (blue line) and SH (red line) electric fields are x-polarized. The radiation pattern for one THz frequency (assuming a point source at $\mathbf{r} = 0$) is sketched in (a) (yellow surface) as well as the plasma (blue surface). In (b-d) the simulated THz radiation profiles in terms of the far field power spectra P_{far} in the ZX ($y = 0$), ZY ($x = 0$), and XY ($z = 0$) planes are presented. We count the azimuthal angles φ_{ZX}, φ_{ZY} counterclockwise from the z-axis, respectively and φ_{XY} from the x-axis. The laser pulse is propagating in positive z direction. In (e-h), the same results are presented for a y-polarized SH electric field normal to the x-polarized FH electric field.

In Chap. 4, a point-like THz radiation normal to the laser propagation direction has been emitted from longitudinal low-frequency currents. In this section, we have seen point-like emission from different transverse currents. The characteristic THz radiation pattern from smallest microplasmas allows a direct determination of the THz-driving-current polarization in future experiments. In Sec. 5.2.2, we will see that this is not possible for longer gas-plasmas and is unique for the shortest microplasmas.

5.1.2.2. Spectral properties

As shown in Fig. 5.1.6(b-c), broadband THz-to-far-infrared emission up to $\omega/(2\pi) = \nu \sim 50$ THz is observed from 2C-laser-induced microplasmas. Such a broad emission spectrum requires a broadband THz emitting current. The power spectrum of the THz current on the optical axis is presented in Fig. 5.1.7(a). The black dashed line specifies the local plasma frequency $\nu_{\mathrm{p}} = \sqrt{q_{\mathrm{e}}^2 n_0/(m_{\mathrm{e}}\epsilon_0)}/(2\pi)$ evolving with the electron density. It appears that the current spectrum is broadened up to ν_{p}. At focus ($z = 0$), the plasma is mostly excited up to about 50 THz.

This broadening of the current power spectrum affects the THz emission properties: Figure 5.1.7(b) shows the angularly integrated THz far-field spectrum for different gas pressures, i.e., different maximum plasma densities. According to the gas pressure, the spectrum broadens up to the maximum plasma frequency $\nu_{\mathrm{p}}(z = 0)$, as indicated by the vertical dotted lines. Similar broadening with increasing gas pressure has been already observed experimentally for much longer plasmas [75]. Here, the broadening was explained by laser propagation effects. Our

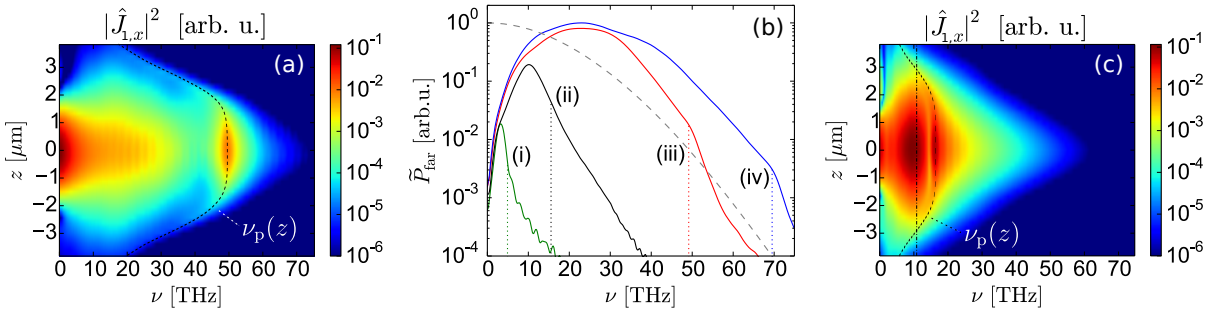

Figure 5.1.7.: (a) Power spectrum of the THz emitting current $J_{1,x}$ on the optical axis ($x = y = 0$) normalized to its respective value at ω_L. The laser and gas parameters are the same as in Fig. 5.1.1(a), in particular $p \approx 1$ bar. The local plasma frequency $\nu_p(z)$ (after ionization) is indicated by the black dashed line. (b) The angularly integrated far-field power spectrum $\tilde{P}_{far}$ in THz spectral range for $p \approx 10^{-2}$ bar (i, green line), $p \approx 10^{-1}$ bar (ii, black line), $p \approx 1$ bar (iii, red line) and $p \approx 2$ bar (vi, blue line). The maximum plasma frequency (at focus) is marked by dotted lines for each curve. Additionally, the normalized power spectrum of the excitation $n_0 E_{L,x}$ at focus is presented as light gray dashed line. (c) Power spectrum of the THz emitting current $J_{1,x}$ on the optical axis ($x = y = 0$) normalized to its respective value at ω_L for $p \approx 10^{-1}$ bar. The local plasma frequency $\nu_p(z)$ (after ionization) is indicated by the black dashed line. In addition, the black dash-dotted line specifies the value $\nu_p(z = 0)/\sqrt{2}$.

Maxwell-consistent simulations show, however, that such laser propagation effects can be ruled out for smallest microplasmas.

For the two lowest gas-pressures, in addition to the broadening up to $\nu_p(z = 0)$, the far-field spectrum reveals a resonant feature at approximately $\nu_p(\mathbf{r} = 0)/\sqrt{2}$. This can be also seen in the current power spectrum in Fig. 5.1.7(c) for $p \approx 0.1$ bar. Now, in addition to the oscillations at the local plasma frequency, the current provides a maximum close to $\nu_p(\mathbf{r} = 0)/\sqrt{2}$ (dash-dotted line). Similar spectral features have been found in experiments with molecular gas-jets in [134]: When increasing the gas-pressure up to $p = 0.7$ bar peaks at $\nu_p/\sqrt{2}$ have been found. For higher pressures, the position of the peak-THz spectrum stagnated as in our simulations. This observations give rise to an interpretation of the microplasma as a plasmonic nanoparticle with characteristic resonant features that is performed in Sec. 5.4.4.

5.1.3. Alternative pump pulse configurations

Besides the classical 2C scheme that has been studied above, alternative configurations have been proposed either to broaden the THz emission spectrum or to enhance the laser-to-THz conversion efficiency [88, 89, 133, 135]. In the following two of them are investigated for the smallest microplasma, again by 3D simulation with ARCTIC.

5.1.3.0.1. Incommensurate frequencies It was already demonstrated that the IC mechanism permits to tune the THz emission spectrum via the pump waveform [88, 133, 135]. The idea behind this tunability lies again in excitation source term $\boldsymbol{\iota}_1$ which is very sensitive to the pump waveform. This property also holds for microplasmas as Fig. 5.1.8 shows: Detuning the frequency of the second color from $2\omega_L$ to $1.8\omega_L$ leads to the excitation spectrum indicated by the dashed gray line in Fig. 5.1.8(a) [cf. Fig. 5.1.7(b)], featuring a maximum around 75 THz. For

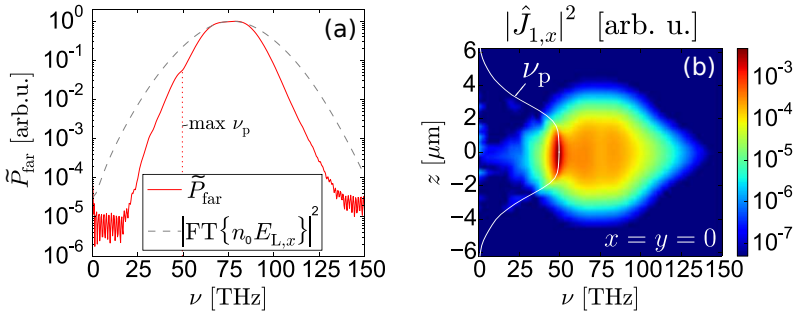

Figure 5.1.8.: (a) Angularly integrated far-field THz power spectrum (red line) and power spectrum of the excitation source $\propto n_0 E_{L,x}$ at focus (light gray dashed line) for incommensurate laser frequencies, i.e., ω_L and $1.8\omega_L$. The other laser and gas parameters are the same as in Fig. 5.1.1(a). The maximum local plasma frequency is marked by the dotted red line. (b) The corresponding current power spectrum on the optical axis, where the local plasma frequency is indicated by the white line.

argon at 1 bar pressure and single ionization at focus, the peak excitation is thus well above the the maximum plasma frequency $\nu_p = 49$ THz. In this case, the emitted THz far-field spectrum follows almost perfectly the excitation spectrum [see Fig. 5.1.8(a)], even though the current shows a strong feature at ν_p [see Fig. 5.1.8(b)].

The laser-to-THz conversion efficiency increases to $\eta_{THz} = 2.04 \cdot 10^{-6}$ compared to the classical 2C scheme where we found $\eta_{THz} = 7.42 \cdot 10^{-7}$. This corresponds to an increase by a factor 2.7. It is typical that currents at higher frequencies lead to stronger emission: the far-field power spectrum of a point source is $\propto \omega_{THz}^2$ (see Sec. 5.2.1). The emission for the incommensurate case takes place at frequencies 2.5 times larger than for the classical 2C scheme from Sec. 5.1 and one might expect an increase by a factor $2.5^2 = 6.25$. The reason that the actual increase is smaller relies in the amplitude of the emitting current that is reduced for the incommensurate case [compare Fig. 5.1.8(b) vs. Fig. 5.1.7(a)]. This is an additional evidence that radiation below the peak plasma frequency radiates in a rather resonant regime.

5.1.3.0.2. Saw tooth Another interesting, more complex pump configuration is the sawtooth waveform. It was shown in [89] that the source term $\boldsymbol{\iota}_1$ driving the THz emitting current density gets maximized by a sawtooth electric field. We test this prediction with a four color (4C) approximation of the sawtooth in the microplasma configuration: we chose the temporal evolution of the laser pulse in focus as $\cos(\omega_L t - \pi/2) + \cos(2\omega_L t + \pi/2)/2 + \cos(3\omega_L t - \pi/2)/3 + \cos(4\omega_L t + \pi/2)/4$ and keep other laser pulse parameters in Eq. (5.1.1) as for the classical 2C case, in particular the pump pulse energy is fixed to $\mathfrak{E}_L = 0.17\mu$J. The source term $\boldsymbol{\iota}_1$ can be evaluated and the 4C set-up gives an increase of the THz yield by a factor 4. The comparison of the far-field spectra in Fig. 5.1.9, reveals a 7.5 times larger conversion efficiency $\eta_{THz} = 5.58 \cdot 10^{-6}$ compared to the standard 2C case. The reason for this increase of THz emission from the microplasma is twofold: Firstly, the excitation is stronger for the four color pulse, as expected [compare Fig. 5.1.9(b) vs. Fig. 5.1.7(a)]. Secondly, the total number of free electrons produced by the four color sawtooth is 2.65 times larger than for the two color pulse.

Already the classical 2C scheme might be challenging to realize in an experiment for smallest microplasmas. The approximation of the saw tooth pulse shape by a four color laser pulse should be even more difficult since all the colors need to have a good spatial and temporal overlap. In the following, we will therefore investigate alternative ways to increase the laser-to-THz conversion efficiency.

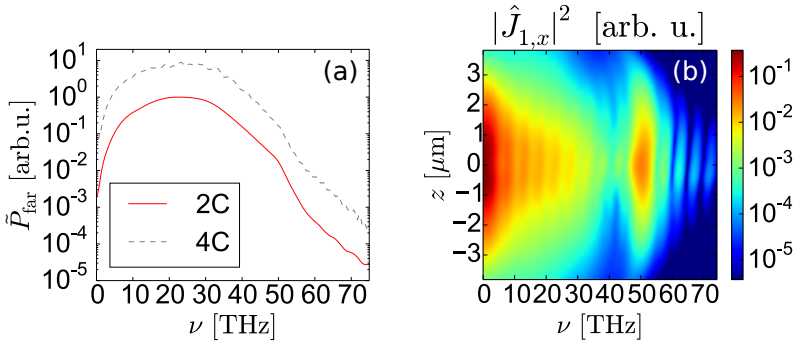

Figure 5.1.9.: (a) Angularly integrated far-field THz power spectrum for a four color sawtooth pulse (dashed line) and a standard two color pulse (red line). The other laser and gas parameters are the same as in Fig. 5.1.1(a). (b) The corresponding current power spectrum on the optical axis.

5.2. Scaling of the laser-to-THz conversion efficiency

The excitation of the plasma by the strongly focused 2C-fs-laser pulse as considered in the previous section is quite effective: For example, the THz current power spectrum in Fig. 5.1.7(a) is just one order of magnitude below the current at the laser frequency $\omega_{\rm L}$. However, the laser-to-THz conversion efficiency $\eta_{\rm THz}$ is of the order of 10^{-6}. This is already one order of magnitude larger than what can be reached with 1C-laser pulses with same energy and exploiting the TC mechanism (cf. Chap. 4). While 1C-laser pulses do not provide a scaling of $\eta_{\rm THz}$ beyond 10^{-6}, it is worth investigating the upscaling for multi-μJ 2C pulses. To this end, we resort to a simple model that estimates the scaling properties of the conversion efficiency with respect to the radiating plasma geometry and benchmark it by rigorous 3D simulations with the fluid code ARCTIC (cf. Sec. 3.2).

5.2.1. The plasma wire model

Simple considerations of the emission from a radiating current structure can explain various tendencies that we observe in our simulations. To this end, we do not consider the origin of the THz radiating current, but just assume that such current exists in a volume with length $L_{\rm p}$ and width $D_{\rm p}$. As pointed out in Sec. 5.1.1.1, the radiating current structure is not necessarily as large as the plasma. However, as for the plasma profile itself, we can assume that the scaling of $L_{\rm p}$ and $D_{\rm p}$ with the laser pulse parameters is the same as long as the laser pulse is not deformed too much, i.e., we are dealing with a microplasma.

When keeping the peak intensity at focus constant while increasing the focal beam width w_0 and laser pulse energy $\mathfrak{E}_{\rm L}$ simultaneously, the following assumptions on the scalings are reasonable in the light of the quasi-monochromatic paraxial approximation in Eq. (I.6):

$$D_{\rm p} \propto w_0\,, \qquad\qquad L_{\rm p} \propto w_0^2\,. \tag{5.2.1}$$

In order to get the scaling of the emitted THz pulse energy $\mathfrak{E}_{\rm THz}$ with $L_{\rm p}$ and $D_{\rm p}$, the following model is proposed: The radiating current structure is assumed to move invariantly with the vacuum speed of light c (or, more precisely, with the group velocity of the pump pulse) and thus

$$\mathbf{J}(\mathbf{r}_\perp, z, t) = \mathbf{J}_0(t - z/c) \tag{5.2.2}$$

in a cylinder with diameter $D_{\rm p}$ and length $L_{\rm p}$. Outside this cylinder, which is centered around

$\mathbf{r} = 0$, we assume a neutral gas and thus zero current density. In temporal Fourier space, the assumption in Eq. (5.2.2) translates into

$$\hat{\mathbf{J}}(\mathbf{r}_\perp, z, \omega) = \hat{\mathbf{J}}_0(\omega) e^{\mathrm{i}\frac{\omega}{c}z} \,. \tag{5.2.3}$$

With this assumption, in the far-field, the radiated power spectrum follows according to Eqs. (2.6.4), (2.6.8)

$$P_{\mathrm{far}} = \frac{\mu_0}{c}\omega^2 \left| \frac{\mathbf{r}}{|\mathbf{r}|} \times \int_V \hat{\mathbf{J}}_0(\omega) \, \frac{e^{\mathrm{i}\frac{\omega}{c}(|\mathbf{r}-\mathbf{r}'|+z')}}{4\pi|\mathbf{r}-\mathbf{r}'|} \, d^3\mathbf{r}' \right|^2 . \tag{5.2.4}$$

where $\mathbf{r} = (x, y, z)^{\mathrm{T}}$ is the position of the detector and V is the plasma volume. The goal is now to simplify Eq. (5.2.4).

We note that the distance $|\mathbf{r} - \mathbf{r}'|$ expands in the far-field by means of Taylor expansion as

$$|\mathbf{r} - \mathbf{r}'| \approx |\mathbf{r}| - \frac{xx' + yy'}{|\mathbf{r}|} - z'\frac{z}{|\mathbf{r}|} \,. \tag{5.2.5}$$

Using this expansion in the exponent in Eq. (5.2.4) and $|\mathbf{r} - \mathbf{r}'| \approx |\mathbf{r}|$ we obtain

$$P_{\mathrm{far}} \approx \underbrace{\left| \frac{\mathbf{r} \times \hat{\mathbf{J}}_0(\omega)}{|\mathbf{r}|} \right|^2}_{=:F_{\mathbf{J}_0}} \underbrace{\left| \int_{-\frac{L_\mathrm{p}}{2}}^{\frac{L_\mathrm{p}}{2}} e^{\mathrm{i}\frac{\omega}{c}z'\left(1-\frac{z}{|\mathbf{r}|}\right)} \, dz' \right|^2}_{=:F_{L_\mathrm{p}}} \times \underbrace{\frac{\mu_0\omega^2}{16\pi^2 c|\mathbf{r}|^2} \left| \int_A e^{-\mathrm{i}\frac{\omega}{c}\frac{xx'+yy'}{|\mathbf{r}|}} \, dx' \, dy' \right|^2}_{=:F_{D_\mathrm{p}}} , \tag{5.2.6}$$

where A is the transverse surface of the plasma.

It is very interesting to note that for our model-current Eq. (5.2.3), the far-field power spectrum separates into three terms that have their own simple role. In order to discuss their dependencies properly, we now switch to standard (ISO) spherical coordinates (r, θ, ϕ) according to

$$x = r\sin(\theta)\cos(\phi) \quad y = r\sin(\theta)\sin(\phi) \quad z = r\cos(\theta) \,. \tag{5.2.7}$$

- The term $F_{\mathbf{J}_0}(\theta, \phi, \omega)$ is mainly characterized by the orientation of the current.
- The term $F_{L_\mathrm{p}}(\theta, \omega)$ is solely determined by the length of the plasma, and can be evaluated as

$$F_{L_\mathrm{p}}(\theta, \omega) = \frac{4c^2 \sin^2\left[\frac{\omega L_\mathrm{p}}{2c}(1 - \cos\theta)\right]}{\omega^2(1 - \cos\theta)^2} \,. \tag{5.2.8}$$

- The term $F_{D_\mathrm{p}}(r, \omega)$ is dependent on the transverse profile of the current structure. For thin plasmas, i.e. $D_\mathrm{p}/\lambda_{\mathrm{THz}} \ll 1$ where $\lambda_{\mathrm{THz}} = c/\nu_{\mathrm{THz}}$, it reads

$$F_{D_\mathrm{p}}(r, \omega) \approx \frac{\mu_0\omega^2 D_\mathrm{p}^4}{256cr^2} \,. \tag{5.2.9}$$

  Thus, the THz pulse energy scales as $\mathfrak{E}_{\mathrm{THz}} \propto D_\mathrm{p}^4$.

Both $F_{\mathbf{J}_0}$ and F_{L_p} depend on the detection angle, which is visualized in Fig. 5.2.1. For a fixed orientation of the current, $F_{\mathbf{J}_0}$ has the toroidal shape as expected for the emission profile of a point source. For a transverse current, i.e., $\mathbf{J}_0 \parallel \mathbf{e}_x$, the hole of the torus is oriented along the

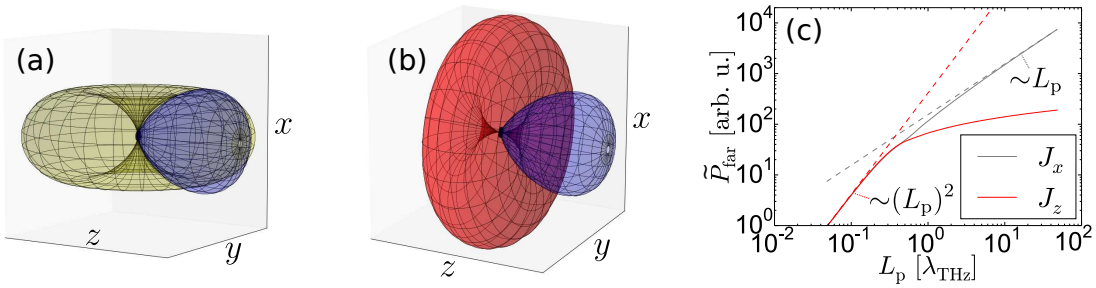

Figure 5.2.1.: Visualization of the angular dependency of the factors $F_{\mathbf{J}_0}$ and $F_{D_{\mathrm{p}}}$ in Eq. (5.2.10). The thin plasma is oriented along the z-axis. In (a), a transverse current $\mathbf{J}_0 \parallel \mathbf{e}_x$ is considered, and the toroidal $F_{\mathbf{J}_0}$ has its hole oriented along the x-direction (green surface). In (b), a longitudinal current $\mathbf{J}_0 \parallel \mathbf{e}_z$ is considered, and the toroidal $F_{\mathbf{J}_0}$ has its hole oriented along the z-direction (red surface). The plasma length dependent $F_{L_{\mathrm{p}}}$ is illustrated in (a,b) in blue for $L_{\mathrm{p}} = 1.6\lambda_{\mathrm{THz}}$. Its fig-shaped lobe is oriented in the laser propagation direction along z. The product between $F_{L_{\mathrm{p}}}$ and $F_{\mathbf{J}_0}$ results in the emission profile. In (c), THz emission scaling in terms of the angularly integrated far-field power spectrum $\tilde{P}_{\mathrm{far}}$ depending on L_{p} for a transverse (J_x) and longitudinal current (J_z) is shown. The scaling for short plasmas (dashed dark red line, J_x and J_z) and long plasmas (dashed light gray line, J_x only) is presented.

x-direction, as shown by the green surface in Fig. 5.2.1(a). For a point source, i.e., $L_{\mathrm{p}} \ll \lambda_{\mathrm{THz}}$, the factor $F_{\mathrm{L_p}}$ is constant, $F_{\mathrm{L_p}} \propto L_{\mathrm{p}}^2$, and gives just a sphere in our present visualization (not shown). For larger L_{p}, i.e., when passing to a line source, $F_{L_{\mathrm{p}}}$ becomes a fig-shaped structure oriented in the laser propagation direction as visualized by the blue surface in Fig. 5.2.1(a). The radiated flux is then proportional to the product of $F_{\mathbf{J}_0}$ and $F_{\mathrm{L_p}}$. Obviously, there is some good angular overlap between the two quantities in the case of a transverse current.

Next, the angularly integrated power spectrum $\tilde{P}_{\mathrm{far}}$ is computed from Eq. (5.2.6) for thin plasmas and transverse resp. longitudinal currents:

$$\tilde{P}_{\mathrm{far}} = \iint_{\Omega} P_{\mathrm{far}}\, r^2 \sin\theta \, d\theta \, d\phi = \frac{\pi \mu_0 c D_{\mathrm{p}}^4}{64} |\mathbf{J}_0(\omega)|^2 \times \int_0^{\pi} \frac{\sin^2\left[\frac{\omega L_{\mathrm{p}}}{2c}(1-\cos\theta)\right]}{(1-\cos\theta)^2} G_{\mathbf{J}_0}(\theta) \, \sin\theta \, d\theta \,, \tag{5.2.10}$$

where

$$G_{\mathbf{J}_0}(\theta) = \begin{cases} 1+\cos^2\theta & \text{for } \mathbf{J}_0 \parallel \mathbf{e}_x \\ 2\sin^2\theta & \text{for } \mathbf{J}_0 \parallel \mathbf{e}_z \end{cases} . \tag{5.2.11}$$

Let us consider a transverse current, i.e., $\mathbf{J}_0 \parallel \mathbf{e}_x$ first. For $L_{\mathrm{p}} \ll \lambda_{\mathrm{THz}}$, we obtain by means of Taylor expansion the scaling $\mathfrak{E}_{\mathrm{THz}} \propto L_{\mathrm{p}}^2$. The solid light gray line in Fig. 5.2.1(c) shows the predicted dependency of the angularly integrated far-field power spectrum $\tilde{P}_{\mathrm{far}}$ on L_{p}. For $L_{\mathrm{p}} \ll \lambda_{\mathrm{THz}}$, we find as expected $\tilde{P}_{\mathrm{far}} \propto L_{\mathrm{p}}^2$, whereas for $L_{\mathrm{p}} \gg \lambda_{\mathrm{THz}}$ and transverse current one gets $\tilde{P}_{\mathrm{far}} \propto L_{\mathrm{p}}$.

It is, of course, also possible to evaluate this simple model in Eq. (5.2.10) for a longitudinal current $\mathbf{J}_0 \parallel \mathbf{e}_z$, as it occurs in the TC mechanism for 1C-fs-laser-induced microplasmas (cf. Chap. 4). For short plasmas, we again obtain by means of Taylor expansion the scaling $\mathfrak{E}_{\mathrm{THz}} \propto L_{\mathrm{p}}^2$. For longer plasmas the situation is different. For a longitudinal current compared to a transverse current, $F_{\mathrm{L_p}}$ remains unchanged, but the toroidal $F_{\mathbf{J}_0}$ is oriented differently,

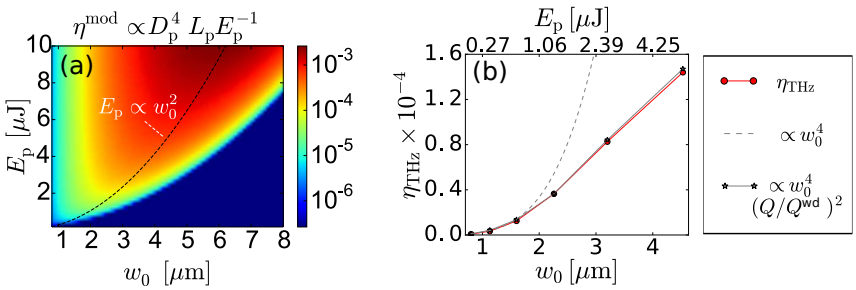

Figure 5.2.2.: (a) Estimation of the laser-to-THz conversion efficiency based on the simple model Eq. (5.2.10) versus pulse energy $\mathfrak{E}_\mathrm{L}$ and beam width at focus w_0. The black dashed line specifies $\mathfrak{E}_\mathrm{L} = 0.17\,\mu\mathrm{J} \times (w_0/0.8\,\mu\mathrm{m})^2$, thus it scales the laser pulse of Fig. 5.1.1(a) to larger focal beam widths w_0 while keeping the peak intensity constant. As the figure shows, the optimum beam width w_0 for a given laser pulse energy is very close to this line. (b) Scaling of laser-to-THz conversion efficiency η_THz following the black dashed line in (a) obtained from rigorous numerical simulations (solid dark red line), model disregarding laser defocusing (light dashed gray line) and model corrected for laser defocusing (solid light gray line, see text).

as shown in Fig. 5.2.1(b). Since the overlap between $F_{\mathbf{J}_0}$ and $F_{\mathrm{L_p}}$ is crucial for efficient THz emission, it is a priori clear that relying on a longitudinal current is detrimental when passing to longer plasmas. Indeed, the corresponding angularly integrated far-field power spectrum $\tilde{P}_\mathrm{far}$ shown in Fig. 5.2.1(c) (solid dark red line) confirms a sublinear scaling with L_p for a longitudinal current. In this light, a particular reason for the saturation of the laser-to-THz conversion efficiency for higher laser pulse energies that was observed for 1C-laser-driven THz generation in Sec. 4.3.3 is the sublinear scaling with the radiating plasma length.

Finally, even if microplasmas are transversally thin, we can investigate the scaling rules for thick emitters in order to see the difference to other approaches. As shown in App. K, if $D_\mathrm{p} \gg \lambda_\mathrm{THz}$ two regimes of emission are possible: (i) $\tilde{P}_\mathrm{far} \propto D_\mathrm{p}^4$ if $D_\mathrm{p}/\lambda_\mathrm{THz} \ll \sqrt{L_\mathrm{p}/\lambda_\mathrm{THz}}$ and (ii) $\tilde{P}_\mathrm{far} \propto D_\mathrm{p}^2$ if $D_\mathrm{p}/\lambda_\mathrm{THz} \gg \sqrt{L_\mathrm{p}/\lambda_\mathrm{THz}}$. The latter regime can be met for example in gas jets [62, 134] or THz generation in nonlinear crystals (cf. Secs. 1.2.3, 1.2.4). Gas plasmas created by a focused laser pulse operate rather in regime (i) and thus offer same as microplasmas a much better scalability.

5.2.2. Up-scaling the efficiency

In the following, the scalability of the laser-to-THz conversion efficiency η_THz in microplasmas is investigated based on the plasma wire model developed in Sec. 5.2.1. The intermediate results obtained from our simple model Eq. (5.2.10) suggest that for the IC mechanism, where THz radiating currents are transverse, increasing η_THz by passing to larger plasma volumes should be possible. As long as the considered plasmas are thin ($D_\mathrm{p} \ll \lambda_\mathrm{THz}$), emitters at different transverse positions radiate coherently. Thus, the emitted THz pulse energy should scale with the emitting plasma surface squared, i.e. $\propto D_\mathrm{p}^4$ in contrast to transversally thick plasmas with the scaling $\propto D_\mathrm{p}^2$. For a line source ($L_\mathrm{p} \gg \lambda_\mathrm{THz}$), according to our model we can therefore expect that $\eta_\mathrm{THz} \propto D_\mathrm{p}^4 L_\mathrm{p}/\mathfrak{E}_\mathrm{L}$, where $\mathfrak{E}_\mathrm{L}$ is the laser pulse energy. We can use this rough estimate for the conversion efficiency to optimize pulse energy $\mathfrak{E}_\mathrm{L}$ versus beam width at focus w_0. Results are shown in Fig. 5.2.2(a), where D_p and L_p have been determined as the plasma width and plasma length defined by the value of electron density that is 10 % of the initial

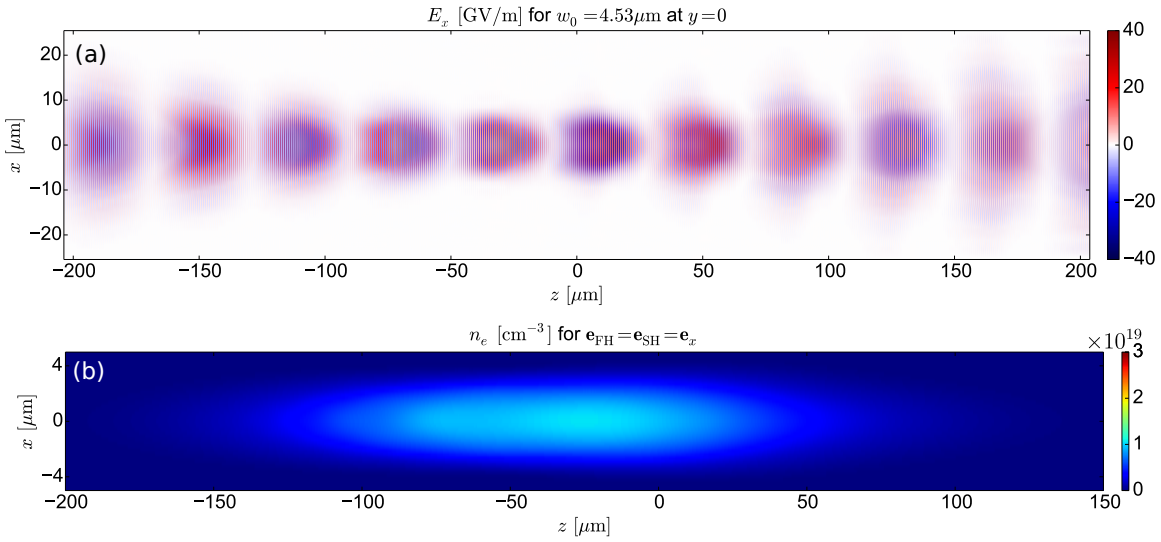

Figure 5.2.3.: (a) Series of snapshots of the electric field E_x for a laser with $w_0 = 4.5\,\mu$m and laser pulse energy $\mathfrak{E}_\mathrm{L} = 5.4\,\mu$J. The other laser and gas parameter are the same as for the smallest microplasma in Fig. 5.1.1(a). (b) Final electron density profile.

atom density. The computation of the electron density profile has been performed employing the paraxial approximation for the electric field [for 2C pulses in analogy to Eq. (I.6)], thus neglecting nonlinear and non-paraxial propagation effects. According to this simple estimate, in order to increase η_THz, one should increase the focal beam width w_0 while keeping the peak intensity constant, i.e., $\mathfrak{E}_\mathrm{L} \propto w_0^2$. The peak intensity should be chosen such that the gas is fully ionized. Then, because $D_\mathrm{p} \propto w_0$ and $L_\mathrm{p} \propto w_0^2$, the overall THz pulse energy $\mathfrak{E}_\mathrm{THz}$ is expected to scale with $\propto w_0^6$, and finally $\eta_\mathrm{THz} \propto w_0^4 \propto \mathfrak{E}_\mathrm{L}^2$. One would also expect a scaling of the final electron charge as $Q^\mathrm{wd} \propto L_\mathrm{p} D_\mathrm{p}^2 \propto w_0^4$.

Let us finally confront these predictions with rigorous full 3D Maxwell-consistent numerical simulation results with ARCTIC (cf. Sec. 3.2). We keep all laser and gas parameters as for the smallest microplasma in Fig. 5.1.1(a), but increase the (vacuum) focal beam width ($w_0 = 0.8 \ldots 4.5\,\mu$m) as well as the laser pulse energy ($\mathfrak{E}_\mathrm{L} = 0.17 \ldots 5.4\ \mu$J), such that the (vacuum) peak intensity stays constant. Figure 5.2.2(b) (solid red line) indeed confirms a dramatic enhancement of the laser-to-THz conversion efficiency η_THz by more than two orders of magnitude. Our simulation results suggest that, under the right focusing conditions, for only 10-μJ laser energy a conversion efficiency well above 10^{-4} can be achieved.

In the numerical simulations, however, a scaling of η_THz below the expected $\propto w_0^4$ (dashed gray line) is found, as clearly visible in Fig. 5.2.2(b). This effect can be attributed to laser defocusing by the free electrons, i.e., a nonlinear propagation effect, which becomes the more pronounced the longer the plasma is. In Fig. 5.2.3(a) a series of snapshots of the laser pulse is presented and allows to track the defocusing process. The laser pulse is focused several tens of micrometers before the vacuum focus at $z = 0$. The peak electric field is reduced from $\sim$ 50 GV/m to $\sim$ 40 GV/m. In Fig. 5.2.3(b) the resulting free electron density profile is shown. For the highest pulse energy of 5.4 μJ, already a 190-μm-long and 6-μm-thick plasma is created. Compared to the smallest microplasmas, where the laser is almost unperturbed by the plasma, the peak electron density is reduced by a factor ~ 3 [cf. Fig. 5.1.1(b)].

w_0 [μm]	0.8	1.13	1.6	2.26	3.2	4.53
Q [nC]	0.014	0.057	0.21	0.67	2.05	5.42
η_{THz} [10^{-5}]	0.074	0.338	1.25	3.65	8.26	14.4
k_Q	4.05	3.69	3.43	3.20	2.80	
k_η	4.39	3.75	3.11	2.35	1.60	
$k_{\tilde{\eta}}$	4.29	4.36	4.24	3.94	4.00	

Table 5.1.: Simulations results varying the focal beam width w_0 for a constant vacuum peak intensity and thus increasing the laser pulse energy (see text).

The simulated values of the electron charge Q versus w_0 and resulting exponents k_Q obtained from nearest neighbours fitting[5] are presented in Tab. 5.1. Between $w_0 = 0.8\,\mu$m and $w_0 = 1.13\,\mu$m, we find the expected exponent $k_Q \approx 4$. The corresponding exponent for the laser-to-THz conversion efficiency k_η is even slightly higher than 4, because we are at the limit to short plasma scaling with $\mathcal{E}_{\mathrm{THz}} \propto L_{\mathrm{p}}^2$. For larger w_0, the exponent k_Q decreases significantly. The exponent k_η decreases even stronger than k_Q, and the question is whether this decrease can be explained by the plasma defocusing only, or some additional parasitic effect is at play.

Even in simulations with strong defocusing, we observe that $L_{\mathrm{p}} \propto w_0^2$ and $D_{\mathrm{p}} \propto w_0$ for the normalized electron density profile, and only the number of created electrons, i.e., the density n_0, is decreasing. Because the source term $\boldsymbol{\iota}_1$ driving the current $\mathbf{J}_1$ is proportional to n_0, we can expect that the conversion efficiency η_{THz} gets simply reduced by a factor $\propto n_0^2 \propto (Q/Q^{\mathrm{wd}})^2$, where Q is the final electron charge extracted from the numerical simulation and $Q^{\mathrm{wd}} \propto w_0^4$ is the ideal final electron charge without defocusing effects. The corresponding exponent $k_{\tilde{\eta}}$ is presented in the last line of Tab. 5.1, and seems to support the scaling law

$$\eta_{\mathrm{THz}} \propto w_0^4 \left(\frac{Q}{Q^{\mathrm{wd}}}\right)^2 \tag{5.2.12}$$

that is additionally visualized in Fig. 5.2.2(b) (solid gray line). Thus, the sub-optimal scaling of η_{THz} in the microplasmas considered here (up to $L_{\mathrm{p}} = 190\ \mu$m) can be attributed solely to plasma defocusing.

5.2.3. Gas-pressure and phase angle dependence

Before investigating the emission properties from the largest microplasmas that lead according to Sec. 5.2.2 to considerable conversion efficiencies above 10^{-4}, the dependence of η_{THz} on gas pressure p and the phase angle ϕ is investigated.

The dependence on p for the smallest and the largest previously considered microplasmas are presented in Fig. 5.2.4(a). In both cases, at low gas pressures we find a scaling with the power $1.414 \approx \sqrt{2}$. Thus, the current cannot be considered to be driven only by the current source term $\boldsymbol{\iota}_1 \propto p$, where $\mathbf{J}_1$ would scale with p and thus η_{THz} with p^2. Consequently, the feedback of the electric field $\tilde{\mathbf{E}}_1$ (cf. Sec. 2.5.3) on the current $\mathbf{J}_1$ is confirmed to be crucial down to low gas-pressures. In Sec. 5.1.2.2, resonant features at low gas pressures that allow the same conclusion have been found for the smallest microplasmas. Here, we find for the smallest and the largest considered microplasma the same scaling of η_{THz} with the gas pressure. Thus, one

[5] $k_Q = \log\left(Q^+/Q^-\right) / \log\left(w_0^+/w_0^-\right)$, where superscripts + and − refer to left and right neighbour, respectively.

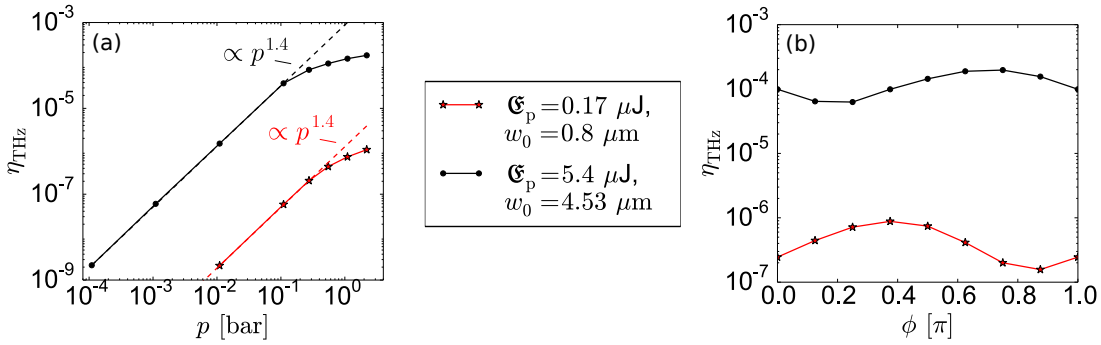

Figure 5.2.4.: Laser-to-THz conversion efficiency versus gas-pressure (a) and phase angle ϕ (b) for the smallest and the largest microplasma in from Fig. 5.2.2(a) with $\mathfrak{E}_{\mathrm{p}}$ and w_0 according to the legend.

would expect to find resonant features also in larger microplasmas. The gas-pressure behavior for larger microplasmas will be detailed in Sec. 5.2.4.

For larger gas pressures, the up-scaling of η_{THz} with p drops in agreement with experimental results for much stronger driving laser pulses in [66]. The deviation from the low-gas-pressure scaling is stronger for larger microplasmas [black curve in Fig. 5.2.4(a)] going hand in hand with the decrease of the peak electron density due to laser defocusing (cf. Sec. 5.2.2).

In Sec. 5.1.1, the relative phase angle between the FH and SH field ϕ has been shown to be important for an efficient excitation by the excitation source $\boldsymbol{\iota}_1$ at low frequencies. In this light, Fig. 5.2.4(b) reveals for small and large microplasmas a surprisingly weak dependence on ϕ. The laser-to-THz conversion efficiency varies only within a factor 10 when changing the phase ϕ in the vacuum focal plane. However, this is reasonable, since as has been shown in Sec. 5.1.1.1, already the linear vacuum propagation of a focused 2C-laser pulse changes ϕ by a value of π along z because of the frequency dependence of the Gouy phase. Moreover, even for the smallest microplasmas when no nonlinear laser propagation effects are at play, the optimum of η_{THz} is not exactly at $\phi = \pi/2$ in contrast to the expectations gained by evaluating the excitation source $\boldsymbol{\iota}_1$ in Sec. 5.1.1. This observation emphasizes again, that the self-action of the electric field $\tilde{\mathbf{E}}_1$ that is included in ARCTIC cannot be neglected for an accurate prediction.

5.2.4. Emission properties of larger microplasmas

In Sec. 5.1, the THz emission properties for smallest microplasmas driven by $\mathfrak{E}_{\mathrm{L}} = 0.17\,\mu$J-laser pulses have been studied: point source THz radiation profiles have been presented, the emission spectrum was shown to range up to about 50 THz and beeing strongly gas-pressure dependent. In Sec. 5.2, by going to larger microplasmas increasing the laser pulse energy by a factor about 30 and adjusting the focusing conditions to it's optimum, the laser-to-THz conversion efficiency was boosted by more than 2 orders of magnitude. Here, the emission properties of larger microplasmas are compared to those of the smallest one from Sec. 5.1.

According to Fig. 5.2.3(b), now the plasma is about 6 μm thick and 190 μm long shaping a line source for THz emitters. In the plasma wire model in Sec. 5.2.1, the plasma-length-dependent factor $F_{L_{\mathrm{p}}}$ in the expression for the far-field spectral power [Eq. (5.2.6)] is a sphere for smallest microplasmas and becomes a fig-shaped forward oriented structure for longer plasmas. Thus, for larger laser pulse energies leading necessarily to longer plasmas the THz emission is expected to be forward directed, in agreement with [95]. Fig. 5.2.5(a,b) shows the angularly resolved far-field spectrum for the largest considered microplasma: Indeed, THz waves are emitted in

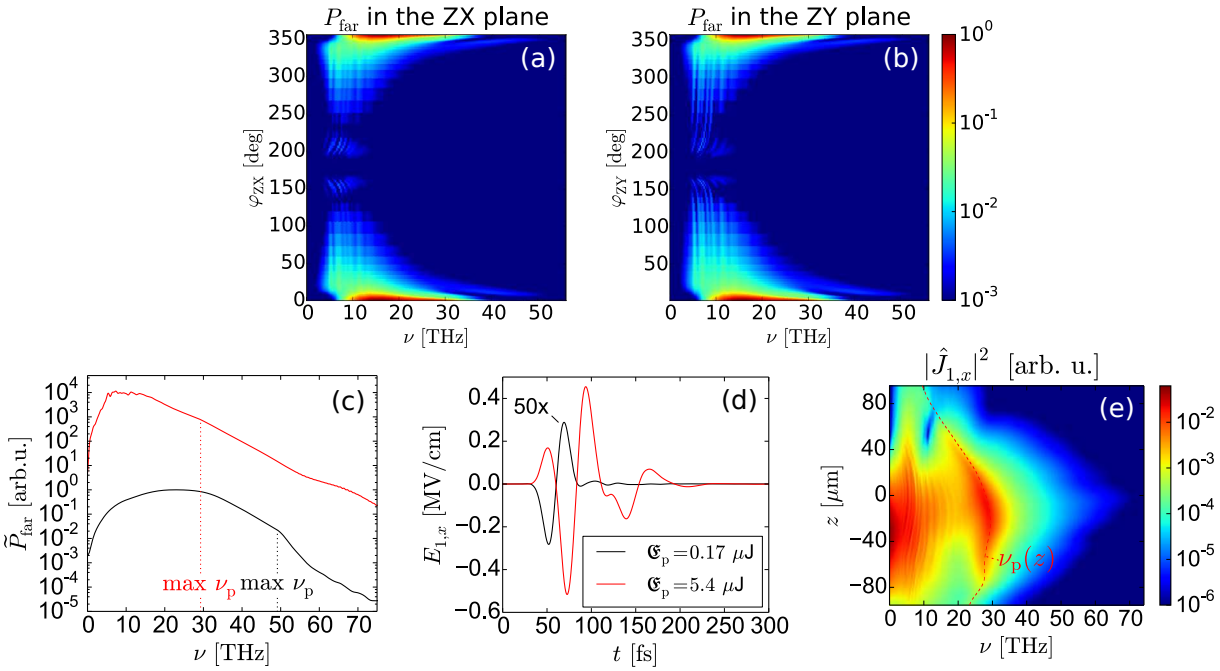

Figure 5.2.5.: (a-b) Angularly resolved THz power spectra in the ZX ($y = 0$) and ZY ($x = 0$) planes for $w_0 = 4.53\,\mu$m, $\mathfrak{E}_L = 5.4\,\mu$J. The 190 µm-long plasma acts as a THz line source, distinguished by the transition from toroidal to forward emission (see text). Other laser and gas parameters are kept as in Fig. 5.2.3. Comparison of the angularly integrated far-field spectra (c) and forward emitted electric fields just behind the plasma (d) between the smallest (black line, $w_0 = 0.8\,\mu$m, $\mathfrak{E}_L = 0.17\,\mu$J) and largest (red line, $w_0 = 4.53\,\mu$m, $\mathfrak{E}_L = 5.4\,\mu$J) considered microplasmas. The black colored time trace in (d) has been enlarged by a factor of 50 for a better comparison. (e) Power spectrum of the THz emitting current $J_{1,x}$ on the optical axis ($x = y = 0$) normalized to its respective value at ω_L for $\mathfrak{E}_L = 5.4\,\mu$J.

the forward direction within an isotropic radiation cone, where lower frequencies are emitted preferably under larger emission angles (for $0 \leq \varphi_{ZX}, \varphi_{ZY} \leq 90°$). Following the plasma wire model, in contrast to smallest microplasmas, the emission profile is not sensitive to the laser polarization: the laser polarization-dependent factor $F_{\mathbf{J}_0}$ is a torus and its product with F_{L_p} is not sensitive to whether the hole of the torus is pointing in the x- or in the y-direction.

For the large microplasma much stronger THz radiation is emitted compared to the smallest microplasma as confirmed by the angularly-integrated THz emission spectrum in Fig. 5.2.5(c). The forward-emitted low-frequency-filtered ($\leq$ 60 THz) electric field just behind the plasma reveals in Fig. 5.2.5(d) for the large microplasma considerable peak THz fields up to 0.5 MV/cm and anyhow 6 kV/cm for the smallest microplasma.

The angularly-integrated THz emission spectrum for the large microplasma in Fig. 5.2.5(c) (red line) is less wide than for the smallest microplasma (black line). The reason is the reduced peak electron density due to laser defocusing (cf. Sec. 5.2.2): For both microplasmas, the maximum plasma frequency determines the width of the spectrum. The power spectrum of the THz-emitting current on the optical axis in Fig. 5.2.5(e) confirms that again strong oscillations at the local plasma frequency are excited and only partially radiate.

A comparison between angularly integrated far-field spectra for $p \approx 1$ bar and $p \approx 0.1$ bar is presented in Fig. 5.2.6(a). Similarly to the smallest microplasma, the spectrum is tunable

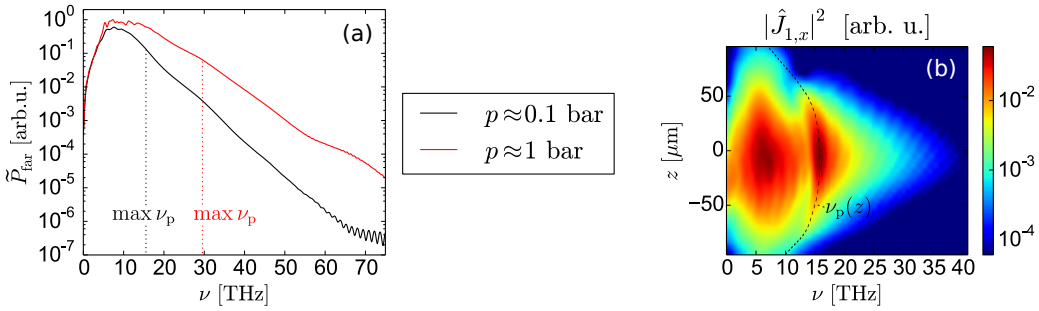

Figure 5.2.6.: (a) Angularly integrated far-field power spectra for laser parameter from Fig. 5.2.3 and two different gas-pressures according to the legend. (b) The power spectrum of the current on the optical axis for $p \approx 0.1$ bar reveals a double peak structure. The black dashed line specifies the local plasma frequency.

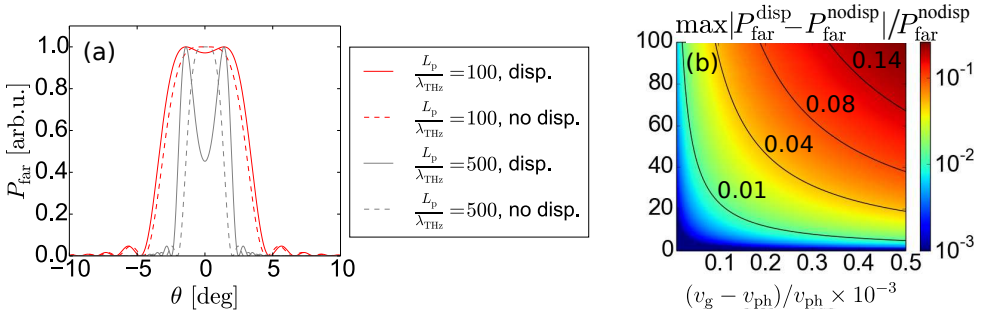

Figure 5.2.7.: In (a) the radiation profile with (solid line, $v_{\rm g} > v_{\rm ph}$) and (dashed line, $v_{\rm g} = v_{\rm ph} = c$) without linear dispersion of argon is shown, as computed from our simplified model of Sec. 5.2.1. Here we used $(v_{\rm g} - v_{\rm ph})/v_{\rm ph} = 3 \times 10^{-4}$, which is a realistic value for argon at ambient pressure (`refractiveindex.info`). In (b) the relative error in the far field power spectrum is shown. Up to $L_{\rm p} = 100 \times \lambda_{\rm THz}$ the error is less than 10 %.

with the gas pressure, but to a smaller extend since for the low gas pressure, the peak electron density and the peak plasma frequency are almost not reduced by laser defocusing. In the power spectrum of the current in Fig. 5.2.6(b) for $p \approx 0.1$ bar, we find again a double peak structure (similar to Fig. 5.1.7(c) for smallest microplasmas): The oscillations at the local plasma frequency are strong but the far-field emission is dominated by the low frequency peak. While for the smallest microplasmas this peak has been found at $\nu_{\rm p}/\sqrt{2}$, here the emission peak is located around $\nu_{\rm p}/2$. A similar qualitative behavior will be found for elliptical beams as well as in 2D geometry in Sec. 5.3.3 and explained by a plasmonic model in Sec. 5.4.4.

5.2.5. The role of linear dispersion

It is known that THz emission from longer plasmas appears as a hollow cone [136, 137]. This effect can be explained by the difference of group velocity of the pump in the plasma $v_{\rm g}$ and the THz phase velocity $v_{\rm ph}$ in the ambient gas, and $v_{\rm g} > v_{\rm ph}$. The plasma wire model presented in Sec. 5.2.1 can be easily extended to the case $c \neq v_{\rm g} \neq v_{\rm ph}$: assume $\mathbf{J}(\mathbf{r}_\perp, z, t) = \mathbf{J}_0(t - z/v_{\rm g})$ in Eq. (5.2.2), and $v_{\rm ph}$ is the phase velocity of the THz wave instead of c. Redoing the computation from Sec. 5.2.1, the plasma length determined term $F_{L_{\rm p}}$ in Eq. (5.2.8) that dominates the

radiation profile for long plasmas becomes

$$F_{L_\mathrm{p}}(\theta,\omega) = \frac{4v_\mathrm{ph}^2 \sin^2\left[\frac{\omega L_\mathrm{p}}{2v_\mathrm{ph}}\left(\frac{v_\mathrm{ph}}{v_\mathrm{g}} - \cos\theta\right)\right]}{\omega^2(1-\cos\theta)^2}\,. \tag{5.2.13}$$

If the plasma length is $L_\mathrm{p} = 100\lambda_\mathrm{THz}$, the dent in the center of the cone in Fig. 5.2.7(a) is almost invisible. Only for $L_\mathrm{p} = 500\lambda_\mathrm{THz}$ and thus practically going to mm-long plasmas, the dent is clearly visible. As the estimation of the error neglecting the linear dispersion in Fig. 5.2.7(b) shows, it is justified to omit the dispersion of argon leading to $v_\mathrm{g} \approx v_\mathrm{ph} = c$ for microplasmas, as we are doing in this work.

5.3. THz generation by elliptical laser beams

As has been shown in Sec. 5.1, THz radiation from smallest microplasmas having a length smaller than the THz wavelength has several outstanding properties compared to emission from longer and wider plasmas:

1. The polarization of the THz emitting current can be identified simply by the emission profile. This additional information is expected to facilitate the identification of the THz generating mechanism in future experiments.
2. The point-like THz emission separates mostly from the laser. This could allow to bring a sample close to the plasma to explore strong THz fields without the necessity of focusing the THz pulse.
3. The laser propagates undistorted by the plasma and reaches peak electric fields as in vacuum leading to high electron densities and thus large number of THz emitters.
4. Many emitters radiate coherently due to small plasma dimensions.
5. The THz emission spectrum is ultra-broad reaching the maximum plasma frequency at 50 THz for a singly ionized gas at ambient pressure.
6. The THz spectrum is strongly tunable by the gas pressure.

Advantages 1. - 4. are based on the short length of microplasmas. However, to have a short plasma by tightly focusing circular beams leads automatically to very thin plasmas. The resulting free electron charge is small and limits the emitted THz pulse energy. Laser-to-THz conversion efficiencies above 10^{-6} are barely reachable and result in only pJ-THz-pulse energies for shortest microplasmas (cf. Sec. 5.1.2).

In the following, a way to circumvent this problem is presented. When focusing a laser beam tightly along one transverse direction (x) and weakly along another transverse direction (y), the diffraction along x will be strong and determine the plasma length that will stay short independently on how large the laser beam along y is. In the following, we define the laser pulse at focus by

$$\mathbf{E}_{\mathrm{L},\perp}(\mathbf{r}_\perp, z=0, t) = \exp\left(-\frac{x^2}{w_{0,x}^2} - \frac{y^2}{w_{0,y}^2} - \frac{t^2}{t_0^2}\right) \times \Big[E_\omega \cos(\omega_\mathrm{L} t)\,\mathbf{e}_\mathrm{FH} + E_{2\omega}\cos(2\omega_\mathrm{L} t + \phi)\,\mathbf{e}_\mathrm{SH}\Big], \tag{5.3.1}$$

where in contrast to Sec. 5.1, the laser has the short beam width $w_{0,x}$ and the long beam width $w_{0,y}$ resulting in a spatially elliptical beam profile. Figure 5.3.1(a,b) presents a snapshot of

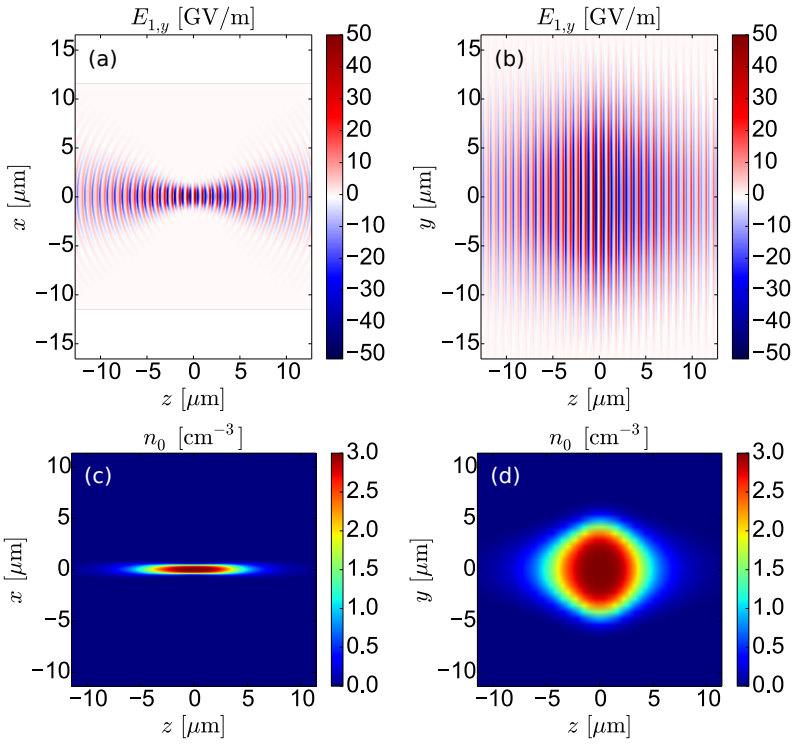

Figure 5.3.1.: Two-color 1.7-μJ elliptical Gaussian laser pulse ($E_\omega = 40$ GV/m, $E_{2\omega} = 20$ GV/m, $t_0 = 50$ fs, $\mathbf{e}_{\mathrm{FH}} = \mathbf{e}_{\mathrm{SH}} = \mathbf{e}_y$) focused down to $w_{0,x} = \lambda_{\mathrm{FH}} = 0.8$ μm, $w_{0,y} = 8$ μm in argon with initial neutral density $n_\mathrm{a} = 3 \cdot 10^{19}$ cm^{-3} ($p \approx 1$ bar). (a-b) Snapshots of the electric field $E_{1,y}$ in two planes when the y-polarized laser pulse is in focus. (c-d) Electron density profile in two planes after the ionization. The laser pulse propagates along z.

the electric field of a laser pulse focused into argon with $w_{0,x} = 0.8\,\mu$m and $w_{0,y} = 8\,\mu$m in two different planes. This laser pulse propagates without a noticeable deformation by the plasma and creates an approximately 10-μm-long and 1-μm-thin plasma along x as shown in Fig. 5.3.1(c). Along y, the plasma is approximately 10-μm-wide leading to a disc-shaped plasma profile in Fig. 5.3.1(d). In the following we investigate THz radiation from elliptical laser beams in two steps.

Firstly, $w_{0,y}$ will be further increased and the plasma more and more extended along y. As will be shown in the following, by increasing the plasma size in the y direction, the THz-pulse energy can be up-scaled. A similar strategy is also used for conventional THz sources: When exploiting OR (cf. Sec. 1.2.3) one tries to increase the nonlinear crystal surface proportional to the driving laser-pulse energy to obtain larger THz pulse energies. In this case, increasing the crystal surface is physically possible. In gas plasmas, when simply focusing a 2C-laser pulse, the control over the plasma dimensions is limited, in particular due to nonlinear propagation effects. Exploiting elliptical beams, we keep the plasma short as requested to avoid nonlinear laser propagation effects. Effectively, we approach to 2D-geometry, but by a real 3D laser beam.

Secondly, THz emission properties for driving elliptical beams will be investigated. Naturally, when approaching the 2D-geometry the response of the plasma separates into two cases, the

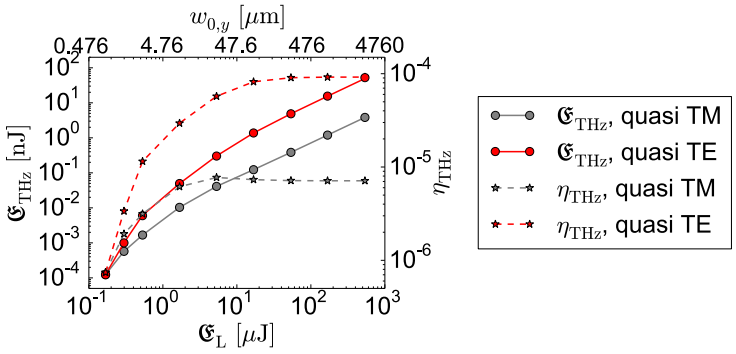

Figure 5.3.2.: THz pulse energy $\mathfrak{E}_{\mathrm{THz}}$ (solid lines) and laser-to-THz conversion efficiency η_{THz} (dashed lines) for elliptical driving laser beams with different long-axis beam widths $w_{0,y} \propto \mathfrak{E}_{\mathrm{L}}$. Hereby two cases are considered: an x-polarized laser pulse (quasi TM, gray lines) and a y-polarized laser pulse (quasi TE, red lines). Other laser pulse parameters are $w_{0,x} = 0.8\,\mu$m, $t_0 = 50$ fs and the gas is argon with an initial neutral density $n_{\mathrm{a}} = 3 \cdot 10^{19}$ cm^{-3} ($p \approx 1$ bar).

transverse electric (TE) and the transverse magnetic (TM) case[6]. We investigate them separately and show that for quasi 2D, i.e., 3D elliptical beams, those two cases can be indeed used to describe any other linear polarization state by superposition[7]. The TE case will be shown to provide 2D-point-like THz emission that allows to access 10-kV/cm-large THz-electric-field amplitudes without focusing the THz pulse. The TM case will be shown to provide resonant features that lead to strongly gas-pressure-tunable ultra-broadband THz spectra.

5.3.1. Up-scaling of the THz pulse energy

When increasing $w_{0,y}$ from the diffraction limit (here $w_{0,y} \approx 0.8\,\mu$m) to several μm or even mm, the size of the plasma along y increases accordingly. Mathematically, terms involving the differential operator ∂_y acting on a field become negligible, as the system becomes quasi translational invariant in the y direction. We will see that "translational invariant" in our context means that the plasma width along y is larger than the plasma wavelength $\lambda_{\mathrm{p}} = c/\nu_{\mathrm{p}}$ in focus. We shall note that the 2D approach has been already used through all the Chapter 4 to describe THz generation for 1C-driving-laser pulses via the TC mechanism. Even if here we investigate a different THz generation mechanism, the IC mechanism, the following results anticipate that real 3D elliptical beams can approach 2D systems in general.

Let us consider the laser-to-THz conversion efficiency $\eta_{\mathrm{THz}} = \mathfrak{E}_{\mathrm{THz}}/\mathfrak{E}_{\mathrm{L}}$ for a linearly increasing focal beam width $w_{0,y}$ and laser pulse energy $\mathfrak{E}_{\mathrm{L}}$ first. Other laser pulse parameters are kept as in Fig. 5.3.1. We consider two cases: the electric laser field is polarized in the long (y) direction (quasi TE) and the electric laser field is polarized in the short (x) direction (quasi TM). The dashed lines in Fig. 5.3.2 present the scaling of the conversion efficiency. For the lowest considered laser pulse energy $w_{0,y} = 0.8\,\mu\mathrm{m} = w_{0,x}$, we get the smallest circular microplasma that has been investigated in Sec. 5.1. Increasing $w_{0,y}$ and thus the size of the plasma in y increases η_{THz} by one order of magnitude for TM and two orders of magnitude to $\eta_{\mathrm{THz}} \approx 10^{-4}$

[6]Please remember, that the transverse electric laser field is y-polarized for the TE case and x-polarized for the TM case.

[7]Please note, that this is possible only for any linear polarization state. When using for example circular polarization, the ionization rate changes compared to the linear one and we cannot just superpose the solution by the TE and TM case.

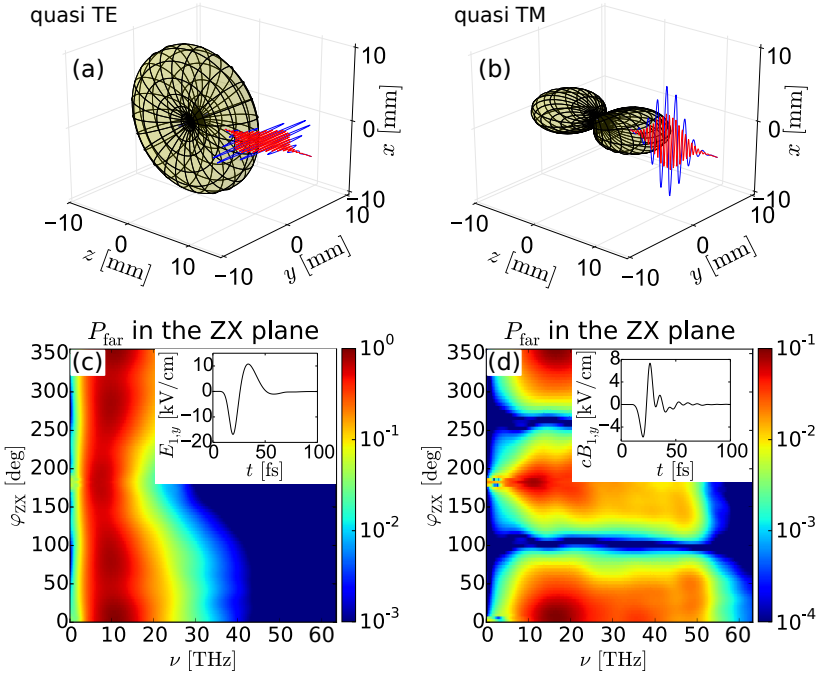

Figure 5.3.3.: Illustration of the far-field radiation pattern from a $D_y = \lambda_{\mathrm{THz}}$-long thin line source oriented along the y-direction. The electric laser field is y-polarized in (a) and x-polarized in (b). (c-d) Simulated THz far-field power spectra in the ZX-plane for a y-polarized laser in (c) and x-polarized laser in (d). Other laser pulse and gas parameter are the same as in Fig. 5.3.1. The insets in (c-d) demonstrate the forward emitted THz pulses just behind the plasma at $z = 12.7\,\mu$m.

for TE. At some point, in both cases the conversion efficiency reaches a constant value. This is a direct consequence of the increasing plasma size in y that forbids emission in the y-direction as shown in App. L. Then the THz pulse energy scales with $\propto D_y \propto w_{0,y}$, where D_y is the approximate size of the plasma in the long y-direction.

The solid lines in Fig. 5.3.2 present the corresponding THz pulse energies. When the conversion efficiency reaches a constant value, the THz pulse energy increases linearly and could be only limited by the stability of the driving laser pulse. For laser pulse energies above 10 μJ, THz pulse-energies reach values of almost 100 nJ. This is 40 times smaller than the record of 4 μJ-strong THz pulses from IR-laser driven gas-plasma based sources [73], but sufficient for some applications requiring strong THz fields (cf. Sec. 1.1.2). In addition, as will be shown in the following section, elliptical-beam-driven gas-plasma-based THz sources pose some interesting features that are not known from other THz sources.

5.3.2. Polarization dependence: TE vs. TM

While for long plasmas mostly the plasma length determines the radiation profiles, we found for short circular microplasmas in Sec. 5.1 a strong dependence on the polarization of the driving laser beam. This finding holds also for strongly focused elliptical beams. When increasing the beam width $w_{0,y}$ of a strongly focused elliptical beam, the radiating plasma is thin in x and z and thick in y. A sketch of the angular radiation patterns from such a transverse line source is presented for y and x polarized emitting current in Fig. 5.3.3(a,b) respectively. In both cases, almost no radiation is emitted along the y-direction. For y-polarization, the angular emission

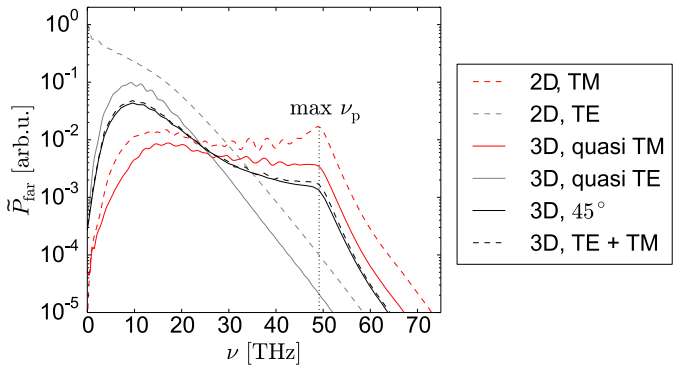

Figure 5.3.4.: Angularly integrated far-field power spectra for the elliptical beam from Fig. 5.3.1 in the case of a y-polarized laser electric field (quasi TE, light gray solid line) and an x-polarized laser electric field (quasi TM, dark red solid line). Corresponding results from 2D simulations with translational invariance in y are presented as dashed lines. The solid dark black line specifies the emission spectrum from a 3D simulation with laser polarization at 45°. The dashed dark black line is the far-field spectrum computed from the superimposed fields for the x-polarized and y-polarized laser in 3D (see text for details).

pattern is almost toroidal similar to a point source. However, since the plasma is elongated along y (here up to few mm), the THz-pulse phase front is rather cylindrically shaped and could be focused by cylindrical mirrors to form a line source of THz radiation. For y-polarization, we obtain a line of forward and backward emission.

In the following, the radiation profiles and then the emission spectra from simulations with ARCTIC (cf. Sec. 3.2) are analyzed for laser parameter as in the caption of Fig. 5.3.1 and x/y-polarized driving lasers. Hereby, the final plasma width is smaller that 1 μm in x and about 10 μm-large in y according to Figs. 5.3.1(c,d). The argon gas at ambient pressure is fully singly ionized with plasma wavelength $\lambda_{\rm p}(\mathbf{r}=0) = c/\nu_{\rm p}(\mathbf{r}=0) = 6.15\,\mu$m in focus. Thus, the size of the plasma in x is significantly smaller and in y larger than $\lambda_{\rm p}(\mathbf{r}=0)$.

The simulated angularly resolved far-field spectra in the ZX-plane are presented in Figs. 5.3.3(c,d). As expected from a line source along y (c), the emission in the plane normal to y is almost angularly independent. Only for the larger emission frequencies the plasma tends to become a line source in the z-direction[8] and thus slightly prefers forward emission at $\varphi_{\rm ZX} = 0°$. For the x-polarized driving laser (b), the simulated emission is confirmed to point in the forward ($\varphi_{\rm ZX} = 0°$) and backward direction ($\varphi_{\rm ZX} = 180°$), and nothing is emitted normal to the laser propagation direction ($\varphi_{\rm ZX} = 90°, 270°$) in agreement with the sketch in Figs. 5.3.3(b).

Considering the THz pulses that are emitted in the forward direction in the insets in Figs. 5.3.3(c,d), we find strong single-cycle THz pulses reaching amplitudes about 10 kV/cm. For the y-polarization case in (c), the THz pulse normal to the laser propagation direction reaches similar amplitudes, that could be easily accessed by placing the sample close to the focal plane. The THz pulse for the TE case in (d) is shorter than for the TM case as a consequence of the emission spectra that show a dramatic difference between the y- and x-polarized laser pulse. For the latter one, the spectrum is significantly broadened up to about 50 THz that corresponds to the maximum plasma frequency max $\nu_{\rm p}$.

The broadening for an x-polarized laser up to max $\nu_{\rm p}$ can be seen even better in the angularly integrated far-field spectrum in Fig. 5.3.4 (dark red solid line), while for the y-polarized

[8] More precise, this happens when the THz wavelength is smaller than the plasma extend in z.

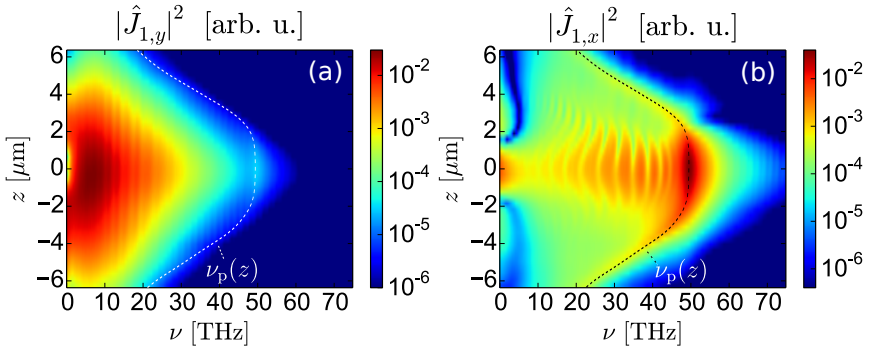

Figure 5.3.5.: Power spectrum of the transverse currents on the optical axis for the y (a) and x-polarized (b) laser pulse with laser and gas parameter same as in Fig. 5.3.1. The local plasma frequency is marked by the dashed line.

laser (light gray solid line) no broadening is found. The corresponding dashed lines show the results of 2D simulations, i.e. $w_{0,y} \to \infty$. There, we can find a similar behavior: no broadening if the laser electric field is oriented in the translational invariant direction y, and a broadening up to max ν_p if the laser electric field points in the direction of the strong electron density gradient, i.e., along x. It is known that the equations that we use to describe the plasma response (cf. Sec. 2.5.1) separate in 2D into two cases: the TE case that governs the fields $B_{1,x}$, $E_{1,y}$, $B_{1,z}$ for a y-polarized driving laser pulse and the TM case that governs the fields $E_{1,x}$, $B_{1,y}$, $E_{1,z}$ for an x-polarized driving laser pulse (see Sec. 5.4.1 for details). Any other linear polarization state in 2D can be written as the superposition of these two cases. For example, an incoming laser pulse that is polarized under 45° will give an electric field solution that can be written as $\mathbf{E} = \mathbf{E}^{\mathrm{TE}}/\sqrt{2} + \mathbf{E}^{\mathrm{TM}}/\sqrt{2}$, where $\mathbf{E}^{\mathrm{TE}}$ and $\mathbf{E}^{\mathrm{TM}}$ are the solutions for a y-(TE) and x-polarized (TM) driving laser pulse respectively. If the 3D elliptical beam approaches the 2D case, this property should hold. We check it by comparing the angularly integrated THz-far-field power spectrum for a simulation with polarization at 45° (dark black solid line) and the result for the superposed fields (dark black dashed line) in Fig. 5.3.4. Both overlap almost perfectly and the 3D elliptical beam is shown to approach well the 2D behavior. We conclude that the spectrum of an arbitrary linearly polarized 3D elliptical beam can be approximated by using the superposed fields from the quasi TE and quasi TM cases. In particular, we demonstrate that the THz emission spectrum can be tuned by rotating the linear polarization of the incoming laser pulse when using elliptical beams.

In the following, we want to detail the origin of the emission properties for quasi TE and quasi TM cases. In Sec. 4.2, for 1C-laser-induced microplasmas, we have seen that longitudinal excitation can lead to oscillations of the current at the local plasma frequency that do not radiate. It is thus interesting to see whether this is also the case for the quasi TE case. Fig. 5.3.5 presents the current power spectrum along the optical axis. We find, that no oscillations at the local plasma frequency are present for the quasi TE case (a) and they are present (and partially radiate) in the quasi TM case (b). This behavior raises the question why no oscillations at the local plasma frequency are observed for the excitation in the quasi translational invariant transverse direction in the TE case, but in the TM case and for a longitudinal excitation. Moreover, it should be clarified why for the TM case the oscillation lead to emission at the plasma frequency, but nothing is emitted when longitudinal currents are excited. A deeper analysis to answer these questions will be performed in Sec. 5.4.

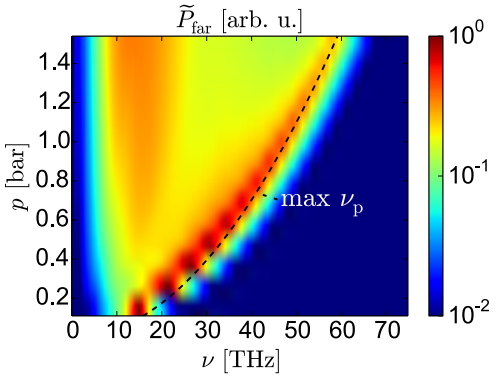

Figure 5.3.6.: Pressure-dependent angularly integrated far-field spectrum for a y-polarized strongly focused laser pulse in 2D (TE). The laser pulse parameter are $w_x = 0.8\,\mu$m, $t_0 = 50$ fs, $E_\omega = 40$ GV/m, $E_{2\omega} = 20$ GV/m. The gas is argon.

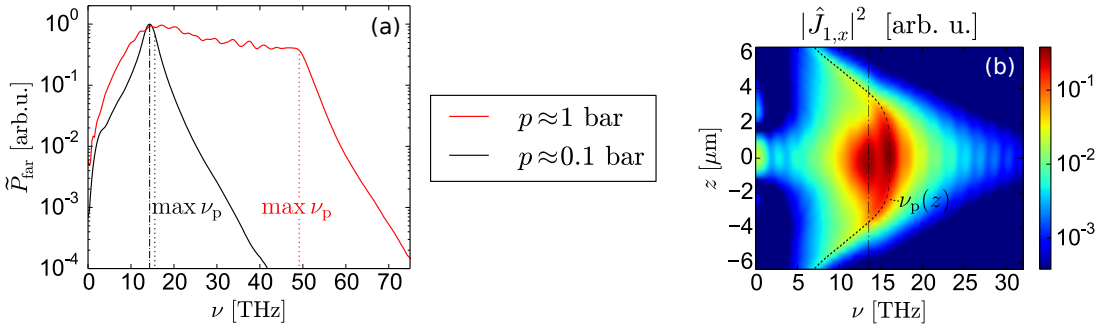

Figure 5.3.7.: (a) Angularly integrated far-field power spectra for the elliptical beam from Fig. 5.3.1(d), i.e., the quasi TM case, for two different gas-pressures according to the legend. The dotted lines specify the maximum plasma frequency. (b) The power spectrum of the current on the optical axis for $p \approx 0.1$ bar reveals a double peak structure. The black dotted line specifies the local plasma frequency explaining one peak. The black dash-dotted line marks the frequency peak $\nu = 13.5$ THz that is close to the maximum of the emission frequency for $p \approx 0.1$ bar in (a). There, this peak is also marked by a black dash-dotted line.

5.3.3. Gas-pressure dependence of the TM case

Finally, the gas pressure dependence of the (quasi) TM case that provides THz emission up to the local plasma frequency according to the previous section is investigated. We have seen already for smallest and larger circular Gaussian beams in Secs. 5.1.2.2, 5.2.4 a gas pressure tunable behavior of THz spectra. Also for the TM case in 2D[9] the spectra are highly gas-pressure-tunable according to Fig. 5.3.6. We observe a low-frequency peak around 16 THz that almost does not move when changing the gas pressure and a peak close to the peak plasma frequency (dashed line) moving with the gas pressure. The gas-pressure-dependent peak is slightly below the peak plasma frequency, 0.8 THz for 0.1 bar and 0.3 THz for 1.4 bar.

One might argue that this shift ordinates from the fact that the plasma is inhomogeneous with smaller plasma frequencies besides the focus. However, as the following analysis of the

[9]Here, we rely on 2D simulations for sake of computational costs. As we have previously seen, they approach well elliptical beams. The major difference is that the emission around the plasma frequency is better pronounced for 2D beams than for 3D elliptical beams.

emission spectrum and the power spectrum of the radiating current shows, the origin of this shift is a resonant feature slightly below the plasma frequency. Figure 5.3.7(a) presents the far field power spectra for $p \approx 0.1$ bar and $p \approx 1$ bar visualizing again the gas-pressure tunability, now for real 3D elliptical beams. Especially for $p \approx 0.1$ bar (black line), the shift of the emission peak (dashed-dotted line) from the maximum plasma frequency (dotted line) is visible. As Fig. 5.3.7(b) shows, the emission frequency peak can be found also in the current power spectrum. It appears in addition to the oscillations at the local plasma frequency. Thus, the shift of the gas-pressure dependent emission peak originates rather from a distinct resonance than from oscillations at the local plasma frequency. This behavior is interpreted in Sec. 5.4.4 by means of a simplified plasmonic model which also clarifies the origin of the shift.

In summary, THz emission from tightly focused elliptical beams has been investigated by rigorous 3D simulations with ARCTIC. We have seen that increasing the laser beam width in one transverse direction can increase the conversion efficiency by 2 orders of magnitude compared to smallest microplasmas to 10^{-4}. Consequently, for mJ-driving laser pulses the THz pulse energy could reach the μJ-level and being useful for strong-THz-field experiments. Moreover, many interesting additional emission features have been found: The emission profile is polarization dependent. If the laser pulse is polarized in the long-beam-width direction, the THz pulse separates from the laser pulse and 10-kV/cm THz-field amplitudes can be accessed without focusing. The microplasma produces a line of THz emission. THz spectra are tunable by the linear polarization of the driving laser pulse. Gas-pressure-dependent spectra give an evidence of resonant THz emission. Those resonant features are shown to exist whenever the electron density changes transversally along distances smaller than the THz wavelength.

5.4. A plasmonic view on spectral properties of THz emission

When comparing plasmonic nanoantennas[10] that are used for example for SH generation [130] with some gas-plasmas that are used for THz generation (e.g. our microplasmas or [75]) one finds many similarities: both consist of a material (metal or gas-plasma) with a strong free electron response that makes it opaque for the generated radiation wavelengths (400 nm or 6 μm-1 mm) and both have dimensions (few nm or few μm) that are comparable or smaller than the plasma wavelength $\lambda_p = c/\nu_p$ (200 nm or $> 6\,\mu$m). While the plasmonic nanoantennas are typically discussed in the framework of plasmonics, i.e. discussing nanoparticle resonances, gas-plasma-based THz generation is usually explained without taking those into account.

However, in our Maxwell consistent 2D and 3D simulations we have found various examples that indicate resonant excitation and partially resonant emission (Secs. 4.4.1, 5.1.2.2, 5.2.4, 5.3.2):

- spectral broadening up to the local plasma frequency for transverse THz electric fields pointing in the direction of strong electron density gradients while no broadening appears if it points in the direction with weakly changing electron density
- gas-pressure tunable spectral peaks below the maximum plasma frequency, especially for low gas pressure
- radiation from currents close to the maximum plasma frequency if those are transverse (IC-mechanism and Gaussian beams in this chapter) and nonradiative oscillations at the local

[10] Plasmonic nanoantennas are sub-wavelength metallic structures. Those have typically pronounced electromagnetic resonances that are often used to enhance the nonlinear response of a metal-dielectric structure.

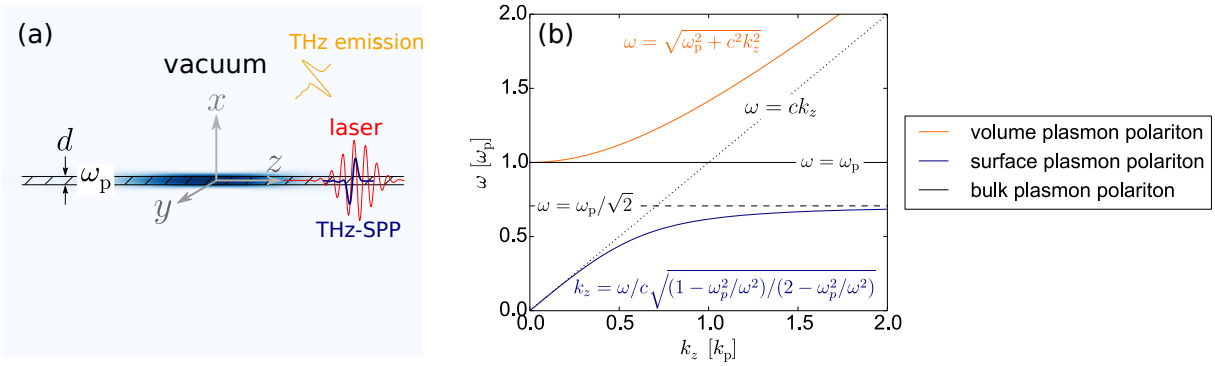

Figure 5.4.1.: (a) Illustration of the plasma slab model: The plasma (dark blue) is approximated by an in the y and z-direction infinitely extended preformed-plasma slab (striped) with plasma frequency ω_p and thickness d, it is surrounded by vacuum. The laser (red) propagates along z and excites the plasma leading to THz emission (orange). (b) Plasmon-polariton dispersion relation for a metal-vacuum interface.

plasma frequency if the emitting currents are longitudinal (TC-mechanism and Gaussian beams in Chap. 4)

To interpret those observations, a very simple plasmonic nanostructure is investigated: a metallic or plasma slab. It should approximate well a plasma with a small size along x and large size along y and z [see Fig. 5.4.1(a)]

Before exploring this structure, let us recapitulate the basic features of the most simple plasmonic structure: a metal-air interface. This structure is assumed to be preformed (existing for all times) and translational invariant in y- and z-direction. Thus, one can determine its modes by the angular frequency ω and spatial frequencies k_y and k_z. We consider w.l.o.g. only modes with $k_y = 0$. Then, the electromagnetic fields of the modes are $\propto \exp[\mathrm{i}(k_z z - \omega t)]$. The modes with $\omega > ck_z$ can radiate into the air half space. The modes with $\omega \leq ck_z$ can propagate only along the interface (see Sec. 5.4.1 for details). Those two regimes have two eigenmodes characterized by its dispersion relations $\omega = \omega(k_z)$ that are imprinted in Fig. 5.4.1(b), the volume plasmon polariton (VPP) and the surface plasmon polariton (SPP) [138]. The VPP (orange line) is a band-edge that separates modes that can propagate along x in the plasma $[\omega(k_z) > \sqrt{\omega_p^2 + c^2 k_z^2}]$ from the modes that cannot propagate along x in the plasma $[\omega(k_z) < \sqrt{\omega_p^2 + c^2 k_z^2}]$. The VPP itself is characterized by a constant field amplitude in the metal and radiates into air. For $k_z = 0$, its frequency is $\omega(k_z = 0) = \omega_p$ and approaches the line $\omega = ck_z$ for large k_z. The SPP (blue line) is a localized solution that propagates along the interface. It starts at $\omega(k_z = 0) = 0$ and approaches the value $\omega_p/\sqrt{2}$ for large k_z.

As will be shown in the following, similar resonances influence the excitation and emission at THz frequencies in a plasma slab. Firstly, we derive equations that govern the electromagnetic fields after excitation in the plasma slab. Secondly, we discuss its response for different types of excitation and (ω, k_z)-pairs. Then, by means of the plasma slab model, we interpret the observations that have been done above concerning: spectral characteristics of the polarization- and gas-pressure dependence in elliptical beams as well as nonradiative oscillation at the plasma frequency.

5.4.1. The plasma slab model

We consider a system as sketched in Fig. 5.4.1(a): A preformed plasma slab with the thickness d in the x-direction and a time-invariant electron density n_0 and collision frequency ν_{ei}. Both are translational invariant in y and z. Above and below the wire we assume a semi-infinite dielectric medium, a cladding[11], with the constant permittivity ϵ_{c}. Thanks to the analogy of the 1st and 2nd order current equation that has been introduced in Sec. 2.5.3, we can consider in the following the general case where $\mathbf{J} \in \{\tilde{\mathbf{J}}_1, \mathbf{J}_2\}$, $\boldsymbol{\iota} \in \{\tilde{\boldsymbol{\iota}}_1, \boldsymbol{\iota}_2\}$, $\mathbf{E} \in \{\tilde{\mathbf{E}}_1, \mathbf{E}_2\}$ and $\mathbf{B} \in \{\tilde{\mathbf{B}}_1, \mathbf{B}_2\}$, i.e., we treat the IC and the TC mechanism by the same theory. Then the current equation $\partial_t \mathbf{J} + \nu_{\mathrm{ei}}\mathbf{J} = q_{\mathrm{e}}^2 n_0/m_{\mathrm{e}}\mathbf{E} + \boldsymbol{\iota}$ and the Maxwell's equations (2.3.3)-(2.3.4) determine the whole response of the system. In the frequency space (see App. A), they can be rewritten for angular frequency $\omega \neq 0$ to

$$\nabla \times \hat{\mathbf{E}} = \mathrm{i}\omega\hat{\mathbf{B}} \tag{5.4.1}$$

$$\nabla \times \hat{\mathbf{B}} = -\frac{\mathrm{i}\omega}{c^2}\epsilon\hat{\mathbf{E}} + \hat{\mathbf{Q}}\,, \tag{5.4.2}$$

where the complex dielectric permittivity of the plasma $\epsilon = \epsilon^{\mathrm{p}}$ for $|x| \leq d/2$ reads

$$\epsilon^{\mathrm{p}} = 1 - \frac{\omega_{\mathrm{p}}^2}{\omega^2 + \mathrm{i}\omega\nu_{\mathrm{ei}}} \tag{5.4.3}$$

and for sake of brevity, we introduce the source term

$$\hat{\mathbf{Q}} = \frac{\mu_0 \boldsymbol{\iota}}{-\mathrm{i}\omega + \nu_{\mathrm{ei}}}\,. \tag{5.4.4}$$

We introduce the space-dependent dielectric permittivity ϵ by setting $\epsilon = \epsilon^{\mathrm{p}}$ for $|x| \leq d/2$ and $\epsilon = \epsilon^{\mathrm{c}}$ (later $\epsilon^{\mathrm{c}} = 1$) for $|x| > d/2$. Same as for ϵ, we consider an excitation that is translational invariant in y, i.e., $\partial_y \hat{\boldsymbol{\iota}} = 0$ and thus $\partial_y \hat{\mathbf{Q}} = 0$. Because of that, we can set all the y-derivatives to zero and Eqs. (5.4.1)-(5.4.2) separate into two sets of equations. The translational invariance of the slab in z allows to write down these two sets of equations in the Fourier space with respect to z ($\partial_z \to \mathrm{i}k_z$) giving

$$\partial_x \breve{E}_y = \mathrm{i}\omega\breve{B}_z \tag{5.4.5}$$

$$\text{(TE)} \qquad -\mathrm{i}k_z\breve{E}_y = \mathrm{i}\omega\breve{B}_x \tag{5.4.6}$$

$$\mathrm{i}k_z\breve{B}_x - \partial_x\breve{B}_z = -\frac{\mathrm{i}\omega}{c^2}\epsilon_1\breve{E}_y + \breve{Q}_y \tag{5.4.7}$$

and

$$\mathrm{i}k_z\breve{E}_x - \partial_x\breve{E}_z = \mathrm{i}\omega\breve{B}_y \tag{5.4.8}$$

$$\text{(TM)} \qquad -\mathrm{i}k_z\breve{B}_y = -\frac{\mathrm{i}\omega}{c^2}\epsilon\breve{E}_x + \breve{Q}_x \tag{5.4.9}$$

$$\partial_x\breve{B}_y = -\frac{\mathrm{i}\omega}{c^2}\epsilon\breve{E}_z + \breve{Q}_z, \tag{5.4.10}$$

where the "$\breve{\ }$" indicates the (ω, k_z)-space according to the definition in App. A. The 1st set is called the transverse electric (TE) case, because the only electric field component E_y is polarized

[11] The name cladding is usually used in plasmonics. There, often the dielectric medium above and below are different and called substrate and cladding.

in the transverse translational invariant direction. Here, the only fields different from zero are $(\breve{B}_x, \breve{E}_y, \breve{B}_z)$. The 2$^{\text{nd}}$ case is called the TM-case correspondingly and describes the evolution of $(\breve{E}_x, \breve{B}_y, \breve{E}_z)$. In the following, in the light of Eqs. (5.4.5)-(5.4.10), we consider three different cases:

(i) TE with transverse excitation in y ($\breve{\iota}_y \neq 0 \neq \breve{Q}_y$ and $\breve{Q}_x = 0 = \breve{Q}_z$)

(ii) TM with transverse excitation in x ($\breve{\iota}_x \neq 0 \neq \breve{Q}_x$ and $\breve{Q}_z = 0 = \breve{Q}_y$)

(iii) TM case with longitudinal excitation in z ($\breve{\iota}_z \neq 0 \neq \breve{Q}_z$ and $\breve{Q}_y = 0 = \breve{Q}_x$).

Please note that (i) corresponds to the THz generation by y-polarized elliptical beams and (ii) by x-polarized elliptical beams as investigated in Sec. 5.3. The TM case with longitudinal excitation corresponds to the excitation by longitudinal ponderomotive forces as investigated in Chap. 4. In the following, the Maxwell's equations Eqs. (5.4.5)-(5.4.10) for the plasma slab are solved for these three cases.

5.4.1.1. TE with transverse excitation in y

Here we concentrate on case (i), i.e., $\breve{\boldsymbol{\iota}} = \breve{\iota}_y \mathbf{e}_y$. Firstly, the general solution inside the plasma and air slab is computed and then the continuity of the transverse fields used to determine the entire solution.

Eqs. (5.4.5)-(5.4.7) give the evolution equation for the transverse field $\breve{E}_y$ inside the plasma and air correspondingly to

$$\partial_x^2 \breve{E}_y - \underbrace{\left(k_z^2 - \frac{\omega^2}{c^2}\epsilon\right)}_{=\Lambda^2} \breve{E}_y = \underbrace{-\mathrm{i}\omega \breve{Q}_y}_{=\breve{S}_y} . \tag{5.4.11}$$

For sake of simplicity, we consider that $\breve{S}_y$ is constant inside the plasma slab and zero outside of it. Then, the general solution in the plasma reads[12]

$$\breve{E}_y^{\mathrm{p}} = A^{\mathrm{p}} \cosh\left(\Lambda^{\mathrm{p}} x\right) + \frac{S_y}{(\Lambda^{\mathrm{p}})^2} \left(\cosh\left(\Lambda^{\mathrm{p}} x\right) - 1\right) , \tag{5.4.12}$$

where $\Lambda^{\mathrm{p}} = k_z^2 - \omega^2/c^2\epsilon^{\mathrm{p}}$. In the positive x-half-space in the cladding

$$\breve{E}_y^{\mathrm{c}} = A^{\mathrm{c}} \exp\left[\mp\Lambda^{\mathrm{c}}\left(x - \frac{d}{2}\right)\right] , \tag{5.4.13}$$

where $\Lambda^{\mathrm{c}} = k_z^2 - \omega^2/c^2\epsilon^{\mathrm{c}}$. If $k_z^2 \geq \epsilon^c\omega^2/c^2$, here we use the "$-$"-sign (later always the upper sign) since for the "+"-sign the field would grow exponentially when $x \to \infty$. If $k_z^2 < \epsilon^c\omega^2/c^2$, here we use the +-sign (later always the lower sign) to obtain only outgoing along x propagating waves[13]. Please note that the negative x-half-space has not to be considered separately since the transverse fields are symmetric in x and the longitudinal fields are antisymmetric since we consider a symmetric $\breve{\iota}_y$ and following App. C.

$\breve{E}_y$ has to be continuous at the plasma-cladding interface. Moreover, $\breve{B}_z$ and thus according to Eq. (5.4.5) $\partial_x \breve{E}_y$ have to be continuous at the interface. These two conditions determine A^{c}

[12] It can be found by firstly computing the solution to the homogeneous Eq. (5.4.11) that is $\breve{E}_y^{\mathrm{p}} = A^{\mathrm{p}} \cosh\left(\Lambda^{\mathrm{p}} x\right) + B^{\mathrm{p}} \sinh\left(\Lambda^{\mathrm{p}} x\right)$. Since $\breve{S}_y$ is symmetric in x, $\breve{E}_y$ has to be also symmetric and thus $B^{\mathrm{p}} = 0$. The particular solution can be found by means of variation of constants.

[13] This result depends on the sign conventions in the definition of the Fourier transform in App. A.

and A^{p} to

$$A^{\mathrm{c}} = A^{\mathrm{p}} \cosh\left(\frac{\Lambda^{\mathrm{p}} d}{2}\right) + \frac{S_y}{(\Lambda^{\mathrm{p}})^2}\left[\cosh\left(\frac{\Lambda^{\mathrm{p}} d}{2}\right) - 1\right] \tag{5.4.14}$$

$$A^{\mathrm{p}} = \frac{\frac{S_y}{\Lambda^{\mathrm{p}}} \sinh\left(\frac{\Lambda^{\mathrm{p}} d}{2}\right) \pm \frac{\Lambda^{\mathrm{c}} S_y}{(\Lambda^{\mathrm{p}})^2}\left[\cosh\left(\frac{\Lambda^{\mathrm{p}} d}{2}\right) - 1\right]}{\underbrace{\mp \Lambda^{\mathrm{c}} \cosh\left(\frac{\Lambda^{\mathrm{p}} d}{2}\right) - \Lambda^{\mathrm{p}} \sinh\left(\frac{\Lambda^{\mathrm{p}} d}{2}\right)}_{=D_1}}, \tag{5.4.15}$$

where we introduced the denominator D_1 that will be further investigated below.

Finally Eqs. (5.4.5)-(5.4.6) determine the magnetic fields to

$$\breve{B}_x = -\frac{k_z}{\omega}\breve{E}_y \tag{5.4.16}$$

$$\breve{B}_z = \frac{\Lambda^{\mathrm{p}}}{\mathrm{i}\omega}\begin{cases} A^{\mathrm{p}} \sinh\left(\Lambda^{\mathrm{p}} x\right) + \frac{S_y}{(\Lambda^{\mathrm{p}})^2} \sinh\left(\Lambda^{\mathrm{p}} x\right) & \text{for } 0 \le x \le \frac{d}{2} \\ \mp \frac{\Lambda^{\mathrm{c}}}{\Lambda^{\mathrm{p}}} A^{\mathrm{c}} \exp\left[\mp \Lambda^{\mathrm{c}}\left(x - \frac{d}{2}\right)\right] & \text{for } x > \frac{d}{2} \end{cases}. \tag{5.4.17}$$

5.4.1.2. TM with transverse excitation in x

Next, case (ii) with $\breve{\iota} = \breve{\iota}_x \mathbf{e}_x$ is considered. Eqs. (5.4.8)-(5.4.10) give the evolution equation for the transverse field $\breve{B}_y$ inside the plasma and air correspondingly to

$$\partial_x^2 \breve{B}_y - \Lambda^2 \breve{B}_y = \underbrace{-\mathrm{i}k_z \breve{Q}_x}_{=\breve{S}_x}. \tag{5.4.18}$$

In analogy to the TE case in the previous section, we obtain in the plasma

$$\breve{B}_y^{\mathrm{p}} = A^{\mathrm{p}} \cosh\left(\Lambda^{\mathrm{p}} x\right) + \frac{S_y}{(\Lambda^{\mathrm{p}})^2}\left(\cosh\left(\Lambda^{\mathrm{p}} x\right) - 1\right) \tag{5.4.19}$$

and in the positive x-half-space in the cladding

$$\breve{B}_y^{\mathrm{c}} = A^{\mathrm{c}} \exp\left[\mp \Lambda^{\mathrm{c}}\left(x - \frac{d}{2}\right)\right]. \tag{5.4.20}$$

The difference to TE appears when applying the continuity conditions at the plasma-air interface: $\breve{B}_y$ is continuous but the continuity of $\breve{E}_z$ does not induce the continuity of $\partial_x \breve{B}_y$ according to Eq. (5.4.10) since ϵ changes at the interface[14]. Applying the continuity conditions determines A^{c} and A^{p} to

$$A^{\mathrm{c}} = A^{\mathrm{p}} \cosh\left(\frac{\Lambda^{\mathrm{p}} d}{2}\right) + \frac{S_y}{(\Lambda^{\mathrm{p}})^2}\left[\cosh\left(\frac{\Lambda^{\mathrm{p}} d}{2}\right) - 1\right] \tag{5.4.21}$$

$$A^{\mathrm{p}} = \frac{\frac{S_x}{\Lambda^{\mathrm{p}}} \sinh\left(\frac{\Lambda^{\mathrm{p}} d}{2}\right) \pm \frac{\epsilon^{\mathrm{p}}}{\epsilon^{\mathrm{c}}} \frac{\Lambda^{\mathrm{c}} S_x}{(\Lambda^{\mathrm{p}})^2}\left[\cosh\left(\frac{\Lambda^{\mathrm{p}} d}{2}\right) - 1\right]}{\underbrace{\mp \frac{\epsilon^{\mathrm{p}}}{\epsilon^{\mathrm{c}}} \Lambda^{\mathrm{c}} \cosh\left(\frac{\Lambda^{\mathrm{p}} d}{2}\right) - \Lambda^{\mathrm{p}} \sinh\left(\frac{\Lambda^{\mathrm{p}} d}{2}\right)}_{=D_2}}, \tag{5.4.22}$$

where we introduced the denominator D_2. Please note the difference compared to D_1 for TE in Eq. (5.4.15), the factor $\epsilon^{\mathrm{p}}/\epsilon^{\mathrm{c}}$.

[14] Note that here $\breve{Q}_z = 0$. The case $\breve{Q}_z \neq 0$ is considered in the following section.

Finally, Eqs. (5.4.8)-(5.4.9) determine the electric fields to

$$\breve{E}_x = \frac{k_z c^2}{\omega\epsilon}\breve{B}_y - \frac{\mathrm{i}c^2}{\omega\epsilon}\breve{Q}_x \tag{5.4.23}$$

$$\breve{E}_z = \frac{\mathrm{i}c^2\Lambda^\mathrm{p}}{\omega\epsilon}\begin{cases} A^\mathrm{p}\sinh\left(\Lambda^\mathrm{p}x\right) + \frac{S_y}{(\Lambda^\mathrm{p})^2}\sinh\left(\Lambda^\mathrm{p}x\right) & \text{for } 0 \le x \le \frac{d}{2} \\ \mp\frac{\Lambda^\mathrm{c}}{\Lambda^\mathrm{p}}A^\mathrm{c}\exp\left[\mp\Lambda^\mathrm{c}\left(x-\frac{d}{2}\right)\right] & \text{for } x > \frac{d}{2} \end{cases} . \tag{5.4.24}$$

5.4.1.3. TM case with longitudinal excitation in z

Finally, case (iii) with $\breve{\boldsymbol{\iota}} = \breve{\iota}_z\mathbf{e}_z$ is considered. Same as for case (ii), the electromagnetic fields are of the TM type described by Eqs. (5.4.8)-(5.4.10). Now in contrast to the previous cases, the longitudinal fields are symmetric and the transverse fields are antisymmetric in x. The transverse magnetic field B_y fulfills the homogeneous Eq. (5.4.18) with $\breve{Q}_x = 0$ [15]. In the plasma

$$\breve{B}_y^\mathrm{p} = A^\mathrm{p}\sinh\left(\Lambda^\mathrm{p}x\right) \tag{5.4.25}$$

and in the positive x-half-space in the cladding

$$\breve{B}_y^\mathrm{c} = A^\mathrm{c}\exp\left[\mp\Lambda^\mathrm{c}\left(x-\frac{d}{2}\right)\right] . \tag{5.4.26}$$

The continuity conditions give

$$A^\mathrm{c} = A^\mathrm{p}\sinh\left(\frac{\Lambda^\mathrm{p}d}{2}\right) \tag{5.4.27}$$

$$A^\mathrm{p} = \frac{-\breve{Q}_z}{\underbrace{\mp\frac{\epsilon^\mathrm{p}}{\epsilon^\mathrm{c}}\Lambda^\mathrm{c}\sinh\left(\frac{\Lambda^\mathrm{p}d}{2}\right) - \Lambda^\mathrm{p}\cosh\left(\frac{\Lambda^\mathrm{p}d}{2}\right)}_{=D_3}} , \tag{5.4.28}$$

where we introduced the denominator D_3. Please note the difference compared to D_2 for TM and a transverse excitation in Eq. (5.4.22), the sinh and cosh are interchanged.

Finally Eqs. (5.4.8)-(5.4.9) determine the electric fields to

$$\breve{E}_x = \frac{k_z c^2}{\omega\epsilon}\breve{B}_y \tag{5.4.29}$$

$$\breve{E}_z = \frac{c^2\Lambda^\mathrm{p}}{\mathrm{i}\omega\epsilon}\left[\frac{\breve{Q}_z}{\Lambda^\mathrm{p}} - \begin{cases} A^\mathrm{p}\cosh\left(\Lambda^\mathrm{p}x\right) & \text{for } 0 \le x \le \frac{d}{2} \\ \mp\frac{\Lambda^\mathrm{c}}{\Lambda^\mathrm{p}}A^\mathrm{c}\exp\left[\mp\Lambda^\mathrm{c}\left(x-\frac{d}{2}\right)\right] & \text{for } x > \frac{d}{2} \end{cases}\right] . \tag{5.4.30}$$

5.4.2. The response of a plasma slab

In the following, the response of the plasma slab to the three previously established cases of excitation is analyzed for a (k_z,ω)-independent constant excitation source $\breve{\boldsymbol{\iota}}$. Hereby, we are interested in resonant features of the structure.

The previously derived coefficients A^p, A^c determine the field strength. When those become large, we can expect an enhanced, resonant excitation. A necessary condition is then that the denominators D_1, D_2, D_3 become zero (or small). In Fig. 5.4.2, the inverse of the denominator is presented for the three cases (column-wise) for $\nu_\mathrm{ei} = 0$ (1^st row) and $\nu_\mathrm{ei} \neq 0$ (2^nd row) in a

[15] Hereby the assumption of a constant excitation in the plasma is used giving $\partial_x\breve{Q}_z = 0$.

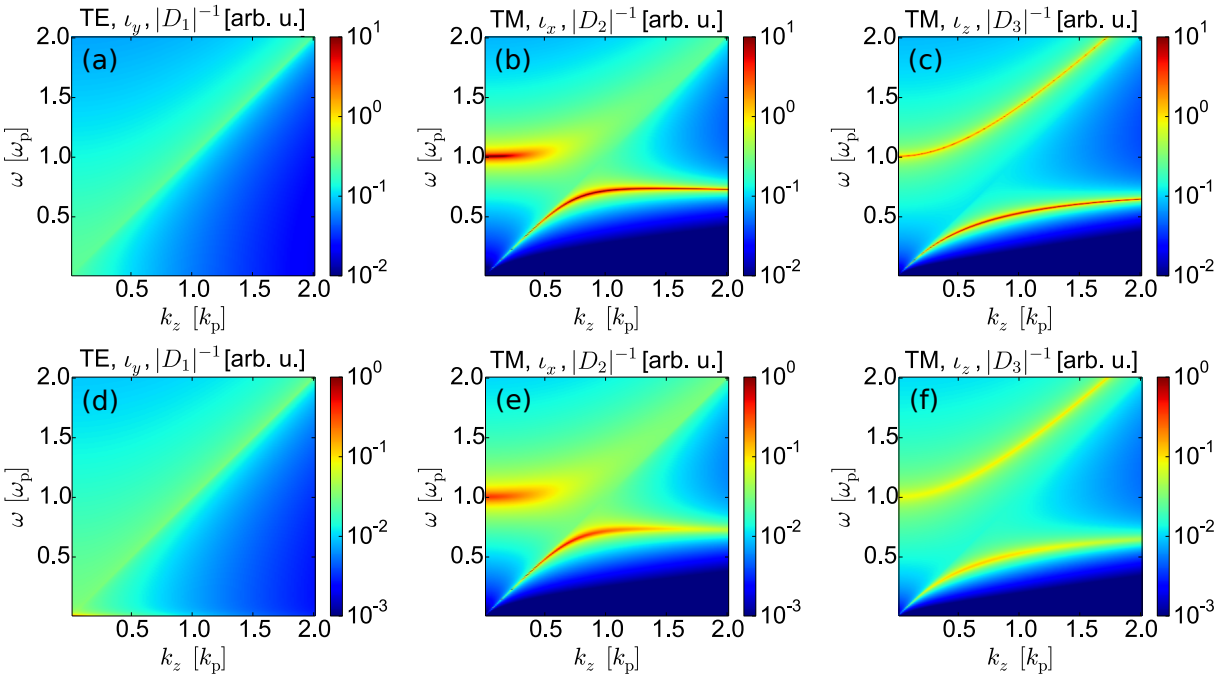

Figure 5.4.2.: Inverse denominator D_i for $\nu_{ei} = 0$ (a-c) and $\nu_{ei} = 13$ ps^{-1} (d-f), where in the slab $\boldsymbol{\iota} = \mathbf{e}_y$ (TE) in the 1st column, $\boldsymbol{\iota} = \mathbf{e}_x$ (TM) in the 2nd column and $\boldsymbol{\iota} = \mathbf{e}_z$ (TM) in the 3rd column. The slab thickness is $d = 1\,\mu$m, the plasma frequency $\nu_p = 49.15$ THz.

saturated color-scale plot. We find no characteristic features for TE (a,d), but two resonance branches for TM and both transverse (b,e) and longitudinal (c,f) excitation. Those are more pronounced for $\nu_{ei} = 0$, but otherwise similar when taking into account collisions or neglecting them.

For $d \to \infty$ the plasma-cladding interfaces separate from each other and one might expect for the slab a similar response as for a single plasma-cladding interface. Indeed, features similar to those in Fig. 5.4.2(e,f) have been already presented for the plasma-air interface in Fig. 5.4.1(b). It agreement with our observations of Fig. 5.4.2(d-f), it is known that such an interface does not provide resonances for the TE case but for the TM case [138]. To see it from our plasma slab model, we make a link from a plasma slab to a single plasma-dielectric interface by considering the boarder case $d \to \infty$. For our plasma slab, the denominator D_1 (TE) goes as $\exp(\Lambda^p d/2)(\mp\Lambda^c - \Lambda^p)/2$ if $d \to \infty$. But this expression is always different from zero since $\epsilon^c \neq \epsilon^p$ for each ω. Thus, one does not obtain any resonances in the TE case. The situation is different for D_2 which goes as $\exp(\Lambda^p d/2)(\mp\Lambda^c \epsilon^p/\epsilon^c - \Lambda^p)/2$ if $d \to \infty$. This expression has zeros that can be shown to coincide with the SPP resonance that is presented in Fig. 5.4.1(b) and explains the lower branch in Fig. 5.4.2(e). The upper branch corresponds to the VPP that is characterized by $\Lambda^p = 0$ explaining the enhancement of D_2 for $\omega \to \omega_p$. Also D_3 that we found for a longitudinal excitation goes as $\exp(\Lambda^p d/2)(\mp\Lambda^c \epsilon^p/\epsilon^c - \Lambda^p)/2$ if $d \to \infty$ such that also here SPPs can be excited in this limit explaining the lower branch in Fig. 5.4.2(f). For D_3, we can immediately see for $\Lambda^p = 0$ characterizing the VPP that $D_3 = 0$ explaining the upper branch in Fig. 5.4.2(f).

It is important to note, that for a finite plasma thickness d, D_2 and D_3 are different, even if they belong both to the TM case. We shall remember that they were obtained for two different

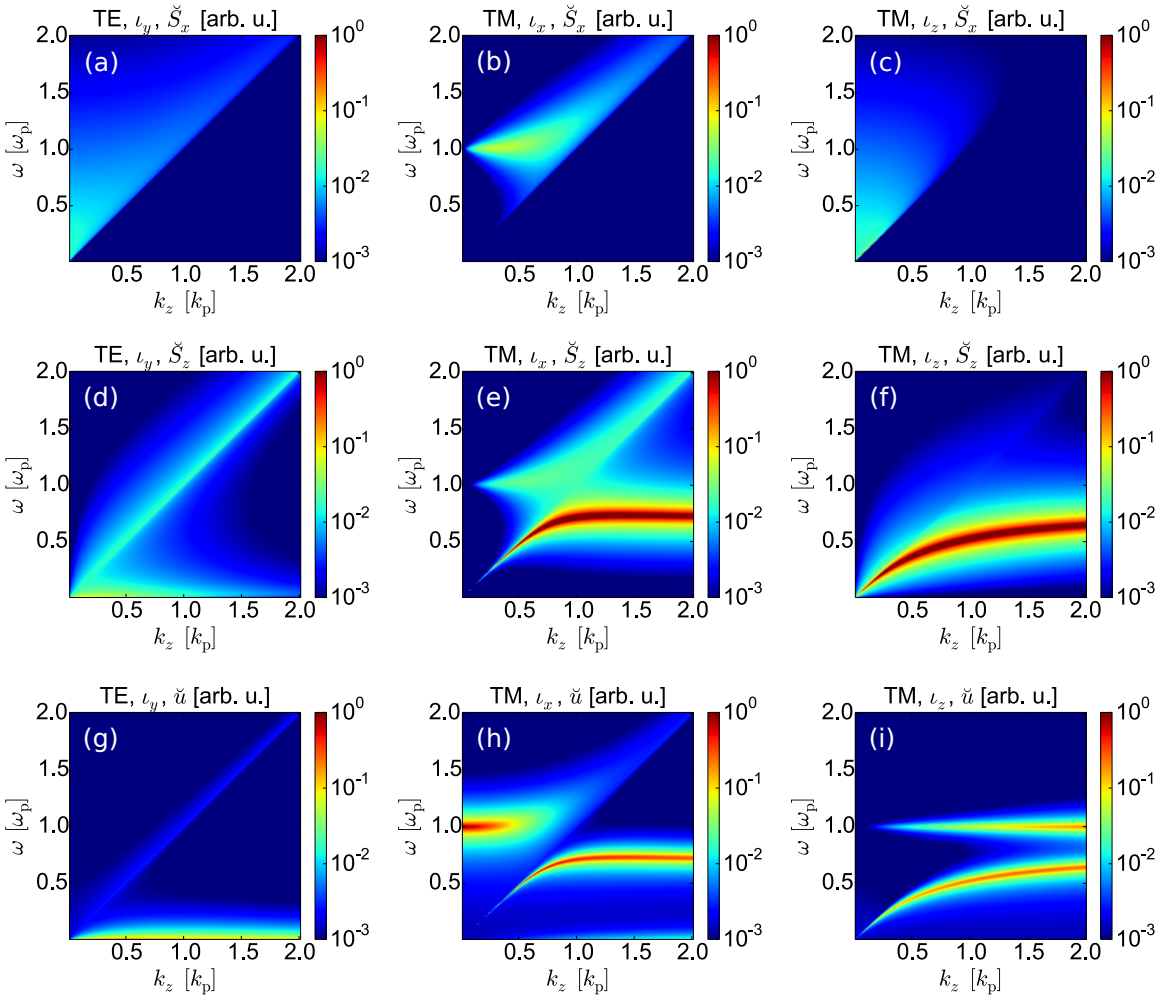

Figure 5.4.3.: Poynting fluxes in the x-direction normal to the slab (a-c) and in the z-direction along the slab (d-f) at $x = 0.51 \cdot d$, i.e., just at the slab surface in the vacuum. Spectral energy $\breve{u}$ in the slab (g-i). In the 1st column $\breve{\boldsymbol{\iota}} = \mathbf{e}_y$ (TE), in the 2nd $\breve{\boldsymbol{\iota}} = \mathbf{e}_x$ (TM) and in the 3rd $\breve{\boldsymbol{\iota}} = \mathbf{e}_z$ (TM) inside the slab. The slab thickness is $d = 1\,\mu$m, the plasma frequency $\nu_p = 49.15$ THz and the collision frequency $\nu_{ei} = 13$ ps^{-1}.

types of excitation. D_2 describes the excitation by a transverse current source along x and D_3 describes the excitation by a longitudinal current source along z. These results in the different responses in Fig. 5.4.2(e) and Fig. 5.4.2(f). While the resonances for the longitudinal excitation in Fig. 5.4.2(f) almost follow the single-interface resonances in Fig. 5.4.1(b), the transverse TM-like excitation in Fig. 5.4.2(e) shifts the resonances closer to ω_p.

Finally, let us analyze how these resonances radiate. To this end we introduce the spectral poynting flux $\breve{\mathbf{S}} = 2/\mu_0 \Re\{\breve{\mathbf{E}} \times \breve{\mathbf{B}}^\star\}$ and the spectral energy density $\breve{u} = \int_{-d/2}^{d/2} (\epsilon_0 |\breve{\mathbf{E}}|^2 + |\breve{\mathbf{B}}|^2/\mu_0)\, dx$. Fig. 5.4.3 presents the emitted flux $\breve{S}_x$ (1st row) and the along the surface guided flux $\breve{S}_z$ (2nd row) just above the plasma-air interface. Due to previous considerations it is not surprising that no features are observed for the TE case in the 1st column. For TM and transverse excitation (2nd column), a VPP-like enhancement of emission at ω_p can be found in (b). For longitudinal excitation (3rd column), no VPP-like enhancement of emission can be found in (c). The reason is that $\Lambda^p d$ is small and the electric field $\breve{E}_z(x = d/2) \propto \sinh(\Lambda^p d/2)$ following

Eq. (5.4.30) becomes also small such that no enhancement of $\breve{S}_x$ is possible. However, the spectral energy density in Fig. 5.4.3(i) reveals that the plasma is excited resonantly at ω_p for all k_z by longitudinal excitations that do not lead to radiation. Those are called bulk plasmon polaritons (BPPs) since they can be also met in homogeneous plasmas. We should note that for both transverse and longitudinal TM excitation a strong SPP-like flux is observed (e,f).

In summary, we have seen three important effects in a plasma slab:

- TE-like excitations, i.e. excitations in the translational invariant direction do not lead to resonances of the plasma slab response
- TM-like transverse excitations provide VPP- and SPP-like resonances
- longitudinal excitation provides resonant enhancement at the plasma frequency, however, the emission at ω_p is not enhanced since d is small

In the following, these observations will be used to interpret better some of tendencies that have been observed in previous rigorous simulations.

5.4.3. Spectral polarization dependence in elliptical beams

In Sec. 5.3.2, we have seen that the THz spectra emitted from elliptical beams depend on the driving laser polarization. In contrast to laser pulses that are polarized in the quasi translational invariant direction y (quasi TE), x-polarized driving pulses (quasi TM) lead to spectral broadening up to ν_p. We use the plasma slab model to show that this broadening is most likely a result of plasmon-polariton-like resonances.

To this end we assume a model excitation source $\boldsymbol{\iota}_1(z) = \boldsymbol{\iota}^\mathrm{mod}(z) = q_\mathrm{e}^2 n_0[\mathbf{E}_\mathrm{L}(x = 0, z)]/m_\mathrm{e}\mathbf{E}_\mathrm{L}(x = 0, z)$ using the on-axis 2D paraxial approximation for the 2C-laser field in analogy to App. I. The laser parameter are the same as in Sec. 5.3.2. We consider the amplitude of the source depending on the temporal frequency ω_L and spatial frequency k_z, i.e., in spatial and temporal Fourier space, in Fig. 5.4.4(a)[16]. We find that the excitation of forward emitting waves ($k_z > 0$) is slightly preferred compared to backward propagating waves ($k_z < 0$). It ranges up to $\omega = \omega_\mathrm{p}$ and $k_z = k_\mathrm{p}$.

Next, we consider the response of the plasma slab to this excitation for the TE case and the TM case using the plasma slab model from Sec. 5.4.1.1 and Sec. 5.4.1.2. The resulting spectral poynting fluxes just above the interface are presented in Fig. 5.4.4(c-f). No resonant features are excited for TE (1$^\mathrm{st}$ column) and we find signatures of VPPs and SPPs for TM (2$^\mathrm{nd}$ column). According to the plasma slab model only waves with $\breve{S}_x \neq 0$ contribute to far-field emission, which we compute as $\hat{P}_x = \int \breve{S}_x \, dk_z$. Using the result from Fig. 5.4.4(c-d) we evaluate the far-field spectrum that is presented in Fig. 5.4.4(g). It reproduces almost perfectly the qualitative difference between the 3D quasi TE and quasi TM simulation results in Fig. 5.3.4: The TE far-field power spectrum is peaked slightly below 10 THz and then decreases rapidly. The TM power spectrum is broadened up to the maximum plasma frequency that has been taken as the plasma frequency of the plasma slab ν_p. According to the plasma slab model, the VPP is responsible for the emission at the plasma frequency. However, as we will discuss in the next section, also the SPP can contribute to far-field emission and slightly shift the emission peak from the plasma frequency towards lower frequencies.

Please note, we have made observations of transverse nonradiating oscillation at the plasma frequency in transversally DC-biased microplasmas in Sec. 4.4 and in elliptical beams for the TM case. Thus, we shall conclude that oscillations at the plasma frequency for the TM case

[16] Please keep in mind that the modulus of the source does not depend on whether $\mathbf{E}_\mathrm{L}$ is x- or y-polarized.

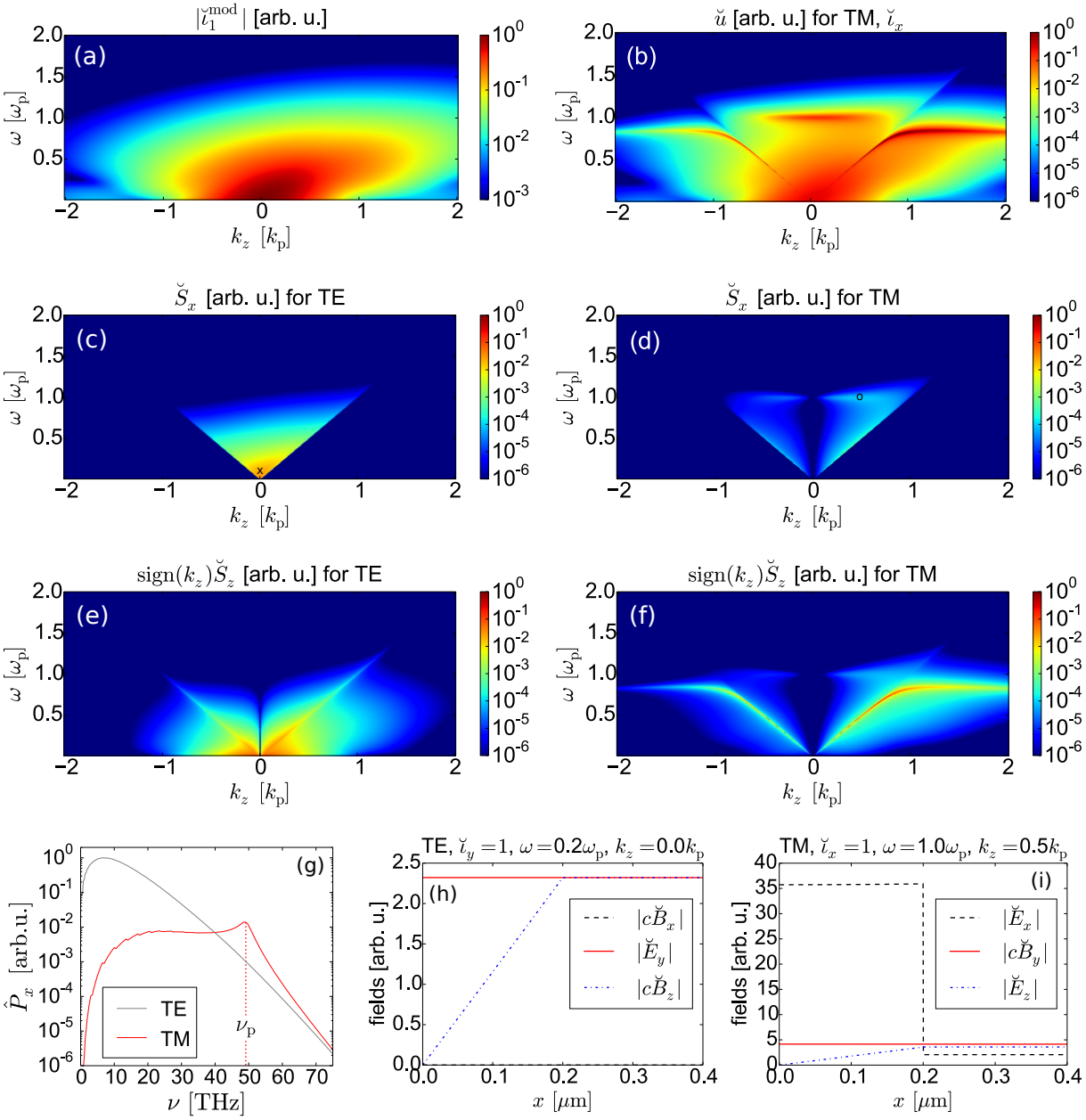

Figure 5.4.4.: Results of the slab model using the on-axis excitation spectrum (a) ι_1^{mod} of a 2D ($\partial_y \equiv 0$) 2C-laser pulse (see text for details). The slab thickness is $d = 0.4\,\mu$m, the plasma frequency $\omega_p/(2\pi) = \nu_p = 49.15$ THz and the collision frequency $\nu_{ei} = 13$ ps^{-1}. (b) Spectral energy $\breve{u}$ in the slab for an x-polarized laser (TM). Spectral poynting fluxes in the x-direction normal to the slab (c,d) and in the z-direction along the slab (e,f) at $x = 0.51 \cdot d$, i.e., just at the slab surface in the vacuum. In (c-f), in the 1st column the laser is y-polarized (TE), in the 2nd column the laser is x-polarized (TM). (g) Comparison of the k_z-integrated far-field spectra for TE and TM according to the plasma-slab model. (h) Field profiles of the mode $\omega = 0.2\omega_p$, $k_z = 0$ that is marked by the black cross in (c). (i) Field profiles of the mode $\omega = \omega_p$, $k_z = 0.5k_p$ that is marked by the black circle in (d).

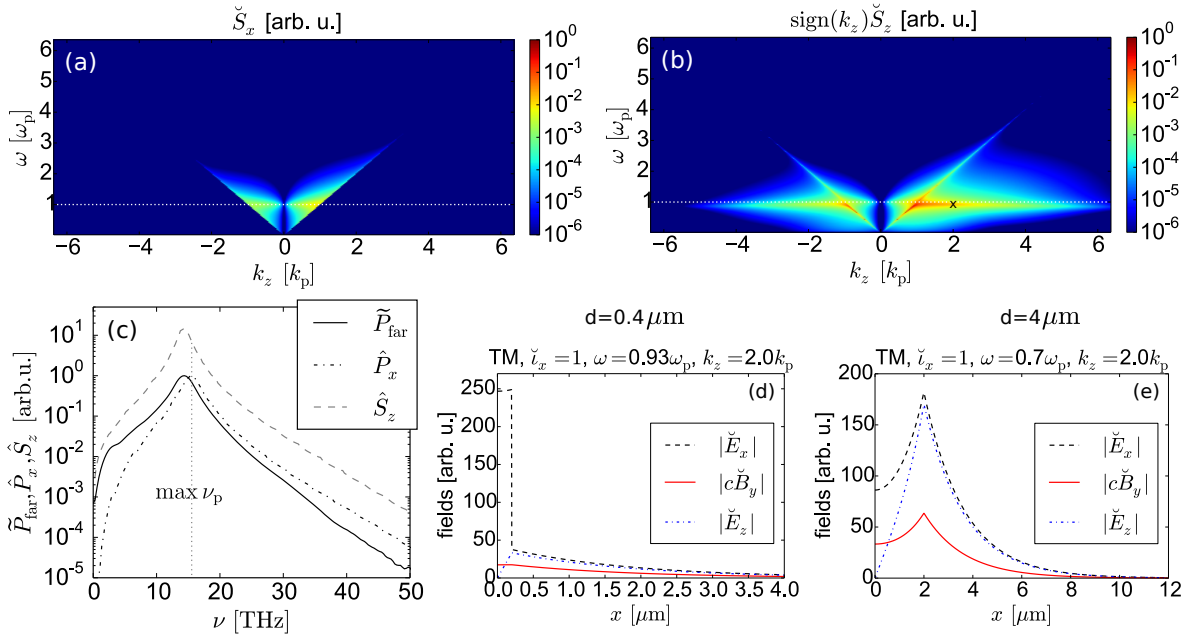

Figure 5.4.5.: Results of the slab model for reduced gas pressure $p \approx 0.1$ corresponding to the plasma frequency $\omega_p/(2\pi) = \nu_p = 15.54$ THz. Other parameter are the same as in Fig. 5.4.4 for an x-polarized laser (TM). (a-b) Spectral pointing fluxes just at the slab surface in the vacuum ($x = 0.51d$). The horizontal white dotted line specifies the plasma frequency. (c) Comparison of the far-field spectra according to the slab model (black dash-dotted line) and the rigorous 3D simulation with ARCTIC (black solid line) same as presented in Fig. 5.3.7. Now, in addition the k_z-integrated poynting flux $\hat{S}_z$ along z is presented (gray dashed line). (d) Field profile of the surface-plasmon-polariton-like mode at $\omega = 0.93\omega_p$, $k_z = 2k_p$ that is marked by the black circle in (b). (e) The same resonance for a thicker slab with $d = 4\,\mu$m, now at $\omega = 0.7\omega_p$ for the same k_z.

are not only radiative. The power spectrum in Fig. 5.4.4(b) reveals that around $\omega = \omega_p$ close to $k_z = 0$ a large electromagnetic energy density is present in the plasma slab, but according to Fig. 5.4.4(d) nothing is emitted there. The field structure in Fig. 5.4.4(i) visualizes that the high electro-magnetic energy density is due to the transverse electric field E_x which cannot contribute to the far-field power spectrum $\hat{P}_x$. It is much stronger than the fields B_y and E_z which can contribute to emission.

5.4.4. Spectra from TM-polarized elliptical beams at low gas pressures

For TM-polarized elliptical beams in Sec. 5.3.3, we have seen that THz emission spectrum is broadened up to the maximum plasma frequency that is gas pressure dependent. According to our previous result, the VPP leading to enhancement of the emission at ν_p can explain this behavior. However, we found in Sec. 5.3.3 in rigorous simulations that the emission peak is typically shifted from the maximum plasma frequency to slightly lower frequencies. This shift was most clearly visible at low gas pressures $p < 1$ bar. In the following, we argue that this behavior indicates SPP-like excitation that finally leads to THz emission.

How is it possible that SPPs, that are waves bounded to the plasma-dielectric interface, lead to emission? The plasma slab model has a drawback: it accounts only for excitation of SPPs but not their emission since the plasma is translational invariant in z. THz-SPPs, as sketched in Fig. 5.4.1(a) (blue color), are excited and propagate along the plasma slab. In reality, however, the plasma is finite having truncations along z. When SPPs reach the plasma truncations, they can be reflected or transmitted leading to emission into the far-field. In the following, we only keep track of SPP excitation to provide an explanation of the previously mentioned shift from the maximum plasma frequency.

We consider the same excitation as in the previous section for the TM case, but now assuming a plasma frequency corresponding to a fully singly ionized gas at 10 times lower gas pressure $p \approx 0.1$ bar. The resulting spectral poynting fluxes are presented in Fig. 5.4.5(a,b). When comparing the guided flux in Fig. 5.4.5(b) with Fig. 5.4.4(f) where the plasma frequency is 10 times higher, much larger k_z in units of $k_\mathrm{p} = \omega_\mathrm{p}/c$ are excited. For large k_z/k_p, the SPPs are excited at a constant frequency slightly below ω_p. Their signature can be seen when considering the k_z-integrated spectral flux $\hat{S}_z = \int \breve{S}_z \, dk_z$ in Fig. 5.4.5(c) that results in a peak slightly below the plasma frequency. For comparison, the emitted power spectrum $\hat{P}_x$ according to the plasma slab model and the far-field power spectrum of the rigorous ARCTIC simulation [same as in Fig. 5.3.7(a)] is shown. While $\hat{P}_x$ does not support the shift from the maximum plasma frequency, the SPP resulting in the frequency peak in $\hat{S}_z$ could be the reason of the small shift from max ν_p. Thus, both VPPs and SPPs can in principle influence the THz emission properties.

Finally, we should comment on the strength of the shift. The SPP frequency for large k_z and a single plasma-air interface is at $\omega = \omega_\mathrm{p}/\sqrt{2}$. For finite d, the SPP-frequency is the higher the smaller d is. For the considered plasma slab the resonance is at $0.93\omega_\mathrm{p}$. Thus, the shift from the maximum plasma frequency depends on the thickness of the plasma. Moreover, according to the large spectral shifts away from the maximum plasma frequency for cylindrical beams and low gas pressures in Secs. 5.1.2.2, 5.2.4, we can expect that the strength of the shift is in general plasma-shape dependent.

In Fig. 5.4.5(d,e), the field structure of the SPP is presented for $d = 0.4\,\mu$m and $d = 4\,\mu$m. Obviously, for thicker plasmas an even stronger SPP is created. However, it is localized withing only few μm and thus is expected to disappear when the electron density gradient is too weak.

5.4.5. Non-radiating oscillations at the plasma frequency

We have seen in Chap. 4 for 1C-laser-driven THz generation with and without an external DC-bias that longitudinal excitations lead to oscillations at the local plasma frequency which do not radiate. In Sec. 4.2, we presented a general solution for non-radiative plasma oscillation [Eq. (4.2.6)]. Here, we want to elaborate the excitation of such oscillations that have been previously introduced as BPPs by the plasma slab model.

To this end we investigate the example of the tightly focused 1C-laser pulse from Sec. 4.3. The excitation spectrum is computed by assuming $\boldsymbol{\iota}^\mathrm{mod} = \iota_z^\mathrm{pond}(x = 0, z)\mathbf{e}_z$ using the 2D on-axis ponderomotive source from App. I. Its spectral amplitude is presented in Fig. 5.4.6(a) preferring slightly more forward waves. Resulting spectral poynting fluxes are shown in Figs. 5.4.6(b,d). No VPP is excited and thus no resonant features are visible in the emission spectrum in Fig. 5.4.6(e). The plasma slab model (light gray line) coincides well with the PIC results (dark red line) that are the same as in Fig. 4.2.3. The deviation at 20 THz might rely on SPPs that are excited according to Fig. 5.4.6(d) but not radiating in the framework of the present plasma slab model.

The fact that no emitting resonant features are present justifies the simplified model in Sec. 4.3.2 that does not account for the plasma-response (except corrections that account for plasma opacity). However, the model in Sec. 4.3.2 was not able to reproduce the result that no

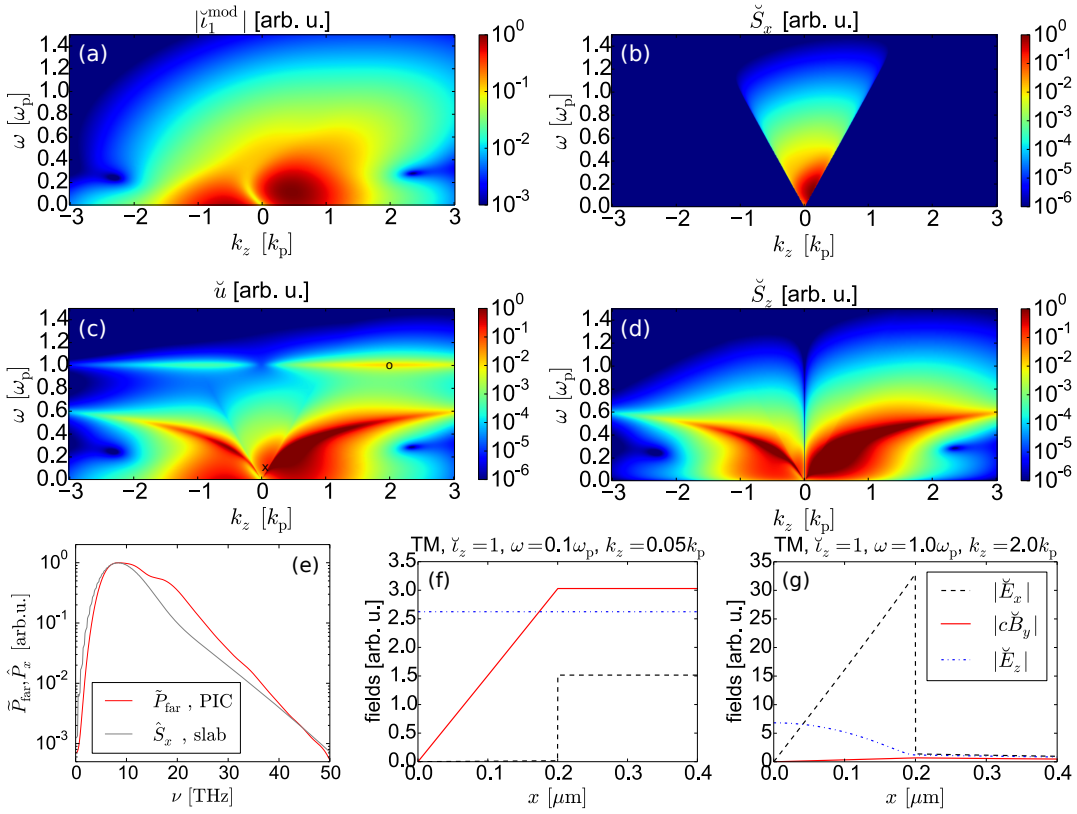

Figure 5.4.6.: Results of the slab model using the on-axis excitation spectrum (a) $\iota_{2,z}^{\text{pond}}$ of a 2D ($\partial_y \equiv 0$) 1C-laser pulse (see text for details). The slab thickness is $d = 0.4\,\mu$m, the plasma frequency $\omega_p/(2\pi) = \nu_p = 49.15$ THz and the collision frequency $\nu_{ei} = 13$ ps^{-1}. Spectral poynting flux in the x-direction normal to the slab (b) and in the z-direction along the slab (d) at $x = 0.51 \cdot d$. (c) Spectral energy $\breve{u}$ in the slab. (e) Comparison of the k_z-integrated far-field spectra according to the plasma-slab model and the PIC simulation same as in Fig. 4.2.3 (red line) in Chap. 4. (f) Field profiles of the mode $\omega = 0.1\omega_p$, $k_z = 0.05k_p$ that is marked by the black cross in (c). (g) Field profiles of the mode $\omega = \omega_p$, $k_z = 2k_p$ that is marked by the black circle in (c).

emission takes place at frequencies close to $\omega = 0$, that is now possible with the plasma slab model.

To visualize the field structure of the emitting modes, one selected emitting mode is characterized in Fig. 5.4.6(f). The corresponding ratio of the electric field amplitudes determines the emission angle θ: $\tan(90° - \theta) = E_x/E_z = 1.5/2.6 \to \theta = 60°$ that is close to the maximum emission angle of 70° as found by PIC simulation results in Sec. 4.3.

In PIC simulations, we found that oscillations at the plasma frequency exist but do not radiate. Also in the framework of the plasma slab model, we find these oscillations as can be seen from the spectral electromagnetic energy density in Fig. 5.4.6(c). The field profile for one selected mode in Fig. 5.4.6(g) displays a strong electric field E_x confirming that these oscillations appear normal to the electron density gradient, along x, in agreement with the nonradiating oscillating solution in Sec. 4.2.

In summary a simplified 2D model of THz emission accounting for resonant plasma response has been developed. It explains the absence of spectral broadening and resonant features for elliptical beams where the excitation takes place in the transverse direction in which the plasma size is larger than the plasma wavelength. If the excitation takes place along strong electron density gradients plasmon-polariton resonances can be excited and lead to THz emission. The plasma slab model confirms that longitudinal excitation can lead to nonradiating oscillations at the plasma frequency for thin plasmas d. The model reproduces spectral features of various simulations, but could be improved by accounting for plasma truncations.

5.5. Conclusions

THz emission from two-color-fs-laser-induced microplasmas has been investigated by means of 3D Maxwell-consistent simulations and simplified models. The conclusions are as follows:

In the strongest focusing case, microplasmas can act as point sources of THz emission, featuring toroidal radiation patterns that determine the orientation of the THz emitting current. This additional information is expected to facilitate the identification of the THz generating mechanisms in future experiments.

Sufficiently thin 2C microplasmas radiate in a resonant regime where the spectral width of the THz emission is broadened up to the maximum plasma frequency that increases with the gas pressure. In real 3D plasmas, also the emission peak frequency increases for low gas pressures, but stays approximately constant for higher gas pressures.

When the thickness of the plasma in polarization direction of the driving laser pulse becomes larger than the smallest plasma wavelength, the resonant features can disappear. This property leads to laser polarization dependent spectral tuning properties of THz emission from elliptical beams that approach the 2D configuration by real 3D laser beams.

A simplified 2D plasmonic plasma slab model that naturally takes into account the plasma response has been developed to further elaborate these spectral features. As the result, spectral broadening behavior could be attributed to plasmon-polariton-like resonances that exist only when the two-color laser is polarized along a strong plasma density gradient. Furthermore, the model confirms that no oscillations at the plasma frequency are emitted into the far field when a thin plasma is excited by longitudinal current sources as for 1C-driving lasers.

Another 3D model that accounts only for the plasma geometry has been developed. It shows that the transverse nature of the ionization currents in two-color pump configuration allows an excellent scalability of the laser-to-THz conversion efficiency, while THz generation mechanisms relying on longitudinal radiating currents are detrimental for the upscaling by increasing the plasma length. Furthermore, the particularly small width of microplasmas favors the up-scaling of the conversion efficiency compared to transversally much wider THz emitting sources like gas jets or nonlinear crystals.

This model was used to optimize the focusing conditions of a circular Gaussian beam for a given laser pulse energy. Focusing conditions leading to fully singly ionized plasmas turned out to be nearly optimal as long as nonlinear propagation effects can be neglected. To scale the optimal focusing conditions with the laser pulse energy, the focal beam width has to be increased with the square-root of the laser pulse energy. By using such optimized configuration, for laser pulse energies around 5 μJ the conversion efficiency can exceed 10^{-4}.

Another possibility to increase the conversion efficiency to the 10^{-4}-level by using elliptical beams has been presented. Besides laser-polarization tunable THz spectra, they offer 2D point-like emission profiles and can acts as THz line sources. By increasing their transverse size for mJ-driving laser pulses 100 nJ-THz-pulse energies could be produced.

6. Summary and outlook

In this thesis, we have theoretically investigated terahertz (THz) generation in fs-laser-induced microplasmas. This novel approach is promising to provide compact and efficient sources of broadband THz radiation. THz radiation has many applications as spectroscopic identification of hazardous substances, THz imaging in biology and medicine, thickness measurements in industrial processes and quality control as well as control over matter (see Sec. 1.1). These applications often require compact pulsed THz sources covering ideally the whole THz range from 0.3 to 30 THz and at least μW-THz-average output powers. For control over matter, THz field amplitudes above 0.1 MV/cm are usually needed.

Conventional THz sources as quantum cascade lasers, photoconductive switches and nonlinear-crystal-based schemes comply with many requirements of THz applications (see Sec. 1.2). Together they can cover almost the whole THz range. They produce THz average powers up to the mW-level while reaching laser-to-THz conversion efficiencies above 10^{-4} and can reach 1 MV/cm-strong THz fields. However, none of them can cover the whole THz gap at one blow. Furthermore, they often suffer from material damage.

Certain limitations of conventional emitters might be resolved by producing THz radiation in fs-laser-induced gas-plasmas (see Sec. 1.3). In a pioneering work, single-color (1C) driving laser pulses have been shown to produce THz emission when ionizing an initially neutral gas [55]. Using a gas-plasma already resolves the problem of material damage. However, laser-to-THz conversion efficiencies only about 10^{-8} were reached by this setup, i.e., far below what can be achieved with conventional sources. Two ways to increase the laser-to-THz conversion efficiency were proposed. Firstly, the conversion efficiency was shown to be enhanced by an external electric field (a DC-bias) for 1C driving laser pulses [56]. Secondly, a frequently used approach employs two-color (2C) mJ-driving-laser pulses. Here, conversion efficiencies can exceed the 10^{-4}-level [57]. Moreover, this scheme is known to produce ultra-broadband THz spectra covering the whole THz range. However, same as many conventional sources these gas-plasma-based approaches require mJ-strong driving laser pulses that limit their compactness and availability.

To miniaturize gas-plasma-based THz sources, Buccheri and Zhang [61] generated THz radiation by strongly focusing an only μJ-weak laser pulse into a gas. In contrast to previously reported approaches with mJ-driving laser pulses creating at least mm-large plasmas, this leads to the formation of a microplasma. However, conversion efficiencies as they can be reached by conventional THz sources and broadband THz-spectra as they can be reached by 2C-mJ-laser-induced gas-plasmas were not reported.

To make a step towards the realization of efficient small-scale THz sources based on laser-gas interaction, the attention of this thesis was set to the theoretical investigation of THz generation in fs-laser-induced microplasmas. To this end, we performed both, Maxwell-consistent modeling of THz emission employing large-scale numerical simulations and simplified analytical models that lead to a better understanding of the results obtained from rigorous simulations. We analyzed the mechanisms of THz generation in 1C-laser-induced microplasmas similar to those that have been investigated experimentally in [61]. Moreover, we applied the ideas that are known from mJ-laser-induced large gas-plasmas, namely DC-biased 1C-laser-induced and 2C-laser-induced gas-plasmas, to increase the laser-to-THz conversion efficiency in microplasmas. The following major steps have been performed and results obtained.

We derived a model based on the Maxwell equations, the non-relativistic Vlasov equation for the electrons, ionization rate equations for multiple ionization and taking elastic electron-ion collisions into account (see Chap. 2). For peak intensities above 10^{14} W/cm^2 and strong focusing conditions generating up to few-hundreds-of-μm-long microplasmas, the neutral polarization response was neglected in front of the free electron response. We derived the three lowest velocity moments of the Vlasov equation leading to continuity, Euler and energy balance equations. These equations and the Maxwell's equations were expanded by means of a multiple-scale analysis. We assumed that any microscopic quantity can be written as a perturbation series. This ansatz results in a hierarchy of equation-sets that can be associated with two THz generating mechanisms.

The lowest order set of equation describes the so-called ionization current (IC) mechanism. It accounts for ionization and the macroscopic current that is driven by the electric field. Moreover, the multiple scale analysis gives an energy equation that accounts for the heating of the electron gas. This allows to introduce an electron-ion collision frequency depending on the electron energy. This set of equations models in particular the THz generation in DC-biased 1C-laser-induced and 2C-laser-induced microplasmas. In some cases, also the often used unidirectional pulse propagation approach can describe THz emission driven by the IC mechanism. However, this approach is unsuitable for microplasmas since it cannot model THz emission at large angles as well as charge separation effects that require a Maxwell-consistent modeling as given by our lowest order set of equations.

The next higher order set of equations describes the so-called transition-Cherenkov (TC) mechanism. It accounts for excitation of the plasma by the ponderomotive source, but also additional ionization, collisional and heating-driven source terms. All these second order source terms can be computed from the lowest order quantities. This set of equations describes the THz generation in many-cycle 1C-laser-induced microplasmas.

In order to solve the model equations, several numerical tools were used and developed. For the numerical solution of the Vlasov equation, the particle-in-cell (PIC) codes OCEAN and CALDER were utilized. For the solution of the lowest order set of multiple-scale equations, the fluid code ARCTIC was developed based on the Yee-solver-version of OCEAN. The ARCTIC code was benchmarked against the PIC code OCEAN by comparing the THz emission spectra for smallest 2C-fs-laser-induced microplasmas in 3D (see Chap. 3).

Because we are working with strongly focused laser beams, it was necessary to develop an algorithm for both, fluid and PIC code, modeling laser beams beyond the paraxial approximation. This algorithm has the big advantage to introduce any arbitrarily shaped laser pulses into electromagnetic codes by prescribing its spatio-temporal shape in a plane (see Sec. 3.3). Nota bene, the novel approach can be useful for a larger community working on electromagnetic codes, in particular for investigation of matter-"structured light"-interaction or interaction of strongly focused laser beams with matter.

By means of our multi-scale model and numerical tools, we investigated THz emission from strongly focused 1C-fs-laser-induced microplasmas (see Chap. 4). The analysis of the current source terms revealed that the IC mechanism is negligible for multi-cycle 1C-laser pulses and the TC mechanism plays the leading role. Here, ponderomotive sources turned out to dominate radiation pressure, convective and diffusive sources. For a Gaussian beam, transverse currents excited by the TC mechanism do not lead to THz emission. The reason is their antisymmetry with respect to the transverse spatial coordinate. It leads to destructive interference in the far-field for an only 1-μm-thin plasma. However, TC-mechanism driven longitudinal currents are symmetric and can radiate. The longitudinal polarization of the radiating currents and the plasma length about 10 μm results in the hollow emission cone with an opening angle $> 70°$ in the presented PIC simulations in agreement with previously reported experimental results [61].

For many-cycle 1C-laser pulses, PIC simulations reveal THz emission up to 20 THz, i.e., far below the peak plasma frequency at about 50 THz in our simulations. Nevertheless, the plasma is strongly oscillating at the local plasma frequency. We have presented an analytical solution showing that even in an inhomogeneous plasma, oscillations at the local plasma frequency can exist without radiating into the far-field. Such non-radiating currents are curl-free. Previously established models imposed a synthetic plasma structure destroying this curl-free property introducing artificial radiation around the plasma frequency [59, 60, 64]. Our results show that the plasma response and shape have to be modeled consistently in order to avoid artificial radiation at the plasma frequency.

We have also developed a simplified model (plasma slab model) that accounts for the response of the plasma with a simplified slab-shape. Applying the longitudinal ponderomotive source to the plasma slab response reproduces well THz emission spectra obtained from PIC simulations (see Sec. 5.4.5). Also here, nonradiating electric field oscillations at the local plasma frequency normal to the electron density gradient were found and could be identified as the bulk plasmon polariton.

The absence of resonantly driven emission allowed to utilize the modified local current model to obtain estimations of the laser-to-THz conversion efficiency for various laser pulse parameter. The conversion efficiency has been shown to saturate to values around $10^{-6}-10^{-7}$ for larger laser pulse energies for different focusing conditions. The opacity of the plasma for THz frequencies turned out to play a crucial role for the saturation behavior. The results have been shown to be in good agreement with PIC simulations.

Moreover, we have investigated the gas pressure dependence of the conversion efficiency. In agreements with previously reported experiments, a quadratic scaling for low gas-pressures was found. This is an additional confirmation that the emission takes place in a rather non-resonant regime. For higher gas-pressures the conversion efficiency tends to saturate.

A similar behavior holds for longitudinally DC-biased 1C-laser-induced microplasmas (see Sec. 4.4). By increasing the gas pressure and bias-voltage, we could boost the conversion efficiency by 2 orders of magnitude compared to un-biased microplasmas. Here, THz emitting currents are excited additionally by a constant external electric field and can be modeled by the IC mechanism. Maxwell consistent simulations with ARCTIC have shown that also when exciting the plasma by an external longitudinal electric field, THz radiation is emitted far below the maximum plasma frequency albeit the plasma oscillates with the local plasma frequency. We exploited the flexibility to adjust the direction of the external electric field to show that the situation changes when applying the constant electric field in the transverse direction. Then in contrast to longitudinal excitation, radiation around the maximum plasma frequency is emitted. This demonstrates that the plasma shape is important for the THz emission spectrum.

Besides 1C-driving-laser pulses, we investigated THz emission from 2C-driving-laser pulses for microplasmas (see Chap. 5). Here, THz emission is induced by the IC mechanism that we have modeled by the code ARCTIC in 3D. In the strongest focusing case, the emitting plasma can act as a point-source of THz emission. Then, the polarization of the THz-emitting current can be determined directly from the toroidal radiation profile. This opportunity appears only for smallest microplasmas, since for larger emitting plasmas the more (forward) directed radiation profile is determined by the plasma length and thickness only.

We have shown that plasmas with a thickness of the order of or smaller than the smallest plasma wavelength along the laser polarization direction radiate in a resonant regime. For linearly polarized Gaussian laser beams, we have found a spectral broadening of the THz emission up to the maximum plasma frequency that is about 50 THz for a fully singly ionized gas at ambient pressure. For low gas pressures the plasma radiates resonantly with a gas-pressure-dependent peak below the maximum plasma frequency.

To interpret this behavior by a simplified model and potentially easily realizable experiments, we proposed to exploit transversally elliptically shaped laser beams that lead to elliptically shaped transverse electron density profiles. Maxwell-consistent 3D simulations have shown that THz emission spectra from elliptical beams are strongly dependent on the direction of the laser electric field vector. The emitted THz fields can be described for each polarization state superposing two fundamental cases: the quasi transverse electric (TE) and transverse magnetic (TM) cases. For the quasi TM case, the electric laser field points into the direction where the plasma is thin. Here, the emission spectrum is broadened up to the maximum plasma frequency. For the quasi TE case, the electric laser field points into the direction where the plasma is thick. Here, the THz emission spectrum is not broadened.

This behavior has been explained by our plasma slab model (see Sec. 5.4.3). For the quasi TM case, surface and volume plasmon polaritons are excited. Those provide resonant features that depend on the gas pressure and explain the spectral broadening. For the quasi TE case, no resonant features are present explaining the un-broadened emission spectrum. These investigations show a route towards THz-plasmonics in plasma-based THz generation schemes.

Furthermore, we have developed a 3D model that allows to estimate the scaling of the laser-to-THz conversion efficiency for various laser pulse energies and focusing conditions for a Gaussian beam (see Sec. 5.2). According to this model, focusing conditions leading to full single ionization in focus are optimum as long as nonlinear propagation effects are weak. Then, increasing the laser pulse energy with the focal beam width while keeping the peak intensity constant boosts the conversion efficiency with the laser pulse energy squared in the optimal case. By using such an optimized configuration, we have shown that already for few-μJ 2C-driving-laser pulses, the laser-to-THz conversion efficiency can exceed the 10^{-4}-level. Two effects play in favor of strong THz emission from 2C-color microplasmas: Firstly, the transverse nature of the ionization currents is advantageous for the up-scaling of the conversion efficiency with the plasma length compared to the TC mechanism and the opacity of the plasma for THz waves appears insignificant. These fundamental advantages of the IC mechanism hold for large and small plasmas. Secondly, exclusively for microplasmas, emitter radiate rather coherently due to the small transverse size of the source.

Besides competitive laser-to-THz conversion efficiencies, 2C-laser-induced microplasmas provide single-cycle broadband-THz pulses reaching strong THz-field amplitudes up to 0.5 MV/cm in the vicinity of the plasma. However, separating the laser pulse from the THz pulse close to the plasma remains challenging. We have shown that strongly focused elliptical beams provide THz pulses with 10 kV/cm-strong field amplitudes emitted normal to the laser propagation direction (see Sec. 5.3). Further investigations are planned involving the exploration of "structured light" to resolve this issue.

Using our algorithm to introduce arbitrarily shaped laser pulses into our fluid code ARCTIC (see Chap. 3), we can exploit even more exotic laser beams. For example, we plan to use the so-called caustic beams [139] to separate the THz pulse from the laser pulse just behind the plasma. If this can be done, strong THz fields could be accessed just in the vicinity of the plasma without strong focusing the THz beam that is limited by the diffraction limit of light.

Also for control over plasmonic effects during the THz generation process, we plan to investigate "structured light". For example, we could expect to switch resonant effects on or off by switching the polarization of a 2C-laser beam: For an azimuthally polarized laser field, the electric field vector is oriented almost normally to the electron density gradient, while for a radially polarized laser field, the electric field vector is almost parallel to the electron density gradient. Since we have shown a strong electron density gradient along the electric laser field to be necessary to excite plasmonic resonances, switching between this two polarization states might provide control over resonant effects. Moreover, employing modern beam shaping techniques,

we could engineer the plasma channel to switch between different plasmonic resonances. Besides resonant THz spectral tuning, we can expect to guide and confine THz pulses. All these considerations are applicable besides gas-plasmas to liquid- or solid-plasmas. These plasmas could be potentially interesting alternatives to gas-plasmas due to their high densities of electrons which are potential emitters. It should be investigated to which extent the radiating plasma volume can be maximized although the opacity for THz waves. For liquid- or solid-plasmas we should keep the Maxwell-consistent treatment, but extend the material response taking into account bounded-electron response and collisional ionization.

Appendices

A. The Fourier transforms

We define the temporal Fourier transform $\hat{f}(\mathbf{r},\omega)$ of a function $f(\mathbf{r},t)$ by

$$\hat{f}(\mathbf{r},\omega) = \frac{1}{2\pi}\int f(\mathbf{r},t)e^{\mathrm{i}\omega t}\,dt \tag{A.1}$$

$$f(\mathbf{r},t) = \int \hat{f}(\mathbf{r},\omega)e^{-\mathrm{i}\omega t}\,d\omega\,. \tag{A.2}$$

Further on, we define the transverse spatial Fourier transform $\bar{f}(\mathbf{k}_\perp,z,\omega)$ of a function $\hat{f}(\mathbf{r},\omega)$ by

$$\bar{f}(\mathbf{k}_\perp,z,\omega) = \frac{1}{(2\pi)^2}\iint \hat{f}(\mathbf{r}_\perp,z,\omega)e^{-\mathrm{i}\mathbf{k}_\perp\cdot\mathbf{r}_\perp}\,d^2\mathbf{r}_\perp \tag{A.3}$$

$$\hat{f}(\mathbf{r}_\perp,z,\omega) = \iint \bar{f}(\mathbf{k}_\perp,z,\omega)e^{\mathrm{i}\mathbf{k}_\perp\cdot\mathbf{r}_\perp}\,d^2\mathbf{k}_\perp\,, \tag{A.4}$$

where $\mathbf{r}_\perp = (x,y)^\mathrm{T}$ and $\mathbf{k}_\perp = (k_x,k_y)^\mathrm{T}$.

In analogy, we define the longitudinal spatial Fourier transform $\breve{f}(\mathbf{r}_\perp,k_z,\omega)$ of a function $\hat{f}(\mathbf{r},\omega)$ by

$$\breve{f}(\mathbf{r}_\perp,k_z,\omega) = \frac{1}{2\pi}\int \hat{f}(\mathbf{r}_\perp,z,\omega)e^{-\mathrm{i}k_z z}\,dz \tag{A.5}$$

$$\hat{f}(\mathbf{r}_\perp,z,\omega) = \int \breve{f}(\mathbf{r}_\perp,k_z,\omega)e^{\mathrm{i}k_z z}\,dz\,. \tag{A.6}$$

Note the difference in the sign of the exponent for temporal and spatial transforms, which is common practice in the optical context. In particular, when one wants to approximate Fourier integrals by finite sums, and resort to discrete Fourier transformations (DFTs) or even fast Fourier transforms (FFTs) [121], it is important to keep track of these sign conventions.

B. Neglecting the neutral polarization in air

Here we show in analogy to Sec. 2.2.2, that the free electron response of the plasma dominates for $I_\mathrm{L}^{(0)} \geq 10^{14}$ W/cm^2 over the response of bound electrons in air. For simplicity, the delayed contribution due to Raman scattering is neglected. Following [72], we assume $n_2 = 12{\cdot}10^{-20}\,\mathrm{cm}^2/\mathrm{W}$ and $\chi^{(1)}_\mathrm{Air} = 2.42{\cdot}10^{-4}$ according to [90]. The single ionization potentials for O_2- and N_2-molecules are taken from [80]. Figure B.1 presents the maximum values of χ_plasma (solid blue line) and χ_NL (solid black line) normalized to $\chi^{(1)}_\mathrm{Ar}$ depending on the laser peak intensity $I_\mathrm{L}^{(0)}$. Obviously, the free electron response dominates for $I_\mathrm{L}^{(0)} \geq 10^{14}$ W/cm^2 over the bound electron response. In contrast to the argon gas, the dominance of the free electron response sets in at even lower intensities. The reason is the lower first ionization potential of O_2-molecules ($I_\mathrm{p}^{(1)} = 12.07$ eV)

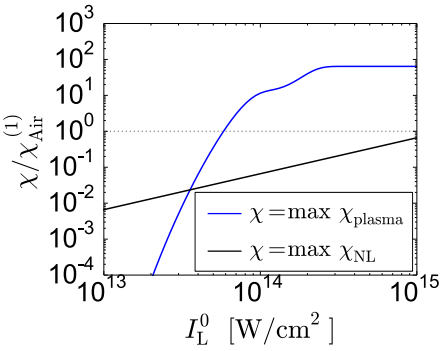

Figure B.1.: Intensity-dependent contributions of the plasma-response and Kerr-response to the susceptibility for a single-color laser pulse with $t_0 = 50$. In both cases the maximum value for all times is taken. The gray dotted line is the linear susceptibility $\chi^{(1)}_{\mathrm{Ar}}$ for a neutral argon gas with $n_{\mathrm{a}} = 2.7 \cdot 10^{19}\,\mathrm{cm}^{-3}$.

compared to argon atoms ($I_{\mathrm{p}}^{(1)} = 15.76$ eV) leading to larger free electron densities at low intensities.

C. Relation between transverse symmetries of the current source and current

Symmetries of the electromagnetic fields and especially of the radiating current are important. In particular, as discussed in Sec. 4.3.1, they can determine whether a current can radiate or not, and thus give hints about the responsible THz generation mechanism in rigorous simulations or experiments.

Here, we concentrate on two symmetries and show that if the current source has one of these symmetries, then the radiated electric fields and the radiating current in the gas-plasma have the same symmetry. The following symmetries of the current source $\boldsymbol{\iota}$ are considered (see Fig. C.1 for visualization):

$$\begin{aligned} \boldsymbol{\iota}_{\mathrm{a}}(\mathbf{r}_\perp, z, t) \cdot \mathbf{e}_\perp &= -\boldsymbol{\iota}_{\mathrm{a}}(-\mathbf{r}_\perp, z, t) \cdot \mathbf{e}_\perp \\ \boldsymbol{\iota}_{\mathrm{a}}(\mathbf{r}_\perp, z, t) \cdot \mathbf{e}_z &= \boldsymbol{\iota}_{\mathrm{a}}(-\mathbf{r}_\perp, z, t) \cdot \mathbf{e}_z\,, \end{aligned} \tag{C.1}$$

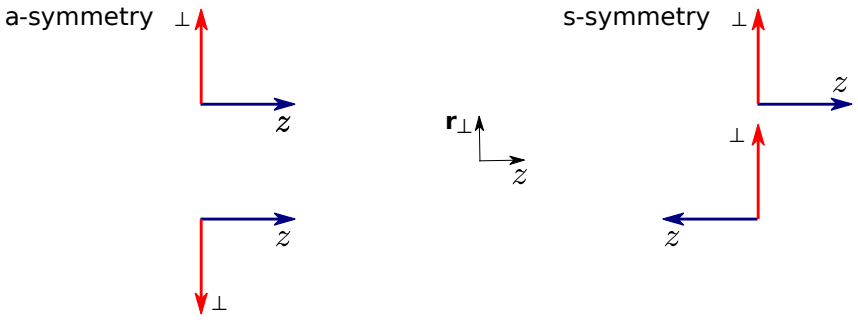

Figure C.1.: Visualization of the a-symmetry and the s-symmetry in Eqs. (C.1)-(C.2).

and

$$\begin{aligned}\boldsymbol{\iota}_\mathrm{s}(\mathbf{r}_\perp,z,t)\cdot\mathbf{e}_\perp &= \boldsymbol{\iota}_\mathrm{s}(-\mathbf{r}_\perp,z,t)\cdot\mathbf{e}_\perp\\ \boldsymbol{\iota}_\mathrm{s}(\mathbf{r}_\perp,z,t)\cdot\mathbf{e}_z &= -\boldsymbol{\iota}_\mathrm{s}(-\mathbf{r}_\perp,z,t)\cdot\mathbf{e}_z\,,\end{aligned} \tag{C.2}$$

with $\mathbf{e}_\perp \in \{(1,0,0)^\mathrm{T},(0,1,0)^\mathrm{T}\}$ and $\mathbf{e}_z=(0,0,1)^\mathrm{T}$. We consider that the laser propagates along the z-axis. The z-coordinate of a field is called the longitudinal component. The components normal to it are called transverse components. For the case in Eq. (C.1), the transverse source is antisymmetric in the transverse direction $\mathbf{r}_\perp=(x,y,0)^\mathrm{T}$ and the longitudinal source is symmetric in $\mathbf{r}_\perp$. We call this symmetry of a vector field "the a-symmetry"[1]. For the case in Eq. (C.2), the transverse source is symmetric in $\mathbf{r}_\perp$ and the longitudinal source is antisymmetric in $\mathbf{r}_\perp$. We call this symmetry of a vector field "the s-symmetry"[2]. Without repeating Eqs. (C.1)-(C.2) for other fields, same as for $\boldsymbol{\iota}$ we use the indices a and s when indicating that the corresponding field has this kind of symmetry.

In the following, we consider the general case $\mathbf{E}\in\{\tilde{\mathbf{E}}_1,\mathbf{E}_2\}$, $\mathbf{B}\in\{\tilde{\mathbf{B}}_1,\mathbf{B}_2\}$, $\mathbf{J}\in\{\mathbf{J}_1,\mathbf{J}_2\}$ and $\boldsymbol{\iota}\in\{\boldsymbol{\iota}_1,\boldsymbol{\iota}_2\}$ whenever no index or tilde is written.

The electron density n_0 depends according to Eq. (2.5.10) explicitly on $|\mathbf{E}_1|$. Independently whether $\mathbf{E}_1$ is a- or s-symmetric, n_0 is symmetric with respect to $\mathbf{r}_\perp$ since it depends only on the modulus of $\mathbf{E}_1$. Thus, $n_0\mathbf{E}$ conserves the symmetry of $\mathbf{E}$. Moreover, $\mathbf{J}_1$ has the same symmetry as $\mathbf{E}_1$ [cf. current Eq. (2.5.11)]. Thus, $\mathbf{E}_1\cdot\mathbf{J}_1$ is symmetric and according to Eq. (2.5.12), $\mathcal{E}_2$ is symmetric with respect to $\mathbf{r}_\perp$. Because of that and Eq. (2.5.9) also ν_ei is symmetric with respect to $\mathbf{r}_\perp$. Thus, besides n_0 also the product with ν_ei does not change the symmetry.

How does the symmetry of $\boldsymbol{\iota}$ influences the symmetries of the other fields? We can decompose the source and analogous the other fields in the following form

$$\boldsymbol{\iota}=\boldsymbol{\iota}_\mathrm{a}+\boldsymbol{\iota}_\mathrm{s}\,. \tag{C.3}$$

Adding/subtracting the current equations Eq. (2.5.22) or Eq. (2.5.16) evaluated at $(\mathbf{r}_\perp,z)$ and $(-\mathbf{r}_\perp,z)$ and using the a- and s-symmetry of the fields gives

$$\partial_t\mathbf{J}_\mathrm{a/s}+\nu_\mathrm{ei}\mathbf{J}_\mathrm{a/s}=\frac{q_\mathrm{e}^2}{m_\mathrm{e}}n_0\mathbf{E}_\mathrm{a/s}+\boldsymbol{\iota}_\mathrm{a/s}\,. \tag{C.4}$$

Hereby, we have used that the product of $\mathbf{J}$ with n_0 or ν_ei does not change the symmetry and taking the time derivative of $\mathbf{J}$ also does not change the symmetry. So, we obtained one equation for the a-symmetry and one for the s-symmetry. The same can be done with the Maxwell's equations[3]. So, when the driving source term is s/a-symmetric, the current and the electromagnetic fields are s/a-symmetric.

In summary, if the transverse components of the current source $\boldsymbol{\iota}\in\{\boldsymbol{\iota}_1,\boldsymbol{\iota}_2\}$ are antisymmetric in the transverse coordinate $\mathbf{r}_\perp$ and the longitudinal component is symmetric, then this is true also for the current, electric and magnetic field. In the other case, if the transverse components of the current source are symmetric in $\mathbf{r}_\perp$ and the longitudinal component is antisymmetric, then this symmetry also passes to the current and electric field. When discussing single-color driving laser pulse in Sec. 4.3.1, we make use of these findings in order to argue that ponderomotively driven antisymmetric transverse currents do not lead to THz emission for thin plasmas.

[1] The label "a" in $\boldsymbol{\iota}_\mathrm{a}$ indicates the fact that the transverse components are antisymmetric in $\mathbf{r}_\perp$.

[2] The label "s" in $\boldsymbol{\iota}_\mathrm{s}$ indicates the fact that the transverse components are symmetric in $\mathbf{r}_\perp$.

[3] The $\nabla\times$- and ∂_t-operator conserve the a-symmetry or s-symmetry. Thus, adding/subtracting Maxwell's Eq. (2.5.14), (2.5.20) or Eq. (2.5.13), (2.5.19) evaluated at $(\mathbf{r}_\perp,z)$ and $(-\mathbf{r}_\perp,z)$ and using the a- and s-symmetry of the fields gives one set of equations for the a-symmetric fields and one set of equations for the s-symmetric fields.

D. Rewriting ι_2 in terms of $\mathbf{J}_1$

Here the nonlinear source term $\boldsymbol{\iota}_2$ in Eq. (2.5.17) of the main text is rewritten such that it contains no electromagnetic fields $\mathbf{E}_1$, $\mathbf{B}_2$ but only $\mathbf{J}_1$. All, the fields depend on $\mathbf{r}$ ant t and thus the arguments are left out for sake of brevity. First, we rewrite the 2^{nd} term in Eq. (2.5.17) as follows

$$\begin{aligned}\frac{q_\mathrm{e}}{m_\mathrm{e}}\mathbf{J}_1\times\mathbf{B}_1 &= -\frac{q_\mathrm{e}}{m_\mathrm{e}}\mathbf{J}_1\times\int_{-\infty}^{t}\nabla\times\mathbf{E}_1\,dt'\\ &= -\mathbf{J}_1\times\nabla\times\int_{-\infty}^{t}\frac{1}{q_\mathrm{e}n_0}\left(\partial_{t'}+\nu_\mathrm{ei}\right)\mathbf{J}_1\,dt'\\ &= -\mathbf{J}_1\times\nabla\times\int_{-\infty}^{t}\frac{\mathbf{J}_1}{q_\mathrm{e}n_0}\left(\nu_\mathrm{ei}+\frac{\partial_{t'}n_0}{n_0}\right)\mathbf{J}\,dt' - \mathbf{J}_1\times\nabla\times\frac{\mathbf{J}_1}{q_\mathrm{e}n_0}\end{aligned} \tag{D.1}$$

Adding the 4^{th} term in Eq. (2.5.17) to Eq. (D.1) and using the vector identity $\mathbf{b}\times(\nabla\times\mathbf{b})+(\mathbf{b}\cdot\nabla)\,\mathbf{b}=\nabla|\mathbf{b}|^2/2$ gives

$$\frac{q_\mathrm{e}}{m_\mathrm{e}}\mathbf{J}_1\times\mathbf{B}_1-(\mathbf{J}_1\cdot\nabla)\frac{\mathbf{J}_1}{q_\mathrm{e}n_0}=-\mathbf{J}_1\times\nabla\times\int_{-\infty}^{t}\frac{\mathbf{J}_1}{q_\mathrm{e}n_0}\left(\nu_\mathrm{ei}+\frac{\partial_{t'}n_0}{n_0}\right)\mathbf{J}\,dt'-\frac{q_\mathrm{e}n_0}{2}\nabla\left|\frac{\mathbf{J}_1}{q_\mathrm{e}n_0}\right|^2. \tag{D.2}$$

Herewith, we identify the last term in Eq. (D.2) as the ponderomotive source term

$$\iota_2^{\text{pond}}=-\frac{q_\mathrm{e}n_0}{2}\nabla\left|\frac{\mathbf{J}_1}{q_\mathrm{e}n_0}\right|^2. \tag{D.3}$$

Moreover using Eq. (2.5.15)-(2.5.16), the 3^{rd} term in Eq. (2.5.17) is rewritten as follows

$$-\frac{\mathbf{J}_1}{q_\mathrm{e}n_0}\left(\nabla\cdot\mathbf{J}_1\right)=-\frac{1}{n_0}\partial_t\left(\mathbf{J}_1n_1\right)+\frac{n_1}{n_0}\left(\frac{q_\mathrm{e}^2}{m_\mathrm{e}}n_0\mathbf{E}_1-\nu_\mathrm{ei}\mathbf{J}_1\right). \tag{D.4}$$

By adding Eq. (D.4) to the 1^{st} term in Eq. (2.5.17) and using again Eq. (2.5.15) we get

$$\frac{q_\mathrm{e}}{m_\mathrm{e}}n_1\mathbf{E}_1-\frac{\mathbf{J}_1}{q_\mathrm{e}n_0}\left(\nabla\cdot\mathbf{J}_1\right)=-\frac{1}{q_\mathrm{e}n_0}\left(\partial_t+\nu_\mathrm{ei}\right)\left(\mathbf{J}_1\int_{-\infty}^{t}\nabla\cdot\mathbf{J}_1\,dt\prime\right) \tag{D.5}$$

Finally, using Eq. (D.2), (D.5) the source term $\boldsymbol{\iota}_2$ in Eq. (2.5.17) of the main text can be rewritten in terms of $\mathbf{J}_1$ to

$$\boldsymbol{\iota}_2=\iota_2^{\text{pond}}-\frac{\mathbf{J}_1}{q_\mathrm{e}}\times\nabla\times\int_{-\infty}^{t}\frac{\mathbf{J}_1}{n_0}\left(\nu_\mathrm{ei}+\frac{\partial_{t'}n_0}{n_0}\right)dt'-\frac{2q_\mathrm{e}}{3m_\mathrm{e}}\nabla\mathcal{E}_{\mathrm{th},2}-\frac{\left(\nu_\mathrm{ei}+\partial_t\right)}{q_\mathrm{e}n_0}\left(\mathbf{J}_1\int_{-\infty}^{t}\nabla\cdot\mathbf{J}_1\,dt'\right). \tag{D.6}$$

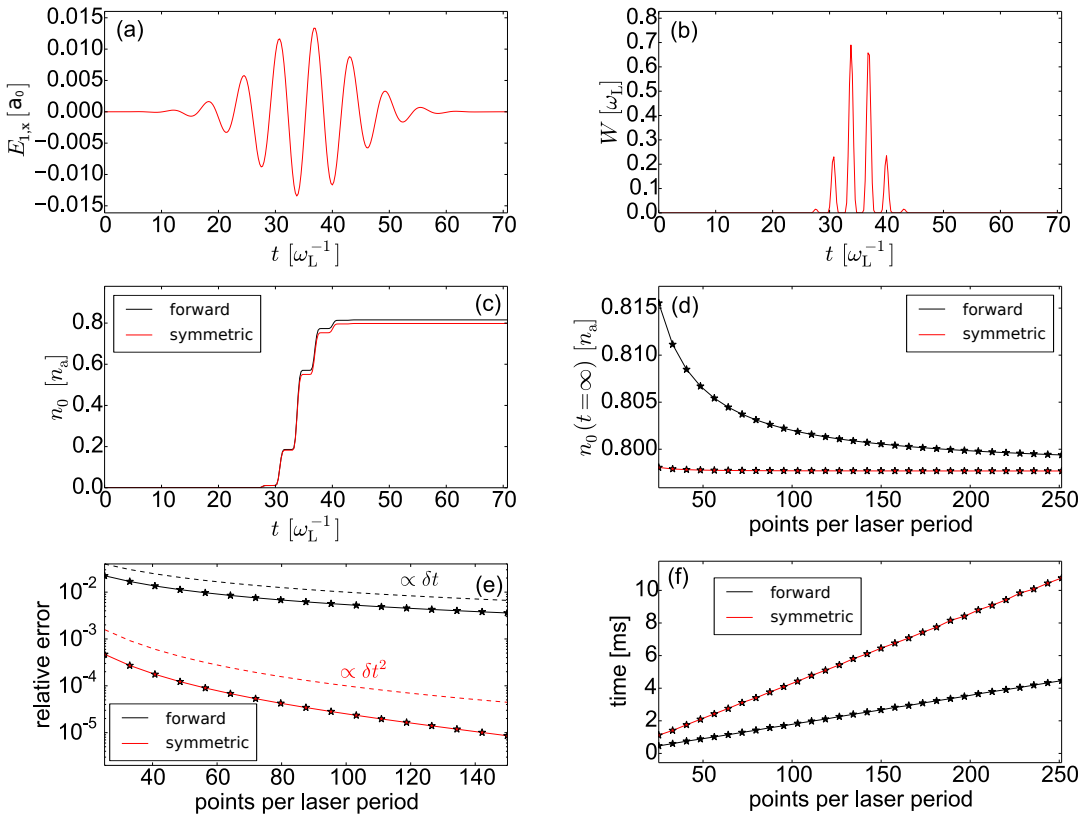

Figure E.1.: Time trace of a few-cycle laser electric field in units of $a_0 = q_e E_L^{(0)}/(cm_e\omega_L)$ (a). The peak intensity is $I_0 = 4 \cdot 10^{14}\,\mathrm{W/cm^2}$ and pulse duration $t_0 = 5\,\mathrm{fs}$. Corresponding ionization rate for Argon (b). Time trace of the electron density n_0 when using symmetric discretization according to Eq. (E.1) (red line) and a simple forward Euler scheme (black line) (c). The temporal resolution is given by $\delta t = 0.25\omega_L$ resolving 25 points per laser oscillation. Scan of the final electron density when varying the number of points per laser oscillation (d). Relative error (solid curves) normalized to the symmetric method with 5000 points per wavelength (e). In addition, two curves $\propto 1/\delta t$ (dashed black line) and $\propto 1/\delta t^2$ (dashed red line) are shown. Required time for the python test routine (f).

E. Discretization of the ionization rate equations

Here, we write down the explicit solution of the discretized ionization rate equations (2.1.8) and test it for a few-cycle pulse. In Sec. (3.2.1), using the symmetric difference quotient that approximates $\partial_t n_{\mathrm{ion}}^{(Z)}(t)$ in terms of $n_{\mathrm{ion}}^{(Z)}(t \pm \delta t/2)$ up to an error $\propto \delta t^2$, we have expressed the ionization rate equations according to Eq. (3.2.1). Taking into account the definition of $\bar{n}_{\mathrm{ion}}^{(Z)}$ in Eq. (3.2.3), the up-date formula for the new ion densities reads

$$n_{\mathrm{ion}}^{(Z)}(t+\delta t/2) = \frac{n_{\mathrm{ion}}^{(Z)}(t-\delta t/2)\left(1-\frac{\delta t}{2}W^{(Z+1)}[\mathbf{E}_1(t)]\right) + \frac{\delta t}{2}W^{(Z)}[\mathbf{E}_1(t)]\bar{n}_{\mathrm{ion}}^{(Z-1)}(t)}{1+\frac{\delta t}{2}W^{(Z+1)}[\mathbf{E}_1(t)]}. \tag{E.1}$$

Now, we test the convergence of the solution by computing the electron density $n_0 = \sum_Z Z n_{\mathrm{ion}}^{(Z)}$ of argon (see Sec. 2.1). The electric field is assumed to be known with $\mathbf{E}_1(t) =$

$E_{\mathrm{L}}^{(0)} \sin(\omega_{\mathrm{L}} t) \exp(-(t/t_0)^2)\mathbf{e}_x$. We consider $I_{\mathrm{L}}^{(0)} = \epsilon_0 (E_{\mathrm{L}}^{(0)})^2/2 = 4 \cdot 10^{14}$ W/cm^2, $\lambda_{\mathrm{L}} = 2\pi c/\omega_{\mathrm{L}} = 0.8\,\mu$m, $t_0 = 5$ fs, i.e., a few-cycle pulse. The corresponding electric field and the ionization rate are shown in Fig. E.1(a-b). Only four ionization events contribute to ionization and thus the electron density in Fig. E.1(c) has four big steps. In addition to the computation according to Eq. (E.1) (red line), the solution with an explicit forward Euler scheme is presented (black line) leading to a slightly overestimated electron density. As the final electron density in Fig. E.1(d) shows, it is worth to use our symmetric discretization scheme that converges much faster than the forward Euler scheme. The error of our scheme in Fig. E.1(e) decreases faster than quadratically with the number of points per laser period whereas the forward Euler scheme has only a linear convergence. In both cases the computation time increases linearly [see Fig. E.1(f)].

F. Fix-point iteration for discrete solution of energy and current equation

Here, we detail the fix-point iteration method for the solution of the nonlinear system of equations (3.2.2)-(3.2.4) in Sec. 3.2.1. Assume $\mathbf{J}_1(t-\delta t/2)$, $\mathcal{E}_2(t-\delta t/2)$, $n_{\mathrm{i}}^{(Z)}(t-\delta t/2)$, $n_{\mathrm{i}}^{(Z)}(t+\delta t/2)$, $n_0(t-\delta t/2)$, $n_0(t+\delta t/2)$ and $\mathbf{E}(t)$ are known. We are looking for an approximation of $\mathbf{J}_1(t+\delta t/2)$, $\mathcal{E}_2(t+\delta t/2)$. Employing the definition of $\bar{n}$ in Eq. (3.2.3) and analogue definitions for $\bar{n}_0$, we proceed as follows:

1. Set
$$\mathcal{E}_2^{(0)}(t+\delta t/2) = \mathcal{E}_2(t-\delta t/2) \tag{F.1}$$

2. Iterate for $1 \le k \le K_{\max}$:
$$\bar{\nu} = \nu_{\mathrm{ei}}\left[\bar{n}_{\mathrm{ion}}^{(Z)}(t), \bar{n}_0(t), \left(\mathcal{E}_2^{(k-1)}(t+\delta t/2) + \mathcal{E}_2(t-\delta t/2)\right)/2\right] \tag{F.2}$$
$$\mathbf{J}_1^{(k)}(t+\delta t/2) = \frac{\bar{n}_0(t)\mathbf{E}_1(t) + \mathbf{J}_1(t-\delta t/2)\,(1/\delta t - \bar{\nu}/2)}{1/\delta t + \bar{\nu}/2} \tag{F.3}$$
$$\mathcal{E}_2^k(t+\delta t/2) = \mathcal{E}(t-\delta t/2) + \frac{\delta t}{2}\mathbf{E}_1(t) \cdot \left(\mathbf{J}_1^{(k)}(t+\delta t/2) + \mathbf{J}_1(t-\delta t/2)\right) \tag{F.4}$$

   as long as $|\mathcal{E}_2^{(k)}(t+\delta t/2) - \mathcal{E}_2^{(k-1)}(t+\delta t/2)| \ge \gamma$, where γ defines the precision or for $k \ge 2$: $|\mathcal{E}_2^{(k)}(t+\delta t/2) - \mathcal{E}_2^{(k-1)}(t+\delta t/2)| > |\mathcal{E}_2^{(k-1)}(t+\delta t/2) - \mathcal{E}_2^{(k-2)}(t+\delta t/2)|$, in the later case the iteration does not converge and the method is inappropriate.

Now, we test the algorithm for a laser pulse similar to the test in Sec. E but with a longer pulse with $t_0 = 25$ fs. Figs. (F.1)(a-c) illustrate the corresponding electric field $E_{1,x}$, the ionization rate and the electron density. The current and the electron energy $E_2 = n_0\mathcal{E}_2$ are shown in Fig. F.1(d-e) using only one iteration ($K_{\max} = 1$). Hereby, the relative error in terms of the final value of E_2 compared to a computation with 5000 points per laser oscillation and $K_{\max} = 10$ is around 10^{-3}. It decreases according to Fig. F.1(f) to the level of the machine precision already after six iterations.

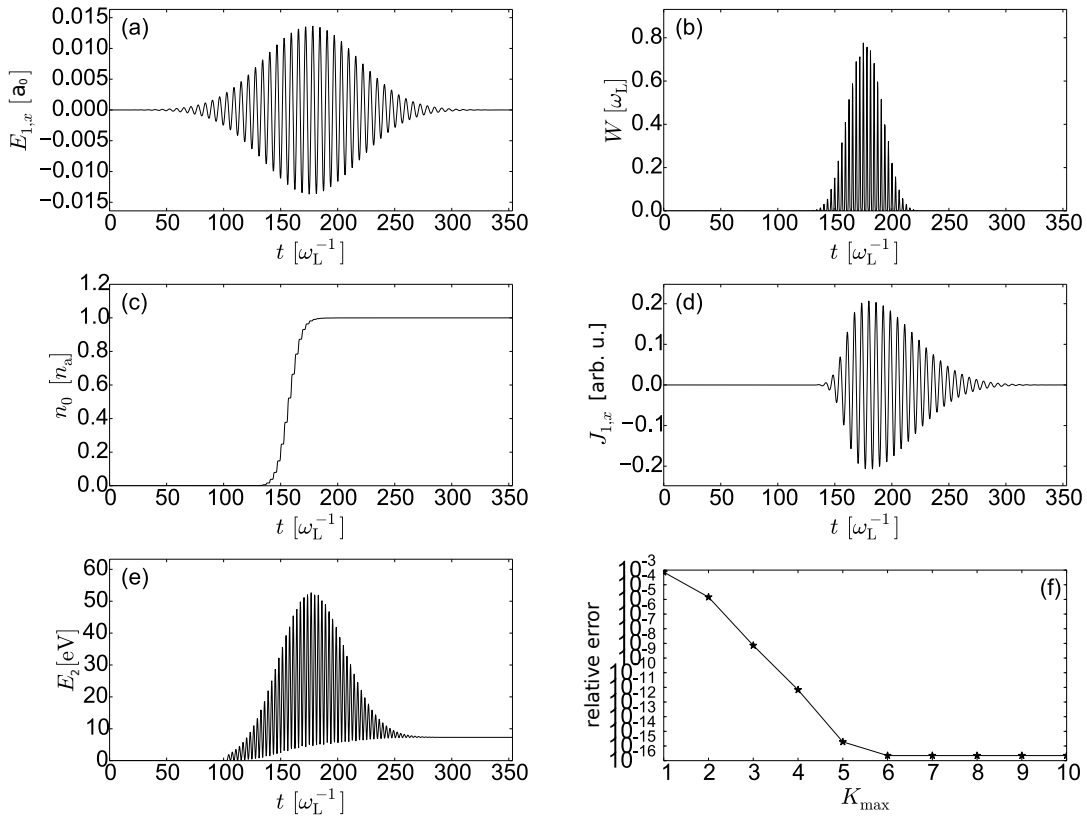

Figure F.1.: Time trace of a few-cycle laser electric field in units of $a_0 = q_e E_L^{(0)}/(cm_e\omega_L)$ (a). The peak intensity is $I_0 = 4 \cdot 10^{14}\,\mathrm{W/cm^2}$ and pulse duration $t_0 = 25\,\mathrm{fs}$. The corresponding ionization rate for Argon in (b). In (c) the time trace of the electron density n_0 is shown that was computed according to Eq. (E.1) with a temporal resolution of $\delta t = 0.25\omega_L$ resolving 25 points per laser oscillation. In (d) and (e), the current and energy per electron are shown solving the heating equation with the Banach Fixed-point iteration and $K_{max} = 1$. Relative electron energy error with respect to a computation with 5000 points per laser oscillation and 10 iterations depending on the number of maximal iterations K_{max} (f).

G. Generating Maxwell consistent solutions using the vector potential in Lorentz gauge

Introducing electromagnetic potentials $\mathbf{A}$, ϕ in Lorentz gauge via

$$\hat{\mathbf{B}} = \nabla \times \hat{\mathbf{A}} \qquad \hat{\mathbf{E}} = \mathrm{i}\omega\hat{\mathbf{A}} - \nabla\hat{\phi} \tag{G.1}$$

$$\nabla \cdot \hat{\mathbf{A}}(\mathbf{r},\omega) = \mathrm{i}\omega\frac{1}{c^2}\hat{\phi}(\mathbf{r},\omega)\,, \tag{G.2}$$

leads to decoupling of ϕ and the components of $\mathbf{A}$, and one finds (in vacuum) [6]

$$k_z^2(\mathbf{k}_\perp,\omega)\bar{\mathbf{A}}(\mathbf{k}_\perp,z,\omega) + \partial_z^2\bar{\mathbf{A}}(\mathbf{k}_\perp,z,\omega) = 0\,. \tag{G.3}$$

In analogy to Eq. (3.3.4), fundamental solutions are the forward (+) and backward (−) propagating, plane or evanescent waves

$$\bar{\mathbf{A}}^{\pm}(\mathbf{k}_\perp, z, \omega) = \bar{\mathbf{A}}_0^{\pm}(\mathbf{k}_\perp, \omega) e^{\pm \mathrm{i} k_z(\mathbf{k}_\perp, \omega)(z - z_0)} \,. \tag{G.4}$$

By plugging Eq. (G.4) into Eq. (G.1), and using Eq. (G.2) to eliminate ϕ, electric and magnetic fields can be expressed in terms of the vector potential at $z = z_0$:

$$\bar{\mathbf{B}}^{\pm}(\mathbf{k}_\perp, z, \omega) = \mathrm{i}\mathbf{k}^{\pm}(\mathbf{k}_\perp, \omega) \times \bar{\mathbf{A}}_0^{\pm}(\mathbf{k}_\perp, \omega) e^{\pm \mathrm{i} k_z(\mathbf{k}_\perp, \omega)(z - z_0)} \tag{G.5}$$

$$\bar{\mathbf{E}}^{\pm}(\mathbf{k}_\perp, z, \omega) = \mathrm{i}\omega \left(1 - \frac{c^2}{\omega^2} \mathbf{k}^{\pm}(\omega) \mathbf{k}^{\pm}(\omega)^{\mathrm{T}} \right) \bar{\mathbf{A}}_0^{\pm}(\mathbf{k}_\perp, \omega) e^{\pm \mathrm{i} k_z(\mathbf{k}_\perp, \omega)(z - z_0)} \,. \tag{G.6}$$

In general, the three components of $\mathbf{A}_0^{\pm}$ can be chosen independently, however, only two components are necessary to prescribe an arbitrary laser pulse [4]. The use of the vector potential can be nevertheless advantageous, because certain beams, like radially polarized doughnut beams [120], can be described by a single (longitudinal) component of the vector potential.

H. Transformation of the 1D current source ι_2 into the co-moving pulse frame

We rewrite the current source Eq. (D.6) in 1D geometry. Using $\partial_x = \partial_y = 0$ and $J_{1,z} = 0$ we get

$$\begin{aligned} \iota_{2,z} = &- \frac{n_0}{2q_\mathrm{e}} \partial_z \left| \frac{\mathbf{J}_1}{n_0} \right|^2 - \frac{J_{1,x}}{q_\mathrm{e}} \partial_z \int_{-\infty}^{t} \frac{J_{1,x}}{n_0} \left(\nu_\mathrm{ei} + \frac{\partial_{t'} n_0}{n_0} \right) dt' \\ &- \frac{J_{1,y}}{q_\mathrm{e}} \partial_z \int_{-\infty}^{t} \frac{J_{1,y}}{n_0} \left(\nu_\mathrm{ei} + \frac{\partial_{t'} n_0}{n_0} \right) dt' - \frac{2q_\mathrm{e}}{3m_\mathrm{e}} \partial_z \left(n_0 E_\mathrm{th} \right) \,. \end{aligned} \tag{H.1}$$

We also find that $\iota_{2,x} = \iota_{2,y} = 0$, so $\boldsymbol{\iota}_2$ is purely longitudinal in 1D. Next we transform $\iota_{2,z}$ into the co-moving pulse frame $(z, t) \mapsto (\xi = z, \tau = t - z/c)$. According to the approximation we made in Eq. (4.1.2), the current $\mathbf{J}_1$ can be calculated directly from the vacuum laser field $\mathbf{E}_\mathrm{L}$. Because $\mathbf{E}_\mathrm{L}$ and thus $\mathbf{J}_1$ do not change their temporal shape upon propagation along z, they are invariant in the new variable ξ and the z derivative transforms as $\partial_z = \partial_\xi - \partial_\tau / c = -\partial_\tau / c$ leading to

$$\boldsymbol{\iota}_2 = \frac{n_0}{2q_\mathrm{e} c} \partial_\tau \left| \frac{\mathbf{J}_1}{n_0} \right|^2 \mathbf{e}_z + \frac{n_0}{q_\mathrm{e} c} \left| \frac{\mathbf{J}_1}{n_0} \right|^2 \left(\nu_\mathrm{ei} + \frac{\partial_\tau n_0}{n_0} \right) \mathbf{e}_z + \frac{2q_\mathrm{e}}{3m_\mathrm{e} c} \partial_\tau \left(n_0 E_\mathrm{th} \right) \mathbf{e}_z \,. \tag{H.2}$$

[4] As shown in Sec. 3.3.2.1, only two electric or magnetic field components can be set independently for a laser pulse ($k_z \neq 0$), the corresponding divergence equation determines the third one. Hence, only two components of $\mathbf{A}_0^{\pm}$ are sufficient to prescribe an arbitrary laser pulse.

I. Ponderomotive source in quasi-monochromatic paraxial approximation

Here, we derive an approximate expression for the ponderomotive source term

$$\boldsymbol{\iota}_2^{\mathrm{pond}} = -\frac{n_0}{2q_\mathrm{e}}\nabla\left|\frac{\mathbf{J}_1}{n_0}\right|^2 . \tag{I.1}$$

The Gaussian 2D laser electric field is computed in the quasi-monochromatic paraxial approximation as

$$\mathbf{E}_\mathrm{L}^{\mathrm{2D}}(x,z,t) \approx \Re\left\{\frac{E_\mathrm{L}^0\, e^{-\frac{x^2}{w_0^2\left(1+\mathrm{i}\frac{z}{z_\mathrm{R}}\right)}-\frac{\tau^2}{t_0^2}-\mathrm{i}\left(\omega_\mathrm{L}\tau-\frac{\pi}{2}\right)}}{\sqrt{1+\mathrm{i}\frac{z}{z_\mathrm{R}}}}\right\}\mathbf{e}_y\,, \tag{I.2}$$

with $\tau = t - z/c$, and the Rayleigh length $z_\mathrm{R} = w_0^2\omega_\mathrm{L}/2c$. The symbol $\Re$ denotes the real part of a complex quantity. In general, the current $\mathbf{J}_1$ has to be calculated by solving the Maxwell's equations coupled to Eqs. (2.5.11) and (2.5.12). However, when using $\mathbf{J}_1$ to calculate the source term ι_2 in order to study the TC mechanism, it is sufficient to approximate (for $\nu_\mathrm{ei} = 0$)

$$\mathbf{J}_1(x,z,t) \approx \frac{q_\mathrm{e}^2}{m_\mathrm{e}}\int_{-\infty}^{t} n_0(x,z,t')\mathbf{E}_\mathrm{L}^{\mathrm{2D}}(x,z,t')\,dt' \approx \frac{n_0 q_\mathrm{e}^2}{m_\mathrm{e}\omega_\mathrm{L}}\Re\left\{\frac{\mathrm{i}E_\mathrm{L}^0\, e^{-\frac{x^2}{w_0^2\left(1+\mathrm{i}\frac{z}{z_\mathrm{R}}\right)}-\frac{\tau^2}{t_0^2}-\mathrm{i}\left(\omega_\mathrm{L}\tau-\frac{\pi}{2}\right)}}{\sqrt{1+\mathrm{i}\frac{z}{z_\mathrm{R}}}}\right\}\mathbf{e}_y\,.$$

In the following computation of $\nabla|\mathbf{J}_1/n_0|^2$ we will omit the z dependent Gouy phase as well as the transverse phase curvature. The former would give a z dependent time shift for ι_2^{pond} of maximum half a laser period, while the latter is almost flat near focus where we look for a good approximation. Thus, both phases are without a greater importance for THz waves. Then, the ponderomotive source writes in terms of the optical intensity

$$\boldsymbol{\iota}_2^{\mathrm{pond}} \approx -\frac{n_0 q_\mathrm{e}^3}{2m_\mathrm{e}^2\omega_\mathrm{L}^2\epsilon_0 c}\nabla\left\{I_\mathrm{L}^{\mathrm{2D}}\left[1+\cos(2\omega_\mathrm{L}\tau)\right]\right\}\,, \tag{I.3}$$

with

$$I_\mathrm{L}^{\mathrm{2D}}(x,z,t) = \frac{\epsilon_0 c\left(E_\mathrm{L}^0\right)^2}{2}\frac{w_0}{w(z)}\,e^{-\frac{2x^2}{w^2(z)}-\frac{2\tau^2}{t_0^2}}\,, \tag{I.4}$$

$$w(z) = w_0\sqrt{1+\left(\frac{z}{z_\mathrm{R}}\right)^2}\,. \tag{I.5}$$

A similar treatment applies to a Gaussian 3D laser electric field

$$\mathbf{E}_\mathrm{L}^{\mathrm{3D}}(\mathbf{r},t) \approx \Re\frac{E_\mathrm{L}^0\, e^{-\frac{x^2+y^2}{w_0^2\left(1+\mathrm{i}\frac{z}{z_\mathrm{R}}\right)}-\frac{\tau^2}{t_0^2}-\mathrm{i}\left(\omega_\mathrm{L}\tau-\frac{\pi}{2}\right)}}{1+\mathrm{i}\frac{z}{z_\mathrm{R}}}\mathbf{e}_y\,. \tag{I.6}$$

One just has to plug the expression for the 3D intensity

$$I_\mathrm{L}^{\mathrm{3D}}(\mathbf{r},t) = \frac{\epsilon_0 c\left(E_\mathrm{L}^0\right)^2}{2}\left[\frac{w_0}{w(z)}\right]^2 e^{-\frac{2x^2+2y^2}{w^2(z)}-\frac{2\tau^2}{t_0^2}} \tag{I.7}$$

into the expression for the ponderomotive source Eq. (I.3). Thus, the longitudinal ponderomotive source $\iota_{2,z}^{\mathrm{pond}}$ for a 2D/3D Gaussian driving pulse, which we need to evaluate our model, reads

$$\iota_{2,z}^{\mathrm{pond}} = -\frac{q_\mathrm{e}^3 n_0 I_\mathrm{L}}{2m_\mathrm{e}^2\omega_\mathrm{L}^2\epsilon_0 c}\left\{\left[\frac{z\left(1-D+\frac{4\mathbf{r}_\perp^2}{w^2(z)}\right)}{z_\mathrm{R}^2+z^2}+\frac{4\tau}{ct_0^2}\right]\times\left[1+\cos(2\omega_\mathrm{L}\tau)\right]+2\frac{\omega_\mathrm{L}}{c}\sin(2\omega_\mathrm{L}\tau)\right\}, \quad \text{(I.8)}$$

where I_L is given by Eq. (I.4) or (I.7), $D = 2$ or 3 is the number of dimensions, and $\mathbf{r}_\perp^2 = x^2$ or $x^2 + y^2$, respectively. Here, the term $\propto z$ appears due to beam focusing, while the term $\propto \tau$ reflects the longitudinal ponderomotive source as it already exist in 1D. Both are equally important in 2D or 3D geometry. The product $n_0 I_\mathrm{L}$ produces THz as well as SH frequencies due to the step-like increase in time of n_0.

J. Non-radiating solutions of the wave equation

We want to show that the general curl-free solution $\mathbf{E}_{2,\mathrm{d}}$ to the wave equation (4.2.1) in the collisionless case ($\nu_\mathrm{ei} = 0$), after the driving pulse has passed ($\boldsymbol{\iota}_2 = 0$, $\partial_t n_0 = 0$), is given by Eq. (4.2.6) of the main text. Because $\nabla \times \mathbf{E}_{2,\mathrm{d}} = 0$, Eq. (4.2.1) reduces to an oscillator equation

$$\partial_t^2 \mathbf{E}_{2,\mathrm{d}} + \frac{q_\mathrm{e}^2 n_0}{m_\mathrm{e}\epsilon_0}\mathbf{E}_{2,\mathrm{d}} = 0\,, \quad \text{(J.1)}$$

and we can write the general solution as

$$\mathbf{E}_{2,\mathrm{d}}(\mathbf{r},t) = \mathbf{g}(\mathbf{r})\exp\left(\mathrm{i}\sqrt{\frac{q_\mathrm{e}^2 n_0}{m_\mathrm{e}\epsilon_0}}t\right). \quad \text{(J.2)}$$

For convenience, Eq. (J.2) is written in complex form, and $\mathbf{g}(\mathbf{r})$ is a complex valued function fulfilling

$$\nabla \times \mathbf{g}(\mathbf{r}) = 0, \qquad \mathbf{g}(\mathbf{r}) \times \nabla n_0(\mathbf{r}) = 0\,. \quad \text{(J.3)}$$

Thus, we can write $\mathbf{g}(\mathbf{r}) = \nabla h(\mathbf{r})$ with some scalar complex valued function $h(\mathbf{r})$. For spatially varying n_0, $\nabla h \times \nabla n_0 = 0$ further implies $h(\mathbf{r}) = f(n_0)$ with some complex valued function f, and we have

$$\mathbf{E}_{2,\mathrm{d}} = \exp\left(\mathrm{i}\sqrt{\frac{q_\mathrm{e}^2 n_0}{m_\mathrm{e}\epsilon_0}}t\right)\nabla f(n_0)\,. \quad \text{(J.4)}$$

Taking the real part of Eq. (J.4), we identify $A(n_0) = |\partial_{n_0} f(n_0)|$ and $\phi(n_0) = \arg\left[\partial_{n_0} f(n_0)\right]$ in Eq. (4.2.6).

K. THz pulse energy scaling for thick plasmas

The plasma wire model in Sec. 5.2.1 contains a priori no restriction on the plasmas thickness. Thus, one can evaluate the plasma thickness-dependent term F_{D_p} in Eq. (5.2.6) for any D_p. When $D_\mathrm{p} \ll \lambda_\mathrm{THz}$, then $F_{D_\mathrm{p}} \propto D_\mathrm{p}^4$. Here, we consider the scaling for $D_\mathrm{p} \gg \lambda_\mathrm{THz}$. In order to perform the integration over x', y' in Eq. (5.2.6), polar coordinates $(r'_\perp, \varphi')$ are introduced as

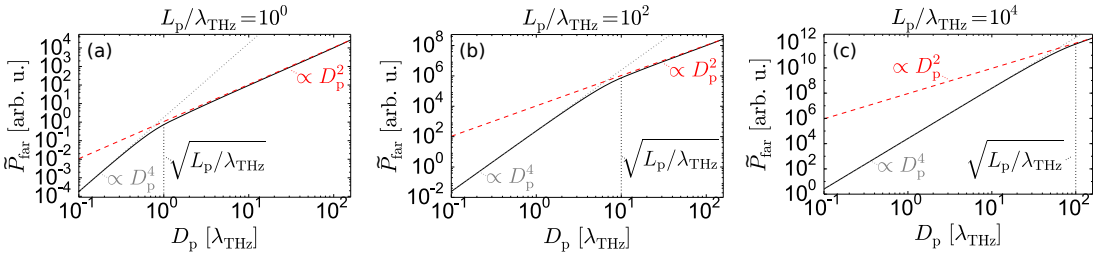

Figure K.1.: Plasma thickness dependency of the angularly integrated far-field power spectrum (solid line) according to the plasma wire model Eq. (5.2.6). The corresponding plasma thickness is given above the graph respectively. The light gray dotted line specifies the $\propto D_p^4$-scaling. The dark red dashed line specifies the $\propto D_p^2$-scaling. The vertical dotted black line specifies the boarder of the two scaling regimes that shifts according to the law $D_p/\lambda_{THz} = \sqrt{L_p/\lambda_{THz}}$.

$x' = r'_\perp \cos\varphi'$, $y' = r'_\perp \sin\varphi'$. Then, using polar coordinates we can write

$$F_{D_p} = \frac{\mu_0\omega^2}{16\pi^2 c|\mathbf{r}|^2}\left|\int_0^{\frac{D_p}{2}} r'_\perp \int_0^{2\pi} e^{-i\frac{\omega}{c}r'_\perp \sin(\theta)\cos(\varphi')}\, d\varphi'\, dr'_\perp\right|^2$$

$$= \frac{\mu_0\omega^2}{4\pi^2 c|\mathbf{r}|^2}\left|\int_0^{\frac{D_p}{2}} r'_\perp J_0\left(\frac{\omega}{c}\sin(\theta)\, r'_\perp\right) dr'_\perp\right|^2 = \frac{\mu_0\omega^2 D_p^4}{64c|\mathbf{r}|^2}\left|\int_0^1 r'_\perp J_0\left(\frac{\omega}{2c}D_p \sin(\theta)\, r'_\perp\right) dr'_\perp\right|^2,$$

where we employed the identity $(x\cos\varphi' + y\sin\varphi')/|\mathbf{r}| = \sin(\theta)\cos(\varphi' - \phi)$, made for each ϕ the substitutions $\varphi' - \phi \to \phi$ and $2r'_\perp/D_p \to r'_\perp$ and utilized the identity for the Bessel function $J_0(x) = \int_0^\pi \exp(ix\cos(\phi'))\, d\phi'/\pi$.

Using this expression, we can compute the far field spectrum depending on D_p by means of Eq. (5.2.6). The results for three different L_p are presented in Fig. K.1. For $D_p \ll \lambda_{THz}$, we find as expected $\tilde{P}_{far} \propto D_p^4$. Otherwise the far-field spectrum increases with D_p^2 for sufficiently large D_p. The boarder of these two regimes depends not only on D_p, but also on L_p. This is the result of competition between F_{D_p} with F_{L_p}. They both select a particular set of angles θ. For large L_p, F_{L_p} prefers θ-angles around 0° while F_{D_p} prefers θ-angles around 0° and 180°. In the light of Eq. (K.1), we can define the cut-off angle $\theta^{cut}_{D_p}$ by setting $\omega D_p \sin(\theta^{cut}_{D_p})/(2c) = 1$ that reduces to $\omega D_p \theta^{cut}_{D_p}/(2c) = 1$ for small $\theta^{cut}_{D_p}$. Similarly due to F_{L_p} in Eq. (5.2.8), we define $\omega D_p[1 - \cos(\theta^{cut}_{L_p})]/(2c) = 1$ and for small $\theta^{cut}_{L_p}$ we set $\omega L_p(\theta^{cut}_{L_p})^2/(2c) = 1$ by means of Taylor expansion. The transition from the F_{L_p}-dominated regime to the F_{D_p}-dominated regime appears at $(\pi D_p/\lambda_{THz})^2 = (\pi L_p/\lambda_{THz})$. As can be seen in Fig. K.1, this transition coincides with the transition of the different scaling regimes.

In summary, if $D_p \ll \lambda_{THz}$, then $\tilde{P}_{far} \propto D_p^4$. For $D_p \gg \lambda_{THz}$, we have two regimes: $\tilde{P}_{far} \propto D_p^4$ if $D_p/\lambda_{THz} \ll \sqrt{L_p/\lambda_{THz}}$ and $\tilde{P}_{far} \propto D_p^2$ if $D_p/\lambda_{THz} \gg \sqrt{L_p/\lambda_{THz}}$.

L. THz pulse energy scaling for elliptical beams

Here, we investigate the THz pulse energy scaling with the radiating plasma dimensions for a tightly focused elliptical beam as discussed in Sec. 5.3. To this end, the plasma wire model from

Sec. 5.2.1 is used. To evaluate the far field power spectrum in Eq. (5.2.6), we assume a cuboid plasma with the length $L_\mathrm{p} \ll \lambda_\mathrm{THz}$, short plasma thickness $D_x \ll \lambda_\mathrm{THz}$ along x and long plasma thickness $D_\mathrm{y} \gg \lambda_\mathrm{THz}$ along y.

Depending on whether the incoming laser beam is x or y polarized, following the plasma wire model the current polarization depending factor reads

$$F_{\mathbf{J}_0} = \begin{cases} \frac{y^2+z^2}{|\mathbf{r}|^2} & \text{for } \mathbf{J}_0 \parallel \mathbf{e}_x \\ \frac{x^2+z^2}{|\mathbf{r}|^2} & \text{for } \mathbf{J}_0 \parallel \mathbf{e}_y \end{cases} . \tag{L.1}$$

The short plasma length implies $F_{L_\mathrm{p}} \approx L_\mathrm{p}^2$. The plasma thickness dependent term can be evaluated as

$$F_{D_\mathrm{p}} = \frac{\mu_0 \omega^2 D_x^2}{4\pi^2 c |\mathbf{r}|^2} \frac{\sin^2\left[\frac{\omega D_y}{2c}\frac{y}{|\mathbf{r}|}\right]}{\left[\frac{\omega}{c}\frac{y}{|\mathbf{r}|}\right]^2} . \tag{L.2}$$

For $D_y \gg \lambda_\mathrm{THz} = 2\pi c/\omega$, F_{D_p} goes to zero if $y \to |\mathbf{r}|$, i.e, if the plasma is very broad along y, no radiation is emitted in the y-direction. In the following, we make use of it by introducing the polar coordinates

$$z = r_\perp \cos\varphi \qquad\qquad x = r_\perp \sin\varphi \tag{L.3}$$

and considering the far-field emission only for small y, i.e., $|\mathbf{r}| \approx r_\perp$. Then, the polarization depending factor simplifies to

$$F_{\mathbf{J}_0} \approx \begin{cases} \cos^2\varphi & \text{for } \mathbf{J}_0 \parallel \mathbf{e}_x \\ 1 & \text{for } \mathbf{J}_0 \parallel \mathbf{e}_y \end{cases} . \tag{L.4}$$

By substituting $\xi = \omega D_y y/(2cr_\perp)$, the angularly integrated power spectrum can be evaluated to

$$\tilde{P}_\mathrm{far} = \int_{-\infty}^{\infty}\int_0^{2\pi} P_\mathrm{far}\, r_\perp \, d\varphi \, dy = L_\mathrm{p}^2 D_x^2 D_y \frac{\mu_0\omega}{4\pi} |\mathbf{J}_0(\omega)|^2 \int_{-\infty}^{\infty} \frac{\sin^2\xi}{\xi^2}\, d\xi \begin{cases} \pi & \text{for } \mathbf{J}_0 \parallel \mathbf{e}_x \\ 2\pi & \text{for } \mathbf{J}_0 \parallel \mathbf{e}_y \end{cases} . \tag{L.5}$$

Thus, independently on laser polarization, the THz pulse energy scales with $\propto D_y$ according to the plasma wire model.

Bibliography

[1] C. Sirtori, "Bridge for the terahertz gap," Nature, vol. 417, p. 132, 2002.

[2] H. Roehle, R. J. B. Dietz, H. J. Hensel, J. Böttcher, H. Künzel, D. Stanze, M. Schell, and B. Sartorius, "Next generation 1.5 µm terahertz antennas: mesa-structuring of InGaAs/InAlAs photoconductive layers," Opt. Express, vol. 18, no. 3, pp. 2296–2301, 2010.

[3] A. Tomasino, A. Parisi, S. Stivala, P. Livreri, A. C. Cino, A. C. Busaccaa, M. Peccianti, and R. Morandotti, "Wideband THz time domain spectroscopy based on optical rectification and electro-optic sampling," Scientific Reports, vol. 3, p. 3116, 2013.

[4] P. G. de Alaiza Martínez, "Generation of intense terahertz sources by ultrashort laser pulses," Ph.D. dissertation, L'université Paris-Saclay, 2016.

[5] P. R. Griffiths, J. A. D. Haseth, and J. D. Winefordner, Fourier Transform Infrared Spectrometry, 2nd ed. New York, NY: Wiley, 1999.

[6] J. D. Jackson, Classical electrodynamics, 3rd ed. New York, NY: Wiley, 1999.

[7] A. G. Davies, A. D. Burnett, W. Fan, E. H. Linfield, and J. E. Cunningham, "Terahertz spectroscopy of explosives and drugs," Materials Today, vol. 11, no. 3, pp. 18 – 26, 2008.

[8] A. Markelz, S. Whitmire, J. Hillebrecht, and R. Birge, "THz time domain spectroscopy of biomolecular conformational modes," Physics in Medicine and Biology, vol. 47, no. 21, p. 3797, 2002.

[9] X. Han, S. Yan, D. Wei, H.-L. Cui, and C. Du, "THz time domain spectroscopy of biomolecular conformational modelabel-free protein detection using terahertz time-domain spectroscopy," International Symposium on Ultrafast Phenomena and Terahertz Waves 2016.

[10] B. B. Hu and M. C. Nuss, "Imaging with terahertz waves," Opt. Lett., vol. 20, no. 16, pp. 1716–1718, 1995.

[11] R. Gente and M. Koch, "Monitoring leaf water content with THz and sub-THz waves," Plant Methods, vol. 11, no. 1, p. 15, 2015.

[12] P. H. Siegel, "Terahertz technology in biology and medicine," IEEE Transactions on Microwave Theory and Techniques, vol. 52, no. 10, pp. 2438–2447, 2004.

[13] E. Berry, G. C. Walker, and A. J. Fitzgerald, "Do in vivo terahertz imaging systems comply with safety guidelines?" Journal of Laser Applications, vol. 15, p. 192, 2003.

[14] V. P. Wallace, E. MacPherson, J. A. Zeitler, and C. Reid, "Three-dimensional imaging of optically opaque materials using nonionizing terahertz radiation," J. Opt. Soc. Am. A, vol. 25, no. 12, pp. 3120–3133, 2008.

[15] C. Yu, S. Fan, Y. Sun, and E. Pickwell-MacPherson, "The potential of terahertz imaging for cancer diagnosis: A review of investigations to date," Quantitative Imaging in Medicine and Surgery, vol. 2, no. 1, pp. 33 – 45, 2012.

[16] M. Yahyapour, N. Vieweg, T. Geobel, H. Roehle, and A. Deninger, "Non-contact thickness measurements with terahertz pulses," WCNDT 2016.

[17] "Toptica plastic inspection," http://www.toptica.com/applications/terahertz-sensing/plastic-inspection/, accessed: 2017-05-02.

[18] E. A. Nanni, W. R. Huang, K.-H. Hong, K. Ravi, A. Fallahi, G. Moriena, R. J. D. Miller, and F. X. Kärtner, "Terahertz-driven linear electron acceleration," Nature communications, vol. 6, p. 8486, 2015.

[19] R. Mankowsky, A. von Hoegen, M. Först, and A. Cavalleri, "Ultrafast reversal of the ferroelectric polarization," Phys. Rev. Lett., vol. 118, p. 197601, May 2017.

[20] T. Kampfrath, K. Tanaka, and K. A. Nelson, "Resonant and nonresonant control over matter and light by intense terahertz transients," Nat. Photon., vol. 7, p. 680, 2013.

[21] P. Y. Han, M. Tani, M. Usami, S. Kono, R. Kersting, and X.-C. Zhang, "A direct comparison between terahertz time-domain spectroscopy and far-infrared fourier transform spectroscopy," Journal of Applied Physics, vol. 89, no. 4, pp. 2357–2359, 2001.

[22] J. Faist, F. Capasso, D. L. Sivco, C. Sirtori, A. L. Hutchinson, and A. Y. Cho, "Quantum cascade laser," Science, vol. 264, no. 5158, pp. 553–556, 1994.

[23] "MPSD broadband time-resolved terahertz spectroscopy." http://qcmd.mpsd.mpg.de/index.php/Broadband-Time-resolved-terahertz-spectroscopy.html, accessed: 2017-04-06.

[24] R. Kazarinov and R. Suris, "Possibility of amplification of electromagnetic waves in a semiconductor with a superlattice," Fizika i Tekhnika Poluprovodnikov, vol. 5, no. 4, p. 797–800, 1971.

[25] M. S. Vitiello, G. Scalari, B. Williams, and P. D. Natale, "Quantum cascade lasers: 20 years of challenges," Opt. Express, vol. 23, no. 4, pp. 5167–5182, 2015.

[26] C. Walther, M. Fischer, G. Scalari, R. Terazzi, N. Hoyler, and J. Faist, "Quantum cascade lasers operating from 1.2 to 1.6 THz," Applied Physics Letters, vol. 91, no. 13, p. 131122, 2007.

[27] C. W. I. Chan, Q. Hu, and J. L. Reno, "Ground state terahertz quantum cascade lasers," Applied Physics Letters, vol. 101, no. 15, p. 151108, 2012.

[28] K. Ohtani, M. Beck, M. J. Süess, J. Faist, A. M. Andrews, T. Zederbauer, H. Detz, W. Schrenk, and G. Strasser, "Far-infrared quantum cascade lasers operating in the AlAs phonon reststrahlen band," ACS Photonics, vol. 3, no. 12, pp. 2280–2284, 2016.

[29] D. Turcinková, G. Scalari, F. Castellano, M. I. Amanti, M. Beck, and J. Faist, "Ultra-broadband heterogeneous quantum cascade laser emitting from 2.2 to 3.2 THz," Applied Physics Letters, vol. 99, no. 19, p. 191104, 2011.

[30] D. Bachmann, M. Rösch, M. J. Süess, M. Beck, K. Unterrainer, J. Darmo, J. Faist, and G. Scalari, "Short pulse generation and mode control of broadband terahertz quantum cascade lasers," Optica, vol. 3, no. 10, pp. 1087–1094, 2016.

[31] M. Tonouchi, "Cutting-edge terahertz technology," Nat. Photon., vol. 1, p. 97, 2007.

[32] D. H. Auston, K. P. Cheung, J. A. Valdmanis, and D. A. Kleinman, "Cherenkov radiation from femtosecond optical pulses in electro-optic media," Phys. Rev. Lett., vol. 53, pp. 1555–1558, 1984.

[33] "Toptica teraflash," http://www.toptica.com/products/terahertz-systems/time-domain/teraflash/, accessed: 2017-04-06.

[34] F. Blanchard, L. Razzari, H.-C. Bandulet, G. Sharma, R. Morandotti, J.-C. Kieffer, T. Ozaki, M. Reid, H. F. Tiedje, H. K. Haugen, and F. A. Hegmann, "Generation of 1.5 μJ single-cycle terahertz pulses by optical rectification from a large aperture ZnTe crystal," Opt. Express, vol. 15, no. 20, pp. 13 212–13 220, 2007.

[35] J. Y. Suen, W. Li, Z. D. Taylor, and E. R. Brown, "Characterization and modeling of a terahertz photoconductive switch," Applied Physics Letters, vol. 96, no. 14, p. 141103, 2010.

[36] Y. C. Shen, P. C. Upadhya, E. H. Linfield, and H. E. Beere, "Ultrabroadband terahertz radiation from low-temperature-grown GaAs photoconductive emitters," Applied Physics Letters, vol. 83, no. 15, pp. 3117–3119, 2003.

[37] P. J. Hale, J. Madeo, C. Chin, S. S. Dhillon, J. Mangeney, J. Tignon, and K. M. Dani, "20 THz broadband generation using semi-insulating GaAs interdigitated photoconductive antennas," Opt. Express, vol. 22, no. 21, pp. 26 358–26 364, 2014.

[38] R. W. Boyd, Nonlinear optics, 3rd ed. Academic Press, 2008.

[39] F. G. Sun, W. Ji, and X. C. Zhang, "Two-photon absorption induced saturation of THz radiation in ZnTe," in Conference on Lasers and Electro-Optics (CLEO 2000). Technical Digest. Postconference Edition. TOPS Vol.39 (IEEE Cat. No.00CH37088), 2000, pp. 479–480.

[40] C. L. Sam, "Laser Damage of GaAs and ZnTe at 1.06 μm," Appl. Opt., vol. 12, no. 4, pp. 878–879, 1973.

[41] T. Löffler, T. Hahn, M. Thomson, F. Jacob, and H. G. Roskos, "Large-area electro-optic ZnTe terahertz emitters," Opt. Express, vol. 13, no. 14, pp. 5353–5362, 2005.

[42] S. M. Harrel, R. L. Milot, J. M. Schleicher, and C. A. Schmuttenmaer, "Influence of free-carrier absorption on terahertz generation from ZnTe(110)," Journal of Applied Physics, vol. 107, no. 3, p. 033526, 2010.

[43] S. A. Ku, C. M. Tu, W.-C. Chu, C. W. Luo, K. H. Wu, A. Yabushita, C. C. Chi, and T. Kobayashi, "Saturation of the free carrier absorption in ZnTe crystals," Opt. Express, vol. 21, no. 12, pp. 13 930–13 937, 2013.

[44] J. Hebling, G. Almási, I. Z. Kozma, and J. Kuhl, "Velocity matching by pulse front tilting for large-area THz-pulse generation," Opt. Express, vol. 10, no. 21, pp. 1161–1166, 2002.

[45] H. Hirori, A. Doi, F. Blanchard, and K. Tanaka, "Single-cycle terahertz pulses with amplitudes exceeding 1 MV/cm generated by optical rectification in LiNbO3," Applied Physics Letters, vol. 98, no. 9, p. 091106, 2011.

[46] S.-W. Huang, E. Granados, W. R. Huang, K.-H. Hong, L. E. Zapata, and F. X. Kärtner, "High conversion efficiency, high energy terahertz pulses by optical rectification in cryogenically cooled lithium niobate," Opt. Lett., vol. 38, no. 5, pp. 796–798, 2013.

[47] C. Vicario, B. Monoszlai, and C. P. Hauri, "GV/m single-cycle terahertz fields from a laser-driven large-size partitioned organic crystal," Phys. Rev. Lett., vol. 112, p. 213901, 2014.

[48] Y. Zhang, X. Zhang, S. Li, J. Gu, Y. Li, Z. Tian, C. Ouyang, M. He, J. Han, and W. Zhang, "A broadband THz-TDS system based on dstms emitter and LTG InGaAs/InAlAs photoconductive antenna detector," Scientific Reports, vol. 6, p. 26949, 2016.

[49] R. Huber, A. Brodschelm, F. Tauser, and A. Leitenstorfer, "Generation and field-resolved detection of femtosecond electromagnetic pulses tunable up to 41 THz," Applied Physics Letters, vol. 76, no. 22, pp. 3191–3193, 2000.

[50] A. Sell, A. Leitenstorfer, and R. Huber, "Phase-locked generation and field-resolved detection of widely tunable terahertz pulses with amplitudes exceeding 100 MV/cm," Optics Letters, vol. 33, no. 23, pp. 2767–2769, 2008.

[51] B. Liu, H. Bromberger, A. Cartella, T. Gebert, M. Först, and A. Cavalleri, "Generation of narrowband, high-intensity, carrier-envelope phase-stable pulses tunable between 4 and 18 THz," Opt. Lett., vol. 42, no. 1, pp. 129–131, 2017.

[52] M. Gensch, L. Bittner, A. Chesnov, H. Delsim-Hashemi, M. Drescher, B. Faatz, J. Feldhaus, U. Fruehling, G. Geloni, C. Gerth, O. Grimm, U. Hahn, M. Hesse, S. Kapitzki, V. Kocharyan, O. Kozlov, E. Matyushevsky, N. Morozov, D. Petrov, E. Ploenjes, M. Roehling, J. Rossbach, E. Saldin, B. Schmidt, P. Schmueser, E. Schneidmiller, E. Syresin, A. Willner, and M. Yurkov, "New infrared undulator beamline at FLASH," Infrared Physics & Technology, vol. 51, no. 5, pp. 423 – 425, 2008, 4th International Workshop on Infrared Microscopy and Spectroscopy with Accelerator-Based Sources.

[53] Z.-M. Sheng, K. Mima, J. Zhang, and H. Sanuki, "Emission of electromagnetic pulses from laser wakefields through linear mode conversion," Phys. Rev. Lett., vol. 94, p. 095003, 2005.

[54] G. L. Carr, M. C. Martin, W. R. McKinney, K. Jordan, G. R. Neil, and G. P. Williams, "High-power terahertz radiation from relativistic electrons," Nature, no. 420, pp. 153–156, 2002.

[55] H. Hamster, A. Sullivan, S. Gordon, and R. W. Falcone, "Short-pulse terahertz radiation from high-intensity-laser-produced plasmas," Phys. Rev. E, vol. 49, pp. 671–677, 1994.

[56] T. Löffler, F. Jacob, and H. G. Roskos, "Generation of terahertz pulses by photoionization of electrically biased air," Applied Physics Letters, vol. 77, no. 3, pp. 453–455, 2000.

[57] K.-Y. Kim, J. H. Glownia, A. J. Taylor, and G. Rodriguez, "Terahertz emission from ultrafast ionizing air in symmetry-broken laser fields," Opt. Express, vol. 15, p. 4577, 2007.

[58] P. Sprangle, J. R. Peñano, B. Hafizi, and C. A. Kapetanakos, "Ultrashort laser pulses and electromagnetic pulse generation in air and on dielectric surfaces," Phys. Rev. E, vol. 69, p. 066415, 2004.

[59] C. D'Amico, A. Houard, S. Akturk, Y. Liu, J. Le Bloas, M. Franco, B. Prade, A. Couairon, V. T. Tikhonchuk, and A. Mysyrowicz, "Forward THz radiation emission by femtosecond filamentation in gases: theory and experiment," New. J. Phys., vol. 10, 2008.

[60] C. D'Amico, A. Houard, M. Franco, B. Prade, A. Mysyrowicz, A. Couairon, and V. T. Tikhonchuk, "Conical forward THz emission from femtosecond-laser-beam filamentation in air," Phys. Rev. Lett., vol. 98, p. 235002, 2007.

[61] F. Buccheri and X.-C. Zhang, "Terahertz emission from laser-induced microplasma in ambient air," Optica, vol. 2, pp. 366–369, 2015.

[62] P. González de Alaiza Martínez, X. Davoine, A. Debayle, L. Gremillet, and L. Bergé, "Terahertz radiation driven by two-color laser pulses at near-relativistic intensities: Competition between photoionization and wakefield effects," Scientific Reports, vol. 6, p. 26743, 2016.

[63] N. A. Zharova, V. A. Mironov, and D. A. Fadeev, "Anisotropic effects of terahertz emission from laser sparks in air," Phys. Rev. E, vol. 82, p. 056409, 2010.

[64] A. Houard, Y. Liu, B. Prade, V. T. Tikhonchuk, and A. Mysyrowicz, "Strong enhancement of terahertz radiation from laser filaments in air by a static electric field," Phys. Rev. Lett., vol. 100, p. 255006, 2008.

[65] T. Löffler and H. G. Roskos, "Gas-pressure dependence of terahertz-pulse generation in a laser-generated nitrogen plasma," Journal of Applied Physics, vol. 91, no. 5, pp. 2611–2614, 2002.

[66] M. D. Thomson, M. Kreß, T. Löffler, and H. G. Roskos, "Broadband THz emission from gas plasmas induced by femtosecond optical pulses: From fundamentals to applications," Laser & Photonics Reviews, vol. 1, no. 4, pp. 349–368, 2007.

[67] Y. Chen, T. jun Wang, C. Marceau, F. Théberge, M. Châteauneuf, J. Dubois, O. Kosareva, and S. L. Chin, "Characterization of terahertz emission from a dc-biased filament in air," Applied Physics Letters, vol. 95, no. 10, p. 101101, 2009.

[68] X. Lu and X.-C. Zhang, "Generation of elliptically polarized terahertz waves from laser-induced plasma with double helix electrodes," Phys. Rev. Lett., vol. 108, p. 123903, 2012.

[69] K. Reimann, "Table-top sources of ultrashort THz pulses," Reports on Progress in Physics, vol. 70, no. 10, p. 1597, 2007.

[70] D. J. Cook and R. M. Hochstrasser, "Intense terahertz pulses by four-wave rectification in air," Opt. Lett., vol. 25, no. 16, pp. 1210–1212, 2000.

[71] K. Y. Kim, A. J. Taylor, S. L. Chin, and G. Rodriguez, "Coherent control of terahertz supercontinuum generation in ultrafast laser-gas interactions," Nat. Photon., vol. 2, p. 605, 2008.

[72] A. Nguyen, P. G. de Alaiza Martínez, J. Déchard, I. Thiele, I. Babushkin, S. Skupin, and L. Bergé, "Spectral dynamics of THz pulses generated by two-color laser filaments in air: the role of kerr nonlinearities and pump wavelength," Opt. Express, vol. 25, no. 5, pp. 4720–4740, Mar 2017.

[73] M. Clerici, M. Peccianti, B. E. Schmidt, L. Caspani, M. Shalaby, M. Giguère, A. Lotti, A. Couairon, F. Légaré, T. Ozaki, D. Faccio, and R. Morandotti, "Wavelength scaling of terahertz generation by gas ionization," Phys. Rev. Lett., vol. 110, p. 253901, 2013.

[74] V. A. Andreeva, O. G. Kosareva, N. A. Panov, D. E. Shipilo, P. M. Solyankin, M. N. Esaulkov, P. González de Alaiza Martínez, A. P. Shkurinov, V. A. Makarov, L. Bergé, and S. L. Chin, "Ultrabroad terahertz spectrum generation from an air-based filament plasma," Phys. Rev. Lett., vol. 116, p. 063902, 2016.

[75] I. Babushkin, W. Kuehn, C. Köhler, S. Skupin, L. Bergé, K. Reimann, M. Woerner, J. Herrmann, and T. Elsaesser, "Ultrafast spatiotemporal dynamics of terahertz generation by ionizing two-color femtosecond pulses in gases," Phys. Rev. Lett., vol. 105, p. 053903, 2010.

[76] F. Brunel, "Harmonic generation due to plasma effects in a gas undergoing multiphoton ionization in the high-intensity limit," J. Opt. Soc. Am. B, vol. 7, no. 4, pp. 521–526, 1990.

[77] I. Babushkin, C. Brée, C. M. Dietrich, A. Demircan, U. Morgner, and A. Husakou, "Terahertz and higher-order brunel harmonics: from tunnel to multiphoton ionization regime in tailored fields," Journal of Modern Optics, vol. 64, no. 10-11, pp. 1078–1087, 2017.

[78] E. Cabrera-Granado, Y. Chen, I. Babushkin, L. Bergé, and S. Skupin, "Spectral self-action of THz emission from ionizing two-color laser pulses in gases," New J. Phys., vol. 17, p. 023060, 2015.

[79] L. V. Keldysh, "Ionization in the field of a strong electromagnetic wave," Sov. Phys. JETP, vol. 20, p. 1307, 1965.

[80] "NIST Atomic Spectra Database," http://www.nist.gov/pml/data/asd.cfm.

[81] M. Uiberacker, T. Uphues, M. Schultze, A. J. Verhoef, V. Yakovlev, M. F. Kling, J. Rauschenberger, N. M. Kabachnik, H. Schroder, M. Lezius, K. L. Kompa, H.-G. Muller, M. J. J. Vrakking, S. Hendel, U. Kleineberg, U. Heinzmann, M. Drescher, and F. Krausz, "Attosecond real-time observation of electron tunnelling in atoms," Nature, vol. 446, pp. 627–632, 2007.

[82] A. J. Verhoef, A. V. Mitrofanov, E. E. Serebryannikov, D. V. Kartashov, A. M. Zheltikov, and A. Baltuška, "Optical detection of tunneling ionization," Phys. Rev. Lett., vol. 104, p. 163904, Apr 2010.

[83] K. Schuh, M. Scheller, J. Hader, J. V. Moloney, and S. W. Koch, "Quantum theory of terahertz emission due to ultrashort pulse ionization of gases," Phys. Rev. E, vol. 88, p. 063102, 2013.

[84] M. Ammosov, N. Delone, and V. Krainov, "Tunnel ionization of complex atoms and of atomic ions in an alternating electric field," Sov. Phys. JETP, vol. 64, p. 1191, 1986.

[85] G. L. Yudin and M. Y. Ivanov, "Nonadiabatic tunnel ionization: Looking inside a laser cycle," Phys. Rev. A, vol. 64, p. 013409, 2001.

[86] C. Bree, A. Demircan, and G. Steinmeyer, "Method for computing the nonlinear refractive index via keldysh theory," IEEE Journal of Quantum Electronics, vol. 46, no. 4, pp. 433–437, 2010.

[87] C. Köhler, "Ultrashort light sources from high intensity laser-matter interaction," Ph.D. dissertation, Technische Universität Dresden, 2012.

[88] I. Babushkin, S. Skupin, A. Husakou, C. Köhler, E. Cabrera-Granado, L. Bergé, and J. Herrmann, "Tailoring terahertz radiation by controlling tunnel photoionization events in gases," New Journal of Physics, vol. 13, no. 12, p. 123029, 2011.

[89] G. de Alaiza Martínez, I. Babushkin, L. Bergé, S. Skupin, E. Cabrera-Granado, C. Köhler, U. Morgner, A. Husakou, and J. Herrmann, "Boosting terahertz generation in laser-field ionized gases using a sawtooth wave shape," Phys. Rev. Lett., vol. 114, p. 183901, 2015.

[90] M. N. Polyanskiy, "Refractive index database," https://refractiveindex.info, accessed on 2017-04-21.

[91] E. R. Peck and D. J. Fisher, "Dispersion of argon," J. Opt. Soc. Am., vol. 54, no. 11, pp. 1362–1364, 1964.

[92] P. B. Corkum, "Plasma perspective on strong field multiphoton ionization," Phys. Rev. Lett., vol. 71, pp. 1994–1997, 1993.

[93] B. Zhou, S. Akturk, B. Prade, Y.-B. André, A. Houard, Y. Liu, M. Franco, C. D'Amico, E. Salmon, Z.-Q. Hao, N. Lascoux, and A. Mysyrowicz, "Revival of femtosecond laser plasma filaments in air by a nanosecond laser," Opt. Express, vol. 17, no. 14, pp. 11 450–11 456, 2009.

[94] J. D. Huba, NRL PLASMA FORMULARY Supported by The Office of Naval Research. Washington, DC: Naval Research Laboratory, 2013.

[95] C. Köhler, E. Cabrera-Granado, I. Babushkin, L. Bergé, J. Herrmann, and S. Skupin, "Directionality of terahertz emission from photoinduced gas plasmas," Opt. Lett., vol. 36, no. 16, pp. 3166–3168, 2011.

[96] A. Debayle, L. Gremillet, L. Bergé, and C. Köhler, "Analytical model for THz emissions induced by laser-gas interaction," Opt. Express, vol. 22, no. 11, pp. 13 691–13 709, 2014.

[97] L. Bergé, S. Skupin, C. Köhler, I. Babushkin, and J. Herrmann, "3D numerical simulations of THz generation by two-color laser filaments," Phys. Rev. Lett., vol. 110, p. 073901, 2013.

[98] Bronstein, I. N. and Semedjajew, K. A. and Musiol, G. and Mühlig, H., Taschenbuch der Mathematik. Verlag Harri Deutsch, 2008.

[99] R. Nuter and V. Tikhonchuk, "Prepulse suppression and optimization of backward raman amplification with a chirped pump laser beam," Phys. Rev. E, vol. 87, p. 043109, 2013.

[100] R. Nuter, L. Gremillet, E. Lefebvre, A. Lévy, T. Ceccotti, and P. Martin, "Field ionization model implemented in particle in cell code and applied to laser-accelerated carbon ions," Physics of Plasmas, vol. 18, no. 3, 2011.

[101] C. K. Birdsall and A. B. Langdon, Plasma physics via computer simulation. New York, NY: Taylor & Francis Group, 2005.

[102] F. Pérez, L. Gremillet, A. Decoster, M. Drouin, and E. Lefebvre, "Improved modeling of relativistic collisions and collisional ionization in particle-in-cell codes," Physics of Plasmas, vol. 19, no. 8, 2012.

[103] K. S. Yee, "Numerical solution of initial boundary value problems involving Maxwell's equations in isotropic media," IEEE Trans. Antennas Propagat., vol. AP-14, pp. 302–307, 1966.

[104] "Finite-difference time-domain method," https://en.wikipedia.org/wiki/Finite-difference_time-domain_method, accessed: 2017-05-04.

[105] A. Taflove, Computational Electrodynamics: The Finite - Difference Time - Domain Method, ser. Antennas and Propagation Library. Artech House, Incorporated, 1995.

[106] S. He and V. H. Weston, "Wave-splitting and absorbing boundary condition for maxwell's equations on a curved surface," Math. Comput. Simul., vol. 50, 1999.

[107] R. Nuter, M. Grech, P. Gonzalez de Alaiza Martinez, G. Bonnaud, and E. d'Humières, "Maxwell solvers for the simulations of the laser-matter interaction," The European Physical Journal D, vol. 68, p. 177, 2014.

[108] E. F. Toro, Riemann solvers and numerical methods for fluid dynamics: A practical introduction. Springer-Verlag, 2009.

[109] T. Esirkepov, "Exact charge conservation scheme for particle-in-cell simulation with an arbitrary form-factor," Computer Physics Communications, vol. 135, no. 2, pp. 144 – 153, 2001.

[110] E. Lefebvre, N. Cochet, S. Fritzler, V. Malka, M.-M. Aléonard, J.-F. Chemin, S. Darbon, L. Disdier, J. Faure, A. Fedotoff, O. Landoas, G. Malka, V. Méot, P. Morel, M. R. L. Gloahec, A. Rouyer, C. Rubbelynck, V. Tikhonchuk, R. Wrobel, P. Audebert, and C. Rousseaux, "Electron and photon production from relativistic laser-plasma interactions," Nucl. Fusion, vol. 43, p. 629, 2003.

[111] R. Mishra, P. Leblanc, Y. Sentoku, M. S. Wei, and F. N. Beg, "Collisional particle-in-cell modeling for energy transport accompanied by atomic processes in dense plasmas," Phys. Plasmas, vol. 20, p. 072704, 2013.

[112] M. Born, E. Wolf, and A. Bhatia, Principles of Optics: Electromagnetic Theory of Propagation, Interference and Diffraction of Light. Cambridge University Press, 1999.

[113] J. Goodman, Introduction to Fourier Optics, ser. McGraw-Hill physical and quantum electronics series. Roberts & Company, 2005.

[114] S. M. Sepke and D. P. Umstadter, "Analytical solutions for the electromagnetic fields of flattened and annular gaussian laser modes. III. Arbitrary length pulses and spot sizes," J. Opt. Soc. Am. A, vol. 23, no. 11, pp. 2295–2302, 2006.

[115] Y. Salamin, "Fields of a gaussian beam beyond the paraxial approximation," Appl. Phys. B, vol. 86, pp. 319–326, 2007.

[116] C. J. R. Sheppard and S. Saghafi, "Electromagnetic gaussian beams beyond the paraxial approximation," J. Opt. Soc. Am. A, vol. 16, pp. 1381–1386, 1999.

[117] S. M. Sepke and D. P. Umstadter, "Analytical solutions for the electromagnetic fields of tightly focused laser beams of arbitrary pulse length," Opt. Lett., vol. 31, no. 17, pp. 2589–2591, Sep 2006.

[118] K. I. Popov, V. Y. Bychenkov, W. Rozmus, and R. D. Sydora, "Electron vacuum acceleration by a tightly focused laser pulse," Physics of Plasmas, vol. 15, p. 013108, 2008.

[119] I. Thiele, S. Skupin, and R. Nuter, "Boundary conditions for arbitrarily shaped and tightly focused laser pulses in electromagnetic codes," Journal of Computational Physics, vol. 321, pp. 1110 – 1119, 2016.

[120] Y. I. Salamin, "Accurate fields of a radially polarized gaussian laser beam," New. J. Phys., vol. 8, p. 133, 2006.

[121] W. H. Press, S. A. Teukolsky, W. T. Vetterling, and B. P. Flannery, Numerical Recipes in C (2Nd Ed.): The Art of Scientific Computing. New York, NY, USA: Cambridge University Press, 1992.

[122] M. Frigo and S. G. Johnson, Fastest Fourier Transform in the West, MIT, http://www.fftw.org, 2014.

[123] R. Nuter, L. Gremillet, E. Lefebvre, A. Lévy, T. Ceccotti, and P. Martin, "Field ionization model implemented in particle in cell code and applied to laser-accelerated carbon ions," Phys. Plasmas, vol. 18, p. 033107, 2011.

[124] T. A. Carlson, C. N. Jr., N. Wasserman, and J. Mcdowell, "Calculated ionization potentials for multiply charged ions," Atomic Data and Nuclear Data Tables, vol. 2, pp. 63–99, 1970.

[125] H. Wang, L. Shi, B. Lukyanchuk, C. Sheppard, and C. T. Chong, "Creation of a needle of longitudinally polarized light in vacuum using binary optics," Nat. Photonics, vol. 2, pp. 501–505, 2008.

[126] I. Thiele, R. Nuter, B. Bousquet, V. Tikhonchuk, S. Skupin, X. Davoine, L. Gremillet, and L. Bergé, "Theory of terahertz emission from femtosecond-laser-induced microplasmas," Phys. Rev. E, vol. 94, p. 063202, 2016.

[127] S. C. Rae and K. Burnett, "Possible production of cold plasmas through optical-field-induced ionization," Phys. Rev. A, vol. 46, pp. 2077–2083, Aug 1992.

[128] V. T. Tikhonchuk, "Comment on "generation of electromagnetic pulses from plasma channels induced by femtosecond light strings"," Phys. Rev. Lett., vol. 89, p. 209301, 2002.

[129] E. Barston, "Electrostatic oscillations in inhomogeneous cold plasmas," Annals of Physics, vol. 29, no. 2, pp. 282 – 303, 1964.

[130] S. B. Hasan, C. Etrich, R. Filter, C. Rockstuhl, and F. Lederer, "Enhancing the nonlinear response of plasmonic nanowire antennas by engineering their terminations," Phys. Rev. B, vol. 88, p. 205125, 2013.

[131] Y. Liu, A. Houard, B. Prade, A. Mysyrowicz, A. Diaw, and V. T. Tikhonchuk, "Amplification of transition-cherenkov terahertz radiation of femtosecond filament in air," Applied Physics Letters, vol. 93, no. 5, p. 051108, 2008.

[132] A. D. Koulouklidis, V. Y. Fedorov, and S. Tzortzakis, "Spectral bandwidth scaling laws and reconstruction of THz wave packets generated from two-color laser plasma filaments," Phys. Rev. A, vol. 93, p. 033844, 2016.

[133] M. D. Thomson, V. Blank, and H. G. Roskos, "Terahertz white-light pulses from an air plasma photo-induced by incommensurate two-color optical fields," Opt. Express, vol. 18, no. 22, pp. 23 173–23 182, Oct 2010.

[134] N. Li, Y. Bai, T. Miao, P. Liu, R. Li, and Z. Xu, "Revealing plasma oscillation in THz spectrum from laser plasma of molecular jet," Opt. Express, vol. 24, no. 20, pp. 23 009–23 017, 2016.

[135] K.-Y. Kim, "Generation of coherent terahertz radiation in ultrafast laser-gas interactions," Physics of Plasmas, vol. 16, no. 5, p. 056706, 2009.

[136] P. Klarskov, A. C. Strikwerda, K. Iwaszczuk, and P. U. Jepsen, "Experimental three-dimensional beam profiling and modeling of a terahertz beam generated from a two-color air plasma," New Journal of Physics, vol. 15, no. 7, p. 075012, 2013.

[137] L. A. Johnson, J. P. Palastro, T. M. Antonsen, and K. Y. Kim, "THz generation by optical cherenkov emission from ionizing two-color laser pulses," Phys. Rev. A, vol. 88, p. 063804, 2013.

[138] S. A. Maier, Plasmonics: Fundamentals and Applications. New York, NY: Springer, 2007.

[139] L. Froehly, F. Courvoisier, A. Mathis, M. Jacquot, L. Furfaro, R. Giust, P. A. Lacourt, and J. M. Dudley, "Arbitrary accelerating micron-scale caustic beams in two and three dimensions," Opt. Express, vol. 19, no. 17, pp. 16 455–16 465, 2011.

Acknowledgments

The one who red this thesis might have noticed that the word “we” appears very often in the manuscript. Here, I take the opportunity to say who the “we” are and thank some people who made this thesis possible.

First of all I want to thank my supervisors Dr. Stefan Skupin and Dr. Rachel Nuter. I knew Stefan already from his lectures at the University in Jena. The opportunity to learn more from him determined the actual choice to join his project in Bordeaux. I learned from him a lot about physics and how to present our work. But, the fortune hit me in this sense twofold. At any moment, I had support not only from Stefan, but also from Rachel. From the beginning, she helped me at any moment and shared her knowledge with me. The later point involves besides techniques of particle-in-cell codes and plasma physics also Bordeaux-highlights. Moreover, I cannot thank enough for all the corrections and suggestions during the compilation of the manuscript. Working together with Rachel and Stefan means for me working in a friendly and constructive atmosphere. Thank You a lot, Stefan and Rachel, for this!

I want also to thank Dr. Luc Bergé for many advices that significantly improved our publications in collaboration. In particular, his corrections and criticism on the multiple-scale analysis in Chap. 2 stimulated its final formulation that is the base for the rest of the manuscript. Also many thanks go to Professor Vladimir Tikhonchuk for sharing his experience with me, and of course the careful reading and corrections of the manuscript. Moreover, I want to thank Dr. Pedro González de Alaiza Martínez who joined our Lab CELIA one year before the completion of this thesis. Thank You very much Pedro for the willingness to discuss at any time.

I want also to thank Dr. Xavier Davoine, Dr. Laurent Gremillet for sharing their experience as well as Alisee Nguyen and Jeremy Dechard from Luc’s team who shared their ideas with me. It is great to work in an open-minded collaborative community to advance the common field of research. Furthermore, many thanks to Dr. Philip Korneev and Dr. Ihar Babushkin for the collaboration and interesting discussions. Many thanks go to Dr. Fabrizio Buccheri whose pioneering work on THz generation in laser-induced microplasmas motivated the present manuscript. Moreover, I want to thank Professor Eduardo Cabrera Granado for offering me to read my thesis and the discussions. I thank again all the collaborators, and hope that also in the future, we can score many exciting results together!

While writing this text, I don’t know how my thesis will be judged and how the defense will proceed. However, I want to thank the examinants Professor Olga Kosareva and Professor Tünde Fülöp in advance for the reading of my thesis and criticism that they have offered to me and my supervisors. Many thanks also to Dr. Evangelos Siminos, Dr. Mark Thomson, Dr. Patrick Mounaix and Professor Eric Cormier, for taking their time and being a part of my jury.

I would also like to thank my previous chiefs Dr. Andreas Brodschelm and Dr. Christoph Menzel. Without Andreas I probably would not have changed from engineering to physics that was retrospectively a correct decision. Without the job as student research assistant working with Christoph on plasmonic slab waveguides, probably, I would not have came up with the idea that also in gas-plasmas plasmonic resonances can play an important role. Christoph was also the first one who had the strength to bear my first steps in writing scientific texts in English for my master thesis. In summary, it seems like I was always lucky to have an excellent supervision. Many thanks to all my supervisors for that!

Finally, I want to thank my small family, my parents Irina and Thomas, my wife Evgeniya and my grand parents Yulia, Genadii, Helga and Peter. They stay in all important questions and decisions behind me and give me a home, wherever I am. I promise to do my best as I did up to now also in the future!

Titre: Étude théorique de la génération térahertz dans les microplasmas induits par laser

Résumé: Nous étudions la génération de rayonnement TeraHertz (THz) dans des microplasmas produits par des lasers femtosecondes. Cette technique est prometteuse pour créer efficacement des sources THz compactes et étendue spectralement (0.3-30 THz), qui intéressent de nombreuses applications, comme l'identification spectroscopique de substances dangereuses ou encore l'imagerie en biologie et médecine. Contrairement aux sources conventionnelles, comme les interrupteurs photo-conducteur, les sources THz basées sur des plasmas ne sont pas limitées par la tenue au flux et couvrent l'ensemble du spectre THz. Afin de modéliser des microplasmas générés par des faisceaux laser fortement focalisés, nous présentons un nouvel algorithme qui permet d'injecter tout type de laser dans des codes électromagnétiques. Nous dérivons aussi un modèle compatible avec les équations de Maxwell qui inclut les deux mécanismes générateurs de THz: le courant d'ionisation (IC) et le mécanisme "Transition-Cherenkov" (TC). Ce dernier mécanisme domine la production de THz pour des lasers à plusieurs cycles optiques, où l'émission est produite par les courants d'électron longitudinaux. Dans le cas des microplasmas où un champ électrostatique externe est ajouté, le taux de conversion énergétique laser/THz peut être augmenté de deux ordres de grandeur via le mécanisme IC lorsque le champs statique ou la pression du gaz sont accrus. De plus, les simulations 3D montrent que pour un faisceau laser à deux couleurs et dans des conditions optimales de focalisation, une énergie laser de 10 micro-Joule est suffisante pour atteindre des taux de conversion bien au-dessus de 10^{-4}. Dans ce cas, la nature transverse du courant IC est cruciale pour accroitre l'efficacité avec la longueur du plasma. En considérant un faisceau laser à deux couleurs de forme elliptique, nous proposons de contrôler les spectres d'émission en exploitant les effets plasmoniques résonants.

Mots clés: Sources terahertz, microplasma, codes électromagnétiques, forte focalisation

---

Title: Theoretical investigations of terahertz generation in laser-induced microplasmas

Abstract: We investigate terahertz (THz) generation in fs-laser-induced microplasmas, which are promising candidates for compact and efficient broadband THz sources (0.3-30 THz). Such sources have various applications as spectroscopic identification of hazardous substances or THz imaging in biology and medicine. Unlike conventional THz sources as photoconductive switches, gas-plasma-based THz sources do not suffer from irreversible material damage and can cover the whole THz range at once. To simulate tightly-focused-laser-induced microplasmas, we propose an efficient numerical algorithm that can introduce any arbitrarily shaped laser pulses into electromagnetic codes. We derive a Maxwell-consistent model that includes two major THz generation mechanisms, the ionization current (IC) and transition-Cherenkov mechanisms (TC). The latter mechanism is shown to dominate for single-color multi-cycle lasers pulses where the emission is driven by longitudinal electron currents. For microplasmas a constant electric field can boost the laser-to-THz converison efficiency by two orders of magnitude via the IC mechanism when increasing the gas-pressure and bias-voltage. Moreover for two-color-driving laser pulses, Maxwell-consistent 3D simulations show, that only 10 μJ laser pulse energy are sufficient to reach conversion efficiencies well above 10^{-4} when optimizing the focusing conditions. Here, the transverse nature of the IC currents is crucial for the up-scaling of the efficiency with the plasma length. By using elliptically-shaped two-color-driving laser beams, we propose to control the emission spectra by exploiting resonant plasmonic effects.

Keywords: THz sources, microplasma, electromagnetic codes, tight focusing

---

Univ. Bordeaux - CNRS - CEA, CEntre Lasers Intenses et Applications, UMR 5107, 33405 Talence, France